Scientifica
2018

LORENZO FRANCESCO LIVI

New quantum simulations with ultracold Ytterbium gases

PREMIO TESI DOTTORATO
FIRENZE UNIVERSITY PRESS – UNIVERSITÀ DEGLI STUDI DI FIRENZE

FIRENZE UNIVERSITY PRESS

ISSN 2612-8039 (PRINT) | ISSN 2612-8020 (ONLINE)

PREMIO TESI DI DOTTORATO

Commissione giudicatrice, anno 2018

Vincenzo Varano, *Presidente della Commissione*

Tito Arecchi, *Area Scientifica*
Aldo Bompani, *Area delle Scienze Sociali*
Mario Caciagli, *Area delle Scienze Sociali*
Franco Cambi, *Area Umanistica*
Paolo Felli, *Area Tecnologica*
Giancarlo Garfagnini, *Area Umanistica*
Roberto Genesio, *Area Tecnologica*
Flavio Moroni, *Area Biomedica*
Adolfo Pazzagli, *Area Biomedica*
Giuliano Pinto, *Area Umanistica*
Vincenzo Schettino, *Area Scientifica*
Luca Uzielli, *Area Tecnologica*
Graziella Vescovini, *Area Umanistica*

Lorenzo Francesco Livi

New quantum simulations with ultracold Ytterbium gases

Firenze University Press
2019

New quantum simulations with ultracold Ytterbium gases / Lorenzo Francesco Livi. – Firenze : Firenze University Press, 2019.
(Premio Tesi di Dottorato ; 78)

https://www.fupress.com/isbn/9788864539898

ISSN 2612-8039 (print)
ISSN 2612-8020 (online)
ISBN 978-88-6453-988-1 (print)
ISBN 978-88-6453-989-8 (online PDF)

Graphic design: Alberto Pizarro Fernández, Lettera Meccanica SRLs
Front cover: © Rik Trottier | Dreamstime.com

***

Peer Review Process

All publications are submitted to an external refereeing process under the responsibility of the FUP Editorial Board and the Scientific Committees of the individual series. The works published in the FUP catalogue are evaluated and approved by the Editorial Board of the publishing house. For a more detailed description of the refereeing process we refer to the official documents published on the website and in the online catalogue (www.fupress.com).

Firenze University Press Editorial Board

M. Garzaniti (Editor-in-Chief), M.E. Alberti, M. Boddi, A. Bucelli, R. Casalbuoni, A. Dolfi, R. Ferrise, M.C. Grisolia, P. Guarnieri, R. Lanfredini, P. Lo Nostro, G. Mari, A. Mariani, P.M. Mariano, S. Marinai, R. Minuti, P. Nanni, A. Orlandi, A. Perulli, G. Pratesi.

Published by Firenze University Press

Firenze University Press
Università degli Studi di Firenze
via Cittadella, 7, 50144 Firenze, Italy
www.fupress.com

This book is printed on acid-free paper
Printed in Italy

Contents

Lorenzo Francesco Livi, *New quantum simulations with ultracold Ytterbium gases*, © 2020 Author(s), content CC BY 4.0 International, metadata CC0 1.0 Universal, published by Firenze University Press (www.fupress.com), ISSN 2612-8020 (online), ISBN 978-88-6453-989-8 (online PDF)

Introduction

In recent years, atomic physics has evolved from a branch of science in which matter is only investigated, primarily by means of spectroscopy, to a platform in which quantum matter is synthesized in its most exotic forms. This breakthrough has been enabled by the realization of degenerate quantum gases of neutral bosonic (Anderson et al., 1995; Davis et al., 1995) and fermionic atoms (DeMarco and Jin, 1999), that allow the realization of systems characterized by a high degree of tunability over several quantum properties. Optical lattices (Bloch, 2005; Jaksch and Zoller, 2005) have played a major role in this context, due to the possibility offered by this tool to mimic the physics of electrons in solids in a clean environment, free from the defects of real systems (Lewenstein et al., 2007; Bloch et al., 2012; Gross and Bloch, 2017). Optical lattices are extremely flexible systems in which a considerable number of quantum parameters, such as the tunnelling strength, the interaction energy or the geometry, can be directly controlled by means of a proper engineering of the optical potentials (Bloch et al., 2008). From this prospect, optical lattices represent an ideal platform to realize Feynman's famous idea of a *quantum simulator* (Feynman, 1982) in which the Hamiltonian of a complex quantum system is mapped onto the Hamiltonian of the simulator, which in turn reproduces the original dynamics of the system in a controllable way (Buluta and Nori, 2009; Georgescu et al., 2014). This approach could overcome the limitations imposed by actual available computer capabilities, allowing the resolution of problems for which an excessive amount of resources would be requested, such as the time evolution or the determination of the ground-state of quantum many-body interacting systems (Trotzky et al., 2012). An interesting feature of quantum simulators is the possibility to reproduce only a defined subset of properties of a more complex system, realizing in this way implementations of simpler *toy-model* of the specific phenomenon of interest. In particular, the realization of toy-models of quantum-Hall systems is a current trend in the context of quantum simulation, in which neutral ultracold quantum gases trapped in optical lattices potentials have emerged as a promising tool (Dalibard et al., 2011; Goldman et al., 2014; Aidelsburger et al., 2011, 2013; Struck et al., 2012; Jiménez-García et al., 2012; Galitski and Spielman, 2013). These systems allow both to shed light on some elusive phenomena and to access regimes of incredibly high magnetic fields which are impossible to obtain in real solid-state systems, paving the way to the observation of exotic phases of matter. This kind of investigation is strongly related to the physics of topology and topological insulator (Goldman et al., 2016), in which the interplay between magnetic fields, spin-orbit coupling and interactions gives rise to a series of fascinating effects (Hasan and Kane, 2010; Kane

Lorenzo Francesco Livi, *New quantum simulations with ultracold Ytterbium gases*, © 2020 Author(s), content CC BY 4.0 International, metadata CC0 1.0 Universal, published by Firenze University Press (www.fupress.com), ISSN 2612-8020 (online), ISBN 978-88-6453-989-8 (online PDF)

and Mele, 2005; Kane and Moore, 2011).

This thesis fits with this context and mainly deals with the simulation of some fundamental properties of quantum-Hall systems by means of fermionic Ytterbium (Yb) atoms confined in optical lattices. Yb is an alkaline-earth-like atom with an electronic structure analogous to the one of the elements of the second column of the periodic table. Two-electron atoms have emerged as a promising tool in the quantum simulation framework due to their rich internal structure which can be used to expand the range of possibilities offered by alkali atoms, for example in the simulation of multicomponent and multi-orbital Hubbard and spin models (Gorshkov et al., 2009; Cazailla and Rey, 2014). A major property of this class of elements is the presence of electronically excited metastable levels (or clock states) characterized by lifetimes of the order of several seconds (Porsev and Derevianko, 2003; Porsev et al., 2004) which have enabled the realization of the most accurate atomic clocks (Hinkley et al., 2013; Bloom et al., 2014), paving the way to a redefinition of the SI second (Derevianko and Katori, 2011; Poli et al., 2013; Ludlow et al., 2015). Remarkably, these metastable states generate a lot of interest also in the context of quantum simulation, where they are treated as a second ground-state of the system. In this thesis we exploit the ability to control this orbital degree of freedom to experimentally investigate some recently proposed schemes of quantum simulation aimed to the realization of toy-models of quantum-Hall systems.

We start with the demonstration (Livi et al., 2016) of the possibility to implement Spin-Orbit Coupling (SOC) with single-photon clock transitions in a system of fermionic ^{173}Yb atoms trapped in a one-dimensional optical lattice, using as pseudospin states the fundamental level and the clock state $^3P_0$ (Wall et al., 2016). This orbital approach to the synthesis of SOC in ultracold gases allows us to overcome some of the limitations imposed, for example, by Raman schemes (Lin et al., 2011), where heating due to the presence of intermediate levels have detrimental effects in the observation of many-body processes.

The implementation of synthetic SOC is the base for a second major experiment in which we exploited the clock coupling to realize an artificial magnetic field for atoms trapped in an optical lattice. The scheme that we adopted relies on the concept of *synthetic dimension*, which is based on the interpretation of an internal degree of freedom of the atom as an extra dimension of the system (Boada et al., 2012; Celi et al., 2014). The combination of a real one-dimensional optical lattice with a two-site synthetic dimension mapped on the fundamental and clock levels of ^{173}Yb allowed us to simulate a two-leg hybrid ladder geometry (Livi et al., 2016). An artificial magnetic field naturally arises in this hybrid 2D lattice as a consequence of the phase imprinted on the atoms by the clock coupling between the synthetic sites. Despite the reduced geometry, this system features some of the fundamental properties of larger Hall systems, one of which is the presence of chiral currents that counter-propagate along the edges (Hügel and Paredes, 2014). We demonstrated the possibility to induce and detect these currents in our artificial system and characterized for the first time their strength as a function of the synthetic flux, a result impossible to achieve in real solid-state systems where magnetic fields of the order of several thousand of Tesla would be required.

This approach to the realization of an artificial gauge field for neutral atoms could be virtually extended to any stable atomic degree of freedom for which a coherent cou-

pling can be induced. In particular, we also implemented a similar scheme mapping the synthetic dimension on the nuclear spins of the fundamental level of ^{173}Yb and realizing the coupling by means of two-photon Raman transitions (Mancini et al., 2015). Similar experiments have been performed with this system, in which the emergence of chiral currents in two- and three-leg ladder geometries has been investigated.

The orbital degree of freeedom of ^{173}Yb can also be exploited to control a new kind of Feshbach resonance, which allows us to tune the scattering properties in a mixture of atoms in different orbital states (Zhang et al., 2015; Cheng et al., 2016). The possibility to tune interactions by means of standard Feshbach resonances (Chin et al., 2010) lacked in two-electron atoms, due to the absence of a hyperfine structure in the fundamental state. We instead experimentally demonstrated (Pagano et al., 2015) how a similar mechanism is possible also for this class of elements, provided that atoms in two different electronic states are considered. In particular, we exploited the *orbital Feshbach resonance* (OrbFR) mechanism to realize a strongly interacting two-orbital gas of ^{173}Yb and characterized the resonance position. The interaction tunability offered by OrbFRs can in future be exploited in combination with the orbital synthetic dimension scheme to investigate the effect of interactions in Hall-like systems, which is a currently debated topic (Barbarino et al., 2015, 2016).

The thesis is organized as follows:

- **Chapter 1** introduces the fundamental properties of Ytterbium, in particular focusing the attention on the emergence of SU(N) interactions and spin-exchange symmetries (Gorshkov et al., 2009). This introduction is followed by a summarizing description of the experimental setup in which the laser systems and the cooling procedure which enables us to obtain a degenerate Yb gas are discussed. Along with this description, a review of the various optical techniques that we developed in order to manipulate and detect the orbital and spin degrees of freedom of Yb atoms is presented. We also briefly introduce the physics of atoms in optical lattices and the formalism of Wannier functions, that constitute a key ingredient for the experimental results presented throughout this work.

- In **Chapter 2** the fundamental properties of quantum Hall physics are introduced. This theoretical introduction mainly deals with the aspects of quantum Hall systems that we experimentally investigate in chapters 4 and 5, which are the presence of edge states, their connection with topology and spin-orbit coupling. Quantum Hall theory is then reviewed from a lattice perspective, introducing the concept of Peierls phase (Peierls, 1933) and discussing how the presence of a magnetic field affects a ladder system or a larger 2D lattice, giving rise to the Hofstadter spectrum (Hofstadter, 1976). The final part of the chapter is instead devoted to a description of the various techniques developed to simulate this kind of physics with ultracold quantum gases, with a main focus on the *synthetic dimension* approach, which constitutes the core of the experimental part of this work.

- **Chapter 3** reviews some of the fundamental properties of the $^1S_0 \rightarrow {}^3P_0$ clock transition excitation in ^{173}Yb. After an introduction of the fundamental physical properties of this peculiar transition, its experimental addressing is discussed.

Spectroscopy in the Lamb-Dicke regime (Dicke, 1953) is introduced and the advantages of this technique in terms of spectroscopic resolution are presented, focusing the attention on the capability of our clock laser system to enable the observation of interaction- and sideband-resolved spectra. The possibility to long-term stabilize our clock laser on an absolute reference through a fiber link with a metrological institute (Clivati et al., 2016) is discussed in the final part of the chapter. Remarkably, thanks to this long-term stabilization, we have been able to improve the absolute value of the $^1S_0 \rightarrow {}^3P_0$ transition for ^{173}Yb by two orders of magnitude with respect to the value previously reported in literature (Clivati et al., 2016). These last topics also constitute a major part of the PhD thesis of my colleague Giacomo Cappellini (Cappellini, 2016).

- **Chapter 4** reports the main experimental results of this work, in which we have exploited the orbital degree of freedom of ^{173}Yb for quantum simulation purposes (Livi et al., 2016). The possibility to implement synthetic spin-orbit coupling (SOC) between two different orbital states of ^{173}Yb atoms trapped in optical lattices is demonstrated through spectroscopic techniques, detecting the SOC-induced broadening of the transition spectrum (Wall et al., 2016). The realization of an artificial magnetic field for neutral atoms with the synthetic dimension approach is then demonstrated using as an extra dimension the two long-lived electronic states of ^{173}Yb. We have directly measured the chiral currents circulating on the resulting two-leg ladder, probing them as a function of the synthetic flux and comparing the results with a theoretical model. The final part of the chapter deals, instead, with the realization of a strongly interacting ^{173}Yb gas exploiting the orbital Feshbach resonance mechanism. In this experiment, the enhancement of interactions is detected observing and evaluating the hydrodynamic expansion of the gas (Pagano et al., 2015).

- **Chapter 5** reviews the complementary approach that we investigated to implement an artificial magnetic field for neutral atoms, in which the synthetic dimension is realized exploiting the nuclear-spin degree of freedom of the fundamental level of ^{173}Yb. Two- and three-leg ladder geometries are realized and the emergence of chiral currents and skipping orbits has been observed (Mancini et al., 2015). This topic also constitutes the main subject of the PhD thesis of my former colleague Marco Mancini (Mancini, 2016).

- **Chapter 6** is instead devoted to some recent results, deviating from the main object of this thesis, in which the properties of clock excitation in bosonic ^{174}Yb have been investigated (Franchi et al., 2017). By means of high-resolution spectroscopic measurements on particles confined in a 3D optical lattice, the scattering lengths and loss rate coefficients for atoms in different collisional channels involving the ground level $^1S_0$ and the metastable state $^3P_0$ are derived. These quantities, that at our knowledge were still unreported in literature before our work, set important constraints for future experimental studies of two-electron atoms for quantum-technological applications.

Publications

The results shown in this thesis are reported in the following references (in chronological order):

- M. Mancini, G. Pagano, G. Cappellini, L. F. Livi, M. Rider, J. Catani, C. Sias, P. Zoller, M. Inguscio, M. Dalmonte, and L. Fallani, *Observation of chiral edge states with neutral fermions in synthetic Hall ribbons*, Science **349**, 1510 (2015)

- G. Pagano, M. Mancini, G. Cappellini, L. F. Livi, C. Sias, J. Catani, M. Inguscio, and L. Fallani, *Strongly interacting gas of two-electron fermions at an orbital Feshbach resonance*, Phys. Rev. Lett. **115**, 265301 (2015)

- C. Clivati, G. Cappellini, L. F. Livi, F. Poggiali, M. Siciliani de Cumis, M. Mancini, G. Pagano, M. Frittelli, A. Mura, G. A. Costanzo, F. Levi, D. Calonico, L. Fallani, J. Catani, M. Inguscio, *Measuring absolute frequencies beyond the GPS limit via long-haul optical frequency dissemination*, Opt. Express **24**, 11865 (2016)

- L. F. Livi, G. Cappellini, M. Diem, L. Franchi, C. Clivati, M. Frittelli, F. Levi, D. Calonico, J. Catani, M. Inguscio, L. Fallani, *Synthetic dimensions and spin-orbit coupling with an optical clock transition*, Phys. Rev. Lett. **117**, 220401 (2016)

- L. Franchi, L. F. Livi, G. Cappellini, G. Binella, M. Inguscio, J. Catani, L. Fallani, *State-dependent interactions in ultracold ^{174}Yb probed by optical clock spectroscopy*, New J. Phys. In press. (2017)

Chapter 1
Making a degenerate Ytterbium gas

Ytterbium (Yb) shares with alkaline-earth metals a similar electronic configuration in which the main features are the presence of two electrons in the outermost s shell and a closed configuration for all the other inner shells. As for the elements of the second group of the periodic table, the lowest-energy excited levels of Yb are determined by excitations of one of the two external electrons that can combine either in singlet ($S = 0$) or triplet ($S = 1$) states. In particular, the fundamental level of Yb is the singlet state $^1S_0$. Quantum mechanics selection rules forbid dipole transitions between singlet and triplet states since the electric dipole operator cannot change the spin of an electron. Selection rules are however strictly observed only in lighter elements and this is not the case of Yb. In heavier atoms the $L - S$ coupling scheme is less accurate since fine-structure corrections become more important as the atomic number increases. As a consequence of this, the quantum number S is not exactly defined and *intercombination* transitions between states with different spin become possible.

Among these transitions, two in particular assume an important role in the physics of ultracold atoms. The first is the intercombination transition $^1S_0 \rightarrow {}^3P_1$, which is commonly employed in laser-cooling schemes. The reduction of validity of the $L - S$ coupling scheme in Yb is well exemplified by the linewidth of this transition which in Yb is $\Gamma \simeq 2\pi\times 180$ kHz, a value several orders of magnitude higher than the one found in lighter two-electron elements such as Mg (0.048 kHz) or Sr (7.4 kHz), for which fine-structure corrections are less important. The other fundamental intercombination transition is the one connecting the ground level with the triplet state $^3P_0$. This is a doubly forbidden transition in which in addition to the spin conservation rule also the angular momentum conservation rule is violated. As a consequence of the violation of two selection rules this transition is characterized by a strongly reduced linewidth (few tens of mHz for fermionic Yb), which results in an impressive Q-factor of the order of 10^{16} that makes it ideal to be exploited for the realization of atomic clocks (Poli et al., 2013; Ludlow et al., 2015; Porsev et al., 2004). Moreover, due to the Heisenberg uncertainty principle, the extremely precise definition of the transition energy is accompanied by an exceptionally long lifetime of the $^3P_0$ state (~ 20 s in Yb) if compared with typical atomic levels. This *metastable state* can somehow be treated as a second ground state for the atomic system, a feature which paves the way for many quantum simulation schemes (Gorshkov et al., 2009; Cazailla and Rey, 2014).

In this chapter we firstly outline the principal physical and chemical properties of Yb, focusing the attention on the transitions employed in the context of the physics of

Lorenzo Francesco Livi, *New quantum simulations with ultracold Ytterbium gases*, © 2020 Author(s), content CC BY 4.0 International, metadata CC0 1.0 Universal, published by Firenze University Press (www.fupress.com), ISSN 2612-8020 (online), ISBN 978-88-6453-989-8 (online PDF)

Isotope	Mass [u] (Ab %)[a]	Nucl. Spin	Nucl. Mag. moment [a] [μ_N]	a_{gg} Scatt. Length [b] [a_0]	$^1S_0 \rightarrow {}^1P_1$ isotopic shift[c] [MHz]	$^1S_0 \rightarrow {}^3P_1$ isotopic shift[d] [MHz]	$^1S_0 \rightarrow {}^3P_0$ isotopic shift[e] [Hz]
168	167.933 (0.13)	0	0	252	1299.4	6041	-
170	169.935 (3.04)	0	0	64	604.4	4673	-
171	170.936 (14.28)	1/2	+0.4919	-3	244.4 $(\frac{1}{2}\|\frac{3}{2})$ 565.7 $(\frac{1}{2}\|\frac{1}{2})$	6191 $(\frac{1}{2}\|\frac{3}{2})$ 254 $(\frac{1}{2}\|\frac{1}{2})$	-1259745597(10)
172	171.936 (21.83)	0	0	-600	-54.7	3386	-
173	172.938 (16.13)	5/2	-0.6776	200	72 $(\frac{5}{2}\|\frac{3}{2})$ -841.4 $(\frac{5}{2}\|\frac{5}{2})$ 0 $(\frac{5}{2}\|\frac{7}{2})$	6189 $(\frac{5}{2}\|\frac{3}{2})$ 4698 $(\frac{5}{2}\|\frac{5}{2})$ 0 $(\frac{5}{2}\|\frac{7}{2})$	0
174	173.939 (31.83)	0	0	105	-588.0	2386	551536050(10)
176	175.943 (12.76)	0	0	-24	-1097.3	1431	-

Table 1.1: Principal properties of the stable Yb isotopes. In order from left: mass in atomic units (1u=1.660539040(20)$\times 10^{-27}$ kg) and relative isotopic abundance, nuclear spin, nuclear magnetic moment, scattering length in the fundamental state, isotopic shift of the $^1S_0 \rightarrow {}^1P_1$ calculated with respect to the ^{173}Yb ($F = \frac{5}{2} - \frac{7}{2}$) transition ($\nu_x - \nu_{173}$), isotopic shift of the $^1S_0 \rightarrow {}^3P_1$ calculated with respect to the ^{173}Yb ($F = \frac{5}{2} - \frac{7}{2}$) transition ($\nu_x - \nu_{173}$), isotopic shift of the $^1S_0 \rightarrow {}^3P_0$ clock transition calculated with respect to the ^{173}Yb absolute frequency 518 294 576 845 268 (10) Hz (Clivati et al., 2016) ($\nu_x - \nu_{173}$).
References: [a]:(Lide, 2004), [b]:(Kitagawa et al., 2008), [c]:(Das et al., 2005), [d]:(Clark et al., 1979), [e]:(Clivati et al., 2016).

ultracold atoms and on the collisional properties. Section 1.2 is instead dedicated to an overview of the experimental apparatus and procedures employed in the Florence Yb laboratory to realize a degenerate gas of Yb. Finally, in section 1.3, the fundamental properties of atoms in optical lattices are discussed.

1.1 Fundamental properties of Ytterbium

Ytterbium, (from the name of the Ytterby village, in Sweden, where this element was discovered), is a rare-earth metal classified in the series of Lanthanides. Its appearance is characterized by a bright silvery luster, and a malleable and quite ductile texture. The atomic number of Yb is $Z = 70$ and the configuration of the fundamental state is [Xe]$4f^{14}6s^2$. Natural ytterbium is a mixture of seven stable isotopes with standard atomic weight 173.04(3) (Lide, 2004). Twenty-six other unstable isotopes are known. Among the stable isotopes five are bosonic (^{168}Yb, ^{170}Yb, ^{172}Yb, ^{174}Yb, ^{176}Yb) and

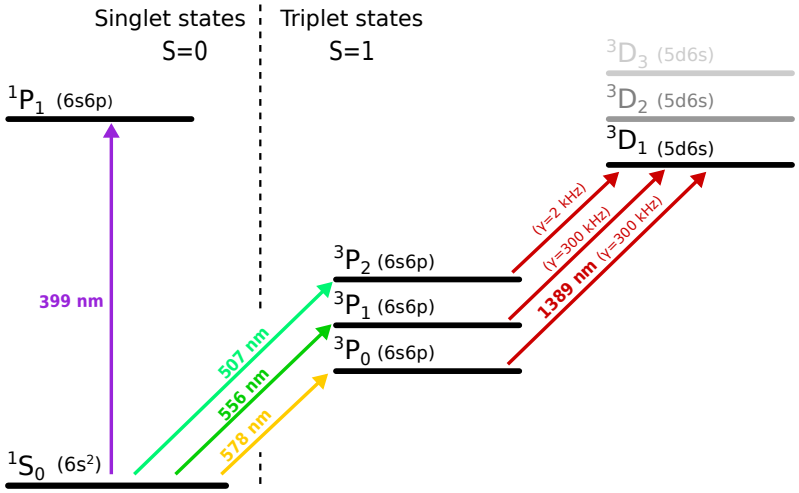

Figure 1.1: Scheme of the lowest energy Yb levels. Also the repumping transitions connecting the ${}^3P$ $(6s6p)$ multiplet with the ${}^3D_1$ $(5d6s)$ state are shown.

two are fermionic (^{171}Yb, ^{173}Yb). Similarly to the other two-electron elements only the fermionic isotopes have a non-zero nuclear spin ($I = 1/2$ for ^{171}Yb and $I = 5/2$ for ^{173}Yb), while the bosonic isotopes are all characterized by $I = 0$. Despite their chemical stability these isotopes weakly react with oxygen to form the compound Yb_2O_3.

In this thesis we essentially deal with the fermionic isotope ^{173}Yb and in minor part with the bosonic ^{174}Yb. The other widely used isotope in the context of atomic physics is ^{171}Yb, which finds application in the realization of the most accurate state-of-the-art atomic clocks (Hinkley et al., 2013). Some fundamental properties of these and of the other Yb stable isotopes are shown in table 1.1.

Due to the zero electronic angular momentum, the fundamental state of Yb is strongly diamagnetic and the only contribution to the magnetic moment comes from the nuclear spin I. In fermionic isotopes (bosonic isotopes have $I = 0$) this results in a pure nuclear magnetic moment given by $\mu = g_I \mu_N \mathbf{I}/\hbar$ where g_I is the nuclear Landè factor. As it depends only on the the nuclear magneton μ_N, the latter quantity is three order of magnitude smaller than the typical magnetic moment of alkali atoms. This strong insensitivity to magnetic fields makes the trapping and cooling of Yb impractical with pure magnetic traps, determining the necessity of an optical manipulation of the atoms in the fundamental state. Dipole trap at 1064 nm, a wavelength widely commercially available and far red-detuned with respect to all the transitions connecting the ground state with excited levels, can be employed for this purpose. The situation is completely different for the state ${}^3P_1$, which features a non-zero electronic angular momentum, enabling the possibility of a magnetic manipulation. This property is exploited for the realization of magneto-optical traps (MOT) in which the intercombination transition ${}^1S_0 \rightarrow {}^3P_1$ at 556 nm is addressed. This transition is preferred over the strongly allowed ${}^1S_0 \rightarrow {}^1P_1$ due to its lower linewidth (180 kHz vs 28 MHz)

which makes it possible to achieve a lower Doppler limited temperature (Inguscio and Fallani, 2013). The 399 nm ${}^1S_0 \rightarrow {}^1P_1$ transition, due to its large linewidth, finds instead application in the realization of a pre-cooling stage by means of Zeeman slower technique.

Yb features the nice property that all the lowest energy excitations starting from the fundamental level are in the visible spectrum, as evidenced in the energy level scheme shown in figure 1.1 and reported in table 1.2, where the main properties of these transitions are listed.

Transition	λ [nm]	$\Gamma/(2\pi)$	Lifetime	Sat. Intensity mW cm^{-2}
${}^1S_0 \rightarrow {}^1P_1$	399.9[a]	28.9 MHz[b]	5.5 ns[b]	60[c]
${}^1S_0 \rightarrow {}^3P_0$	578.4[a]	43.5 mHz ^{171}Yb 38.5 mHz ^{173}Yb[d]	~ 20 s	$\sim 5 \times 10^{-9}$
${}^1S_0 \rightarrow {}^3P_1$	555.8[a]	180 kHz[b]	860 ns[b]	0.14[c]
${}^1S_0 \rightarrow {}^3P_2$	507.3[a]	25 mHz ^{171}Yb 22 mHz ^{173}Yb[e]	~ 30 s	$\sim 2 \times 10^{-8}$ [e]

Table 1.2: Main properties of Yb lower-energy transitions. Table references: [a]:(Meggers and Tech, 1978), [b]:(Blagoev and Komarovskii, 1994), [c]:(Sugawa et al., 2013), [d]:(Porsev and Derevianko, 2003), [e]:(Yamaguchi, 2008).

1.1.1 Ground state collisional properties - SU(N) symmetry

In the ground state of fermionic isotopes, the zero electronic angular momentum determines the absence of hyperfine interaction and hence a perfect decoupling between the nuclear spin and electronic part of the wavefunction. As a consequence of this perfect decoupling, the s-wave scattering length for interparticle collisions in the fundamental state does not depend on the nuclear spin except for the restrictions imposed by fermionic antisymmetry. This independence of the collisional properties with respect to the spin projection imply that *spin-changing collisions* are forbidden and that consequently, given an atomic sample composed by a spin mixture, the relative spin populations are conserved in time. To formalize this argumentation we can consider two atoms with angular momentum f and projections of the angular momentum on the quantization axis m_1 and m_2. After a collision the two particles can be projected in a state characterized by the spin projections m_3 and m_4, for which, due to the momentum conservation rule, the relation $m_1 + m_2 = m_3 + m_4$ must hold. An interaction of this kind can be described with the potential (Widera et al., 2006; Ho, 1998):

$$V(r) = \sum_{F=0}^{2f} g_F \mathcal{P}_F \, u(r) \tag{1.1}$$

where $\mathcal{P}_F$ is the projector on the two-particle state with total spin F (being the particle spins equal to f, F can assume all even the values between 0 and $2f$), g_F is the

spin-dependent potential amplitude and $u(r)$ is the spatial dependence of the potential, where r is the interparticle distance[1]. Writing the two-particle state wavefunction as the product of a spatial and a spin part

$$|\psi\rangle \equiv |\phi_0(r)\rangle_1 |\phi_1(r)\rangle_2 \otimes |f, m_1; f, m_2\rangle \tag{1.2}$$

and decomposing the projector $\mathcal{P}_F$ in the sum

$$\mathcal{P}_F = \sum_{M=-F}^{F} |F, M\rangle\langle F, M|, \tag{1.3}$$

where M is the projection of F on the quantization axis, we have that the collisional mechanism that generates the atomic pair m_3 and m_4 starting from m_1 and m_2 is possible provided that the expression

$$\sum_{F=0}^{2f} \sum_{M=-F}^{F} \langle f, m_3; f, m_4|F, M\rangle\langle F, M|f, m_1; f, m_2\rangle \, g_F \tag{1.4}$$

is not vanishing, where $\langle f, m_i; f, m_j|F, M\rangle$ are Clebsch-Gordan coefficients. If the spin-independence of the potential is assumed, all the collisional channels F_i have identical strength and the $g_F \equiv g$ can be excluded by the sum. Using now the completeness relation of the $\{F, m_F\}$ Hilbert space, the expression 1.4 reduces to $g\,\langle f, m_3; f, m_4|f, m_1; f, m_2\rangle$ which is not vanishing only if $m_1 = m_3$ and $m_2 = m_4$, i.e. if no spin-changing collisions occur.

This demonstration can be further formalized considering the nuclear spin permutation operators S_m^n which destroy an atom in the nuclear spin state m and create another atom in the spin state n. It can be proved (Gorshkov et al., 2009; Cazailla and Rey, 2014) that these operators satisfy the SU(N) algebra (where $N = 2I + 1$) and that commute with the Hamiltonian describing an interacting two-electron gas, implying the conservation of the relative spin populations. For this reason, an unpolarized six-spin-components ^{173}Yb gas can be treated as a gas with SU(6) symmetry. Due to spin conservation, the dynamics of a gas with spin lower than six can be reproduced starting from a ^{173}Yb gas in which some spin components are missing. A two-spin ^{173}Yb mixture, for example, perfectly reproduces the dynamics of a SU(2) gas.

The argumentation carried on for the fundamental state is obviously valid also for the clock state $^3P_0$, which also has vanishing electronic angular momentum. In fermionic isotopes, however, due to a small admixture of higher-lying P states with $J \neq 0$ arising from the hyperfine interaction (this mechanism is explained in detail section 3.1) the spin independence of the scattering lengths is slightly reduced and variation of the order of $\delta g_F/g_F \sim 10^{-3}$ are expected (Gorshkov et al., 2009). In the fundamental state, instead, where no hyperfine mixing can be present the predicted deviation from a pure SU(N) model is of the order of $\delta g_F/g_F \sim 10^{-9}$ (Gorshkov et al., 2009).

[1]If, for example, the Huang-Yang pseudopotential is considered, $g_F = 4\pi\hbar^2 a_F/m$, where a_F is the s-wave scattering length and m is the reduced atomic mass, and $u(r) = \delta(r)\frac{d}{dr}(r\cdot)$.

1.1.2 Collisions in a ${}^1S_0 - {}^3P_0$ mixture - the exchange interaction

Up to now we have investigated only the collisional properties of fermionic atoms all characterized by the same electronic state ${}^1S_0$ or ${}^3P_0$. If this constrain is relaxed and we enable a two-orbital $g-e$ mixture to interact, a new collisional channel opens in which the two particles can exchange their spin. The possibility to exploit this interaction with two-electron fermions paves the way to the quantum simulation of quantum magnetism phenomena where the spin exchange plays a prominent role, such as the Kondo model (Gorshkov et al., 2009). To explain how this kind of interaction emerges in a two-orbital gas we can consider two fermionic Yb atoms with different projections of the spin on the quantization axis ($\uparrow$ and $\downarrow$) and different electronic states ${}^1S_0 = g$ and ${}^3P_0 = e$. Due to the fermionic statistic, the two-atom wavefunction must be antisymmetric for particle exchange and hence it can be written as

$$\Psi_{\pm}(\mathbf{r_1},\mathbf{r_2}) = \frac{1}{2}\underbrace{\left(|eg\rangle \pm |ge\rangle\right)}_{\text{Orbital part}} \otimes \underbrace{\left(|\uparrow\downarrow\rangle \mp |\downarrow\uparrow\rangle\right)}_{\text{Spin part}} \otimes \underbrace{\phi(\mathbf{r}_1)\phi(\mathbf{r}_2)}_{\text{Spatial part}} = |\Psi_{\pm}\rangle \tag{1.5}$$

where $\phi(\mathbf{r})$ is the spatial wavefunction (assumed identical for both atoms). In a more compact notation (where the exchange symmetry is implicit) we can write the orbital-symmetric (spin-singlet) state $|\Psi_+\rangle$ and the orbital-antisymmetric (spin-triplet) state $|\Psi_-\rangle$ as

$$|\Psi_{\pm}\rangle = |eg^{\pm}\rangle\, \phi(\mathbf{r_1})\phi(\mathbf{r_2}) \tag{1.6}$$

in which

$$|eg^{\pm}\rangle = \frac{1}{\sqrt{2}}\left(|g\uparrow, e\downarrow\rangle \pm |g\downarrow, e\uparrow\rangle\right) \tag{1.7}$$

The states $|eg^{\pm}\rangle$ are in general characterized by different scattering lengths that we identify as $a_{eg}^{\pm}$. Given the two scattering lengths, the interaction potential that describes the scattering in the $|eg^{\pm}\rangle$ basis can be written as

$$V_{int}(\mathbf{r_1}-\mathbf{r_2}) = g_0\, \left(a_{eg^+}\, \mathcal{P}_{eg^+} + a_{eg^-}\, \mathcal{P}_{eg^-}\right)\, U(\mathbf{r_1},\mathbf{r_2}) \tag{1.8}$$

where $g_0 = \frac{4\pi\hbar^2}{m}$ (m is the atomic mass), $\mathcal{P}_{eg^+}$ and $\mathcal{P}_{eg^-}$ are respectively the projectors on the states $|eg^+\rangle$ and $|eg^-\rangle$ and $U(\mathbf{r_1},\mathbf{r_2})$ is the spatial part of the potential. The two projectors, expressed in the compact notation 1.7, read

$$\mathcal{P}_{eg^{\pm}} = \frac{1}{2}\left(\underbrace{|g\uparrow, e\downarrow\rangle\langle g\uparrow, e\downarrow| + |g\downarrow, e\uparrow\rangle\langle g\downarrow, e\uparrow|}_{\mathcal{V}} \pm \underbrace{|g\downarrow, e\uparrow\rangle\langle g\uparrow, e\downarrow| + |g\uparrow, e\downarrow\rangle\langle g\downarrow, e\uparrow|}_{\mathcal{V}_{ex}}\right) \tag{1.9}$$

where $\mathcal{V}$ keeps unchanged the spin of the two particles while $\mathcal{V}_{ex}$ exchange the two spins. Given the expression above for the projectors, we have that the interaction potential can be written as

$$V_{int}(\mathbf{r_1}-\mathbf{r_2}) = g_0\, \left[\left(\frac{a_{eg^+}+a_{eg^-}}{2}\right)\mathcal{V} + \left(\frac{a_{eg^+}-a_{eg^-}}{2}\right)\mathcal{V}_{ex}\right]\, U(\mathbf{r_1},\mathbf{r_2}). \tag{1.10}$$

Thanks to the term proportional to $\mathcal{V}_{ex}$, the interaction potential V_{int} can connect states in which the spin of the two particles is exchanged, such as $|g\uparrow, e\downarrow\rangle$ and $|g\downarrow, e\uparrow\rangle$

$$\langle g\downarrow, e\uparrow|V_{int}|g\uparrow, e\downarrow\rangle = g_0\, \left(\frac{a_{eg^+}-a_{eg^-}}{2}\right)\, \iint \mathrm{d}\mathbf{r_1}\, \mathrm{d}\mathbf{r_2}\, \phi(\mathbf{r_1})^2\phi(\mathbf{r_2})^2 U(\mathbf{r_1},\mathbf{r_2}). \tag{1.11}$$

This last relation demonstrates how spin-exchange interactions, which have no classical analogue, can affect a two-orbital - two-electron gases. The strength of the spin-exchange depends on the scattering lengths differences $\delta a_{eg} = a_{eg^+} - a_{eg^-}$ and vanishes if $a_{eg^+} = a_{eg^-}$ in analogy with a SU(N) gas in which spin populations are conserved due to the spin-independence of the scattering length. Fermionic Yb is an ideal candidate for experiments in which spin-exchange interactions are required, due to the large difference in the scattering properties of the states $|eg^{\pm}\rangle$ (in ^{173}Yb, for example, $\delta a_{eg} \simeq 3000\, a_0$ (Cappellini et al., 2014)). This interaction is at the basis of the *orbital Feshbach mechanism* that we experimentally investigate in section 4.3.

1.2 A quantum degenerate Yb gas

In this section we provide a summarizing description of the procedure adopted in our experiment to achieve quantum degeneracy in a Yb ultracold gas. The starting point of the experiment is a Yb atomic beam exiting from an oven at a temperature of the order of ∼500 °C. After a Zeeman slowing of the atoms operated on the $^1S_0 \rightarrow {}^1P_1$ transition at 399 nm, the particles are loaded in a magneto-optical trap (MOT) working at the intercombination transition $^1S_0 \rightarrow {}^3P_1$ at 556 nm. The MOT stage is followed by the loading of the atoms in a 1064 nm in-vacuum optical resonator, where optical dipole trapping and a first stage of evaporative cooling is performed. From the resonator atoms are loaded in a second 1064 nm strongly-focused trap, moving the waist of which the particles are transferred in a 26-cm-distant glass cell. Here a final stage of evaporative cooling is performed by means of a 1064 nm crossed dipole trap. All the science experiments are performed inside the glass cell where several laser beams aimed at the optical manipulation and trapping of the atoms converge. A detailed description of this experimental sequence is provided in section 1.2.3. A brief, preliminary description of the laser sources employed in the experiment, is instead reported in section 1.2.1 and 1.2.2.

1.2.1 Resonant light laser sources

In this section we provide a short description of the laser sources employed to excite the atomic transitions $^1S_0 \rightarrow {}^1P_1$ at 399 nm, $^1S_0 \rightarrow {}^3P_1$ at 556 nm, and $^1S_0 \rightarrow {}^3P_0$ at 578 nm. As it is difficult to find commercial lasers with suitable power and spectral characteristics in those regions of visible spectrum, we generate all the three resonant frequencies by means of second-harmonic generation. A detailed description of the 399 nm and 556 nm laser sources can be found in (Pagano, 2015, 2011). For a complete description of the 578 nm laser source we refer instead to references (Cappellini et al., 2015; Cappellini, 2016, 2012).

399 nm laser source

In order to excite the $^1S_0 \rightarrow {}^1P_1$ transition we generate 399 nm light through second-harmonic generation. The starting point is the 798 nm light delivered by a fiber-coupled tapered-amplifier laser-diode system TOPTICA TA PRO. The 1.1 W of 798 nm light generated by the TOPTICA laser is injected in a home-made bow-tie doubling

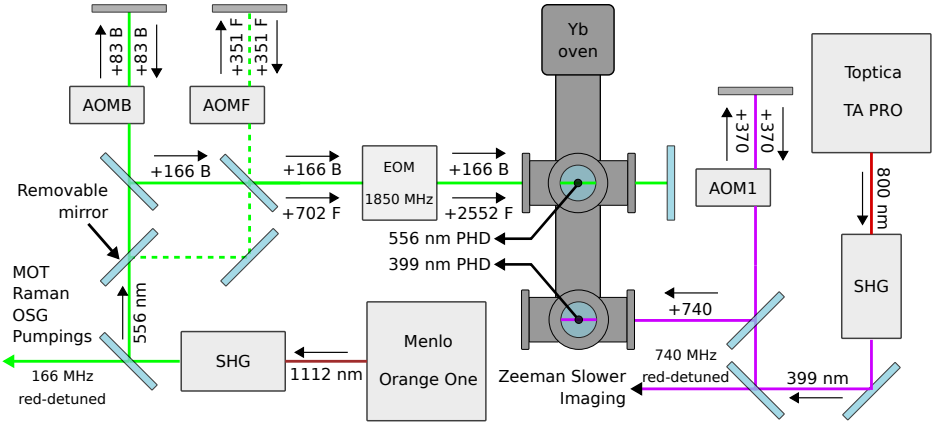

Figure 1.2: 556 nm and 399 nm lasers locking scheme on Yb atomic reference. The labels on the laser beams report the shift in MHz with respect to the light exiting from the doubling cavities (in the 556 nm setup, B and F refer, respectively, to the shifts of the bosonic and fermionic setup. See the main text for details. All the AOMs are in double passage.

cavity in which an LBO crystal stabilized at the temperature of 55 °C converts it into 480 mW of 399 nm radiation. The frequency of the cavity modes (the free spectral range is 749 MHz) is stabilized on the laser light by means of the Haensch-Couillaud technique (Hansch and Couillaud, 1980), acting on a piezo stack mounted on the back of one cavity mirrors. The lock of the 399 nm light on the atomic line ${}^1S_0 \rightarrow {}^1P_1$ is performed simply by means of saturation spectroscopy, interrogating a collimated Yb atomic beam along the direction orthogonal to the motion of the atoms, in such a way to suppress the Doppler broadening. As shown in figure 1.2, the atomic beam is generated by a secondary oven identical to the main-experiment oven. Being the Doppler broadening smaller than the linewidth, no Doppler-free technique is needed and simple saturation spectroscopy is employed. To this purpose light is frequency-modulated by means of an AOM (AOM1 in figure 1.2) and the classical lock-in scheme (Nagourney, 2010) is employed to generate an error signal starting from the collected fluorescence spectrum. The lock frequency setpoint is chosen accordingly to the isotope we decide to work with. While for ^{174}Yb a single absorption line is present, for ^{173}Yb we choose to lock the light on the ${}^1S_0(F = 5/2) \rightarrow {}^1P_1(F = 7/2)$ transition (see table 1.1). Due to the presence of the modulating AOM, the light coming out from the cavity is stabilized on a frequency 740 MHz red-detuned with respect to the atomic ${}^1S_0 \rightarrow {}^1P_1$ line.

556 nm laser source

As for the ${}^1S_0 \rightarrow {}^1P_1$ transition, the light at 556 nm employed for the excitation of the ${}^1S_0 \rightarrow {}^3P_1$ atomic line is generated by means of second-harmonic generation starting from 1112 nm infrared light. This light is delivered by a fiber laser Menlo Systems model ORANGE ONE and is used to pump a Lithium Tantalate ($LiTaO_3$) doubling

crystal placed inside a bow-tie home-made cavity. Also in this case the frequency of the cavity modes (the FSR is 567 MHz) is locked on the laser light by means of the Haensch-Couillaud technique and 1.05 W of frequency-doubled light are obtained starting from 1.7 W of infrared radiation (conversion efficiency $\sim 60\%$). Due to the reduced linewidth of the ${}^1S_0 \rightarrow {}^3P_1$ transition, Doppler-free saturation spectroscopy is employed to lock the laser on the atomic line. To this purpose two counter-propagating light beams are used to interrogate the Yb atomic beam described in the previous section and the resulting signal coming from fluorescence light is collected by a photomultiplier and employed to feed a standard lock-in scheme. To lock on the ^{174}Yb isotope the spectroscopy light is modulated by means of a 83 MHz double-passage AOM (AOMB in figure 1.2). The lock is performed on the ${}^1S_0(J=0) \rightarrow {}^3P_1(J=1)$ transition and in order to address only the $(J=0, m_J=0) \rightarrow (J=1, m_J=0)$ magnetic insensitive line, π-polarized light is used and a small magnetic field is applied. A similar approach for the lock on the ^{173}Yb isotope is complicated by the presence of six absorption lines, one for each nuclear spin component, that are sensitive to fluctuations of the magnetic field and worsen the SNR, contributing each to the signal with one sixth of the total intensity. To overcome this difficulty the lock on the fermionic isotope is performed locking the laser on the bosonic ^{174}Yb and covering the 2386 MHz isotopic shift between ^{174}Yb and ^{173}Yb by frequency-shifting the spectroscopy light with a 1850 MHz resonant EOM (which in this scheme is the element employed to frequency modulate the light) and a double passage AOM (AOMF in figure 1.2). Both schemes stabilize the laser light at a frequency 166 MHz red-detuned with respect to the transition employed for the MOT (that is the ${}^1S_0(F=5/2) \rightarrow {}^3P_1(F=7/2)$ for the fermion and ${}^1S_0(J=0) \rightarrow {}^3P_1(J=1)$ for the boson). A mirror on a removable magnetic mount is employed to switch between the bosonic/fermionic lock configurations.

578 nm laser source

The 578 nm laser source that we use to excite the ${}^1S_0 \rightarrow {}^3P_0$ transition is by far the most complicated laser system present in the laboratory. Also in this case, due to the absence of a commercially available high-power small-linewidth 578 nm laser, we generate the light by means of second-harmonic generation, starting from the 1156 nm infrared radiation delivered by a quantum dot laser diode. The diode is mounted in a home-made extended cavity in Littrow configuration. The peculiarity of the system is the presence of an intra-cavity EOM which is used for fast corrections of the laser frequency up to 500 kHz. The 200 mW of infrared light generated by the diode are used to inject a $LiNbO_3$ doubling crystal placed inside a bow-tie cavity stabilized by means of the Haensch-Couillaud method. The crystal delivers $\sim$50 mW of 578 nm light which is split into two branches, one used for frequency stabilization on a high-finesse ($\mathcal{F} \simeq 1.7 \times 10^5$) ultra-low-expansion (ULE) cavity, the other to be used in the experiment for the excitation of the ${}^3P_0$ state. The lock on the ULE cavity is performed on the mode of the cavity nearest to the atomic transition (the FSR is 1.5 GHz) by means of the Pound-Drever-Hall technique (Black, 2001). To this purpose, as shown in figure 1.3, a double-passage AOM placed along the lock branch (AOM1 in figure 1.3) is used to shift the frequency of the light in such a way that the frequency on the spectroscopy

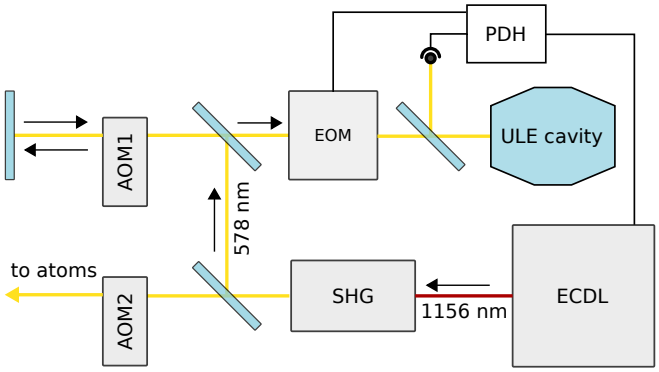

Figure 1.3: Conceptual scheme of the 578 nm laser setup. See the main text for details.

branch is red-shifted by 40 MHz with respect to the atomic transition. This shift is covered by a second AOM placed on the spectroscopy branch (AOM2 in figure 1.3) which is employed to fine-correct the laser frequency. With the lock on the ULE cavity we obtain a final linewidth of the laser of the order of few tens of Hz on the timescale of $\sim$15 min. For longer times the linewidth is degraded by the ageing of the ULE cavity glass, which determines a shift of the cavity modes of the order of 5 kHz / day, and by long-term erratic oscillations that we attribute to uncompensated thermal effects. This problem can be overcome with a long-term lock on a metrological reference, as described in section 3.5.

1.2.2 Trapping laser sources

Far-red-detuned optical potentials are essential in the manipulation of alkaline-earth and alkaline-earth-like atoms, since, as a consequence of the magnetic insensitivity of the ground state, magnetic trapping is impossible for this class of elements. Dipole potentials are a fundamental consequence of the matter-radiation interaction and emerge due to the dipole moment $\mathbf{p} = \alpha\mathbf{E}$ induced on the atoms by the radiation's electric field $\mathbf{E}$, where α is the atomic polarizability. Since α depends on the internal state of the atoms, also the dipole potential will be different for different atomic internal states. In case of red-detuned radiation and negligible saturation, the expression of the dipole potential U_{dip} for a multi-level atom in the internal state ν is (Grimm et al., 2000)

$$U^{\nu}_{dip}(\omega, \mathbf{r}) = -\frac{3\pi c^2}{2} I(\mathbf{r}) \sum_n \left(\frac{1}{\omega^3_{\nu,n}} \frac{\Gamma_{\nu,n}}{\omega_{\nu,n} - \omega} \beta_{\nu,n} \right) \tag{1.12}$$

where I is the radiation intensity, $\omega/(2\pi)$ is its frequency, $\omega_{\nu,n}/(2\pi)$ are the frequencies of the transitions connecting the atomic state ν with other atomic states n, $\Gamma_{\nu,n}/(2\pi)$ is the lifetime these transitions and $\beta_{\nu,n}$ their branching ratio.

Here we provide a short description of the 1064 nm and 759 nm laser sources employed, respectively, to provide the light used for the evaporative cooling and for the realization of an optical lattice in our setup. Additional information can be found in (Pagano, 2015; Mancini, 2016).

1064 nm laser source

We use light at 1064 nm to trap atoms in the fundamental $^1S_0$ state. This is an antitrapping wavelength for the $^3P_0$ and, consequently, cannot be employed to confine atoms in the metastable state. Radiation at 1064 nm is generated by a Coherent Nd:Yag Mephisto MOPA 45 laser delivering up to 45 W of light with a linewidth below 100 kHz. The infrared radiation delivered by the laser is split into three branches whose power is controlled by means of three independent double-frequency AOMs (Frohlich et al., 2007).

The light of the first branch is employed to inject the in-vacuum optical cavity used for the first evaporation cooling stage inside the MOT cell. The cavity is injected with 1.8 W of radiation that are enough to produce an optical potential with a trap depth of 800 μK (see section 1.3 for further details). Light reflected from the optical cavity is instead used to stabilize the frequency of the Mephisto laser by means of the Pound-Drever-Hall (PDH) technique. The locking scheme employed is quite complicated and is based on two PID servo controllers processing the slow and fast part of the PDH signal (Pagano, 2015). The fast component of the error signal acts on the internal piezo of the seed laser and performs fast corrections of the laser frequency. The slow component of the error signal is instead used to control the temperature of the seed in order to perform slow high-range frequency corrections.

The light delivered by the second of the three branches ($\simeq$ 4 W) is employed to realize the transport beam which is used to transfer the atoms from the center of the MOT cell to the 26-cm-distant science cell via an optical tweezers setup realized with a focusing lens mounted on a low-vibration translation stage (see section 1.3 for further details).

The third branch (3.5 W) finally provides the light used in combination to the transport beam to realize a crossed dipole trap in the center of the science cell, where the final evaporation cooling stage is performed.

759 nm laser source

For ytterbium, 759 nm is a special wavelength that allows for the simultaneous trapping of both atoms in the $^1S_0$ and in the $^3P_0$ states, as we will discuss in section 1.3. We employ this radiation to realize a three dimensional optical lattice (or in some experiments a 3D trap) in the center of the science cell. Light at 759 nm is generated with a Ti:Sa laser (Coherent MBR 110) pumped with a single-mode 532 nm Coherent Verdi V18. The 3.5 W of 759 nm light delivered by the Ti:Sa laser are split into three branches, which are used to realize the beams of the three optical lattices. The power of each branch is controlled by means of a double-frequency AOM. Finally, a small portion of light is injected into a confocal cavity which is employed to monitor the single-mode operation of the MBR.

1.2.3 Cooling procedure

At room temperature Yb is a solid with an extremely low vapor pressure. In order to generate a reliable source of gaseous monoatomic Yb for the experiment it is thus necessary to heat the metallic sample, increasing in this way the pressure. Ytterbium

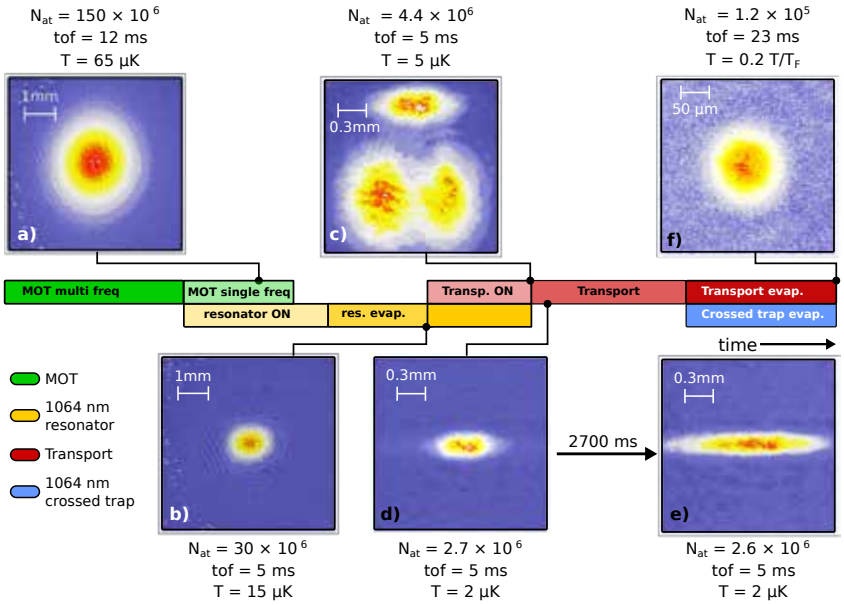

Figure 1.4: Time-of-flight images, number of atoms and temperature of the atomic cloud at several points of the ^{173}Yb experimental cooling sequence. **a:** Atomic cloud at the end of the single frequency MOT stage. **b:** Atomic cloud at the end of the evaporation in the 1064 nm optical resonator. **c:** Atoms trapped in the transport beam just after the resonator has been turned off. Atoms not trapped in the transport beam are released by the resonator and appear as two clouds at the bottom of the image. **d:** Atoms at the beginning of the transport procedure. **e:** Atoms after 2.7 s in the transport beam (before moving the beam waist). The waiting time does not alter the temperature nor the atom number. **f:** Fermi degenerate gas (SU(6) mixture) at the end of the evaporation in the 1064 nm crossed trap at the center of the glass cell.

vapor is generated inside an oven heated at the temperature of 485 °C. The oven is filled with ∼15 g of Yb chunks produced by Sigma-Aldrich. According to the relation that links the vapor pressure to the temperature for Yb (Lide, 2004)

$$\log(P[\text{atm}]) = 9.111 - \frac{8111}{T[\text{K}]} - 1.0849\log(T[\text{K}]) \tag{1.13}$$

a vapor pressure of ∼0.1 Torr is expected inside the oven. The resulting Yb gas is collimated by means of an array of 100 small tubes, 1 cm long and with an internal diameter of 0.2 mm.

The gas exiting from the array of tubes is then decelerated from a mean velocity of 340 m s^{-1} to few m s^{-1} by means of a 50 cm long Zeeman slower. Zeeman slowing is performed exploiting the 399 nm strongly allowed $^1S_0 \rightarrow {}^1P_1$ transition with a 983 MHz red-detuned σ^- counter-propagating beam. Seven coils are disposed along the Zeeman slower pipe in order to generate a magnetic field which keeps the atoms resonant with the 399 nm radiation. The atoms sufficiently decelerated by the Zeeman slower are then captured by a magneto-optical trap (MOT) operated with 556 nm light

resonant with the $^1S_0 \rightarrow {}^3P_1$ transition. The MOT is realized with a standard configuration consisting in three pairs of counter-propagating σ^+/σ^- beams along the three spatial directions (Foot, 2012). Due to the narrowness of the $^1S_0 \rightarrow {}^3P_1$ transition, the range of atomic velocities captured by the trap is increased splitting the laser intensity on a comb of 18 frequencies separated by 600 kHz. This multi-frequency stage lasts for 20 s, which is the time necessary to saturate the MOT achieving a stable number of atoms. At the end of the 20 s we end up with about $N_F = 1.5 \times 10^8/N_B = 1.0 \times 10^9$ of ^{173}Yb/^{174}Yb atoms trapped in the MOT, with a temperature of $T \simeq 60$ μK, as shown in figure 1.4-a.

As soon as the MOT loading is completed, the in-vacuum 1064 nm optical resonator placed at the center of the MOT chamber is turned on with a 200 ms exponential ramp and the MOT is switched to single-frequency operation. The resonator is a Fabry-Perot cavity with a finesse $\mathcal{F} \simeq 1570$ and a free spectral range of 1.67 GHz. Atoms are transferred from the MOT to the center of the resonator cavity with an efficiency $\simeq 80\%$ by means of the magnetic field generated by three additional coils, exploiting the high magnetic sensitivity of the $^3P_1$ state. The loading in the resonator is followed by the turning off of the MOT beams, after which a first evaporation ramp is performed by lowering the resonator power from 1.8 W to 0.6 W with a 670 ms long exponential ramp. As shown in figure 1.4-b, at the end of this stage we obtain a sample consisting of about $3 \times 10^7/5 \times 10^8$ ^{173}Yb/^{174}Yb atoms with a temperature of 3 μK trapped in the cavity. At this point a 70 μK deep optical trap with a waist of $30\,\mu$m is generated in the center of the resonator turning on the 1064 nm transport beam by means of a 400 ms exponential ramp. Once the resonator beam is turned off (see figures 1.4-c,d) about $4\times10^6/9\times10^6$ ^{173}Yb/^{174}Yb atoms remain confined inside the trap formed by the transport beam. Atoms are then transferred from the center of the MOT chamber to the center of the 26.4-cm-distant glass science cell by moving the waist of the transport beam. In order to translate the waist position, the lens that focuses the beam is moved by means of an air-bearing translator stage AEROTECH ABL 1500b. The transport procedure has a duration of 2.5 s, a 70% efficiency and determines an increase of the sample temperature of only 2 μK (Livi, 2012). The alignment of the transport beam with respect to the glass cell is shown in figure 1.5 where it is labelled as ODT_1.

Once the atoms are in the center of the cell, another 1064 nm beam (ODT_2 in figure 1.5) with 60 μm waist is adiabatically turned on. This beam, which propagates in a direction orthogonal to the transport beam, forms with the latter a crossed optical dipole trap where the final stage of evaporative cooling is performed. Quantum degeneracy is reached by lowering the depth of the transport beam and of the orthogonal trapping beam with two simultaneous exponential ramps characterized both by the same duration T_r and different decay constant τ_{r1} and τ_{r2}, respectively for the transport and the orthogonal beams. The optimized ramp parameters are set accordingly to the isotope and, in the case of fermionic ^{173}Yb, accordingly to the spin mixture we want to cool.

Fermi degeneracy for a six spin mixture of ^{173}Yb atoms, for example, is obtained decreasing the transport power from 3.5 W (70μK) to 30 mW and the power of the orthogonal beam from 3 to 1 W with ramp parameters: $T = 4000$ ms and $\tau_{r1} = \tau_{r2} = -1000$ ms. The gas obtained with this procedure is characterized by a temperature $T = 0.2\,T_F$ where T_F is the Fermi temperature, and a number of atoms $N_{at} \simeq 1.2\times10^4$. The result of this procedure is shown in figure 1.4-f.

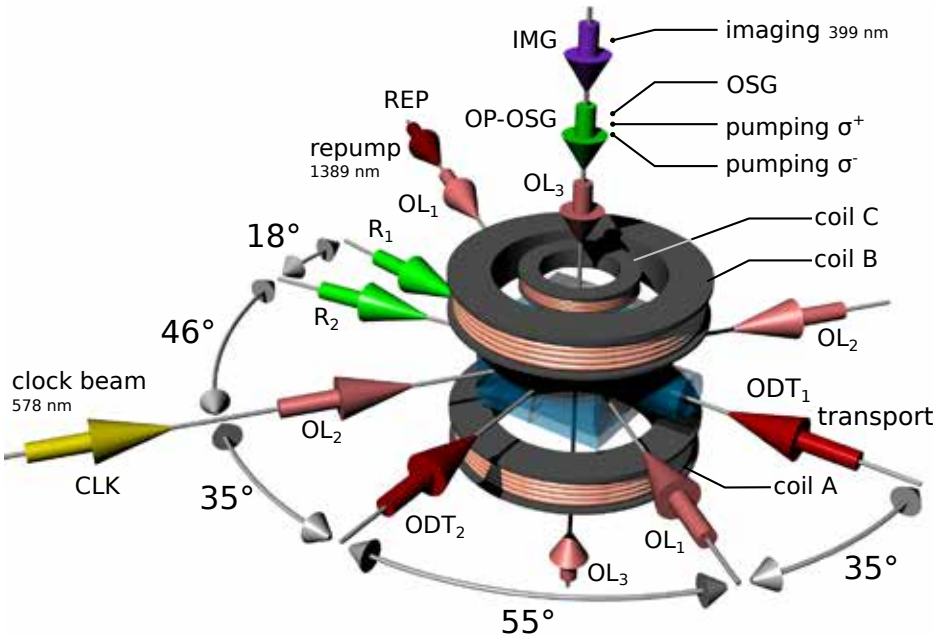

Figure 1.5: Pictorial representation of the glass cell setup. The cell is equipped with three coils (COIL A, B and C in figure) used to generate magnetic fields up to 170 G at the center of the cell. Coils A and B are in Helmholtz configuration. Several lasers converge at the center of the cell, where quantum degeneracy is reached, to trap and manipulate atoms. Among these lasers there are: the 1064 nm optical trap (ODT_1 and ODT_2), the three optical lattices (OL_1, OL_2 and OL_3), the 399 nm imaging beam (IMG), the Raman beams (R_1 and R_2) and the 1389 nm repump beam (REP). OP-OSG represents instead a set of three 556 nm beams composed by the σ^+/σ^- pumping beams and optical Stern-Gerlach beam. The 578 nm clock laser beam can be aligned along several path, as discussed in section 4.2.3. Here it is represented co-aligned with lattice OL_2, a configuration often employed in the experiments described in chapter 4.

Bose-Einstein condensation of ^{174}Yb atoms, instead, is obtained decreasing the transport power from 3.5 W (70μK) to 30 mW and the power of the orthogonal beam from 3 to 1 W with ramp parameters: $T = 2500$ ms and $\tau_{r1} = \tau_{r2} = -2200$ ms. In this case the gas obtained is characterized by a condensed fraction $f_C \simeq 70\%$ and a number of atoms $N_{at} \simeq 2.5 \times 10^4$.

The optical dipole trap at the end of the evaporative cooling is characterized by the trap frequencies $\omega_{x,y,z} = \{53.8(5), 99.5(5), 93.6(5)\}$ evaluated by inducing and detecting dipole oscillations.

Atomic population in the ground state is finally detected by means of a standard absorption imaging technique, exploiting the cycling transition $^1S_0 \rightarrow {}^1P_1$ (for ^{173}Yb $F = 5/2 \rightarrow F = 7/2$). The imaging beam is aligned with the vertical direction, as it shown in figure 4, where it is labelled as IMG. Additional information regarding the imaging procedure can be found in (Pagano, 2015).

1.2.4 Ground-state atoms - Manipulation and detection

After the transfer in the science glass cell, the optical manipulation of the six nuclear spin states of the ^{173}Yb ground level is the starting point for several of the subsequent experimental sequences. These optical manipulations are performed exploiting the $^1S_0(F = 5/2) \rightarrow {}^3P_1(F = 7/2)$ transition, that due to its narrowness makes it possible to address the six nuclear spins individually, provided the presence of a magnetic field removing the spin degeneracy. In particular, a proper choice of the detuning of the light with respect to the atomic transition allows us to:

- *Define the number of initial spin components in the gas:* SU(N) mixtures are prepared exploiting resonant σ^+/σ^- transitions connecting the states $^1S_0(F = 5/2, m_F)$ with the excited levels $^3P_1(F = 7/2, m_F \pm 1)$. A series of such resonant light pulses is employed to optically transfer the population of the nuclear spin m_F in the states $m_F + 1/m_F - 1$, respectively, if σ^+/σ^- transitions are used, as it is shown in figure 1.6-a. To this purpose a 23 G magnetic field is used to split adjacent spins in the $^3P_1$ manifold by $\Delta_Z = 2\pi \times 13.7$ MHz, in such a way that each pumping process is characterized by a well defined frequency. Magnetic fields are generated by means of three coils, indicated as COIL A, B and C in figure 1.5. Coil A and B are in Helmholtz configuration and generate fields up to 150 G at the center of the cell. The small coil C, instead, is usually employed to generate bias fields up to 20 G.

  The preparation of SU(N) mixtures with 2<N<5 is performed before the final evaporative cooling stage, giving the atoms the possibility to scatter many photons and to be optically pumped without being kicked out off the trap. In order to prepare a SU(2) $m_F = \pm 5/2$ mixture, for example, we start from a homogeneous SU(6) unpolarized gas and perform two series of σ^+/σ^- pumping processes, the first transferring the $m_F = \pm 1/2$ spin states in the $m_F = \pm 3/2$ and the second transferring the $m_F = \pm 3/2$ into the $m_F = \pm 5/2$, as it is sketched in figure 1.6-b. The $\sigma^{+,-}$-polarized light necessary for the process is provided by two distinct beams which are part of the OP-OSG beam-set in figure 1.5. A spin-polarized gas can be prepared exploiting an additional blast pulse on one of the closed transitions $^1S_0(F = 5/2, m_F = \pm 5/2) \rightarrow {}^3P_1(F = 7/2, m_F = \pm 7/2)$ at the end of the evaporation stage that kicks out the unwanted spin from the final (shallow) trap;

- *Detect the spin distribution by means of Optical Stern-Gerlach (OSG) technique* (Taie et al., 2010; Stellmer et al., 2011): Due to the magnetic insensitivity of the Yb ground state, the standard magnetic Stern-Gerlach technique cannot be employed to spatially resolve the six nuclear components. We instead exploit the spin-dependent dipole force exerted by a 566 MHz red-detuned beam to optically separate the spin populations. In order to do this, a focused beam with $60\,\mu$m waist (one of the three beams which compose the OP-OSG beam-set in figure 1.5) is slightly misaligned with respect to the atomic cloud, in such a way that the dipole force induces an acceleration on the atoms. This spin-resolved detection is performed applying a 13 mW OSG pulse during the first 1.5 ms of time of flight. A bias magnetic field is turned on during the detection in order to define

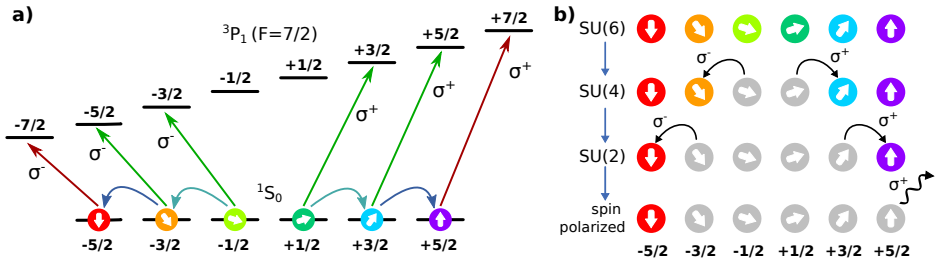

Figure 1.6: **a:** Scheme of the optical pumping processes employed to generate SU(N) spin mixtures. σ^+/σ^- processes indicated with a solid arrow are performed before the final evaporation of the gas. Blast pulse indicated with a red arrow are instead performed after the final evaporation. **b:** Sketch of the experimental sequence used to generate SU(4), SU(2) mixtures or spin polarized gases starting from a SU(6) unpolarized spin mixture.

a quantization axis for the nuclear spin projections. An example of SU(6) OSG detection is reported in figure 1.7-a;

- *Coherently couple the nuclear spin states:* coherent transfer of population between different nuclear spin states is performed exploiting Raman transitions in which the $^3P_1$ manifold is used as virtual excited state. The alignment of the two Raman beams exploited for this scope is shown in figure 1.5, where they are labelled as R_1 and R_2. Section 5.1.1 is dedicated to the description of these Raman processes;

- *Perform spin-selective imaging*: Exploiting a strategy similar to the optical pumping we are able to eliminate unwanted spin populations during time of flight, performing in this way spin-selective imaging. This technique is described in section 5.2.1.

1.2.5 Metastable $^3P_0$ atoms - Manipulation and detection

During this thesis we have implemented an imaging routine which enables the detection of atoms in the metastable $^3P_0$ state. The imaging scheme is based on the dipole-allowed 1388.8 nm transition connecting the $^3P_0$ state with the (5d6s)$^3D_1$ with a 300 kHz natural linewidth. Once excited in the $^3D_1$ state the atoms can decay via spontaneous emission in any of the three levels of the ^3P manifold. However, due to the low branching ratio towards the state $^3P_2$ (see table 1.3), atoms essentially de-excite to the state $^3P_0$ (branching ratio 65%) and $^3P_1$ (branching ratio 34%), from which they decay in the fundamental state $^1S_0$, that represents a dark state for the process. Imaging is then performed on the ground-state population with the technique described in the previous section. Due to the low branching ratio of the $^3D_1 \rightarrow {}^3P_2$ decay, theoretical calculations predict that almost all the population is transferred from the metastable state $^3P_0$ to the fundamental level in a relatively low time ($\sim 10\,\mu$s) when an excitation power of 1 mW/cm^{-2} is considered (Franchi, 2016).

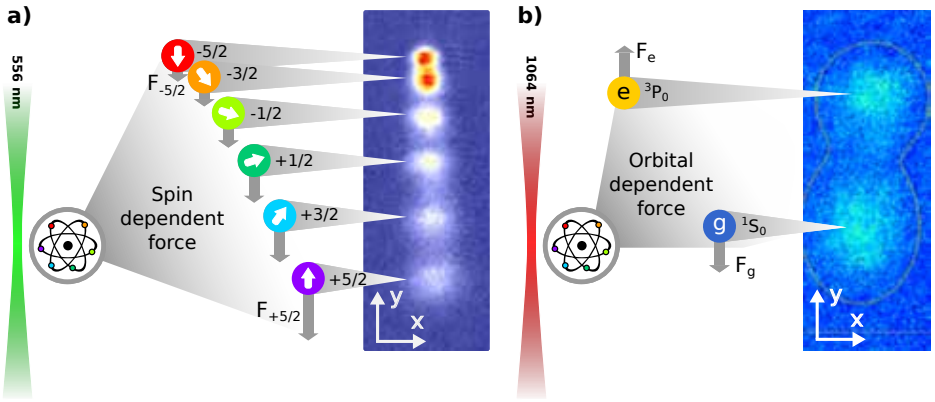

Figure 1.7: **a:** Example of OSG detection on a SU(6) ^{173}Yb spin mixture. Spin dependent force is exerted by a 556 nm beam, 566 MHz red-detuned with respect to the MOT frequency. **b:** Example of simultaneous detection of atoms in the orbital states $^1S_0$ and $^3P_0$. Orbital dependent force is exerted by a 1064 nm beam slightly misaligned with respect to the trap.

In order to excite the $^3P_0 \rightarrow {}^3D_1$ transition we employ a DFB fiber-coupled laser-diode model NLK1E5GAAA produced by NEL Laser Diodes which generates $\sim$20 mW at 1388.8 nm. We excite the atoms with a beam (labelled as REP in figure 1.5) characterized by a waist of 150 μm and with a power of $\sim$ 10 mW, that are enough to determine a 2 GHz power broadening of the transition. No locking is performed on the laser frequency, which is left in free running. The complete experimental sequence employed to detect atoms in the metastable state is described at the beginning of section 6.6. We also implemented a routine to simultaneously observe atoms in the fundamental $^1S_0$ and in the metastable $^3P_0$ state. The scheme adopted is a sort of *"orbital optical Stern-Gerlach"* procedure in which we employ a 1064 nm beam, slightly misaligned with respect to the atomic cloud, to spatially separate atoms in the two electronic states.

Transition	Wavelength λ [nm]	Probability [b] Γ [s^{-1}]	Branching Ratio
$^3D_1 \rightarrow {}^3P_0$	1388.8	1.7×10^6	63.8%
$^3D_1 \rightarrow {}^3P_1$	1539.1	9.5×10^5	35.2%
$^3D_1 \rightarrow {}^3P_2$	2092.6	2.7×10^4	1.0%

Table 1.3: Fundamental properties of the transitions connecting the (5d6s)$^3D_1$ state with the (6s6p)^3P manifold. Transition probabilities Γ can be calculated starting from the reduced matrix elements of the dipole operator $\langle {}^3D_1||\hat{d}||{}^3P_J\rangle$ given in reference (Porsev et al., 1999) with the relation $\Gamma = \omega_J^3/(9\pi\epsilon_0\hbar c^3)|\langle {}^3D_1||\hat{d}||{}^3P_J\rangle|^2$ (Steck, 2007) where $\omega_J/(2\pi)$ is the transition frequency. References: [b]: (Porsev et al., 1999).

This wavelength is trapping for the fundamental state and repulsive for the metastable state, and consequently exerts opposite forces on atoms belonging to different orbital levels. The experimental sequence developed to perform this two-orbital detection starts shining a 1064 nm pulse during the first 3.5 ms of time of flight. The beam used for the pulse is the 1064 nm beam orthogonal to the transport beam employed to realize the crossed dipole trap in which optical evaporation is performed (ODT_2 in figure 1.5). The beam is slightly misaligned during the pulse thanks to a piezoelectric mirror which controls the pointing. After the orbital Stern-Gerlach pulse, atoms in the $^3P_0$ state are pumped in the fundamental level with the procedure described before. Only at this point standard $^1S_0$ imaging is performed. A typical result of this experimental sequence is reported in figure 1.7-b.

1.3 Optical lattices

Optical lattices provide a unique tunable platform in which neutral atoms can mimic several features of electrons in crystalline solids. In their simplest form, optical lattices are far-detuned spatial-periodic potentials generated by the standing wave formed by two phase-locked counter-propagating laser beams. Considering the two beams as planar waves with wavelength λ, the resulting potential is commonly expressed as:

$$V_L(x) = s\, E_r \cos^2(k_L x) \tag{1.14}$$

where $k_L = 2\pi/\lambda$ is the lattice wavenumber and the potential height is expressed as a function of the lattice recoil energy $E_r = \frac{\hbar^2 k_L^2}{2m}$ in which m is the atomic mass. Given the expression 1.14, the spacing between neighbouring lattice sites is $d = \pi/k_L = \lambda/2$. The energy spectrum can be derived starting from the resolution of the time-independent Schroedinger equation associated to the potential $V_L(x)$, which reads

$$\left(-\frac{\hbar^2}{2m}\frac{\partial^2}{\partial x^2} + sE_r \cos^2(k_L x)\right)\Psi(x) = E\,\Psi(x) \tag{1.15}$$

whose solutions are the Bloch eigenfunctions

$$\Psi_{n,k}(x) = e^{ikx} u_{n,k}(x) \tag{1.16}$$

in which the functions $u_{n,k}(x)$ are characterized by the lattice periodicity and k is the lattice quasimomentum. Remarkably (Ashcroft and Mermin, 1976), a similar periodicity exists also in momentum space, where both the eigenfunctions and their associated energies are invariant under translations of multiples of the reciprocal lattice vectors. As a consequence of this translation symmetry, it is possible restrict the momentum space analysis to the primitive cell of the reciprocal lattice, which is defined as *first Brillouin zone* (FBZ). As it is shown in figure 1.8-a, the energies allowed in the FBZ define the band structure $\varepsilon(n,k)$ of the lattice, where n labels the band index. Extension to the 3D cubic case (figure 1.8-b) is straightforward being the problem separable. The band dispersion depends on the strength of the lattice potential and in the limit $s \gg 1$ reduces to the band structure of a harmonic oscillator characterized by a trapping frequency $\nu = \omega/(2\pi)$ with

$$\omega = 2\sqrt{s}\frac{E_r}{\hbar}. \tag{1.17}$$

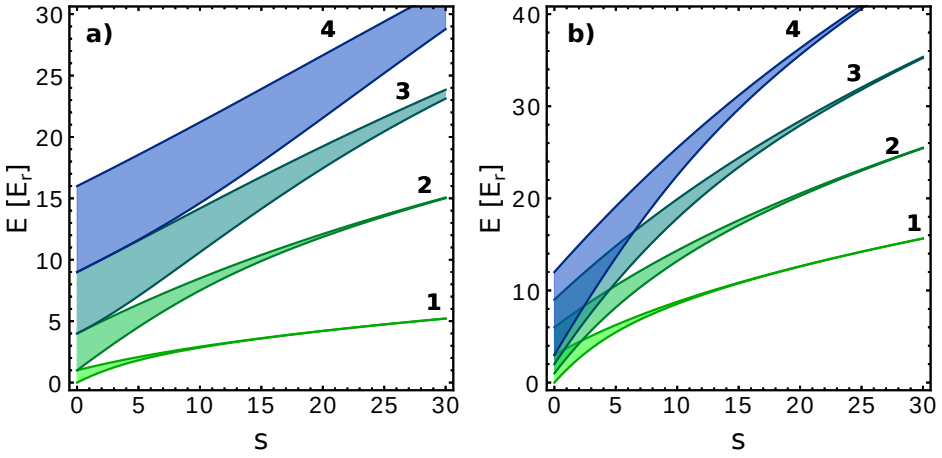

Figure 1.8: First four energy bands for a one-dimensional lattice (**a**) and a three-dimensional isotropic cubic lattice (**b**). For the 3D case the gap between the first two bands opens starting from $s = 2.2\, E_r$.

The depth parameter s obviously depends on the AC Stark shift exerted on the atoms by the lattice potential, which in turn is a function of the atomic polarizability $\alpha_\nu(\lambda)$, where ν labels the atomic quantum state. In particular, taking into account that the peak intensity in an optical lattice is four times the intensity of each of the two beams generating the lattice (here we suppose the two beams to have the same intensity), we have

$$s = \frac{2}{\epsilon_0\, c\, E_r(\lambda)}\, \mathrm{Re}[\alpha_\nu(\lambda)]\, I \tag{1.18}$$

where I is the intensity of each of the two beams. The dependence of the lattice depth on the atomic quantum state constitutes a limit for some applications in which two atomic states with different polarizabilities are simultaneously confined in the lattice[2]. When dealing with two-electron atoms, this state dependence of the lattice potential may represent a serious drawback, for example in the context of atomic clocks, where different polarizabilities of the ${}^1S_0$ and ${}^3P_0$ states lead to a lattice-induced shift of the clock transition. The problem is solved realizing lattices at the so-called *magic wavelength* λ_L for which the polarizabilities of the ${}^1S_0 = g$ and ${}^3P_0 = e$ states are identical, that is

$$\alpha_g(\lambda_L) = \alpha_e(\lambda_L). \tag{1.19}$$

As it can be observed in figure 1.9, Yb is characterized by several magic wavelengths in the visible spectrum. Among these wavelengths, the only one not too near to an atomic transition which would determine a too strong scattering of photons is $\lambda_L = 759.34$ nm (Dzuba and Derevianko, 2010), that is the one commonly employed to realize optical lattices for Yb atoms, as it is in our case.

[2]The lattice differential light shift can indeed be exploited in some quantum simulation schemes to localize one atomic state leaving the other delocalized, as it is needed for example in the simulation of the Kondo lattice model (Gorshkov et al., 2009).

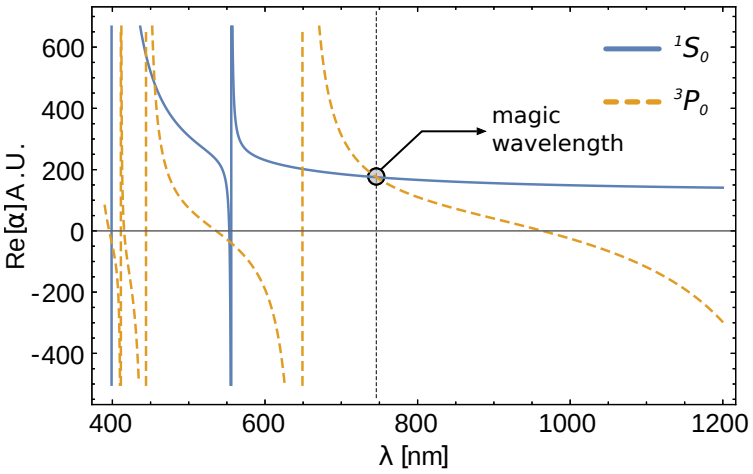

Figure 1.9: Real part of the polarizability of the $^1S_0$ and $^3P_0$ levels of Yb calculated starting from the expression 1.12. Polarizabilities are expressed in atomic units (AU). The conversion factor between polarizability in AU and SI units is: $\alpha(\text{SI}) = 1.648 \times 10^{-41}\alpha(\text{AU})$. A more accurate calculation performed by means of relativistic many-body calculations can be found in (Dzuba and Derevianko, 2010) and gives for the magic wavelength the value 759.34 nm.

1.3.1 Wannier functions and optical lattice properties

For increasing lattice depths atomic wavefunctions tend to localize in proximity of a lattice site and their description in terms of Bloch functions is not convenient. In this case a more appropriate formalism is given by the so called *Wannier functions*, which are defined starting from the Bloch function $\phi_{n,k}(x)$ as

$$w_n(x - \ell d) = A \int_{FBZ} e^{-i(k\,\ell\,d+\theta_{n,k})}\,\phi_{n,k}(x)\;\mathrm{d}k \tag{1.20}$$

where ℓ is an integer, d is the lattice spacing and $\theta_{n,k}$ is a phase factor, and the integral domain is the first Brillouin zone. In general, the phase factors $\theta_{n,k}$ are chosen in such a way to realize the so called *maximally localized Wannier functions* (MLWF) for which the quantity

$$\Delta x^2 = \langle w_n(x)|x^2|w_n(x)\rangle - (\langle w_n(x)|x|w_n(x)\rangle)^2. \tag{1.21}$$

is minimized (Marzari et al., 2012; Pini, 2014). MLWF form a complete set of orthogonal elements, that for increasing depth of the lattice potential collapse on the harmonic oscillator eigenfunctions in the different lattice sites.

In terms of the MLWF, we can define the two fundamental physical quantities that characterize the physics in an optical lattice, i.e. the tunnelling strength t and the on-site two-particles interaction energy U. In particular, the tunnelling strength for a one-dimensional lattice is defined as

$$t_{i,j} = \int \mathrm{d}x\, w_n^*(x - x_i)\left(-\frac{\hbar^2}{2m}\nabla^2 + s\,E_r\cos^2(k_L x)\right) w_n(x - x_j) \tag{1.22}$$

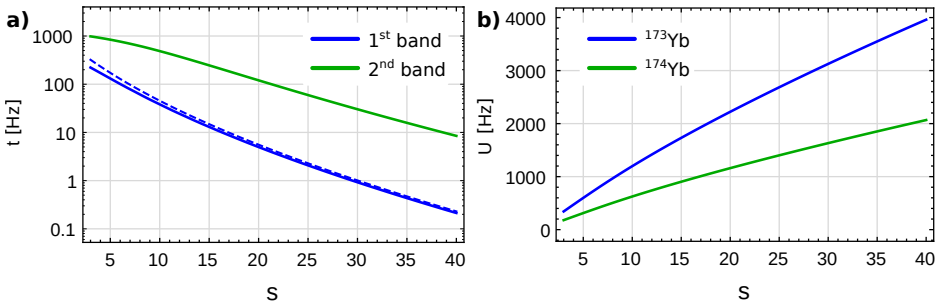

Figure 1.10: **a:** Tunnelling parameter t/h for Yb atoms in the fundamental (blue line) and in the first excited band (green line) of a one dimensional lattice operated at the magic wavelength $\lambda_L = 759.34$ nm. Tunnelling strength in the fundamental band is compared with the approximate result obtained with the formula $t = \frac{4}{\sqrt{\pi}} E_r \, s^{3/4} \, e^{-2s^{1/2}}$ (Bloch et al., 2012) (blue dashed line). **b:** Interaction energy in the fundamental band of a 3D isotropic optical lattice operated at the magic wavelength $\lambda_L = 759.34$ nm for two ^{173}Yb atoms (blue line) or two ^{174}Yb atoms (green line).

while for the interaction energy, in the limit of validity of the Hubbard-model and for a 3D isotropic lattice, we have

$$U = \frac{4\pi\hbar^2 \, a}{m} \left[\int \mathrm{d}x \, w_n^4(x) \right]^3 \tag{1.23}$$

where m is the atomic mass and a is the s-wave scattering length. For increasing a the relation 1.23 is no longer valid and the interaction energy saturates to the gap between the first and the second lattice band (Busch et al., 1998). Tunnelling strengths and interaction energies for the isotopes ^{173}Yb and ^{174}Yb for the range of lattice depths commonly employed in the experiment are reported in figure 1.10.

The expression of the lattice Hamiltonian in the MLWF basis takes the name of *tight binding approximation*. In this basis, which is particularly convenient to solve problems for which a momentum-state representation is difficult (as we will see in sections 4.2.1 and 5.1.2), the one-dimensional lattice Hamiltonian reads

$$H = -t \sum_j \hat{a}_j^\dagger \hat{a}_{j+1} + \text{ H.c.} \tag{1.24}$$

where $\hat{a}^\dagger$ is the creation operator for a particle localized at site j in the lattice. Here we have assumed that the dynamics is restricted to the fundamental band of the lattice and that tunnelling couplings beyond nearest neighbours are suppressed (both assumptions are reasonably well justified for a degenerate gas of atoms in optical lattices with $s \gtrsim 5$).

1.3.2 Experimental implementation and procedures

In our experiment we realize a 3D cubic optical lattice at the magic wavelength $\lambda_L = 759.44$ nm. The lattice is realized by means of three pairs of linearly-polarized

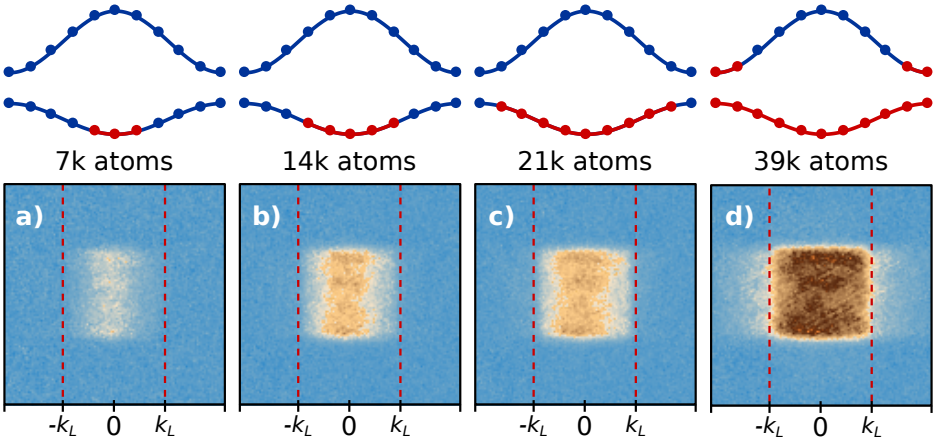

Figure 1.11: **a-d:** Band mapping for several fillings for a 3D lattice with depths $s_{x,y,z} = \{6, 30, 30\}$. On the top of each panel a sketch of the filling of the fundamental and first excited bands is shown. The square shape in the last panel correspond to the FBZ (integrated along the vertical axis).

counter-propagating beams (labelled as OL_1, OL_2 and OL_3 in figure 1.5) intersecting at the center of the glass cell along three orthogonal directions. Two of the three lattices are in the horizontal plane defined by the 1064 nm crossed dipole trap (the two orthogonal lattices are rotated by 36° with respect to the crossed trap beams) while the third is along the vertical direction. The beam waist at the position of the atoms is $w_0 \simeq 100\,\mu$m, which is sufficient to induce a $s = 30$ lattice depth[3] with a power of $P_0 \simeq 500$ mW. Each of the three beam pairs is equipped with a beam sampler that deviates part of the light on a photodiode, by means of which their power is monitored. The photodiode signal is used to feed a PID servo controller that tunes the beam intensity accordingly to an external set point by regulating the RF power of an AOM. In most of the experiments, the atoms are loaded in the lattice at the end of the evaporative cooling (after spin mixture preparation in the case of ^{173}Yb) with a $T = 150$ ms adiabatic exponential ramp characterized by a time constant $\tau = 20$ ms. The ramp is slow enough to avoid Landau-Zener tunnelling towards higher bands. For sufficiently deep isotropic 3D lattices ($s > 6$) the lattice-induced potential is strong enough to overcome gravity and consequently the 1064 nm trap can be turned off at the end of the loading. The geometry of the system can be decided changing the number of lattices confining the atoms, from 0D (employing three deep lattices) to 1D or 2D (employing respectively two or one deep lattices, the vertical one in the latter case). All the experiments described in this thesis are performed manipulating atoms trapped in an optical lattice, both because this allows us to control the sample geometry and because of the confinement-induced advantages of which a spectroscopy measurement can benefit,

[3]Calibration of the lattice depth is performed by means of the amplitude modulation method (Hundt, 2011) in which the gap ΔE_2 between the fundamental and the second excited lattice bands is measured by modulating the lattice intensity at frequency $f_m \simeq \Delta E_2$ and evaluating the dependence of the atom loss as a function of f_m.

as it is discussed in section 3.3.

The quasimomentum distribution (QD) inside the lattice can be accessed with the band mapping technique (Greiner et al., 2001; Köhl et al., 2005) which allows mapping the QD into a velocity distribution, which in turn is measured through standard absorption imaging. In order to perform band mapping, the lattices must be turned off adiabatically with respect to the inverse of the band gap, but faster with respect to the trap period (which never exceeds few tens of Hz). In order to perform an adiabatic band mapping process for lattice depths spanning from $s = 5$ to $s = 30$ we turn off the lattices with an adiabatic ramp characterized by a duration $T = 1.2$ ms and a decay constant $\tau = 0.3$ ms. Band mapping results for various band fillings in a 3D lattice with depths $s_{x,y,z} = \{6, 30, 30\}$ are shown in figure 1.11.

Chapter 2
Quantum physics with real and synthetic magnetic fields

Since its first experimental observation in 1980 by von Klitzing (Klitzing et al., 1980), the physics related to the quantum Hall effect gained crescent attention in the scientific community, as it can be inferred by the huge number of scientists awarded with the Nobel prize for their discoveries in this research field, from von Klitzing itself (1985), to R. B. Laughlin, H. L. Strmer and D. C. Tsui (1998) for the fractional quantum Hall effect, arriving to D. J. Thouless, F. D. M. Haldane and J. M. Kosterlitz (2016) for their theoretical discoveries of topological phase transitions and topological phases of matter. Quantum Hall states are apparently very similar to ordinary insulators in the sense that both systems are characterized by finite energy gaps and by electrons bound in closed orbits. As first pointed out by Halperin (Halperin, 1982), the peculiar transport properties that characterize the quantum Hall states distinguishing them from ordinary insulators can be ascribed to the presence of some current-carrying electron states that are localized on the boundary of the sample and extend on its perimeter. Edge states represent a hallmark of quantum Hall physics and to their experimental investigation by means of quantum simulation is dedicated part of the experimental section of this thesis (see chapters 4 and 5). For this reason, the first section of this chapter is dedicated to a very introductory discussion about the physics of edge states and to a description of their properties. In order to provide the theoretical basis for the experimental part of this work, in section 2.2 we investigate how the presence of a periodic potential affects the physics of quantum Hall states, focusing in particular the attention on the Harper-Hofstadter model (Harper, 1955). Finally in section 2.3 we discuss how the quantum Hall physics can be efficiently simulated in the ultracold atoms platform taking advantage of several techniques developed in the last years that make it possible to emulate the effects of magnetism with neutral particles (Gerbier and Dalibard, 2010). We can go a step further and simulate not only the effect of magnetism but also the space in which particles move. As we discuss in section 2.3.2 an *extra dimension* can be efficiently encoded in an internal degree of freedom of a neutral particle and allow the realization of ladder geometries naturally pierced by a synthetic flux (Celi et al., 2014). Here we provide a detailed description of this innovative approach to the simulation of magnetism with neutral atoms while in sections 4.2 and 5.1.2 its experimental realization will be investigated.

Lorenzo Francesco Livi, *New quantum simulations with ultracold Ytterbium gases*, © 2020 Author(s), content CC BY 4.0 International, metadata CC0 1.0 Universal, published by Firenze University Press (www.fupress.com), ISSN 2612-8020 (online), ISBN 978-88-6453-989-8 (online PDF)

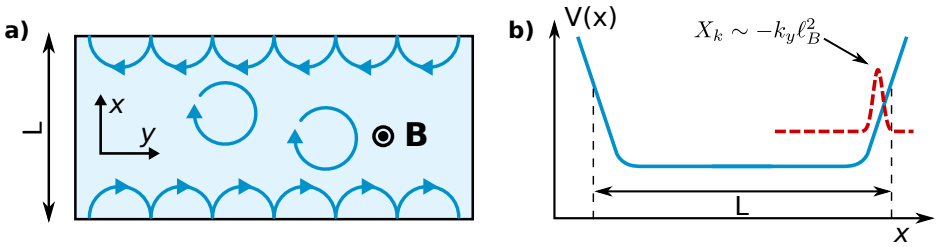

Figure 2.1: **a:** Semiclassically, in a quantum Hall bar electrons in the bulk orbit around fixed positions and do not carry current. At the edge, the specular reflection of the motion result in chiral skipping orbits carrying a non zero current. **b:** From a quantum mechanical prospect, the position and momentum of the IQHE wavefunction are locked. The energies of wavefunctions localized near the edge (dashed red curve in figure) are lifted due to the presence of the confining potential $V(x)$ and this result in a non vanishing group velocity $v_k = 1/\hbar\, \partial\epsilon_k/\partial k$ that has opposite sign at the two edges of the sample.

2.1 Edge currents and edge states in a Hall bar

Edge states play a fundamental role in the description of the paradigmatic features of many intriguing physical effects, such as the Quantum Hall Effect or the transport properties in the class of materials known as topological insulators, just to mention two of the most celebrated examples. From a semiclassical prospect, edge states can be assimilated to the *skipping semicircular orbits* performed on the boundary of a 2D slab by an electron gas subjected to a magnetic field B perpendicular to the slab itself. In such a system, as a consequence of the Lorentz force, an electron of charge e and mass m will undergo a circular motion characterized by an angular frequency $\omega_c = e\,B/(m\,c)$. Close to the edge the charged particles do not have enough space to complete a circle and so they are reflected by the boundary of the slab, starting a new semicircular orbit in the same direction, as it is pictorially shown in figure 2.1-a. Although this is a very naive model, a fundamental property of the charge transport in this kind of systems already emerges: even in equilibrium, thanks to the skipping-orbit motion of the particles along the boundary, each edge of the slab carries a current and these currents are *chiral*, meaning that they can flow in a unique direction which is determined only by the relative orientation of the magnetic field and the edge itself. This implies that in absence of an electric field parallel to the plane of the slab, the currents carried by opposite edges have the same magnitude but different chirality, ensuring in this way that the total flowing current vanishes. On the other hand in the bulk of the 2D material, where the particles can complete a circular orbit, no current flow is possible. Let's now review the same argumentation from a quantum mechanic prospect, focusing the attention on the role played by the edge states in the Integer Quantum Hall Effect (IQHE). We consider a slab having a finite size L along the $\hat{x}$ direction and an infinite length along $\hat{y}$ pierced by a magnetic field B aligned with $\hat{z}$. If we describe the edges of the slab with a confining potential $V(x)$ then, in the Landau gauge, the

Hamiltonian describing an electron in this system is

$$H = \frac{1}{2m}\left(p_x^2 + (p_y + e\,B\,x)^2\right) + V(x). \tag{2.1}$$

From the IQH theory (Yoshioka, 2002; Giuliani and Vignale, 2005; Tong, 2016; Girvin, 1999) we know that in the fundamental Landau level the eigenfunction of the 2.1 are gaussian wavepackets characterized by a length $\ell_B = \sqrt{\hbar/(eB)}$ and having the functional form

$$\psi(x,y) = A\, e^{ik_y y} e^{-\frac{1}{2\,\ell_B^2}(x-X_k)^2} \tag{2.2}$$

where A is a normalization constant and X_k, the expectation value of the wavefunction position, is $X_k = -k_y \ell_B^2$. If now we assume $V(x)$ to be smooth on the lengthscale of ℓ_B, it is possible to Taylor-expand the potential experienced by each wavepacket centered in X_k and at the first order we thus have $V(x) = V(X_k) + (\partial V/\partial x)|_{x=X_k}(x - X_k)$. The effect of the linear expansion term of $V(x)$ in the Hamiltonian 2.1 is the same produced by an electric field aligned with the $\hat{x}$ direction. We know from the IQHE theory that this results in a drift velocity in the $\hat{y}$ direction given by

$$v_y = -\left.\frac{1}{e\,B}\frac{\partial V}{\partial x}\right|_{x=X_k}. \tag{2.3}$$

The drift velocity calculated starting from the last expression depends on the position X_k of the wavefunction considered. In particular, since the first derivative of $V(x)$ changes its sign near opposite edges $\pm L/2\hat{x}$, we will have that eigenstate localized near the edges will experience opposite drift velocity depending on which of the two edges is considered. One can derive the same result considering that at the edges the energy of the wavefunction is lifted by the confining potential $V(x)$. Since the momentum along the $\hat{y}$ direction is directly linked to the wavepacket position by the relation 2.2 we have that the group velocity $v_k = 1/\hbar\,\partial\epsilon_k/\partial k$ will thus acquire opposite values at different edges as it is explained by figure 2.1-b.

The quantum approach thus leads to the same important result of the simple classical model discussed before: in a Hall bar edges carry a non zero current that is characterized by a well-defined chirality. These chiral edge currents have a lot of remarkable properties: first of all the presence of a gap between the bulk and the edge modes prevents the disorder to admix these states with states deeper in the sample in such a way that current might leak away from the edge. Moreover, the chiral nature of the current guarantees that electrons cannot be reflected by an impurity, as they have to move only in one direction, meaning that edge transport is robust against the presence of impurities or disorder.

2.1.1 Connections with topology

Edge states are intimately related to the topological aspects of the IQHE (Hasan and Kane, 2010; Kane and Moore, 2011; Hatsugai, 1993). QH states represent the fundamental example of 2D topological systems characterized by an insulating gapped bulk and conductive gapless edges which are protected against small deformations in the system parameters. The topological invariant associated with this kind of topological

systems is the Chern number n_c which is an integer coinciding with the quantized Hall conductance σ_{xy} in units of $e^2/\hbar$

$$\sigma_{xy} = -\frac{e^2}{\hbar} n_c. \tag{2.4}$$

The topological nature of the Chern invariant derives from a geometric interpretation of the Hall conductance as a curvature of a two dimensional parameter space, as pointed out in (Avron et al., 2003) and first established in a seminal paper by Thouless, Kohmoto, Nightingale and den Nijs (Thouless et al., 1982). Being an integer, the value of n_c cannot be changed continuously and defines an equivalence class of gapped systems. As a result of the topological nature of the IQHE, states characterized by different Chern numbers cannot be smoothly deformed one into the other without closing the bulk energy gap separating the highest occupied electronic band from the lowest empty band, in a similar way in which surfaces characterized by a different genus cannot be deformed one into the other without the creation of one or more holes in some points. The profound consequence of this argumentation is that at an interface between two materials characterized by different Chern numbers, such as an IQH state with $n_{c1} = 1$ and the vacuum with $n_{c2} = 0$, as one moves across the boundary the gap must close and reopen again in the region characterized by a different value of the topological invariant. As it is pictorially shown in figure 2.2-a, at the interface, where the gap vanishes, the presence of low energy gapless electronic modes is thus expected: these modes are nothing but the edge states introduced before.

It is evident that a link exists between the edge states, which live on the surface of the system, and the Chern number, which is a topological property that instead characterizes the bulk. This link is summarized by the famous argument known as *bulk-boundary correspondence* (Hasan and Kane, 2010) which states that at an interface the difference Δn_c between the Chern numbers of the two adjacent materials is equal to the difference between the number of right N_R and left N_L moving edge states branches present at the interface

$$\Delta n_c = N_R - N_L \tag{2.5}$$

A deeper interpretation of the relation between the edge states and the topological character of the IQHE has been carried out by Hatsugai (Hatsugai, 1997) but goes beyond the scope of this work.

2.1.2 The role of Spin and Spin-orbit coupling

Up to now we have discussed only about systems in which the transport and topological properties emerge as a consequence of the presence of an external magnetic field which breaks the time-reversal symmetry. This constraint can be released if a different class of materials is considered, in which the role of the magnetic field is played by the spin-orbit coupling (SOC) (Kane and Mele, 2005; Hasan and Kane, 2010; Qi and s. Zhang, 2010; Moore, 2010; Manoharan, 2010). SOC is a momentum-dependent force characterized by a direction determined by the spin, acting in this way as a sort of spin-depending magnetic field. In some materials, the presence of SOC leads to a new kind of topological states, known as quantum spin Hall (QSH). We can imagine a QSH

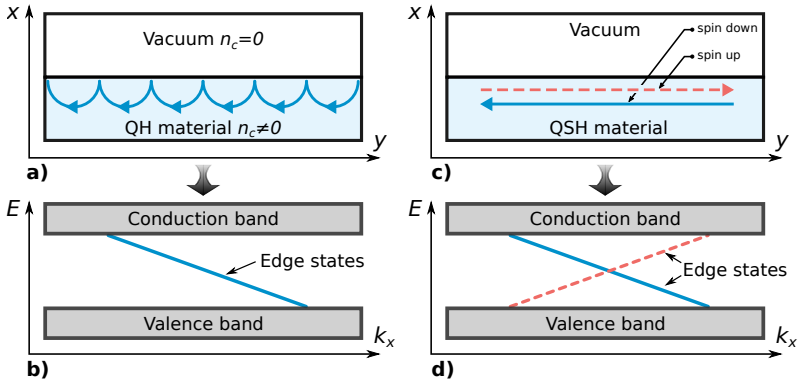

Figure 2.2: **a:** In the integer quantum Hall effect edge states appear at the interface between two materials characterized by a different topological invariant, the *Chern number*. **b:** From a topological prospect, at the interface the energy gap of the two materials must vanish and edge states emerge. **c:** In a quantum spin Hall system at the boundary two counter-propagating spin currents flow. **d:** The spectrum associated to this kind of materials shows at least two branches of edge states protected by the Kramers theorem.

state as the superposition of two QH states (one for the spin-up, the other for the spin-down electrons) characterized by an opposite direction of propagation at the edges, as it shown in figure 2.2-c. The resulting system has an insulating bulk, as a QH state, but at the edges, as an effect of the SOC, two spin currents propagates in opposite directions. Since the two currents cancel each other, the total current flowing at the edges, and so the Hall conductance, are both vanishing. As in the QH states, the QSH edge states are protected by backscattering, meaning that an electron propagating on the boundary cannot change its direction as the consequence of the scattering with a (non magnetic) impurity. Differently from the QH, this property does not come out from the chiral nature of the current (after all we have two currents propagating in opposite directions on each edge) but is the result of a quantum destructive interference associated to the backscattered paths. What is important in this kind of systems is the role played by the time-reversal symmetry (TRS), which is not broken in a QSH state. As it can be observed in the spectrum associated to a QSH state (see figure 2.2-d) TRS (which acts swapping the spin and the momentum of a particle), connects states with spin-up and positive momenta with states with spin-down and negative momenta. This fulfills the requirements of the Kramers theorem which for half-integer time-reversal-symmetric systems predicts that each energy level must be at least doubly degenerate. As an effect of the Kramers theorem the point at $k = 0$ where the branches for the spin-up and spin-down particles intersect must be twofold degenerate (this is a time-reversal-invariant momentum (TRIM) point) and a gap cannot be opened with an adiabatic deformation of the band structure. It comes out that this property can be associated to a new kind of topological invariant, as it was pointed out by Kane and Mele in reference (Kane and Mele, 2005) and this eventually leads to the definition of a new kind of topological materials, known as 2D topological insulators.

2.2 Hall physics on a lattice

We have seen that in the continuum a 2D electron gas subjected to a strong magnetic field exhibits a series of interesting physical properties: in particular, the presence of a gapped bulk and the existence of conductive states at the edges lead to the quantization of the Hall conductance and to the definition of a quantum state characterized by a topological behaviour, the Integer Quantum Hall. Surprisingly, a similar physics holds if a 2D lattice is superimposed to a QH state. One of the main effects induced by the presence of a periodic potential is the splitting of the Landau levels in several subbands the number of which depends on the flux of the magnetic field piercing each of the lattice unit cells. Actually, when a lattice is present, two lengthscales dominate the resulting system, one being the magnetic length $\ell = \sqrt{e\hbar/B}$ and the other the lattice spacing a (we suppose to deal with a square lattice). This means that if we consider a finite-size system then the application of periodic boundary conditions will require both the number of unit cells of the periodic potential and the number of states in each Landau level $N_L = A/(2\pi\ell^2)$ (where A is the area of the system), to be integers. This leads to a redefinition of the Brillouin zone dimension and to the appearance of a less trivial gap structure that we will investigate in section 2.2.1. A fundamental ingredient for many schemes of quantum simulation is the presence of a periodic potential. In section 2.2.2 we review how quantum Hall system are affected by such a potential deriving the Harper-Hofstadter Hamiltonian. Finally, in section 2.3.2 we discuss how quantum Hall systems can be simulated in the context of ultracold atoms and introduce the experimental techniques adopted in this thesis.

2.2.1 Magnetic Brillouin zone

The Hamiltonian describing a 2D non-interacting electron gas in an uniform magnetic field orthogonal to the 2D plane and subjected to a periodic potential $V(x, y)$ can be written as

$$H = \frac{1}{2m}(\mathbf{P} + e\mathbf{A})^2 + V(x, y) \tag{2.6}$$

where e is the elctron charge and the vector potential $\mathbf{A}$ is a function only of the $\hat{x} - \hat{y}$ coordinates in such a way to generate a magnetic field $\mathbf{B} = B\hat{z}$ perpendicular to the plane of the electron gas. We assume the periodic potential to be characterized by a unit cell having dimensions a and b respectively along the $\hat{x}$ and $\hat{y}$ directions, in such a way that the corresponding Bravais lattice is defined as

$$\mathbf{R} = n\,a\,\hat{x} + m\,b\,\hat{y} \tag{2.7}$$

with n and m integers. The periodic potential is thus invariant under the application of the operator

$$T_R = e^{(i/\hbar)\,\mathbf{R}\cdot\mathbf{p}} \tag{2.8}$$

which shifts the position by a vector $\mathbf{R}$ of the Bravais lattice. The operator T_R however does not commute with the Hamiltonian 2.6 because otherwise this would imply $A(\mathbf{r}) = A(\mathbf{r} + \mathbf{R})$, a condition not necessarily always satisfied. Anyway, in the symmetric gauge ($\mathbf{A} = (\mathbf{B} \wedge \mathbf{r})/2$), it is possible to define a new set of translation operators

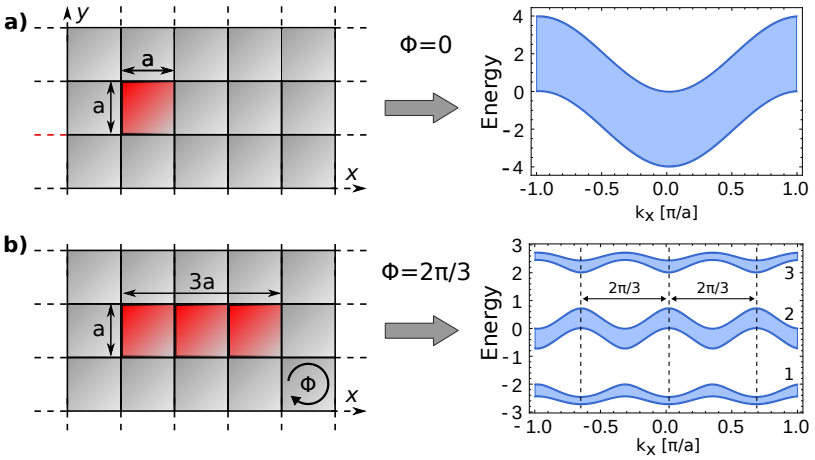

Figure 2.3: Effect of a magnetic field on a periodic potential. **a:** In absence of a magnetic field the unit cell of a 2D square lattice in real space measures $a \times a$ and the Brillouin zone has periodicity $2\pi/a$. **b:** If a magnetic field having rational flux $\phi = 2\pi\, p/q$ through each lattice cell is present ($\phi = 2\pi/3$ in figure) the periodicity of the system changes and the resulting unit cell is q times enlarged while the Brillouin zone reduces to $2\pi/(qa)$. Moreover, the shrinking of the Brillouin zone corresponds to the appearance of q sub-bands in the energy spectrum.

that commute with the Hamiltonian. These new *magnetic translation operators* are defined as (Kohmoto, 1985; Bernevig, 2013)

$$\hat{T}_R = T_R\, e^{(i\,e/\hbar)\,(\mathbf{B}\wedge\mathbf{R})\cdot\mathbf{r}/2} \tag{2.9}$$

and verify the relation $[H, \hat{T}_R] = 0$. Unfortunately, differently from the usual translation operators defined in 2.8, the magnetic translation operators do not commute one with the other. In particular we have

$$\hat{T}_{a\hat{x}}\hat{T}_{b\hat{y}} = e^{2\pi i\phi}\,\hat{T}_{b\hat{y}}\hat{T}_{a\hat{x}} \tag{2.10}$$

where $\phi = (eB/\hbar)\,ab$ is the magnetic flux through a unit cell of the lattice. As a consequence of the relation 2.10 it is not possible to label the eigenstates of H using simultaneously the eigenvalues of $\hat{T}_{a\hat{x}}$ and $\hat{T}_{b\hat{x}}$, a requirement necessary to construct a proper Brillouin zone. It is however possible to find a set of $\hat{T}_R$ commuting operators if some special values of the flux are chosen. One possibility is to choose ϕ to be an integer in the relation 2.10: this is a trivial case since it coincides with the absence of magnetic flux. The other possibility is to choose a rational value of the magnetic flux $\phi = p/q$ with p and q co-prime integers. In this last case the commutator between $\hat{T}_{a\hat{x}}$ and $\hat{T}_{b\hat{x}}$ still does not vanish but on the other hand, if the operators $\hat{T}_{q\,a\hat{x}}$ and $\hat{T}_{b\hat{x}}$ are considered, then the 2.10 becomes

$$\hat{T}_{qa\hat{x}}\hat{T}_{b\hat{y}} = e^{2\pi i(eB/\hbar)\,qab}\,\hat{T}_{b\hat{y}}\hat{T}_{qa\hat{x}} = e^{2\pi i(\phi\,q)}\,\hat{T}_{b\hat{y}}\hat{T}_{qa\hat{x}} = \hat{T}_{b\hat{y}}\hat{T}_{qa\hat{x}} \tag{2.11}$$

and so $[\hat{T}_{qa\hat{x}}, \hat{T}_{b\hat{y}}] = 0$. We can therefore conclude that if a q-times enlarged unit cell having dimensions $q\,a\,\hat{x} \times b\,\hat{y}$ is considered, then it is possible to find a set of translation operators that commute one with the other and with the Hamiltonian, defining in this way a set of good quantum numbers to label the eigenstates of H. This enlarged unit cell defines a new Brillouin zone which has dimensions

$$-\frac{\pi}{qa} < k_x < \frac{\pi}{qa} \qquad -\frac{\pi}{b} < k_y < \frac{\pi}{b} \tag{2.12}$$

that takes the name of *magnetic Brillouin zone* (MBZ). Since the MBZ is q-times smaller than the Brillouin zone, if the lattice has size $L_1 \times L_2$, the number of state in each MBZ is $N_{MBZ} = L_1 L_2/(q\,a\,b)$ suggesting that the resulting spectrum decomposes in q subbands each having N_{MBZ} states. This result is sketched in figure 2.3-b for a square lattice pierced by a magnetic flux per plaquette $\Phi = 2\pi/3$ and compared with the case in which a magnetic flux is not present (figure 2.3-a). Obviously one can also view the same argumentation from the Landau levels point of view, concluding that as a consequence of the presence of a periodic potential each Landau level splits into q sub-levels. The implications of this result will be discussed in the following section.

2.2.2 Tight binding model in presence of a magnetic field

Let's now move towards the formalism typical of solid-state physics and investigate how the presence of a magnetic field affects one of the most paradigmatic models describing particles interacting with a periodic potential: the tight binding single-particle model. For a system of particles moving in a 2D rectangular lattice, in the second quantization formalism, the non interacting tight binding Hamiltonian reads

$$H = -t_x \sum_{\langle i,j \rangle} \hat{a}^\dagger_{i+1,j} \hat{a}_{i,j} - t_y \sum_{\langle i,j \rangle} \hat{a}^\dagger_{i,j+1} \hat{a}_{i,j} + \text{ H.c.} \tag{2.13}$$

where t_x and t_y are the tunnelling energies characterizing the hopping between adjacent lattice sites respectively in the $\hat{x}$ and $\hat{y}$ directions, $\hat{a}_{i,j}$ is the annihilator operator for a particle localized at the site $\{i, j\}$ and $\langle\ \rangle$ indicates a sum that runs only over the nearest neighbour lattice sites. To understand how the Hamiltonian 2.13 is modified in presence of a magnetic field $\mathbf{B} = \nabla \wedge \mathbf{A}$, we must take into account the effect induced by the vector potential $\mathbf{A}$ on a particle moving in the region of space where $\mathbf{A}$ is defined. Actually, from a quantum mechanical prospect, $\mathbf{B}$ does not contain the full information necessary to capture how a charged particle is influenced by the presence of an electromagnetic field and it turns out that a description of magnetism in terms of the vector potential $\mathbf{A}$ can unveil some nonclassical results, as argued by Aharonov and Bohm in their seminal paper (Aharonov and Bohm, 1959). In particular the two authors pointed out that the wavefunction of a particle having charge q and moving on a path γ from point $\mathbf{r_1}$ to $\mathbf{r_2}$ in a region where the vector potential $\mathbf{A}(\mathbf{r})$ is defined, will pick up a phase given by

$$\phi(\mathbf{r_1} \to \mathbf{r_2}) = \frac{q}{\hbar} \int_\gamma \mathbf{A}(\mathbf{r}) \cdot d\mathbf{r} \tag{2.14}$$

that takes the name of *Aharonov-Bohm phase*. It is interesting to note that also a particle that moves in a region where **B** is zero but **A** is defined, such as the external part of an infinite long solenoid, will experience an Aharonov-Bohm phase, despite the absence of a non-zero magnetic field. The phase 2.14 is a geometric phase: it does not depend on the time it takes to the particle to move from $\mathbf{r_1}$ to $\mathbf{r_2}$ nor on its velocity, but instead depends only on the path which is followed. In particular, if a closed path is considered, then the 2.14 becomes

$$\phi(\mathbf{r_1} \to \mathbf{r_1}) = \frac{q}{\hbar} \oint_\gamma \mathbf{A}(\mathbf{r}) \cdot d\mathbf{r} = \frac{q}{\hbar} \iint_{A_\gamma} \mathbf{B}(\mathbf{r}) \cdot d^2 r \tag{2.15}$$

where A_γ is the area enclosed by the curve γ. In the case of a closed path a particle will thus pick up a phase that is proportional to the magnetic field flux piercing the loop itself. This is an interesting result because it does not depend on the particular gauge chosen to express the vector potential **A**.

Coming back to our original goal keeping in mind the expressions 2.14 and 2.15, it seems natural that the effect induced by the presence of a magnetic field can be included in the tight binding Hamiltonian if the hopping energy t is replaced with

$$t \to t\, e^{-i\frac{q}{\hbar}\int_{r_1}^{r_2} \mathbf{A}(\mathbf{r})\cdot d\mathbf{r}} \tag{2.16}$$

where r_1 and r_2 are the positions of two adjacent lattice sites and the path chosen for the line integral is the shortest connecting the two points. The substitution 2.16 can be interpreted in terms of the Aharonov-Bohm phase accumulated by a particle during the hopping between two neighbouring lattice sites and in this context takes the name of *Peierls phase* (Peierls, 1933). The expression 2.16 is valid only in the tight-binding regime and if the cyclotron frequency associated to the magnetic field is smaller than the energy gap between the fundamental and the first excited lattice bands (Dalibard et al., 2011), but have also been investigated outside of these regimes (Nenciu, 1991). For non-interacting particles, the Peierls substitution allows us to express the tight-binding Hamiltonian in the presence of a magnetic field $\mathbf{B} = \nabla \wedge \mathbf{A}$ as

$$H = -t_x \sum_{\langle i,j \rangle} e^{-i\frac{q}{\hbar}\int_{r_{i,j}}^{r_{i+1,j}} \mathbf{A}(\mathbf{r})\cdot d\mathbf{r}} \hat{a}^\dagger_{i+1,j}\hat{a}_{i,j} - t_y \sum_{\langle i,j \rangle} e^{-i\frac{q}{\hbar}\int_{r_{i,j}}^{r_{i,j+1}} \mathbf{A}(\mathbf{r})\cdot d\mathbf{r}} \hat{a}^\dagger_{i,j+1}\hat{a}_{i,j} + \text{ H.c.} \tag{2.17}$$

where $r_{i,j}$ indicates the position of a lattice site inside the Bravais lattice. Let's now suppose that the lattice is pierced by an orthogonal and uniform magnetic field $\mathbf{B} = B\hat{e}_z$. In the Landau gauge, where the vector potential reads $\mathbf{A} = -By\hat{e}_x$, only the hopping terms along the $\hat{x}$ direction will pick up a phase factor. For this particular case, if we assume the lattice spacing to be a along the $\hat{x}$ direction and b along $\hat{y}$, the Peierls substitution reads

$$t \to t\, e^{i\frac{q}{\hbar}\int_{r_{i,j}}^{r_{i+1,j}} By\, dx} = t\, e^{i\frac{q}{\hbar} B\, a\, (jb)} = t\, e^{i\frac{q}{\hbar}\, j\Phi} \tag{2.18}$$

where $\Phi = abB$ is the magnetic field flux through one lattice unit cell and jb is the $\hat{y}$ position of the two sites involved in the hopping dynamics. In particular, for a particle performing a closed loop around one lattice plaquette, the total accumulated phase will be simply given by $\phi = q\Phi/\hbar$, independently from the chosen gauge. Consequently,

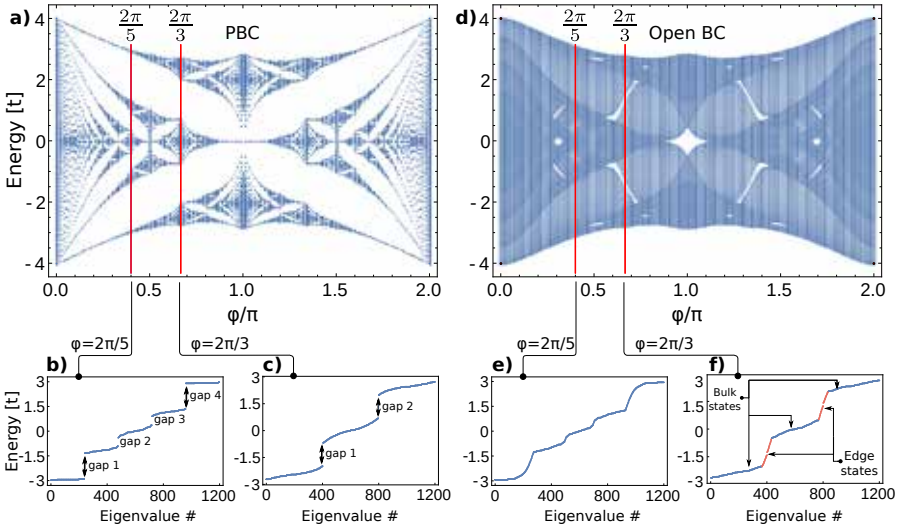

Figure 2.4: Hofstadter butterfly spectrum in the presence of periodic boundary conditions (**a**) and with open boundary conditions (**d**). The spectra have been evaluated on a 200×6 2D lattice with complex tunnelling along the short dimension, solving numerically the Hamiltonian 2.19 with the conditions $t_x = t_y = t$. The energy of the eigenstates is reported as a function of the magnetic flux piercing the lattice cells. (**b**) and (**d**) are the Hamiltonian eigenenergies for the rational flux values $\phi = 2\pi\, p/q = 2\pi/5$ and $\phi = 2\pi\, p/q = 2\pi/3$ respectively. Clearly q subbands appears in each spectrum and $q-1$ gaps open as a consequence of the presence of the magnetic flux. In the open boundary conditions spectra (**e**) and (**f**), evaluated for the same flux values, the gaps close and edge states appear.

in the Landau gauge, the tight binding Hamiltonian reads

$$H = -t_x \sum_{\langle i,j \rangle} e^{-i\frac{q}{\hbar} j\, \Phi}\ \hat{a}^{\dagger}_{i+1,j}\hat{a}_{i,j} - t_y \sum_{\langle i,j \rangle} \hat{a}^{\dagger}_{i,j+1}\hat{a}_{i,j} + \text{H.c.} \tag{2.19}$$

In momentum space, the Schroedinger equation related to the Hamiltonian 2.19 can be recasted as (Bernevig, 2013)

$$-2t_x \cos(k_y a + 2\pi\Phi j)\psi_j(k) - t_y(e^{ik_y b}\psi_{j+1}(k) + e^{-ik_y b}\psi_{j-1}(k)) = E(k)\psi_j(k) \tag{2.20}$$

and takes the name of Harper equation (Harper, 1955). If plotted as a function of the magnetic field flux, the energy spectrum associated to the 2.20 shows a fractal structure known as Hofstadter butterfly (Hofstadter, 1976). An example of this spectrum, evaluated diagonalizing the Hamiltonian 2.19 for a lattice having 200×6 sites and periodic boundary conditions along both dimensions is reported in figure 2.4a. As we anticipated before, for a rational value of the flux $\phi = 2\pi\, p/q$, q subbands appear in the spectrum and $q-1$ gaps open. This behaviour is clear in figure 2.4-b and 2.4-c, where the eigenvalues of the system are reported in order of increasing energy respectively for $\phi = 2\pi/5$ ($q = 5$) and $\phi = 2\pi/3$ ($q = 3$). In the same spectrum, evaluated

in the presence of open boundary conditions (see figure 2.4-d,e,f), the gaps close and the magnetic subbands structure disappears. The new states that fill the gaps are edge states that emerge naturally as a consequence of the boundary imposed to the system, as it is expected in a quantum Hall bar.

2.2.3 Ladder systems

To clarify some of the concepts introduced in the present section, we can consider a very simple toy model of quantum Hall physics in the presence of a periodic potential, that is a two-leg ladder pierced by an uniform magnetic field. With the term *ladder* we refer to a 2D lattice in which the number of sites along one dimension (let's say $\hat{e}_x$) far exceeds the number of sites along the other ($\hat{e}_y$). In particular, a two-leg ladder is characterized by the presence of only two sites along the short dimension as it is pictorially represented in figure 2.5-a. As we will discuss later in this chapter, despite its simplicity, this model is gaining attention in the framework of ultracold atoms because of its possible applications in the context of quantum simulation (Hügel and Paredes, 2014).

Form a theoretical point of view the Hamiltonian that describes a system of non-interacting atoms in a two leg-ladder subjected to a magnetic field flux Φ per plaquette in the Landau gauge is

$$H = -t_x \sum_j \left(e^{i\Phi/2}\, \hat{a}^\dagger_{j+1} \hat{a}_j + e^{-i\Phi/2}\, \hat{b}^\dagger_{j+1} \hat{b}_j \right) - t_y \sum_j \left(\hat{a}^\dagger_j \hat{b}_j \ + \ \text{H.c.} \right) \tag{2.21}$$

where $\hat{a}^\dagger_j / \hat{b}^\dagger_j$ are respectively the creation operator for a particle at site j in the upper and lower leg of the ladder, t_x and t_y are the tunnelling amplitude respectively along the long and short dimension and $\Phi/2$ is the Peierls phase associated to the magnetic field piercing the system. Following reference (Hügel and Paredes, 2014) the same Hamiltonian in momentum space reads

$$\hat{H}(k) = \epsilon_0(k) I + \xi \sigma_x + \sin(\Phi/2)\sin(k)\sigma_z \tag{2.22}$$

where $\epsilon_0(k) = \cos(\Phi/2)\cos(k)$, $\xi = t_y/2t_x$ and $\sigma_{x,z}$ are Pauli matrices. The presence of the term proportional to σ_z in the last expression can be interpreted as an effective spin-orbit coupling acting on the atoms confined in the lattice in which the two legs play the role of the spin projections of an effective spin 1/2. At a fixed flux particles in the upper leg (spin up) minimize their energy for positive values of the momentum k while particles in the lower leg (spin down) minimize the energy for negative momenta. This behaviour is inverted if the magnetic field flux is changed in sign as we expect for a Hall system. The spin momentum locking induced by the magnetic field on the eigenstates of the ladder is evidenced in the spectra reported in figure 2.5 where the band dispersion relative to the upper leg (solid line in panel 2.5-b) and lower leg (solid line in panel 2.5-c) are reported for the flux $\Phi = 0.75\pi$ and equal couplings $t_x = t_y$. The spectra have been evaluated taking into account the simple analytical form of the Hamiltonian wavefunctions, whose eigenvalues are given by

$$E_\pm(k) = -\epsilon_0(k) \pm \sqrt{\xi^2 + \sin^2(\Phi/2)\sin^2(k)} \tag{2.23}$$

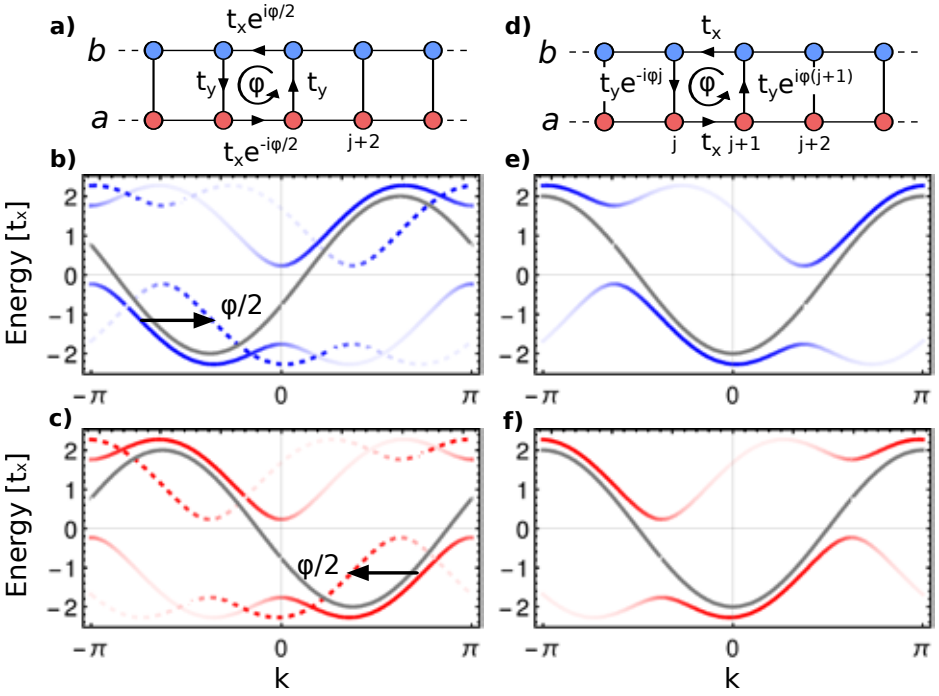

Figure 2.5: Two-leg ladders. Sketch of a two-leg ladder pierced by an uniform magnetic flux in the "unphysical" gauge (**a**) (complex tunnelling along the long dimension) and in the "physical" gauge (**d**) (complex tunnelling along the short dimension). **b-c** spectra in the "unphysical" gauge of the upper leg (b) and of the lower leg (c) for the flux $\Phi = 0.75\pi$: solid blue-red lines for $t_x = t_y$, dotted blue-red lines are the same spectra in the "physical gauge", grey lines for $t_y = 0$. **e-f** spectra in the "physical" gauge of the upper leg (e) and of the lower leg (f) for the flux $\Phi = 0.75\pi$: solid blue-red lines for $t_x = t_y$, grey lines for $t_y = 0$. In b-c-e-f the intensity of the colors reflects the squared module of the wavefunction.

while the expression of the eigenvectors in a 2D Hilbert space is

$$\psi_{\pm}(k) = \frac{\{\xi,\ \sin(\Phi/2)\sin(k)\}}{\sqrt{\xi^2 + \sin^2(\Phi/2)\sin^2(k)}}. \tag{2.24}$$

This very simple system features some of the peculiar properties of a real quantum Hall system on a lattice. Despite the absence of a bulk, the two spin-momentum locked eigenvectors can be interpreted as chiral currents circulating on the border of this only-edge system. These currents depend on the flux of the magnetic field and reverse as the flux changes its sign.

It should be observed that the gauge chosen for the Hamiltonian 2.21 makes it particularly easy to rewrite the problem in momentum space, but gives rise to an "unphysical" situation in which, in the absence of interleg coupling ($t_y = 0$) the band dispersions of the two legs are not symmetric with respect to the center of the Bril-

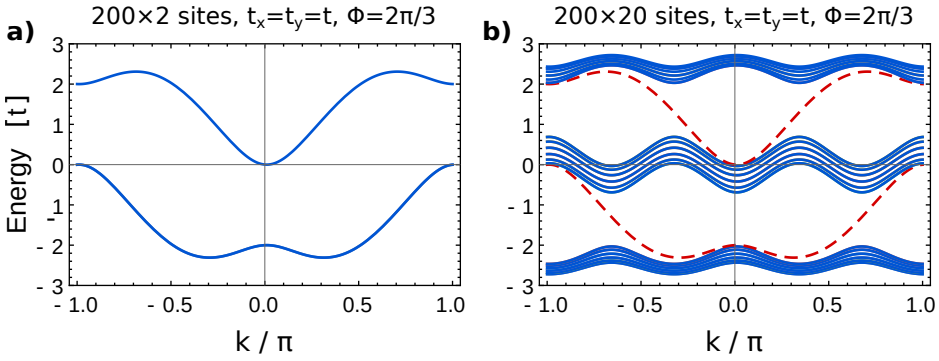

Figure 2.6: Energy bands for **(a)** a two-leg ladder with 200×2 lattice sites (PBC along the long dimension) pierced by a magnetic flux $\Phi = 2\pi/3$ per plaquette **(b)** a bigger ladder having 200×20 sites. The two-leg ladder bands exactly reproduce the edge states energy of the the bigger ladder (red dashed lines). The two spectra have been calculated diagonalizing the Hamiltonian 2.25 in the "unphysical" gauge with the software *Mathematica.*

louin zone (grey dotted lines in figures 2.5-a and 2.5-b). The "physical" behaviour can be recovered shifting the upper/lower leg spectrum by $\Phi/2$ towards positive/negative momenta (blue-red dashed lines in figure 2.5-a,b). This transformation is equivalent to writing the Hamiltonian in a different gauge in which the complex tunnelling is along the short dimension of the ladder, as it is pictorially represented in figure 2.5-d. In this "physical" gauge the Hamiltonian reads

$$H = -t_x \sum_j \left(\hat{a}^\dagger_{j+1} \hat{a}_j + \hat{b}^\dagger_{j+1} \hat{b}_j \right) - t_y \sum_j \left(e^{ij\Phi}\, \hat{a}^\dagger_j \hat{b}_j \;+\; \text{H.c.} \right) \tag{2.25}$$

and gives rise to the spectra reported in figure 2.5-e for the upper leg (solid blue line) and in figure 2.5-f for the lower leg (solid red line). In this gauge, in the absence of interleg coupling, the two spectra are correctly centered in the middle of the Brillouin zone (grey lines in figures 2.5-e,f).

Despite the impossibility to observe the Hofstadter spectrum in such a reduced-size system, Hgel and Paredes in reference (Hügel and Paredes, 2014) point out a remarkably interesting correspondence between the eigenstates and energy bands of a ladder and the ones of the Hofstadter model. In particular, the authors demonstrate that the chiral edge states and energy bands of the Hofstadter model for a rational flux $\phi = 2\pi\, p/q$ per plaquette are respectively equal to the eigenstates and eigenenergies of a $(q-1)$-leg ladder with the same magnetic flux and tunnelling couplings. This noticeable property is shown in figure 2.6-b,c where the case $\Phi = 2\pi/3$ is investigated for a two-leg ladder with 200×2 lattice sites (PBC on the long dimension) and a bigger 200×20 ladder.

2.3 Realization of synthetic magnetic fields with ultracold atoms

In the last two decades a lot of effort has been devoted towards the proposal and the experimental realization of efficient techniques to use ultracold atoms to simulate the physics of charged quantum particles interacting with an electric or magnetic field (Lewenstein et al., 2012; Bloch et al., 2008). As it usually happens in the framework of quantum simulation (QS), this effort is not motivated only by the necessity to shed light on some open problems of condensed-matter physics, overcoming with the QS the difficulties encountered in the study of complex phenomena in solid-state systems, but it is also driven by the possibility to realize new quantum phases never observed in nature, as well as to access regimes which are impossible to achieve in real systems. Just to give a very simple example, the observation of the Hofstadter spectrum introduced in the previous section in a real 2D crystal characterized by a lattice spacing $a = 5$ Å would require a magnetic field of the order of 10^8 G to induce a 2π phase shift on an electron circulating around a lattice plaquette, a value far beyond the actual technological possibilities. This precludes the investigation of the fractal structure of the Hoftsadter butterfly in a conventional crystal and makes the experimental observation of this iconic spectrum a prerogative of the quantum simulation.

In this prospect, ultracold atoms and especially ultracold atoms in optical lattices offer a clean and fully tunable platform that can be potentially employed for the simulation of both integer and fractional (Paredes et al., 2003) Hall-like systems, spin-orbit coupled systems (Galitski and Spielman, 2013), topological insulators and exotic topological phases (Goldman et al., 2016) of matter not yet observed. Several schemes have been proposed to circumvent the most evident obstacle to the QS of this kind of physics with ultracold atoms, that is the absence of charge. Atoms are neutral particles and so the simulation of the physics of magnetism necessarily requires to mimic the coupling between matter and the electromagnetic field gauge potential. The general approach for the realization of these *artificial gauge fields* (Dalibard et al., 2011; Dalibard, 2015; Goldman et al., 2014; Lewenstein et al., 2007) is the emulation of the quantum mechanical effect induced by a real vector potential on a charged particle as it moves in a region where the potential is defined, that is the Aharonov-Bohm phase. The idea is that, if one finds a way to induce a geometric phase on a particle moving in space, then this phase can be associated to a vector potential and eventually to the presence of a "synthetic" magnetic field even if the particle is neutral in charge.

Historically, the first attempts to simulate magnetism with neutral ultracold atoms were performed with particles free to move in 3D space and were aimed at finding a way to mimic the minimal substitution $\mathbf{P} \rightarrow \mathbf{P} - q\mathbf{A}$ for a neutral particle. The simplest way to meet this target is to exploit a rotating quantum gas observing the formal analogy between the Coriolis force $F_C = 2m\,\mathbf{v}\wedge\mathbf{\Omega}$ with $\mathbf{\Omega} = \Omega\hat{e}_z$ and the Lorentz force $F_L = q\,\mathbf{v} \wedge \mathbf{B}$ (Cooper, 2008) where $\mathbf{\Omega}$ is the angular velocity vector and $\mathbf{v}$ is the velocity of the particles. As pointed out in reference (Dalibard et al., 2011), the Hamiltonian in the gas rotating frame can be recast in such a way that the momentum term can be rewritten as

$$\mathbf{P} \rightarrow \mathbf{P} - m\Omega(x\hat{e}_y - y\hat{e}_x), \tag{2.26}$$

which is analogous to the minimal substitution induced by the presence of the magnetic field $q\mathbf{B} = 2m\mathbf{\Omega}$. A completely different approach to the problem is the one

introduced by the group of I. Spielman at JQI (Lin et al., 2009a,b), where internal spin states of bosonic ^{87}Rb are coupled together using a pair of Raman beams. Thanks to the Raman coupling the energy spectrum of the resulting system is characterized by several minima (up to 3 in the $F = 1$ manifold) and around each minimum the energy dispersion is approximated by

$$E(k_x) = \hbar^2(k_x - k_{min})^2/2m^* \tag{2.27}$$

where k_{min} is the momentum corresponding to one of the energy minima and m^* is the effective mass. Again, this last expression resembles the minimal substitution $\mathbf{P} \rightarrow \mathbf{P} - q\mathbf{A}$ and can be interpreted as a light-induced uniform vector gauge potential. Being uniform, this vector potential is associated to a zero magnetic field. This limitation can be overcome if the atoms are subjected to a real magnetic field gradient (Lin et al., 2009b), making in this way the Raman detuning position dependent.

2.3.1 Gauge fields on a lattice

A lot of theoretical schemes have also been proposed for the realization of artificial gauge fields for neutral atoms trapped in optical lattices (Dalibard et al., 2011). This framework represents a more natural platform for the simulation of condensed-matter systems because of the obvious analogy with the periodic potential to which electrons in solids are subjected. Optical lattices make also easy to tune the interaction energy between particles within the same site by simply changing the lattice depth and can so be exploited to investigate the effect of interactions in Hall-like systems.

In the framework of optical lattices, the realization of artificial gauge fields is accomplished engineering an effective Peierls phase for atoms hopping between neighbouring sites, in such a way that a non-zero phase shift is imprinted on the wavefunction of a particle orbiting around a lattice plaquette. This kind of implementation of an artificial gauge field requires the realization of a complex matrix tunnelling element in the tight-binding regime. One of the first methods proposed to accomplish this task relies on the concept of *laser assisted tunnelling* and was proposed by Jaksch and Zoller in 2003 (Jaksch and Zoller, 2003). In this scheme two long-lived internal states of an atom, that we label as g and e, are trapped in two 2D state-dependent sublattices characterized by the same lattice spacing d along the $\hat{e}_x$ and $\hat{e}_y$ directions but spatially shifted by $d/2$ along $\hat{e}_x$. Each sublattice is engineered in such a way to trap only one of the two states and repel the other, and tunnelling between adjacent sites of the same sublattice is supposed to be completely suppressed. In such a system laser light resonant with the $g \rightarrow e$ transition induces a hopping along the $\hat{e}_x$ direction between neighbouring sites of different sublattices and the resulting tunnelling amplitude is given by (Gerbier and Dalibard, 2010)

$$t^x_{eg}\, e^{i\mathbf{q}\cdot\mathbf{r_g}} = \frac{\hbar\Omega}{2}\, e^{i\mathbf{q}\cdot\mathbf{r_g}} \int w_g(\mathbf{r}) e^{i\mathbf{q}\cdot\mathbf{r}} w^*_e(\mathbf{r} - d/2\,\hat{e}_x)\, d\mathbf{r} \tag{2.28}$$

where Ω and $\mathbf{q}$ are the laser Rabi frequency and wavevector and $w_{g,e}(\mathbf{r})$ are the Wannier functions, respectively relative to a g and an e atom, that are shifted by half the lattice spacing along the $\hat{e}_x$ direction. For proper values of the laser wavevector, the hopping term 2.28 contains an imaginary component, thus giving rise to a complex

matrix element and consequently to a non-zero Peierls phase. The problem related to this approach is that the imprinted phase associated to a tunnelling event change sign if the hopping occurs along the $+\hat{e}_x$ or along the $-\hat{e}_x$ directions, creating in this way a staggered flux. Schemes to rectify the flux have been proposed (Jaksch and Zoller, 2003) but involve the presence of additional lasers (Aidelsburger et al., 2013; Kennedy et al., 2013; Gerbier and Dalibard, 2010). Another strategy that can be employed to realize an artificial gauge field in a lattice involves the so called *Floquet engineering* and it is based on a time-periodic modulation or shaking of the quantum system (Aidelsburger et al., 2015; Fläschner et al., 2016). A possible implementation of this scheme exploits a superlattice in which adjacent site are characterized by an energy offset Δ in such a way that tunnelling between them is strongly suppressed. If a modulation potential having the form $V(x,t) \sim \cos(\omega t + \theta(x))$ with $\omega = \Delta/\hbar$ is applied to the system, then hopping between neighbouring sites can be restored and the effective tunnelling matrix element is given by $t = t_{eff}\, e^{i\theta(x)}$ where $\theta(x)$ is the spatial phase associated to the modulation potential. A proper choice of the modulation can thus give rise to a Peierls phase and so to an artificial gauge field for particles trapped in the superlattice. This strategy is to some extent more general than the laser assisted tunneling approach previously described because it does not rely on the addressing of the internal atomic structure to work. Heating induced by the periodic driving and excitation to higher lattice bands represent anyway strong limitations to the application of the Floquet engineering method.

2.3.2 The synthetic dimension approach

Another, more innovative approach to the realization of gauge fields for neutral atoms in optical lattices relies on the concept of *synthetic dimensions* (Boada et al., 2012) and constitutes the core of the experimental part of this thesis. By *synthetic dimension* we refer to an extra dimension encoded in a non-spatial degree of freedom of the physical system of interest. Since the idea is to emulate the physics of a particle in a real lattice, a strong requirement is that the Hamiltonian governing the dynamics in the synthetic dimension must be analogous to a lattice Hamiltonian. This means that the "spatial coordinate" in the extra dimension must be discrete and that each synthetic lattice site must be coupled to only two other sites in a sequential way.

Before proceeding in the description of how a fictional extra dimension can be exploited to generate an artificial gauge field, it is useful to list some of the possible approaches investigated over the last years to realize a synthetic dimension, focusing the attention in particular on the various methods employed to induce a coherent tunnelling among the synthetic lattice sites. Among the various strategies proposed to deal with the problem of the realization of a synthetic dimension, some of the most promising from an experimental point of view are:

- *Synthetic dimension encoded in the internal spin degree of freedom of a neutral atom:* this method was proposed by A. Celi *et al.* in the theoretical group of M. Lewenstein at ICFO (Celi et al., 2014) and experimentally realized in the context of this thesis (Mancini et al., 2015) and in the group of I. Spielman at JQI (Stuhl et al., 2015). It is based on the interpretation of the spin states of a hyperfine level of a neutral atom as the fictitious sites of a synthetic lattice. A

magnetic field is used to remove the degeneracy between the hyperfine sublevels while the coherent coupling in the extra dimension is realized exploiting resonant laser fields (Raman for example) that enable the synthetic hopping from one spin state to a neighbouring one. If combined with a real optical lattice, this extra dimension allows the realization of lattice systems characterized by up to four dimensions. A drawback of this approach is constituted by the limit imposed to the number of synthetic lattice sites by the spin degeneracy $N = 2F + 1$ of the atomic hyperfine level considered. This means that, for example, up to 6 lattice sites can be realized exploiting the ground state of ^{173}Yb (which is characterized by $F = 5/2$), while up to 10 sites can be realized with the ground state of ^{40}K ($F = 9/2$).

- *Synthetic dimension encoded in the orbital degree of freedom of a neutral atom:* proposed by M. Wall *et al.* (Wall et al., 2016) in the theoretical group of A. M. Rey at JILA and experimentally realized in the context of this thesis (Livi et al., 2016) and in the group of J. Ye at JILA (Kolkowitz et al., 2017), this method is perfectly analogous to the one previously described, with the exception that the synthetic dimension is encoded not in the spin but in two distinct long-lived electronic levels of the atom. These two levels can be represented, for example, by the ground and the clock states of alkaline-earth and alkaline-earth-like elements, such as Sr or Yb. Being the number of lattice sites along the synthetic dimension limited to 2, this method allows only the realization of ladder systems when combined with a real lattice. Differently with respect to the spin approach, the two synthetic lattice sites are separated by an optical energy and a clock laser is required to induce a coherent coupling between them.

- *Synthetic dimension encoded in harmonic trap levels:* This is an approach introduced by H. M Price *et al.* at the INO-CNR BEC Center in Trento (Price et al., 2017) and not yet experimentally realized. The idea is to re-interpret the standard harmonic oscillator eigenstates of a harmonic trap as lattice sites along a synthetic dimension. The coupling between neighbouring synthetic sites is controlled by the application of a time-periodic potential characterized by a modulation frequency quasi-resonant with the harmonic trap levels energy difference.

- *Synthetic dimension encoded in momentum states:* this scheme for the realization of a synthetic dimension for ultracold atoms has been experimentally investigated in the group of B. Gadway at the University of Illinois (An et al., 2017). The implementation of this method relies on the laser coupling of a discrete set of momentum states of an atomic BEC, that are interpreted as synthetic lattice sites in an extra dimension. The coupling between different momentum states is realized using two-photon Bragg transitions driven by two counter-propagating laser beams. A second set of Bragg beams, characterized by a wavelength incommensurated with respect to the first pair of beams, allows the realization of an additional synthetic dimension.

- *Synthetic dimension in non-atomic systems:* as a final point, it is interesting to note that the concept of synthetic dimension is gaining attention also in fields not directly related with the ultracold atoms context. In reference (Ozawa et al.,

2016) for example, the authors propose to encode an artificial dimension in the resonant modes of a ring cavity, realizing in this way an array of syntetic lattice sites coupled by a time-dependent modulation of the dielectric properties of the cavity itself.

Let's now move back to our original purpose and see how the synthetic dimension approach can be exploited to realize an artificial gauge field for neutral atoms. We will focus the attention only on the methods investigated in the experimental part of this thesis (the first two of the previous list), in which the synthetic dimension is encoded in an internal degree of freedom of a neutral atom. If combined with a one-dimensional optical lattice the synthetic dimension gives rise to a hybrid ladder characterized by a real and an artificial dimension, as it is represented in figure 2.7. Lattice sites positions in this hybrid ladder can be conveniently labelled as $\{n, j\}$, where n refers to the position along the synthetic dimension while j labels the sites along the real optical lattice. In this kind of system we have a natural tunneling matrix element t for particles hopping between neighbouring sites along the real dimension while the tunnelling between synthetic sites is provided by means of laser radiation characterized by a Rabi frequency Ω_n that couples the synthetic site n with $n+1$. Let's now suppose that the wavevector of the laser radiation is aligned with the real optical lattice. In case of resonant coupling the time-dependence of the radiation electric field can be eliminated by means of a rotating wave approximation and we remain with a spatial-dependent only phase of the field, whose value is given by

$$\phi = k_R x + \phi_0 \tag{2.29}$$

where k_R is the wavevector of the laser radiation. The crucial detail at this point of our description is that the wavefunction of atoms tunnelling between two sites along the synthetic dimension will pick up a phase factor which depends on their position in the real optical lattice, as a consequence of the complex space-dependent phase 2.29 that characterizes the electric dipole matrix element. Indeed, the tunnelling process along the synthetic dimension is enabled only by the exchange of a photon (or more photons if for example a Raman transition is considered) with the radiation field. An atom located in the real lattice site j will thus pick up a phase $\exp(i\,\phi_j) = \exp(i\,k_R\,aj)$, where a is the real lattice spacing, when it absorbs a photon to hop from the hybrid ladder site $\{n, j\}$ to $\{n+1, j\}$. Conversely, a synthetic tunnelling event in the opposite direction is characterized by a $-\phi_j$ phase change. If the radiation wavelength is not an integer multiple of the real lattice spacing then $\exp(i\,\phi_j)$ has a non vanishing imaginary part and can thus be interpreted as a Peierls phase associated to the synthetic tunnelling event. In particular, if the Rabi frequency Ω_n is associated to the strength of the tunnelling, it is possible to write the synthetic matrix tunnelling element as

$$t^{synth.}_{n\to n+1} = \frac{\Omega_n}{2}\, e^{i\,k_R\,aj}|n+1\rangle\langle n| = \frac{\Omega_n}{2}\, e^{\pi\, i\, k_R/k_L\, j}|n+1\rangle\langle n| = \frac{\Omega_n}{2}\, e^{i\Phi\, j}|n+1\rangle\langle n| \tag{2.30}$$

where the dependency of the matrix element on the lattice wavevector k_L has been made explicit and $\Phi = \pi\, k_R/k_L$ is the synthetic Peierls phase. Following this approach it is thus possible to realize an artificial gauge field in the Landau gauge on a hybrid ladder. In particular, a particle orbiting around the ladder's plaquette $\{j, n\} \to \{j, n+1\} \to \{j-1, n+1\} \to \{j-1, n\} \to \{j, n\}$ will pick up a phase shift equal to $\Phi\, j$ when it

moves on the $\{j,n\} \to \{j,n+1\}$ link and $-\Phi\,(j-1)$ when it moves from $\{j-1,n+1\}$ to $\{j-1,n\}$, meaning that Φ is the phase associated to the artificial magnetic field flux piercing one ladder cell. If both the coupling laser field and the real lattice are realized in the optical domain, then Φ, depending only on the ratio k_R/k_L, can assume values of the order of the unity, which are several orders of magnitude higher than the ones achievable in real solid-state systems.

With the expression 2.30 for the tunnelling in the synthetic dimension, assuming that atoms in the real lattice are in the tight-binding regime, the physics of the hybrid system is well captured by the tight-binding-like Hamiltonian

$$H_{ladder} = \sum_{j,n} \left(-t\, \hat{a}^{\dagger}_{j+1,n} - \frac{\Omega_n}{2} e^{i\Phi\, j} \hat{a}^{\dagger}_{j,n+1} \right) \hat{a}_{j,n} + \text{ H.c.} \tag{2.31}$$

where j labels the spatial index, n labels the position in synthetic dimension, $\hat{a}^{\dagger}_{j,n}$ is the creation operator for a particle located in the position $\{j,n\}$ in the hybrid ladder and Ω_n is the Rabi frequency associated to the tunnelling from the site n to $n+1$ along the synthetic dimension.

Note that in the Hamiltonian above the phases $\phi_j = \Phi\, j$ live on the links of the hybrid lattice, playing the role of the spatial components of a $U(1)$ *lattice gauge field* to which the $U(1)$ on-site gauge transformation of the field operators

$$\hat{a}_{j,n} \to \hat{a}'_{j,n} = e^{i\,\chi_{j,n}} \hat{a}_{j,n}. \tag{2.32}$$

is associated. The transformation above leaves the spectrum of the system invariant but defines the new phases

$$\phi_j \to \phi_j + \chi_{j,n} - \chi_{j,n+1} \tag{2.33}$$

for hopping processes along the synthetic dimension and $\phi_i = \chi_{j,n} - \chi_{j+1,n}$ for hopping processes along the real dimension. Despite this redefinition, the cumulative phase acquired by a particle that undergoes a closed loop around a plaquette of the lattice is left invariant by the $U(1)$ transformation and can consequently be associated to the presence of an external static magnetic field induced by the gauge potential experienced by the atoms on the plaquette links. In what follows we will consider only fields of this kind that must not be confused with dynamical gauge fields in which the fields are influenced by the atomic motion.

From an experimental point of view, the synthetic dimension approach to the realization of an artificial gauge field is characterized by several advantages over the other methods described in the previous section. Among these advantages it is possible to list:

- *A strongly reduced heating of the atomic sample:* no shaking lattices nor time-modulated potential are involved in the synthetic dimension approach. The only source of heating is the spontaneous emission from atomic levels resonant or quasi-resonant with the laser field that provides the coupling in the synthetic dimension. If Raman transition are employed to generate the synthetic tunnelling the spontaneous emission can be suppressed increasing the detuning of the Raman resonance with respect to the intermediate excited states. This is particularly

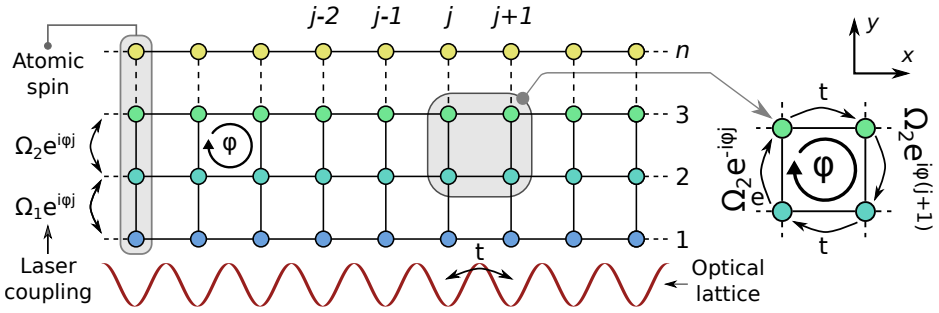

Figure 2.7: Sketch of the synthetic ladder realized combining a one-dimensional optical lattice with an internal atomic degree of freedom, such as, for example, the spin. Laser radiation provides the synthetic coupling in the artificial dimension. Atoms tunnelling along the synthetic lattice pick up a phase that depends on their position in real space, as if they are influenced by a vector potential.

convenient for two-electrons atoms as the Raman transition can be driven by using laser light at an intercombination transition (as it will be discussed with more details in chapter 5). The heating is further reduced if the synthetic dimension is realized exploiting two long-lived electronic levels coupled together by a clock laser (as further discussed in the experimental chapter 4) as in this case no other intermediate excited states are present.

- *A simple experimental realization:* In the simplest possible scheme only two laser fields are required to realize the artificial gauge field: one to generate the real one-dimensional optical lattice and another to provide the coupling in the synthetic dimension. No superlattices or potential gradients are needed.

- *An easy tunability of the synthetic magnetic flux:* Since the magnetic field flux per plaquette Φ is proportional to the momentum k_R transferred by the coupling laser field to the atoms, to change Φ it is enough to modify the angle θ at which $\mathbf{k_R}$ intersects $\mathbf{k_L}$, in such a way to have $\Phi = \pi\, k_R/k_L \cos(\theta)$.

- *A uniform flux in each lattice cell:* By construction, the flux in each plaquette of the hybrid ladder is uniform and the magnetic field associated to the artificial gauge potential always points in the same direction (orthogonal to the plane of the ladder) for all the cells. Being not staggered, no flux rectification tecniques are needed.

- *The possibility to address individually each leg of the ladder:* since in the synthetic ladder each leg is encoded in a different internal degree of freedom of the atom, by exploiting state selective imaging techniques it is possible to address each leg individually. This for example allows a direct observation of the edges of the system, a very hard task to achieve in all optical-lattice-based systems.

On the other hand, there are some clear drawbacks in the utilization of the synthetic dimension approach to realize artificial gauge fields. The first and more evident has

been already pointed out in the introduction to the method and is represented by the limit imposed to the number of lattice sites along the synthetic dimension by the spin degeneracy. As a matter of fact with this method only the realization of ladder-like systems is allowed. Another drawback is represented by the experimental difficulty that can be encountered in the engineering of tunnelling matrix elements characterized by the same strength for all the spin-spin couplings along the synthetic dimension. As pointed out in the Hamiltonian 2.31, the tunnelling strength Ω_n in the synthetic dimension depends on the spin state and it can result to be hard to engineer a system in which all the couplings have the same strength. This drawback can indeed be exploited to tune the number of synthetic lattice sites as it will be discussed in chapter 5.

As a final note, it should be observed that this approach can be extended to more than two dimensions exploiting additional optical lattices. A 3D optical lattice combined with a synthetic dimension, for example, realizes a four-dimensional system that could allow the investigation of exotic phenomenaa, such as the 4D Hall effect (Price et al., 2015). On the other hand, the possibility to engineer complex boundary conditions along the synthetic dimension can be exploited to realize non-trivial topological geometries (Boada et al., 2015).

2.3.3 Synthetic dimension or synthetic Spin-Orbit coupling?

In the spin ladder approach to the realization of a synthetic dimension, the tunnelling along the extra dimension is provided by the exchange of photons with a laser radiation field. As a matter of fact this implies that, as an atom moves along the synthetic ladder changing its spin, it must also exchange momentum with the photons of the coupling radiation field. Since this results in a lock of the spin to the atomic momentum, the method described so far can also be interpreted as a way to realize synthetic spin-orbit coupling (SOC) in ultracold quantum gases. As it has already been pointed out in the introduction to this chapter, SOC is an intriguing phenomenon that in solid-state systems can give rise to novel classes of materials such as topological insulators or topological superconductors (Hasan and Kane, 2010). In condesed-matter systems SOC originates as a consequence of the extremely high electric field (of the order of trillions of volts per meter) present at the atomic level, a regime extremely inaccessible in the laboratory frame. Synthetic SOC and quantum simulation with ultracold atoms could thus provide a novel platform to study SOC-related effects in solid-state systems (Galitski and Spielman, 2013).

To formalize how synthetic SOC emerges in an ultracold atom system we can consider two spin states labelled as $\uparrow$ and $\downarrow$ in free space, coupled together by a Raman radiation field. To flip the spin atoms must exchange a momentum equal to $\delta k = 2k_0$ with the Raman field. We suppose δk to be aligned along the $\hat{e}_x$ direction. Fixing $\hbar = 1$, the Hamiltonian that captures the physics of this system is

$$H = \begin{pmatrix} \frac{k_x^2}{2m} - \frac{\delta}{2} & \frac{\Omega}{2} e^{2ik_0 x} \\ \frac{\Omega}{2} e^{-2ik_0 x} & \frac{k_x^2}{2m} + \frac{\delta}{2} \end{pmatrix} \tag{2.34}$$

where k_x is the atomic momentum along the $\hat{e}_x$ direction, m is the atomic mass, Ω is the Raman Rabi frequency and δ is the Raman transition detuning. The Hamiltonian

2.34 can be recast in a more enlightening form applying the unitary transformation $\hat{H} = UHU^{\dagger}$ with U given by (Zhai, 2012)

$$U = \begin{pmatrix} e^{-ik_0 x} & 0 \\ 0 & e^{ik_0 x} \end{pmatrix} \tag{2.35}$$

After the transformation [1] the Hamiltonian reads

$$\hat{H} = \begin{pmatrix} \frac{(k_x+k_0)^2}{2m} - \frac{\delta}{2} & \frac{\Omega}{2} \\ \frac{\Omega}{2} & \frac{(k_x-k_0)^2}{2m} + \frac{\delta}{2} \end{pmatrix} \tag{2.36}$$

and can be rearranged in terms of the Pauli matrices to give

$$\hat{H} = \frac{(k_x + k_0\sigma_z)^2}{2m} + \frac{\delta}{2}\sigma_z + \frac{\Omega}{2}\sigma_x. \tag{2.37}$$

The term $k_0\sigma_z$ in the last expression can be interpreted either as a synthetic vector potential or as the source of a synthetic SOC. This is more evident if a spin rotation along $\hat{e}_y$ is performed exchanging $\sigma_x \to \sigma_z$ and $\sigma_z \to -\sigma_x$. As a consequence of this transformation the Hamiltonian becomes

$$\hat{H} = \frac{(k_x - k_0\sigma_x)^2}{2m} - \frac{\delta}{2}\sigma_x + \frac{\Omega}{2}\sigma_z. \tag{2.38}$$

where the kinetic term can be read as a mix of Rashba $(k_x\sigma_x + k_y\sigma_y)$ and Dresselhaus $(k_x\sigma_x - k_y\sigma_y)$ SOC.

The same problem in presence of an optical lattice will be discussed in section 4.1.

[1] In order to transform the Hamiltonian, it must be taken into account that x and k_x are operators with commutator $[x, k] = i$. In general for two operators A and B for which the relation $[A, [A, B]] = 0$ holds (as it is for x and k) we have that $[f(A), B] = [A, B]\frac{\partial f}{\partial A}$ where f is a function of the operator A. This implies that $[e^{\pm ik_0 x}, k_x] = \mp k_0 e^{ik_0 x}$. Accordingly to this result, the diagonal elements of the transformation $\hat{H} = UHU^{\dagger}$ are given by $\frac{1}{2m}\, e^{\mp ik_0 x}\, k_x^2\, e^{\pm ik_0 x} \mp \frac{\delta}{2} = \frac{1}{2m}\,(k_x \pm k_0)^2 \mp \frac{\delta}{2}$.

Chapter 3
Addressing the $|^1S_0\rangle \rightarrow |^3P_0\rangle$ clock transition in ^{173}Yb

The possibility to address the clock transition in ^{173}Yb is a fundamental requirement for many quantum-simulation schemes involving alkaline-earth and alkaline-earth-like atoms Gorshkov et al. (2009). The first part of this chapter is devoted to the description of the mechanism that enables the excitation of the $|^1S_0\rangle \rightarrow |^3P_0\rangle$ clock transition in the fermionic isotopes of this class of atoms. The fundamental properties of the transition are then described and the techniques employed to suppress the Doppler broadening in spectroscopic measurements are discussed. The spectroscopic capabilities of our clock laser are then presented, evidencing in particular the possibility to resolve the interaction peaks in a multicomponent spin gas confined in an optical lattice. The final part of the chapter is instead devoted to the description of some high-accuracy spectroscopic measurements enabled by the possibility to lock our clock laser on a metrological reference. These measurements led to the determination of the absolute frequency of the clock transition in ^{173}Yb with an unprecedented precision.

3.1 The hyperfine mixing mechanism

In fermionic Yb, the $^1S_0 \rightarrow {}^3P_0$ clock transition violates the selection rules imposing that the initial and final total electronic angular momentum (respectively J_i and J_f) must be not simultaneously vanishing and that the variation of the spin number ΔS must be equal to zero and consequently it should not be allowed at any order. However, as intercombination transitions characterized by $\Delta S \neq 0$ are allowed if the spin-orbit interaction mixes states with different spin quantum number S, similarly, a transition in which $J_i = J_f = 0$ can occur in the presence of a mechanism that mixes states with different quantum number J. In alkaline-earth and alkaline-earth-like fermionic isotopes this mechanism is represented by the hyperfine interaction between the nuclear magnetic moment I and the total electronic angular momentum J.

At the origin of the hyperfine interaction is the effect induced on the atomic nucleus by the electromagnetic field generated by electrons belonging to incomplete shells.

In general, the hyperfine coupling Hamiltonian, H_{hf}, may be represented as a sum over multipole nuclear moments $\mathcal{M}^{(k)}$ of rank k combined with the electronic coupling operators $\mathcal{T}^{(k)}$ of the same rank so that the total interaction is rotationally and P–invariant (Porsev and Derevianko, 2003). For states as the $|^3P_0\rangle$, for which $J = 0$,

Lorenzo Francesco Livi, *New quantum simulations with ultracold Ytterbium gases*, © 2020 Author(s), content CC BY 4.0 International, metadata CC0 1.0 Universal, published by Firenze University Press (www.fupress.com), ISSN 2612-8020 (online), ISBN 978-88-6453-989-8 (online PDF)

H_{hf} can be truncated to the magnetic-dipole part and we have

$$H_{hf} = \boldsymbol{\mu}^{(1)} \cdot \mathcal{T}^{(1)} \tag{3.1}$$

where $\boldsymbol{\mu}$ is the nuclear magnetic dipole operator and $\mathcal{T}^{(1)}$ is a rank one operator acting on the electronic space. The determination of the matrix elements of the hyperfine operators $\mathcal{T}^{(1)}$ requires sophisticated approaches based on many-body perturbation theory methods and will not be discussed here. Since H_{hf} is a scalar quantity, it will conserve the total angular momentum $F = I + J$ and its projection M_F on the quantization axis. However, due to the presence of the rank one operator $\mathcal{T}^{(1)}$, states with different electronic angular momentum J can be coupled, and this, in the basis $|\alpha, J, I, F, M_F\rangle$, gives rise to first order corrections to the bare atomic eigenstates having the form

$$|\alpha, J, I, F, M_F\rangle^{(1)} = \sum_{\alpha' J'} |\alpha', J', I, F, M_F\rangle \frac{\langle \alpha', J', I, F', M'_F | H_{hf} | \alpha, J, I, F, M_F\rangle}{E(\alpha', J') - E(\alpha, J)}. \tag{3.2}$$

where α is the set of all the additional quantum numbers necessary to define the atomic state and $E(\alpha, J)$ are the energies of the atomic levels. In particular, exploiting the Wigner-Eckart theorem, it is possible to demonstrate that the correction above is proportional to

$$\langle \alpha', J', I, F', M'_F | H_{hf} | \alpha, J, I, F, M_F\rangle \propto \delta_{FF'} \delta_{M_F M_{F'}} \langle \alpha' J' || \boldsymbol{T}^{(1)} || \alpha J\rangle \tag{3.3}$$

which evidences that H_{hfs} is not diagonal in J and so gives rise to eigenstates in which J is not defined. In particular, being $\mathcal{T}$ an operator of rank one, the new atomic states will be defined by a linear combination of unperturbed states characterized by the same quantum number F and J' ranging from $J - 1$ to $J + 1$. As a consequence, the metastable state $|^3P_0\rangle$ will be defined by the mixing

$$|^3P_0\rangle = \alpha |^3P_0^0\rangle + \beta |^3P_1^0\rangle + \gamma |^1P_1^0\rangle \tag{3.4}$$

where the superscript "^{0}" indicates the bare atomic eigenstates and $\beta, \gamma \ll 1$. Because of the mixing with the bare states $|^1P_1\rangle$ and $|^3P_1\rangle$, the metastable state 3.4 inherits an electric-dipole coupling to the fundamental state $|^1S_0\rangle$. The resulting transition linewidth is $\Gamma = 38.5$ mHz (Porsev et al., 2004) corresponding to a lifetime of about 23 s.

Because of this extremely reduced linewidth, the saturation intensity of the transition (Foot, 2012)

$$I_{sat} = \frac{\hbar \omega_0^3 \Gamma}{12 \pi c^2} \tag{3.5}$$

is characterized by the exceptionally low value $I_{sat} = 4.7 \times 10^{-11}$ mW mm^{-2}. This means that the transition width can be easily power-broadened with relatively small laser light intensities: just to give an example, 4 mW mm^{-2} of laser light intensity are enough to obtain a 1 kHz broadening.

3.2 Magnetic properties of the transition

The presence of a non-zero nuclear moment in the fundamental $|^1S_0\rangle = g$ and metastable $|^3P_0\rangle = e$ states gives rise to a magnetic substructure which is identical for

both the two atomic levels. In ^{173}Yb this substructure is characterized by $2F+1=6$ nuclear spin sublevels with the projection of the spin on the quantization axis ranging from $m_F = -5/2$ to $m_F = +5/2$. The degeneracy among these sublevels can be removed exploiting an external magnetic field which induces a Zeeman shift given by

$$\Delta E_z = g_F \, m_F \, \mu_B \, B \tag{3.6}$$

where g_F is the Landé factor. Neglecting diamagnetic corrections to the nuclear magnetic moment (Boyd et al., 2007), the Landé factors g_F^g and g_F^e (respectively for the electronic levels g and e) are in principle identical, since for states characterized by $J=0$ the expression for g_F reduces to [1]

$$g_F = -\frac{m_e}{m_p} \, g_I \tag{3.7}$$

where m_e and m_p are respectively the mass of the electron and the mass of the proton and g_I is the magnetic nuclear factor (g_i = -0.6776 for the ^{173}Yb). This argumentation, however, refers to the ideal case and can be applied only to the bare $|^3P_0\rangle$ state. In the real case, the small admixture with the $|^3P_1\rangle$ and $|^1P_1\rangle$ that characterizes the hyperfine mix 3.4 is enough to slightly modify the wavefunction of the bare $|^3P_0\rangle$ state making the Landé factors g_F^e and g_F^g to be different. In particular. it comes out that the magnetic sensitivity of the two states is (Porsev et al., 2004)

$$\Delta E_g/h \simeq +207.4 \, m_F \, B \, [\text{Hz/G}] \tag{3.8}$$

for the ground state [2] and

$$\Delta E_e/h \simeq +320.8 \, m_F \, B \, [\text{Hz/G}] \tag{3.9}$$

for the clock state, meaning that a differential Land factor $\delta_g = g_F^e - g_F^g = +8.1 \times 10^{-5}$ can be defined.

The existence of a difference in the magnetic sensitivity of the g and e levels has an important consequence in the experimental addressing of the clock transition since it makes possible, just exploiting an external magnetic field, to individually address the nuclear spin sublevels of the fundamental state. For example, if π transitions $^1S_0(F=5/2, m_F) \rightarrow {}^3P_0(F=5/2, m_F)$ are considered, the nuclear-spin projection is conserved and for each m_F the transition frequency is shifted by

$$\Delta E_\pi(m_F)/h = 113 \, m_F B \, [\text{Hz/G}], \tag{3.10}$$

meaning that magnetic fields of few Gauss are enough to split clock lines characterized by a typical power-broadened linewidth of the order of 100 Hz. The complete scheme of all the possible transitions connecting the fundamental level g with the metastable state e is reported in figure 3.1.

[1] If the hyperfine structure is taken into account, the Landé factor is given by (Steck, 2015) $g = g_J \frac{F(F+1)+J(J+1)-I(I+1)}{2F(F+1)} - g_I \frac{m_e}{m_p} \frac{F(F+1)+I(I+1)-J(J+1)}{2F(F+1)}$. This implies that for the atomic levels $^1S_0$ and $^3P_0$ for which $J=0$, the Landé factor reduces to $g = -\frac{m_e}{m_p} g_I$.

[2] For the $|^1S_0\rangle$ ground state the Landé factor is exactly $g_F = -m_e/m_p \, g_i$ where for ^{173}Yb ($I=5/2$) we have $g_I = -0.67989/I = -0.271956$ (Lide, 2004) and consequently $g_I = 207.4$ Hz/G.

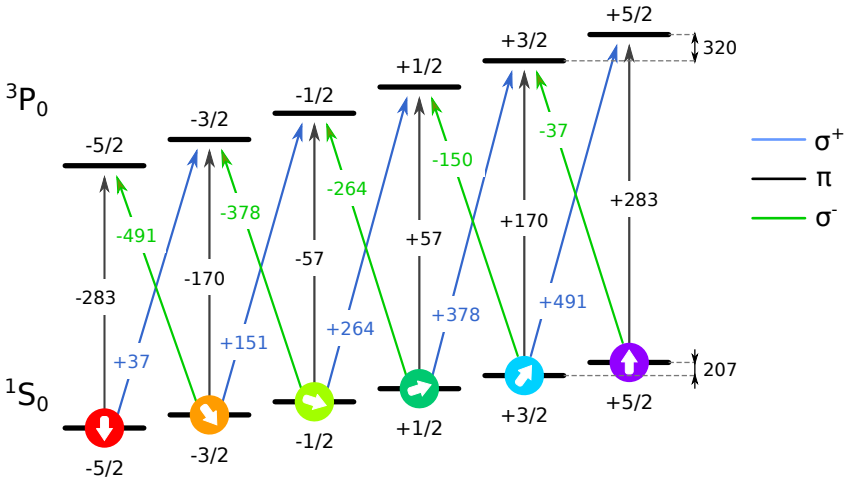

Figure 3.1: Diagram of all the possible transitions connecting the ground state $|^1S_0\rangle$ magnetic sublevels with the metastable state $|^3P_0\rangle$ sublevels in ^{173}Yb. The first-order Zeeman shifts are calculated with respect to the absolute value of the frequency transition and are reported in Hz/G.

The transition frequency is affected also by a second-order Zeeman shift $\Delta E_z^{(2)}$ that induces a quadratic dependence on the resonance position as a function of the external magnetic field applied. This shift, which is spin-independent, can be expressed as

$$\Delta E_z^{(2)} = \beta\, B^2 \tag{3.11}$$

with $\beta = -0.064(2)$ Hz/G^2 (Cappellini, 2016).

3.3 Spectroscopy of tightly-confined atoms in optical lattices

Free-space spectroscopy does not represent a suitable choice to exploit the very large quality factor of an optical clock resonance. In free space atoms absorb light with a frequency that depends on their velocity and on the momentum transferred by the absorbed photon to the particles, accordingly to the relation

$$\omega_{abs} = \omega_0 + \mathbf{k}\cdot\mathbf{v} + \frac{\hbar k^2}{2m} \tag{3.12}$$

where ω_0 is the absolute transition frequency, $\mathbf{k}$ is the photon momentum and $\mathbf{v}$ is the atom velocity. The two terms $\mathbf{k}\cdot\mathbf{v}$ and $\hbar k^2/2m$ in the equation above take into account, respectively, the frequency shift due to the Doppler effect and the recoil shift due to the exchange of momentum with the radiation field that occurs as a consequence of the absorption or emission of a photon by the atom.

The Doppler term leads to a broadening of the resonance width, that for a classical gas at temperature T, is given by (Foot, 2012; Bransden and Joachain, 2003)

$$\Delta\nu_D = \sqrt{\frac{8\,k_B\,T\,\ln(2)}{m}}\,\frac{1}{\lambda_0} \tag{3.13}$$

where $\lambda_0 = 2\pi c/\omega_0$ is the transition wavelength. This *Doppler broadening* limits the minimum width of the resonance to few kHz even in conditions of strong degeneracy of the gas and represents usually the dominant term of broadening when a clock transition is considered. As an example, in our typical experimental conditions, for a gas characterized by a temperature of 10 nK, we expect a Doppler broadening of 3 kHz, a value far exceeding the contribution of power broadening, which can be reduced to just tens of Hz employing laser intensities of the order of few μW mm^{-2}. The various techniques proposed to suppress Doppler broadening, such as saturation spectroscopy, generally rely on the interrogation of the small fraction of the atomic sample satisfying the velocity condition $\mathbf{k}\cdot\mathbf{v} \ll \Gamma$, where Γ is the natural width of the transition, and consequently lead to a reduction of the SNR. These problems are of particular relevance in the optical clock framework where all broadenings beyond the natural linewidth lead to a deterioration of the stability that can be achieved (Poli et al., 2013).

The most successful approach to circumvent these limitations is to perform spectroscopy of tightly confined atoms in the so-called *Lamb-Dicke regime* (Dicke, 1953). In this configuration, if the confinement is strong enough to make the extension of the atomic wave packet smaller than the atomic transition wavelength, then, due to the Heisenberg's uncertainty principle, in momentum space the spread of the atomic wavefunction will be larger than the transition photon momentum. As a result of this, at the leading order, the absorption of a photon will not change the motional state of the atom in the trap and consequently both the recoil shift an Doppler broadening will be suppressed.

To formalize this argumentation we can consider a two-level atom confined in a harmonic potential characterized by a spacing between the energy levels $\Delta E_{ho} = \hbar\omega$. Let's label the two levels of the atomic system with $|g\rangle$ and $|e\rangle$ and the motional states of the atomic wavefunction inside the trap with $|n\rangle$. If light resonant with the $|g\rangle \to |e\rangle$ transition is shined onto the atom, the probability that the absorption of a photon is accompained by the change of the motional state from $|n\rangle$ to $|n'\rangle$ will be given by

$$P_{n\to n'} = |\langle e|\hat{D}|g\rangle\, \langle n'|e^{ikR}|n\rangle|^2 \tag{3.14}$$

where $\hat{D}$ is the electric dipole operator and R is the wavefunction center of mass. If R is expressed in terms of the ladder operators $\hat{a}$ and $\hat{a}^\dagger$ of the harmonic oscillator and only the motional part of the above expression is considered, then we have

$$P_{n\to n'} \propto |\langle n'|e^{ik\, a_{ho}(\frac{a+a^\dagger}{\sqrt{2}})}|n\rangle|^2 = |\langle n'|e^{i\eta(a+a^\dagger)}|n\rangle|^2 \tag{3.15}$$

where $a_{ho} = \sqrt{\hbar/(m\,\omega)}$ is the harmonic oscillator length and $\eta = a_{ho}k/\sqrt{2}$ takes the name of Lamb-Dicke parameter. When $\eta \ll 1$, a condition that is fulfilled if the recoil energy $E_{rec} = \hbar^2k^2/(2m)$ associated to the absorption of a photon is much smaller than the harmonic oscillator frequency, then the expression above can be Taylor-expanded and at the first order, we have

$$P_{n\to n'} \propto |\langle n'|1 + \eta(a + a^\dagger)|n\rangle|^2 = |\delta_{n,n'} + \eta\sqrt{n+1}\delta_{n',n+1} + \eta\sqrt{n}\delta_{n',n-1}|^2. \tag{3.16}$$

This last expression clearly shows that in the limit $\eta \ll 1$ the most intense line in the absorption or emission spectra is the one for which the motional state of the atomic wavefunction is conserved, i.e. $n = n'$. For this particular line, which is usually

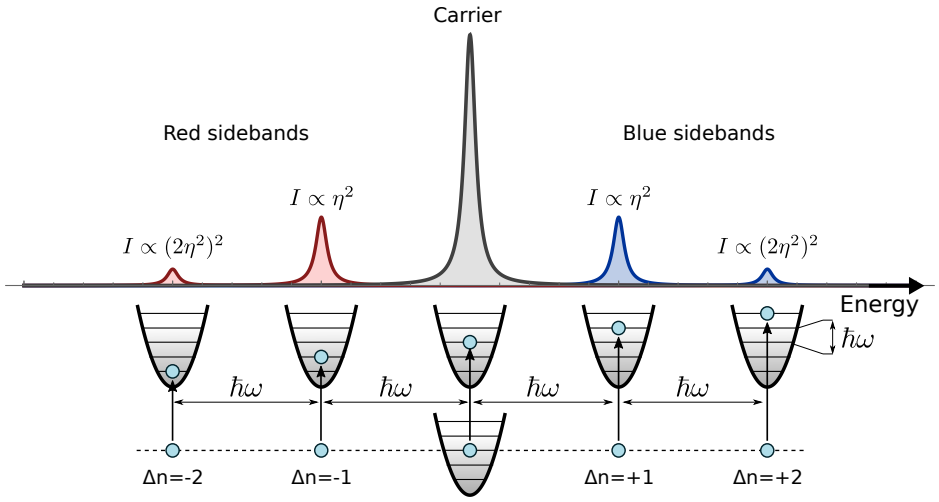

Figure 3.2: Pictorial representation of the sideband-resolved spectrum of a two level atom confined in a harmonic trap in the Lamb-Dicke regime. The predicted intensity of the sidebands with respect to the carrier is reported as a function of the Lamb-Dicke parameter η. The energy spacing between the sidebands is the same as the spacing between the harmonic levels of the confining potential $\delta E = \hbar\omega$.

referred to as *the carrier transition*, the Doppler broadening is suppressed as well as the recoil shift, since the exchange of photons with the radiation field does not affect the spatial part of the atomic wavefunction.

On the other hand, transitions characterized by $n' = n+1$ and $n' = n-1$ are respectively referred to as *first blue sideband* and *first red sideband*, and have an intensity reduced roughly by a factor η^2. These transitions are energy-shifted with respect to the carrier respectively by $\pm\hbar\omega$, meaning that they can be individually addressed if the broadening of the transition is less than the energy separation between two consecutive levels of the harmonic trap.

If the Lamb-Dicke parameter is increased, for example reducing the confinement frequency ω, the excitation to higher sidebands with frequency shift $f_{n\to n'} = (n' - n)\hbar\omega$ becomes possible, but these will be characterized by a transition strength which scales as $P_{n\to n'} \propto (n\eta^2)^{|n-n'|}$, as it is pictorially shown in figure 3.2. It should be anyway observed that the excitation towards red sidebands is possible only if states with $n' < n$ are available in the trap. This means that if all the atoms are in the fundamental vibrational level, no red sidebands will be observed in the spectrum.

As a final note, it should be mentioned that the argumentation carried out up to this point involves atoms confined in a harmonic trap. If an optical lattice is considered as the confining potential, a reduction of the spacing between the energy levels will occur as a consequence of the anharmonicity when levels with increasing energy are taken into account. While this does not affect the signal of the carrier, the shape of the sidebands will be broadened. This effect, for atoms mostly occupying the fundamental lattice band and not-so-deep lattices, is due to the broadening of the excited bands

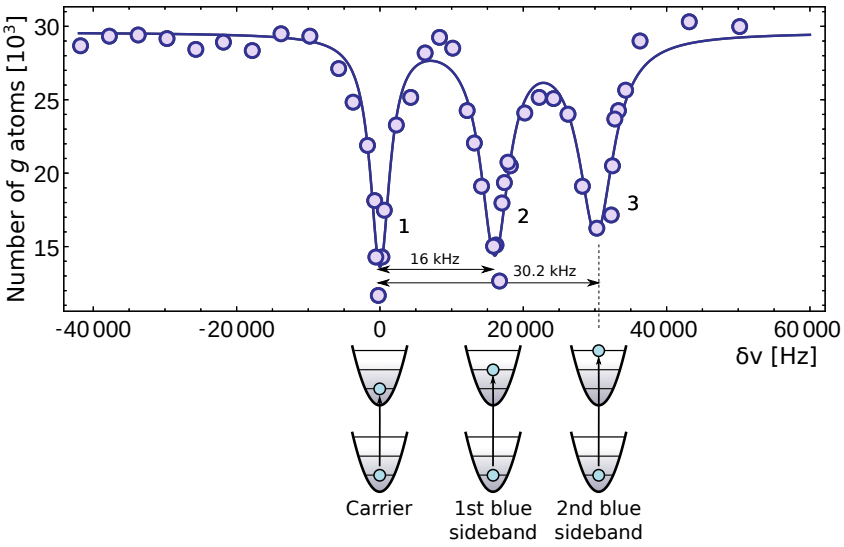

Figure 3.3: Sideband-resolved spectrum of the clock transition of a spin polarized ^{173}Yb gas trapped in a 3D lattice with a depth $s \simeq 22$. In the spectrum, in addition to the carrier transition, it is possible to observe the first two lattice blue sidebands. The absence of red sidebands implies that all the atoms occupy the fundamental lattice band before the clock excitation. The frequency spacing between the peaks matches the spacing between lattice bands at $s = 22\, E_R$.

caused by the lattice anharmonicity which results in an increased tunnelling rate if compared with the fundamental band.

Similarly, a broadening of the carrier can occur if the lattice is not performed at the magic wavelength since in this configuration the carrier frequency depends on the motional state of the atoms. Also in this case this problem does not emerge if atoms in the fundamental vibrational state are considered.

Sideband-resolved spectra

We have thus seen that a strong confinement of the atoms can be used to circumvent both the Doppler and recoil effects in an atomic transition. To fulfil this condition, entering in the so-called *Lamb-Dicke regime*, it is necessary that the parameter

$$\eta = \sqrt{\frac{E_{abs}}{\hbar\omega}} \tag{3.17}$$

satisfies $\eta \ll 1$, where E_{abs} is the recoil energy associated to the absorption of a photon resonant with the atomic transition and ω is the harmonic frequency characterizing the trap. In this case the confining potential is strong enough that atoms can be excited from the state $|^1S_0\rangle = g$ to $|^3P_0\rangle = e$ without altering the spatial component of their wavefunction, and, for sufficiently long interrogation times, the width of this resonance will be limited only by the natural linewidth Γ, by power broadening and

by the linewidth of the exciting laser. In particular, since we are considering a clock transition characterized by an extremely long lifetime ($\tau \simeq 23$ s), in all the cases considered in this thesis the natural linewidth of the transition will always be negligible with respect to the power broadening contribute which is given by

$$\Gamma_{PB} = \Gamma\sqrt{\frac{I}{I_{sat}}} \tag{3.18}$$

where I_{sat}, the saturation intensity, is defined in section 3.1. An example of spectroscopy performed in these conditions is shown in figure 3.3. The spectrum has been acquired shining a 100 ms clock laser pulse on a sample of $m_F = -5/2$ spin-polarized atoms trapped in a 3D optical lattice operated at the magic wavelength. The lattice depth is 22 E_{rec} along all the three spatial directions, where $E_{rec} = \hbar^2 k_L^2/(2m)$ is the lattice recoil energy. This depth corresponds to a harmonic confinement frequency $\omega = 2\sqrt{s}E_{rec}/\hbar \simeq 2\pi \times 18.6$ kHz which, considering that the recoil energy associated to the absorption of photon at 578 nm is $E_{abs}/h = 3.4$ kHz, gives for the parameter η the value $\eta \simeq 0.42$, ensuring in this way that spectroscopy is performed in a mildly Lamb-Dicke regime. In this kind of measurements, the spectroscopic signal is given by the number of atoms remaining in the g state after the clock excitation and so a dip in the spectrum is expected for resonant laser frequencies. Three absorption lines are visible in the spectrum: one relative to the carrier transition, labelled as (1) in figure, and two relative to the first two blue sidebands, respectively labelled as (2) and (3). No red sidebands are visible, a feature that indicates that atoms occupy only the first vibrational state of the lattice. It should be observed that in the spectrum reported in the figure, the peaks relative to the two sidebands are characterized by an area comparable with the carrier peak while, for $\eta = 0.42$, we expect the first and second sideband signals to be, respectively, 0.18 and 0.12 times the carrier signal. This disagreement with the theoretical prediction could be explained with the long interrogation time (100 ms) that is more than enough for atoms excited to higher bands to tunnel towards neighbouring sites, inelastically collide with other excited atoms (for example via p-wave principal-quantum-number-changing collisions since s-wave collisions are inhibited in a spin-polarized fermionic sample) and leave the trap due to the released kinetic energy, increasing in this way the depletion signal.

State-dependent interaction-resolved spectra

In the previous example an atomic sample containing spin-polarized particles has been considered. In that case, due to the fermionic nature of ^{173}Yb, the Pauli exclusion principle forbids the simultaneous occupation of a lattice site by two or more identical atoms and consequently, if all the particles are in the fundamental vibrational state of the trap, no more than one atom can occupy each lattice site. On the contrary, if a multicomponent spin gas is considered, the occupation of a lattice site by more than one particle is allowed, even if the atoms share the same vibrational state, provided that their spin is different. If we focus the attention on a two-spin component gas, we expect to observe two kinds of absorption peaks: the first due to the excitation of atoms in single-particle-occupied lattice sites and the other given by the excitation of two-particle states composed by two atoms interacting within the same lattice site. In

the latter case, even if only one of the two atoms is excited from the g to the e state, a shifted resonance is expected in the spectrum if the interaction energy before and after the excitation is different. In the limit of the validity of the Fermi-Hubbard model, as we have already seen in section 1.3.1, this shift is given by

$$\Delta U_{ge} = \frac{4\pi\hbar^2(a_{gg} - a_{ge})}{m} \int w^4(\mathbf{r})\, d\mathbf{r}. \tag{3.19}$$

where a_{gg} and a_{ge} are the s-wave scattering lengths relative to the interaction of the two particles respectively before and after the excitation, $w(\mathbf{r})$ are the lattice Wannier function and m is the atomic mass. In our specific case, if we consider only two spins (labelled with $\uparrow$ and $\downarrow$), then the only two-particle state allowed by the antisymmetrization of the wavefunction for two atoms sharing the same vibrational level of the trap and the same electronic level g is

$$|gg\rangle = |\phi_g\phi_g\rangle \otimes \frac{|\uparrow\downarrow\rangle - |\downarrow\uparrow\rangle}{\sqrt{2}} \tag{3.20}$$

where ϕ_g defines the electronic part of the wavefunction and only the spin part is antisymmetric for exchange of the two particle. The scattering length associated to two atoms interacting in the $|gg\rangle$ state is 199.4 a_0 (Kitagawa et al., 2008), a value that is independent on the spin thanks to the SU(N) nature of the interactions in the ^{173}Yb, as we have seen in section 1.1.1. Starting from $|gg\rangle$, if one of the two atoms is excited to the e state, the requirement that the electronic part of the wavefunction must be symmetric for exchange of the particles does not hold any more and we can have the spin-singlet and spin-triplet states

$$|eg^{\pm}\rangle = \frac{1}{2}\left(|\phi_g\phi_e\rangle \pm |\phi_e\phi_g\rangle\right) \otimes \left(|\uparrow\downarrow\rangle \mp |\downarrow\uparrow\rangle\right) \tag{3.21}$$

where the vibrational state of the two particles is supposed to be unchanged by the excitation. It comes out that because of the different exchange symmetry of the electronic wavefunctions, these two states are associated to very different molecular potentials characterized by very different scattering lengths. The determination of the scattering length a_{eg^-} associated to $|eg^-\rangle$ can be easily performed evaluating how the spectroscopic peak associated to the state shifts as a function of the magnetic field (Scazza et al., 2014) and resulted to be

$$a_{eg^-} = (219.5 \pm 2.0)\, a_0. \tag{3.22}$$

A similar measurement can not be performed for the state $|eg^+\rangle$ as a consequence of the saturation of the interaction energy to the gap between the fundamental and the first excited band, a situation in which the Hubbard model is no longer valid, as we already discussed in section 1.3.1. Due to this reasons, the scattering length associated to this state has been measured indirectly, exploiting the spin-exchange interaction phenomenon (Cappellini et al., 2014) and the orbital Feshbach resonance mechanism (Höfer et al., 2015) (see section 4.3) and the value calculated resulted to be $a_{eg^+} = (3300 \pm 300)\, a_0$ in the first case and $a_{eg^+} = 1878\, a_0$ in the second case.

Actually it comes out that the states 3.21 are eigenstates of the two-particle system only in the absence of an external magnetic field. If a magnetic field $\mathbf{B} = B\hat{e}_z$ is

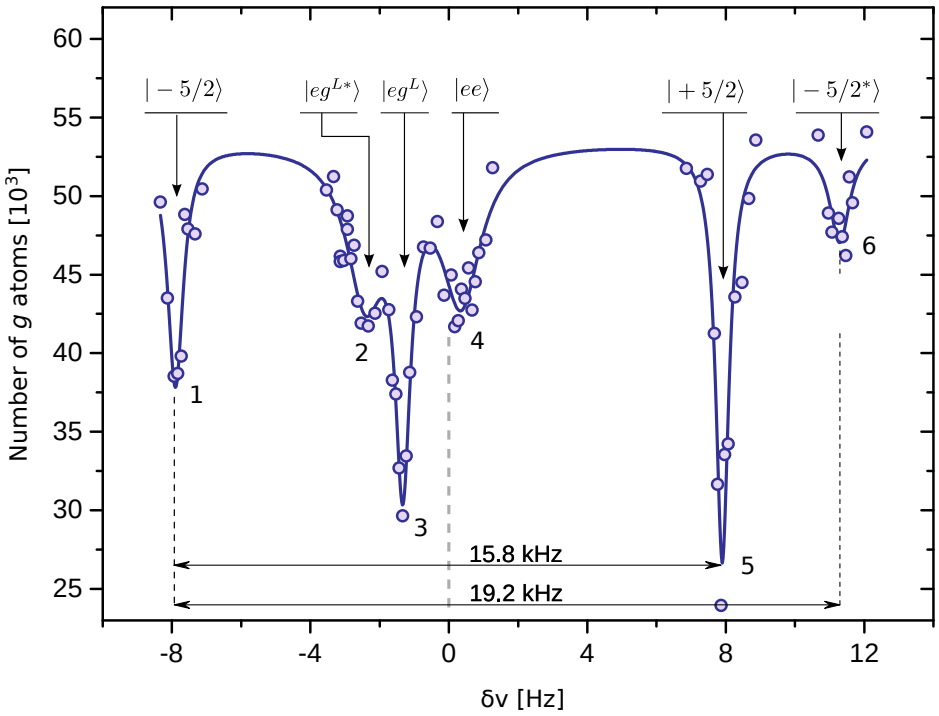

Figure 3.4: Clock transition spectrum of an SU(2) ^{173} Yb sample (spin $m_F = \pm 5/2$) trapped in a $s = 30$ isotropic 3D lattice. For the identification of the peaks see the main text.

present, the Zeeman Hamiltonian $H_z = g_\alpha \mu_B F_z B$, where g_α is the Land factor relative to the electronic state $\alpha = \{g, e\}$, couples the two states and the new eigenstates of the system will be given by the quantum superposition

$$|eg^L\rangle = \alpha(B)|eg^+\rangle + \beta(B)|eg^-\rangle \qquad |eg^H\rangle = \beta(B)|eg^+\rangle - \alpha(B)|eg^-\rangle \tag{3.23}$$

where $|eg^L\rangle$ is the state characterized by lower energy and $\{\alpha(0), \beta(0)\} = \{0, 1\}$ at $B = 0$, while at very high magnetic field $\{\alpha(+\infty), \beta(+\infty)\} = \{1/\sqrt{2}, 1/\sqrt{2}\}$. Finally, if two atoms are simultaneously excited to e with the absorption of two photons, the state

$$|ee\rangle = |\phi_e \phi_e\rangle \otimes \frac{|\uparrow\downarrow\rangle - |\downarrow\uparrow\rangle}{\sqrt{2}} \tag{3.24}$$

can be addressed, corresponding to a scattering length (Scazza et al., 2014)

$$a_{ee} = (306.2)\, a_0. \tag{3.25}$$

Figure 3.4 reports a typical clock transition spectrum of a two component ($m_F = \pm 5/2$) gas confined in a 3D optical lattice ($s = 30$) operated at the magic wavelength. The very weak intensity of the clock laser light shined onto the sample ($I = 10$ μW mm^{-2}) strongly reduces the power broadening to few tens of Hz, allowing for the

complete separation of the single-particle peaks from their sidebands and revealing the two-particles interaction shifted peaks. The laser light is π-polarized and consequently the spin projection of the atoms is not affected by the absorption of a photon. The complete identification of the resonance observed in the spectrum is reported in references (Cappellini et al., 2014; Scazza et al., 2014). The easiest peaks to identify are the ones labelled as (1) and (5) in the figure, which are respectively relative to the excitation of atoms with spin projection $m_F = -5/2$ and $m_F = +5/2$ in single-occupied lattice sites. The distance between the two peaks depends on the external magnetic field applied (28 G in this case) accordingly to the relation 3.10. The peaks labelled as (2), (3) and (4) are instead relative to the excitation of two-particles states. In particular, after spectroscopic measurements performed varying the external magnetic field (Cappellini et al., 2014; Scazza et al., 2014; Cappellini, 2016; Livi, 2014), it is possible to associate resonance (3) to the excitation of the state $|eg^L\rangle$, resonance (5) to the excitation of the state $|ee\rangle$ and finally the resonance (2) to the excitation of a process analogous to $|eg^L\rangle$ in which one of the two atoms initially occupies the first excited lattice band. Resonance (6), instead, is the first blue sideband relative to the $m_F = -5/2$ single-particle peak. At small magnetic fields the state $|eg^H\rangle \simeq |eg^+\rangle$ is not directly addressable starting from $|gg\rangle$ (Cappellini, 2016) because of the Clebsch-Gordan coefficients determining a vanishing Rabi coupling to $|eg^+\rangle$. Anyway it can be populated exploiting the *spin-exchange mechanism* introduced before.

3.4 Coherent addressing of the transition

The coherent transfer of atomic population from the g to the e state is a fundamental ingredient in many quantum information and simulation protocols. The possibility to perform sideband-resolved clock spectroscopy of atoms confined in a deep optical lattice allows us to drive the transition between two distinct stable quantum states, separated by an optical energy, in a sort of text-book environment in which the effect of the spontaneous emission due to the finite lifetime of the excited level can be ignored. We can experimentally prove this coherent driving of the transition inducing Rabi oscillations on the atomic sample (Inguscio and Fallani, 2013; Cohen-Tannoudji and Guéry-Odelin, 2011). To do this we simply shine the clock light on the atoms trapped in a 3D optical lattice and record the number of atoms in the g state as a function of the pulse duration. Figure 3.5 reports an example of Rabi oscillations relative to a spin-polarized atomic sample in the $m_F = -5/2$ spin state confined in a deep $s = 30\, E_r$ (where E_r is the recoil energy) cubic optical lattice. The Rabi frequency Ω can be obtained with a sinusoidal fit of the experimental data ($\Omega = 2\pi \times 547$ Hz for the dataset reported in figure). Ω represents a fundamental quantity in our experimental investigation since it provides a direct measurement of the strength of the clock coupling, a parameter that enters in our Hamiltonian models for the simulation of a quantum Hall ladder with the synthetic dimension approach, as we have already discussed in section 2.3.2. The measurement of the Rabi frequency Ω also provides an estimation of the power-broadened transition linewidth Γ_s thanks to the relation

$$\Gamma_s = \Gamma\sqrt{1 + \frac{2\Omega^2}{\Gamma^2}} \tag{3.26}$$

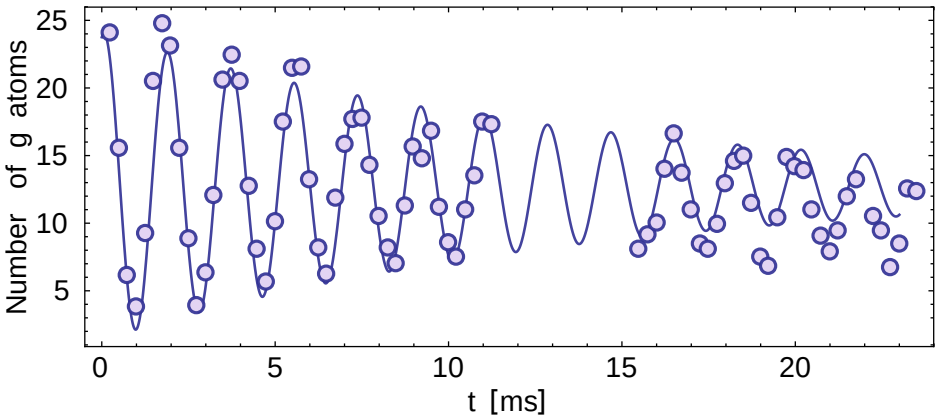

Figure 3.5: Rabi oscillation between the electronic states $^1S_0$ and $^3P_0$ relative to a spin polarized $m_F = -5/2$ atomic sample trapped in a $s = 30\, E_r$ isotropic 3D optical lattice.

where Γ is the natural linewidth. In our case we always work in the regime where $\Gamma \ll \Omega$ and consequently we can approximate $\Gamma_s = \sqrt{2}\,\Omega$.

The experimental data reported in figure show a clear damping on the timescale of 15 ms. We do not have a clear explanation for this behaviour. It cannot be ascribed to interactions-induced decoherence since we are dealing with spin-polarized fermions confined in the fundamental vibrational level of a deep optical lattice. A possible explanation of the observed decoherence can be attributed to fluctuations of the magnetic field which in turn can induce fluctuations on the transition frequency. This attribution is justified by the long coherence time (of the order of 100 ms, see section 6.5) that we observe inducing clock Rabi oscillations in a bosonic sample for which the transition frequency shows a weaker dependence on the magnetic field with respect to the fermionic case. This observation also rules out the finite linewidth of the clock laser as the limiting factor to the observed loss of contrast. Further experimental investigation are anyway needed to clearly identify the origin of the observed damping.

3.5 Fiber-link-enhanced spectroscopy

The 5 kHz-day ULE cavity drift discussed in section 1.2.1 strongly limits the possibility to address the clock transition for long times, especially in conditions in which the power broadening is strongly reduced. A 100 Hz broadened resonance, for example, can be continuously addressed for just $\sim$ 30 minutes, a time sufficient to acquire only a few tens of experimental points in the best case scenario. A linear correction on the laser frequency can be employed to suppress the long-term effects of the ULE drift, but it does not represent a definitive solution because of the presence of a residual non-linear drift component that is characterized by an unpredictable time behaviour, as we already discussed in section 1.2.1. This limitation can be overcome by referencing our clock laser to the ultrastable optical reference at 1542 nm generated at INRiM, the Italian metrological institute located in Turin, and transferred to LENS via a long-

haul 642-km-long fiber link. By disciplining our clock laser on the INRiM signal we demonstrated the possibility to transfer the frequency accuracy of a metrological institute to a remote non-metrological laboratory, where it can be exploited to perform science experiments without the necessity of an in-loco atomic clock (Clivati et al., 2016). Here only a very concise description of the fiber-link infrastructure will be given and the attention will be mainly focused on the science results that the long-term stabilization of the clock laser has allowed. A very detailed description of the fiber-link setup can be found in reference (Cappellini, 2016).

The ultrastable frequency reference delivered by INRiM is generated in Turin employing a 1542 nm fiber laser stabilized on a ULE cavity (Clivati et al., 2011). On the long-term, the laser is phase-locked to a hydrogen maser referenced to a Cesium fountain primary frequency standard with 2×10^{-16} relative frequency accuracy (Levi et al., 2014). This optical reference is disseminated to LENS via a fiber link named LIFT (Italian Link for Frequency and Time) (Levi et al., 2013; Calonico et al., 2014) that has been implemented on a dark fiber of the Italian National Research and Education Network administrated by the consortium GARR. A series of 9 bidirectional amplifiers are installed along the fiber path to compensate for the signal attenuation, for a total amplification of 165 dB. Part of the light that reaches the LENS end-point in Florence is backreflected to Turin in order to perform fiber-noise cancellation. At LENS the optical power of the reference laser delivered by the fiber-link is about 40 nW, a value too low to be efficiently employed to stabilize our laser and consequently a regeneration stage is needed. For this purpose a laser module at 1542 nm, built by Redfern Integrated Optics (RIO), is phase-locked on the reference signal and its light is fiber-delivered to the various LENS laboratories requiring the INRiM frequency reference in a point-to-star configuration. The regenerated light is sent to our laboratory through a 150 m long optical fiber that is not phase stabilized. This fiber introduces an instability on the frequency of 10^{-15}, which is beyond our stability goals and consequently fiber-noise cancellation is not required. In our laboratory the incoming light is employed to frequency-stabilize a frequency comb (Menlo Systems FC1500-250-WG) that in this way inherits the 10^{-14} stability at 1 s of the reference signal. The comb provides a frequency bridge between the 1542 nm reference signal and the 1156 nm light of the clock laser before frequency doubling. The beatnote between the clock 1156 nm light and the nearest comb tooth is measured with a Beat Detection Unit, averaged over 20 s and compared with a setpoint frequency to obtain an error signal. This error signal is finally employed to feed a digital PI servo-controller which stabilizes the beatnote by controlling the DDS that drives the clock laser AOM on the ULE branch. This scheme makes it possible to completely suppress the long-term fluctuations of our clock laser, reaching a stability of 10^{-15} at 1000 s of interrogation time. This value is two orders of magnitude better than the 10^{-13} level of fractional frequency stability achievable with GPS-based frequency dissemination systems, which up to now represent the most widespread time and frequency reference standard for the majority of industrial and research applications worldwide (Lombardi, 2008).

To prove the benefit deriving from the long-term stabilization of the laser we performed a simple experiment in which the clock transition has been scanned many times over a period of several hours with and without the stabilization of the clock laser on the 1542 nm optical reference. The spectroscopic measurement performed without

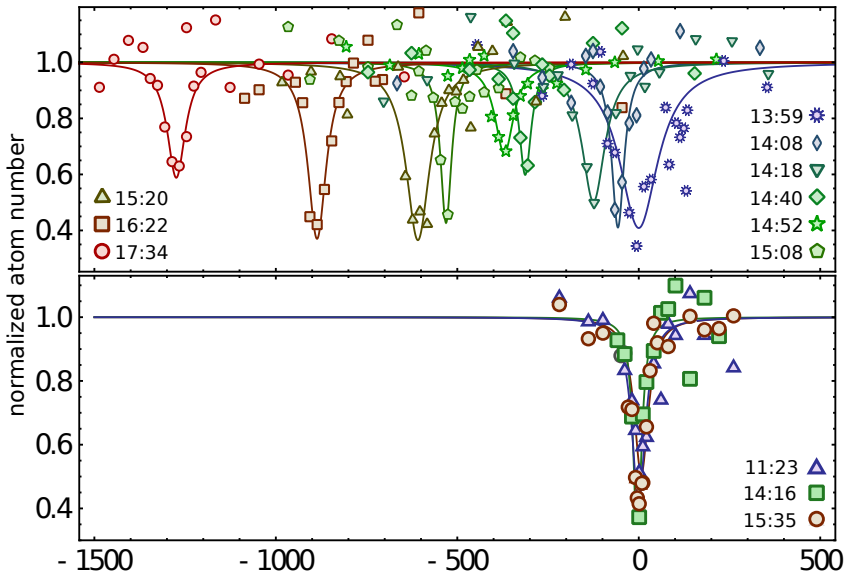

Figure 3.6: Clock laser spectroscopy of a spin polarized ^{173}Yb gas confined in a 3D ($s = 30$) optical lattice. **a:** spectroscopic measurement performed with the clock laser not referenced to the ultrastable 1542 nm frequency reference provided by INRiM show an apparent shift in time of the resonance position due to the aging drift of the ULE cavity which stabilize the laser frequency. **b:** the stabilization of the clock laser on the 1542 nm optical reference

any compensation of the laser drift are shown in figure 3.6-a. Here the clock transition has been probed nine times over a period of 3.5 hours with the laser locked only to the ULE cavity. Spectroscopy has been performed shining a 100 ms long clock pulse on a $m_F = -5/2$ spin-polarized ^{173}Yb atomic sample trapped in a 3D lattice ($s = 30$) operated at the magic wavelength. The laser intensity is 10 μW cm^{-2} in such a way to limit the power broadening to $\sim$50 Hz. The spectra reported in figure clearly evidence an apparent drift of the transition frequency, that results to be shifted by 1300 Hz during the entire duration of the experiment. Also the shape of the resonance line is affected by the uncompensated drift: even if the power broadening did not change during the whole experiment, resonances acquired with a scan performed with the same direction as the drift result to be broader than those acquired scanning the laser frequency in the direction opposite to the drift. The situation completely changes if the clock laser is stabilized on the INRiM ultrastable optical reference. The spectra acquired taking advantage of the fiber-link infrastructure are reported in figure 3.6-b. Despite a four-hours long interrogation time, no apparent drift of the transition frequency can be observed in the three resonances and the linewidth always remains below 50 Hz.

In a second experiment we exploited the incredible degree of frequency stability offered by the disciplination of our clock laser on the optical reference provided by INRiM to measure the absolute frequency of the clock transition in ^{173}Yb. Remarkably, this measurement improves the value reported in literature by two orders of mag-

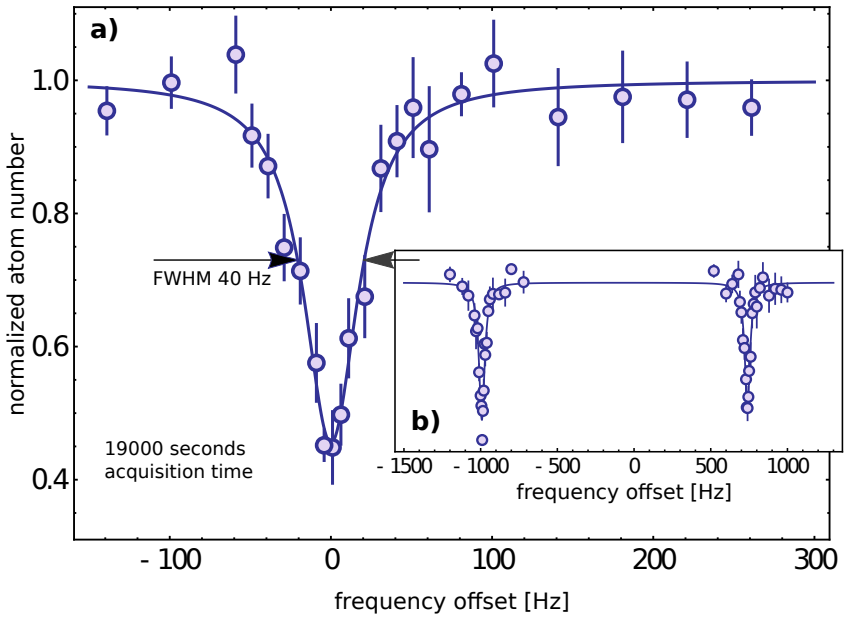

Figure 3.7: **a:** Long-term addressing of the clock transition (5.2 hours). The error bars indicate the standard deviation of the mean over approximately 10 repeated measurements. The lines are fits with Lorentzian functions. The zero values for the horizontal scales are chosen arbitrarily. **b:** Clock transition relative to the $m_F = \pm 5/2$ spin state. The mean value of center of the two resonances is used to extract the absolute value of the clock transition. frequency (see text).

nitude (Hoyt et al., 2005). The experiment has been carried out performing clock spectroscopy on a spin-polarized atomic sample loaded in 3D lattice operated at the magic wavelength. The number of atoms loaded in the lattice (about 2×10^4) and their temperature ($T = 0.2\,T_F$ with $T_F \simeq 2$ kHz $\times h/k_B$) have been chosen in order to negligibly populate the lattice excited bands. To measure the absolute frequency of the transition an external magnetic field has been applied in order to resolve the Zeeman structure of the line. For π-transitions, the differential Zeeman shift of the g and e levels determines a shift of the resonance position which is given by the expression 3.10. We exploited this Zeeman dependence of the resonance position to determine the unbiased value of the absolute frequency. For this purpose we measured the transition frequency relative to the spin components $m_F = \pm 5/2$, feature an opposite first order Zeeman shift, accordingly to equation 3.10. The resonances have been probed with 100-ms-long π-polarized light pulses with an intensity low enough to limit the power broadening to few tens of Hz, as it is shown in figure 3.7-a. Six different scans of the two spin transitions have been performed over a period of three months and during each scan the acquisition has been continuously alternated between $\pm 5/2$ polarized samples in such a way to suppress interaction-induced shifts. The acquisition time of the six different runs ranges from 2000 to 19000 s for a total measurement time of 40000 s. The resulting spectra have been fitted with two lorentzian curves

as it is shown in figure 3.7-b. The absolute frequency $\nu_{\pm 5/2}$ relative to the spin resonances can be easily evaluated thanks to the metrological chain which stabilizes the clock laser, and from their mean value $\nu_c = (\nu_{+5/2} + \nu_{-5/2})/2$ a first estimation of the absolute frequency of the transition can be provided. This value has been corrected for the shifts due to the second-order Zeeman shift (-0.59(3) Hz, corresponding to a magnetic field B = 3.031(5) G, evaluated from the splitting between $\nu_{+5/2}$ and $\nu_{-5/2}$), the black-body radiation (-1.24(5) Hz for a temperature of the room of 298 K) and the gravitational redshift (2.277(5)Hz) induced by the different height on the geoid of Florence and Turin. The corrected value of the absolute frequency of the clock transition in ^{173}Yb that we estimate is

$$\nu_{173} = 518\,294\,576\,845\,268(10)\ \text{Hz}, \tag{3.27}$$

where the leading source of uncertainty (8 Hz) is determined by the lattice AC-Stark shift, while the error introduced by the metrological chain is limited to 2 Hz, corresponding to a relative uncertainty of 4×10^{-15}. A detailed analysis of the uncertainties affecting the measurement can be found in (Cappellini, 2016).

Chapter 4
Quantum simulation with ^{173}Yb atoms exploiting the orbital degree of freedom

The ability to coherently control the optical transition that connects the ground state $^1S_0$ with the metastable clock state $^3P_0$ enriches the accessible Hilbert space of alkaline-earth and alkaline-earth-like atoms with an additional degree of freedom that can be exploited in quantum-simulation schemes as a second ground state (Gorshkov et al., 2009; Cazailla and Rey, 2014). In recent years, due to the high degree of tunability and flexibility offered by ultracold atomic systems, these schemes have been extended to the theoretical and experimental investigation of topological phases of matter (Goldman et al., 2016). In this chapter we present a series of experiments in which we have been able to successfully simulate some basilar properties of topological systems exploiting the orbital degree of freedom of ^{173}Yb.

A prime element for the emergence of nontrivial topological properties is the presence of spin-orbit coupling (SOC) locking the spin of the particles to their motion (Galitski and Spielman, 2013; Zhai, 2015). The emergence of SOC in the context of ultracold atoms has been already investigated with alkaline elements exploiting two-photon Raman transitions (Lin et al., 2011). In section 4.1 we demonstrate an alternative approach (Livi et al., 2016) in which SOC is synthesized in optical lattices by means of the absorption of single clock-light photons eliminating a major cause of heating that plagues the Raman implementation with alkaline fermions. The implementation of synthetic SOC is preliminary to the experiment presented in section 4.2 in which interpreting the two long-lived electronic states of ^{173}Yb as a *synthetic dimension* (Celi et al., 2014) we have been able to simulate a two-leg ladder subjected to a strong gauge potential, realizing a toy-model for the investigation of quantum Hall physics with ultracold atoms. In particular, we evidenced the onset of chiral currents circulating on the edge of the system and characterized the behaviour of the currents as a function of the synthetic magnetic flux.

Finally, in section 4.3 we discuss how atom-atom interactions in a $^1S_0 - {}^3P_0$ mixture can be tuned taking advantage of the *orbital feshbach resonance* scheme, recently proposed in (Zhang et al., 2015) and experimentally realized in (Pagano et al., 2015; Höfer et al., 2015).

4.1 Synthetic Spin-Orbit Coupling

In section 2.3.3 we have already discussed how a Spin-Orbit coupling (SOC) interaction can be efficiently synthesized with ultracold quantum gases exploiting an internal degree of freedom of the atom. This scheme was first realized in alkali atoms employing two-photon Raman transitions (Lin et al., 2009a), which couple two different hyperfine spin states of the electronic ground-state manifold with a transfer of momentum. However, the Raman approach inevitably suffers from heating mechanisms associated to the spontaneous emission from near-resonant intermediate states (Cheuk et al., 2012; Wang et al., 2012). While this heating does not prevent the observation of non-interacting processes or mean-field effects, it could represent a problematic issue for the investigation of many-body phenomena in which interactions play a fundamental role. As proposed in reference (Wall et al., 2016), these limitations can be overcome if synthetic SOC is realized exploiting the long-lived electronic states of alkaline-earth and alkaline-earth-like atoms, which can be efficiently coupled using single-photon clock transitions, avoiding in this way the detrimental effects due to the spontaneous emission from intermediate states. In this section we demonstrate how this scheme can be efficiently employed to realize a synthetic SOC interaction exploiting the $|^1S_0\rangle \rightarrow |^3P_0\rangle$ clock transition in ultracold ^{173}Yb atoms confined in an optical lattice. The first part of the section is dedicated to a theoretical description of how SOC can be implemented and probed with atoms trapped in an optical lattice using the technology developed in the context of optical atomic clocks, while in the last part of the section the experimental results are presented and discussed.

4.1.1 Implementation of synthetic SOC in optical lattices

In the previous chapter (see section 3.3) we have discussed the possibility to drive an optical transition without Doppler and recoil shifts by exploiting the confining potential provided by a deep optical lattice. This is true as long as the lattice bands can be considered flat, in such a way that the energy of an atom does not depend on its quasi-momentum inside the Brillouin zone. On the other hand if the lattice depth is reduced, the energy bands become wider and the momentum transferred from the radiation field to the atoms can result in an energy shift of the transition which can be detected if larger than the spectroscopic resolution. Here we consider the particular case in which a clock laser drives the transition at frequency $\nu_C = c/\lambda_C$ with $\lambda_C = 578$ nm between the states $|^1S_0\rangle = g$ and $|^3P_0\rangle = e$ of ^{173}Yb, and assume that the atoms are trapped in a one-dimensional lattice operated at the magic wavelength $\lambda_L = 2\pi/k_L = 759$ nm for which the light shifts induced on g and e are identical. In these circumstances the energy dispersion of the lattice bands is identical for both the ground and excited state and the absorption of a photon connects the state $|g, k\rangle$ with the state $|e, k + \delta k\rangle$ where $k = \tilde{k}a \in [-\pi, \pi)$ is the product of the lattice quasimomentum $\tilde{k}$ and the lattice spacing $a = \lambda_L/2$ and

$$\delta k = \pi \frac{\lambda_L}{\lambda_C} \tag{4.1}$$

is the momentum transferred to an atom as a consequence of the absorption of a photon, as it is shown in figure 4.1-a. The connection of states characterized by different

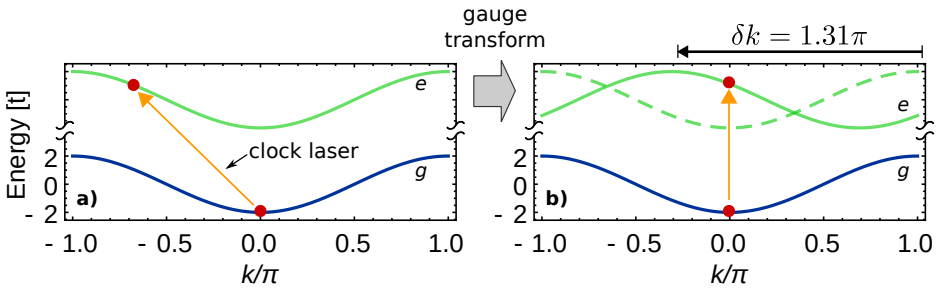

Figure 4.1: **a:** Sketch of the energy bands induced by an optical lattice for the g (solid blue line) and for the e electronic states (solid green line). The lattice is operated at the magic wavelength and consequently the band dispersions are identical for both the states. The clock transition between g and e connects states with different momentum and can be interpreted as a SOC interaction. **b:** By an appropriate gauge transform (see equation 4.3) the e band is shifted by the momentum transferred by the clock excitation and the $g \rightarrow e$ transition can be represented as a momentum conserving process. The example reported in figure corresponds to a 1.31π momentum shift, which is realized in our experiment when the lattice and the clock laser are co-aligned.

quasimomentum can be interpreted as the emergence of a SOC interaction between the two electronic states involved in the clock transition that consequently can be treated as pseudospin projections of an effective $J = 1/2$ spin.

This argumentation can be formalized starting from the Hamiltonian that governs a system of non-interacting spin 1/2 particles trapped in a one-dimensional optical lattice potential. In rotating wave approximation, the Hamiltonian in momentum space reads

$$H = \sum_{k,\alpha} E_{\alpha,k} \hat{n}_{\alpha,k} - \sum_{k} \left(\frac{\Omega}{2} \hat{a}^{\dagger}_{e,k+\phi} \hat{a}_{g,k} + \text{ H.c.} \right) \tag{4.2}$$

where $\hat{a}_{\alpha,k}$ is the annihilation operator for a particle with quasimomentum k in the electronic state $\alpha = \{g, e\}$, $\hat{n}_{\alpha,k} = \hat{a}^{\dagger}_{\alpha,k} \hat{a}_{\alpha,k}$ is the number operator, Ω is the Rabi frequency associated to the laser coupling, $\phi = \pi \delta k / k_L$ and $E_{\alpha,k} = -2t \cos(k) + \delta_{\alpha}$ where t is the lattice tunnelling energy and $\delta_{g,e} = \pm \delta/2$ is the laser frequency detuning with respect to the atomic transition. If the gauge transformation

$$U(\hat{a}) : \hat{a}_{e,k+\phi} \rightarrow \hat{a}_{e,k} \tag{4.3}$$

is performed, the Hamiltonian becomes diagonal in momentum space and in the $\{g, e\}$ pseudospin basis can be written as

$$\hat{H} = \begin{pmatrix} -2t \cos(k) - \frac{\delta}{2} & -\frac{\Omega}{2} \\ -\frac{\Omega}{2} & -2t \cos(k + \phi) + \frac{\delta}{2} \end{pmatrix} \tag{4.4}$$

This gauge transformation, as it is shown in figure 4.1-b, makes it is possible to sketch the transition as a momentum-preserving process (vertical arrow) between the g-band and a momentum-shifted e-band, which enlights the dependence of the transition energy on the momentum state k. By summing the term $t(\cos(k) + \cos(k + \phi))$ to the

Hamiltonian diagonal elements, the expression 4.4 can be explicitly written as an effective SOC interaction

$$\hat{H} = -\mathbf{B}(k) \cdot \mathbf{S} \tag{4.5}$$

where $\mathbf{B}(k) = \frac{1}{2}\{\Omega, 0, 2t(\cos(k) - \cos(k+\phi)) + \delta\}$ and $\mathbf{S} = \{\sigma_x, \sigma_y, \sigma_z\}$ is the vector composed by the Pauli matrices.

4.1.2 Spectroscopic signatures of SOC

If the laser coupling between the g and the e states is sufficiently low, the lattice bandwidth can exceed the power-broadened clock resonance linewidth and, consequently, the clock laser can be exploited to address the band in a momentum- and energy-selective way. If SOC is present, the clock excitation connects two momentum-displaced lattice bands and this energy-selective addressing results in an enhanced response at the edges of the spectrum, provided that the g band is initially completely filled. This feature is related to the divergences in the density of states induced by the van Hove singularities of the optical lattice (Van Hove, 1953) and can be regarded as a spectroscopic signature of the presence of a synthetic SOC interaction, as pointed out in reference (Wall et al., 2016).

From a theoretical point of view, the spectroscopic response $\mathcal{S}(\omega)$ emerges as a consequence of the convolution of the spectroscopic resolution function $\mathcal{L}(\omega)$ and the joint density of states $\rho(\omega)$ of the two lattice bands involved in a transition at frequency ω, i.e.

$$\mathcal{S}(\omega) = \int_{-\infty}^{+\infty} \mathcal{L}(\omega' - \omega)\, \rho(\omega')\, \mathrm{d}\omega'. \tag{4.6}$$

The joint density of states $\rho(\omega)$ can be evaluated using the relation

$$\rho(\omega)\, \mathrm{d}\omega = \rho(k)\, \mathrm{d}k \tag{4.7}$$

where $\rho(k)$, the density of states in momentum space, is constant for a one-dimensional lattice and consequently the expression for $\rho(\omega)$ reduces to $\rho(\omega) \propto \mathrm{d}k/\,\mathrm{d}\omega$. To solve this equation the relation $\hbar\omega = E_0 + 2t(\cos(k) - \cos(k+\phi))$ must be inverted in order to express k as a function of ω and then derived with respect to ω. This problem can be solved analytically and gives for $\rho(\omega)$ the expression

$$\rho(\omega) \propto \sqrt{\frac{1}{-\hbar^2\omega^2 + 8t^2(1 - \cos(\phi))}} \tag{4.8}$$

which is characterized by two divergences located at $\omega = \pm t\sqrt{8(1-\cos(\phi))}/\hbar = \pm 4t \sin(\phi/2)/\hbar$. The physical spectroscopic response can be determined convolving the joint density of states 4.8 with a Lorentzian lineshape

$$\mathcal{L}(\omega) \propto \frac{1}{\Gamma^2/4 + \omega^2} \tag{4.9}$$

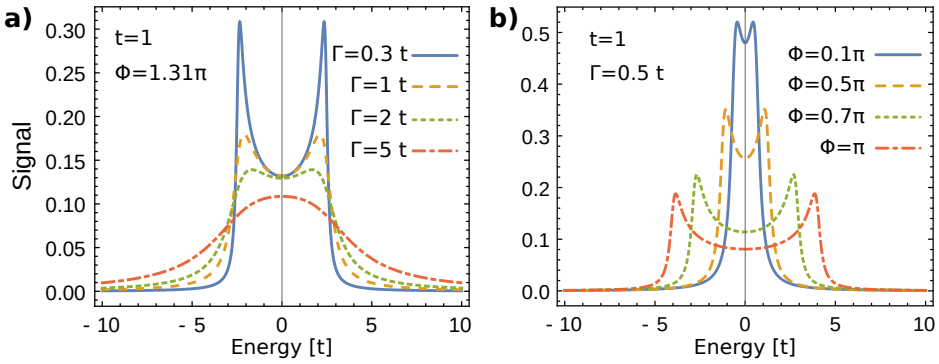

Figure 4.2: Spectroscopic signature of spin-orbit coupling for fixed tunnelling strength and flux, varying the clock laser power broadening **(a)** and for fixed tunnelling strength and power-broadening, varying the flux **(b)**. All the signals are normalized.

where Γ is the instrumental resolution limit. The mathematical expressions for $\rho(\omega)$ and $\mathcal{L}(\omega)$ allow for an easy resolution of the integral 4.6 exploiting the residue [1] theorem, which gives

$$\mathcal{S}(\omega) \propto \mathrm{Re}\left[\sqrt{\frac{1}{-\hbar^2\left(\omega+\frac{i\Gamma}{2}\right)^2+8t^2(1-\cos(\phi))}}\right], \tag{4.10}$$

where the real part limits the solution to the physical domain. The expected behaviour of the evaluated spectroscopic response as a function of the lattice depth and laser resonance broadening are reported, respectively, in figures 4.2-a and 4.2-b.

4.1.3 Experimental observation of SOC

In order to experimentally observe the spectroscopic signatures of SOC described in the precedent subsection, we trap an ultracold spin-polarized ^{173}Yb Fermi gas in a one dimensional optical lattice potential $V(x) = sE_r\cos^2(k_Lx)$ operated at the magic wavelength $\lambda_L = 2\pi/k_L = 759$ nm. The lattice depth s expressed in terms of the recoil energy $E_r = \hbar^2k_L^2/2m$ where m is the atomic mass, determines the tunnelling energy t between neighbouring lattice sites. An additional 1D deep lattice freezes the atomic motion along the vertical direction, avoiding atoms falling due to the gravity force. The total atom number is tuned around $N_{at} = 2\times10^4$, in such a way that the first lattice band is completely occupied while the population in the excited bands is negligible. SOC is then induced shining an 800-ms-long π-polarized clock pulse at $\lambda_C = 578$ nm on the atomic sample. The clock laser beam is co-aligned with the one-dimensional lattice and, consequently, the momentum imparted to the atoms in units

[1] The integral has the form $\int_{-\infty}^{+\infty}\frac{1}{(\omega-\omega_0)^2+A^2}\sqrt{\frac{1}{B^2-\omega^2}}\,\mathrm{d}\omega$ and features two real poles located at $\omega = \pm B$ and two complex poles located at $\omega = \pm\omega_0 \pm iA$. The integral can be evaluated with standard complex analysis resolution methods (Ablowitz and Fokas, 2003) taking into account that the only non vanishing residues are the one evaluated in the complex poles for which we have $\mathrm{Res}(\omega = \omega_0 + iA) = \frac{1}{2iA}\frac{1}{\sqrt{B^2-(\omega-\omega_0+iA)^2}}$.

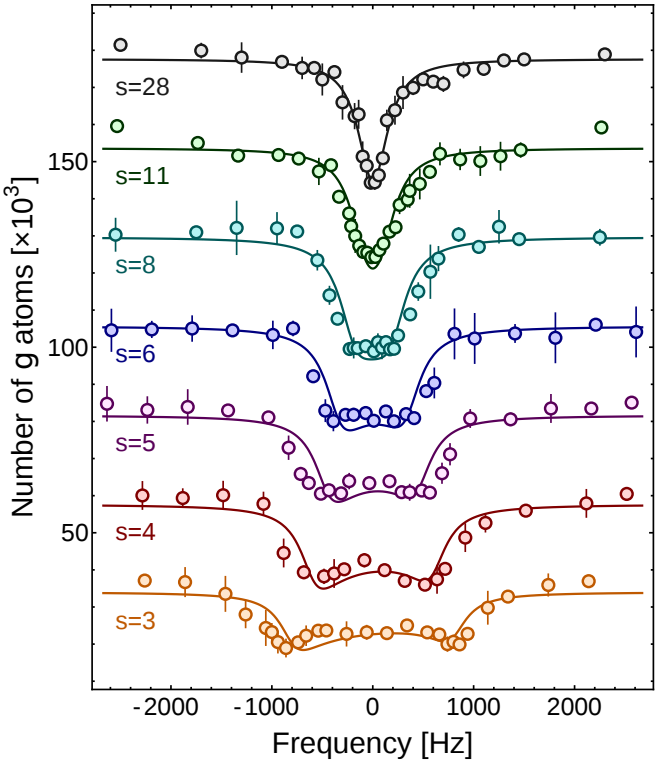

Figure 4.3: Spectra of the clock transition for different lattice depths. Datasets with $s \geq 4$ have been offset vertically for the sake of presentation. The curves are the result of a single-particle theoretical model, with vertical amplitude and offset as only fit parameters. All the experimental spectra have been measured shining the clock laser light along the lattice direction and using only an additional transverse (vertical) optical lattice to hold the atoms against gravity. Spectra acquired at low lattice depth feature an enhanced response on the edge that can be associated to a SOC interaction induced by the clock light.

of the quasimomentum k will be $\phi = 1.31\pi$, as derived from equation 4.1. Figure 4.3 shows a collection of clock spectra for different lattice depths, from $s = 28$ to $s = 3$, illustrating the crossover between clock spectroscopy in the Lamb-Dicke regime at large s to momentum-selective excitations at small s. While for high s the flatness of the lattice energy bands results in a pure Lorentzian shape of the resonance line, for shallow lattices the resonance acquires the "M" shaped profile previously derived that can be ascribed to an effective induced SOC interaction between the two electronic states of the atoms involved in the transition. All the spectra reported in the figure have been acquired with the clock laser disciplined to the optical frequency reference delivered by INRiM. This is a crucial requirement for this kind of measurements since we are observing features characterized by a width of the order of few hundreds of Hz, a value comparable with the laser drift in the time necessary to acquire one spectrum

(~ 1 hour).

The width w_s of the spectra reported in figure 4.3 is related to the momentum transfer and to the tunnelling strength, being $w_s = 8t|\sin(\delta k)|$ for a fully occupied first lattice band. The resonances have been fitted with the mathematical model previously introduced, which assumes the spectroscopic signal to be the convolution between the joint density of states of the momentum-displaced g and e lattice bands and the spectroscopic response obtained at high lattice depth, a condition for which tunnelling is negligible. The latter response can be approximated with a Lorentzian line profile with a half width at half maximum of 170 Hz, as derived from a fit of the measured spectrum at $s = 28$. The fits, in which the only free parameters are the vertical offset and the vertical scaling, show a remarkably good agreement with the experimental data.

4.2 Hall physics with a synthetic two-leg ladder

As already discussed in section 2.3.2, an internal degree of freedom of a neutral atom can be regarded as a synthetic discrete dimension. An artificial coherent coupling between these synthetic lattice sites in combination with a real one-dimensional optical lattice gives rise to a hybrid two-dimensional ladder naturally pierced by an artificial gauge field. In this section we demonstrate the experimental implementation of this approach exploiting the two long-lived $|^1S_0\rangle = g$ and $|^3P_0\rangle = e$ electronic states of ^{173}Yb as a synthetic dimension. Since only two sites are present in this case along the synthetic dimension, the resulting system can be viewed as a hybrid two-leg ladder. We investigated the equilibrium properties of this ladder system focusing the attention on the chiral counter-propagating currents that circulate along the two edges as a consequence of the presence of the artificial magnetic flux. Finally, we will discuss how this rather simple experimental approach makes it possible to easily tune the strength of the artificial field allowing the investigation of the behaviour of the chiral currents as a function of the piercing synthetic flux.

4.2.1 Chiral currents

In the synthetic dimension picture the g and e electronic states of ^{173}Yb can be treated as a synthetic dimension with only two lattice sites, where the tunnelling is provided by a clock laser coherently driving the $g \to e$ transition. As we have already discussed in section 2.3.2, the phase imprinted by the laser coupling on the atomic wavefunction can be interpreted as a Peierls phase if we imagine to combine the two-sites synthetic dimension with a real optical lattice. In the physical gauge (see section 2.2.3) the resulting hybrid ladder system, which is sketched in figure 4.4-a, is described by the tight binding Hamiltonian

$$H = -\hbar \left[\left(t \sum_{j,\alpha} \hat{a}^\dagger_{j+1,\alpha} \hat{a}_{j,\alpha} + \frac{\Omega}{2} \sum_j e^{i\Phi j} \hat{a}^\dagger_{j,e} \hat{a}_{j,g} + \text{H.c.} \right) + \sum_{j,\alpha} \delta_\alpha \, \hat{a}^\dagger_{j,\alpha} \hat{a}_{j,\alpha} \right] \tag{4.11}$$

where t is the real-lattice tunnelling energy, Ω is the Rabi frequency associated to the tunnelling strength along the rungs of the ladder, $\delta_{g,e} = \pm\delta/2$ is the laser detuning with respect to the resonance and $\hat{a}_{j,\alpha}$ is the annihilation operator for a particle in

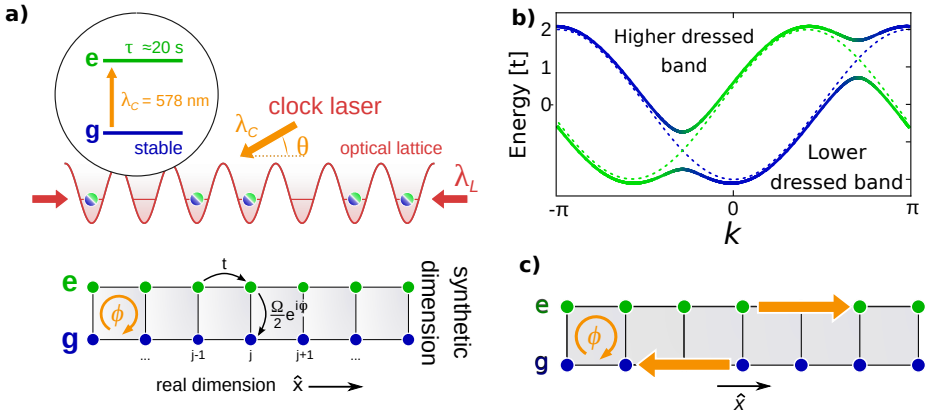

Figure 4.4: **a:** Sketch of the two-leg hybrid ladder realized combining a shallow optical lattice with a synthetic two-sites dimension encoded in the $|^1S_0\rangle = g$ and $|^3P_0\rangle = e$ long-lived electronic states of ^{173}Yb. **b:** Dressed (thick, solid) and bare energy bands (thin, dashed) of the ladder Hamiltonian for $\phi = 1.31\pi$ and $\Omega = t$. The color of the thick lines reflects the state composition of the dressed bands (e: green, g: blue): the different composition as a function of k can be interpreted as chiral currents flowing in opposite directions along the two legs of the synthetic ladder. **c:** Sketch of the chiral currents circulating along the edges of the ladder.

the electronic state $\alpha = \{g, e\}$ located in the j-th site of the real lattice. The phase ϕ originates as a consequence of the laser coupling and in the synthetic-dimension approach can be interpreted as the effect of an artificial magnetic flux piercing one cell of the ladder. This flux is constant on the whole ladder and in the case in which the coupling laser and the lattice are co-propagating its value is given by

$$\Phi = \pi \frac{k_C}{k_L} \tag{4.12}$$

where k_L and k_C are, respectively, the wavevector of the lattice and of the coupling laser light. The expression 4.11 can be equivalently written in momentum space and diagonalized thanks to the gauge transformation 4.3. The resulting gauge-transformed Hamiltonian can be conveniently expressed in the matrix form 4.4, that allows for a numerically simple determination of the energy spectrum and eigenstates composition. An example of energy band dispersion associated to the transformed Hamiltonian is reported in figure 4.4-b for a flux $\Phi = 1.31\pi$ in the limit of zero coupling $\Omega = 0$ (dotted lines) and for $\Omega = t$ (thick lines). The colors of the thick lines reflect the eigenstate composition as a mix of the ground state g (blue) and of the excited state e (green). The dressed spectrum reported in figure clearly evidences an asymmetry in the band dispersion associated to the two electronic states g and e, that can be attributed to the effect of a synthetic SOC interaction. In the synthetic dimension picture this asymmetry can be equivalently interpreted as the emergence of a chiral current that circulates on the legs of the ladder (see figure 4.4-c), as it is expected at the boundaries of a Hall bar pierced by a magnetic field. The following part of this section is devoted to the experimental investigation of these currents.

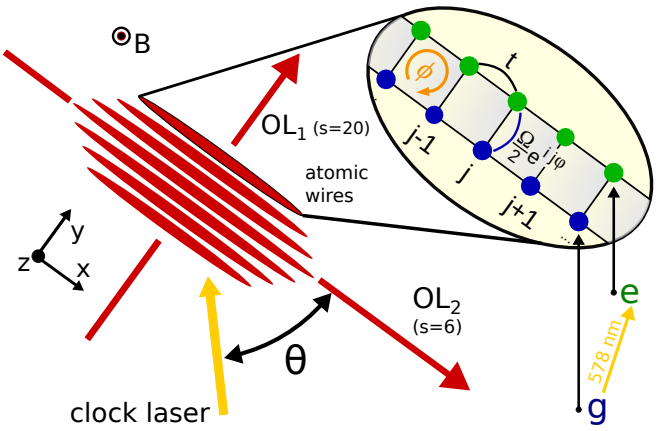

Figure 4.5: Sketch of the experimental setup used for the observation of the chiral currents. An array of fermionic wires is realized confining the atoms by means of two deep lattices OL_1 and OL_3, (not shown, in the plane orthogonal to the picture). Each wire is a realization of a two-leg hybrid ladder in the synthetic dimension picture. The angle θ at which the clock laser intersects the wires defines the syntehtic flux Φ.

4.2.2 Experimental observation of the chiral currents

The observation of the edge currents described so far is conceptually easy in the synthetic-dimension approach since the two legs of the ladder are encoded in different electronic states of the atoms, and can consequently be addressed and imaged individually. As discussed before, in an equilibrium dressed state of the ladder Hamiltonian 4.11 (or equivalently of the Hamiltonian 4.4 if the problem is solved in momentum space) each leg (or equivalently each electronic state) is characterized by a different momentum distribution that, due to the SOC interaction, is expected to show a net opposite asymmetry with respect to the center of the Brillouin zone. These asymmetric momentum distributions imply that, at equilibrium, atoms on different legs propagate with opposite velocities, a behaviour that can be interpreted in terms of chiral edge currents. From an experimental point of view, the procedure that we followed to induce and observe these edge currents is reported in figure 4.6 and requires, first of all, to load the lowest dressed state of the Hamiltonian 4.11. To accomplish this task we start realizing by evaporative cooling in the 1064 nm optical dipole trap (see section 1.2.3 for more details) a spin-polarized ($m_F = -5/2$) ultracold ^{173}Yb gas with a temperature of 0.2 T_F ($T_F \simeq 2$ kHz h/k_B). The number of atoms is set to be $N_{at} \simeq 1.2 \times 10^4$, in such a way not to populate the higher dressed band of the ladder Hamiltonian 4.11. The gas is then loaded in a 3D cubic optical lattice operated at the magic wavelength $\lambda_L = 2\pi/k_L = 759$ nm for which the light shift of the g and e states is identical. The lattice potential is turned on with an adiabatic 150-ms-long exponential intensity ramp and superimposed to the 1064 nm optical dipole trap. Only at the end of the intensity ramp the dipole trap is adiabatically turned off with a 200-ms-long linear ramp, leaving the lattice as the only confining potential. The lattice depths $s_{x,y,z}$, expressed in units of the recoil energy $E_r = \hbar^2 k_L^2/2m$, where m is the atomic mass, are set to $s_x = 6$

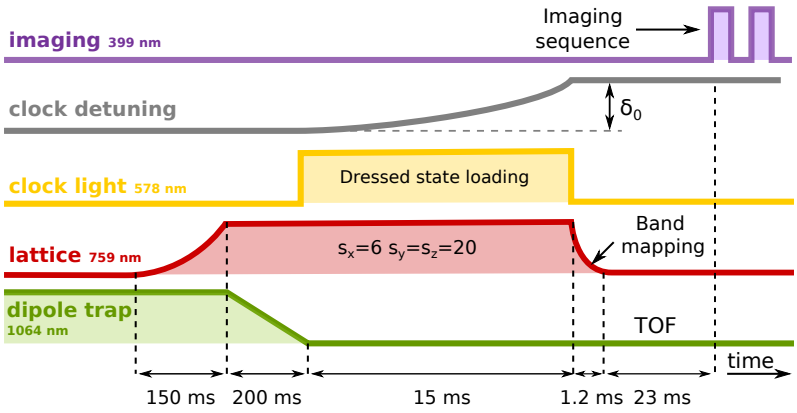

Figure 4.6: Experimental sequence employed for the observation of the chiral currents.

and $s_y = s_z = 20$, in such a way that on the timescale of the experiment tunnelling is allowed only along the $\hat{e}_x$ direction, for which we have $t \simeq 2\pi \times 140$ Hz. As a consequence of the strong confinement along $\hat{e}_y$ and $\hat{e}_z$, the system can be treated as an array of ~ 1000 one dimensional fermionic tubes, each of which in the synthetic-dimension picture constitute the real dimension of a hybrid ladder.

At this point, in order to load the lowest dressed state of the ladder Hamiltonian, the $g \to e$ coupling, that in the synthetic dimension picture plays the role of the tunnelling along the rung of the ladder, must be switched on. To do this, a 150 G magnetic field is turned on in order to resolve the nuclear atomic Zeeman substructure and the 578 nm π-polarized clock laser light, initially red-detuned by δ_i with respect to the $g(m_F = -5/2) \to e(m_F = -5/2)$ transition, is shined on the atomic sample. The clock laser detuning δ is then progressively reduced with an adiabatic frequency sweep ramp characterized by the analytical form

$$\delta(t) = \delta_i - (\delta_i - \delta_f)\left(\frac{1 - e^{-t/\tau}}{1 - e^{-T/\tau}}\right) \tag{4.13}$$

where T is the duration of the ramp and the final detuning δf is $\delta_f = 0$. From a quantum-optic prospect, the effect of the detuning ramp can be viewed as an adiabatic transfer of the population from the south pole of the Bloch sphere, which corresponds to the g state, to the equator of the sphere where the quantum superposition $(|g\rangle + |e\rangle)/\sqrt{2}$ is realized. During the whole process the intensity of the 578 nm laser light remains constant and the value Ω of the associated Rabi frequency at resonance determines the parameters δ_0, τ and T that we set for the detuning ramp. Note that during this phase the disciplination of our clock laser to the INRiM metrological reference resulted to be absolutely necessary, since we observed that shifts of the final detuning value of few hundreds of Hz strongly alter the strength of the chiral currents. The value of Ω is experimentally determined performing a Rabi oscillation measurement on a spin-polarized gas trapped in a deep 3D isotropic lattice. The measured value of Ω is then used to find a suitable set of parameters for the detuning ramp. This is done performing a simulation of the evolution of the system that consists in the numerical

resolution of the Schroedinger equation

$$i\frac{\mathrm{d}\Psi_k(t)}{\mathrm{d}t} = \begin{pmatrix} 2J\cos(kd) - \delta(t) & \Omega/2 \\ \Omega/2 & 2J\cos(kd+\Phi_k) \end{pmatrix} \Psi_k(t) \tag{4.14}$$

where d is the lattice spacing, J is the tunnelling strength, $\delta(t)$ is the detuning ramp 4.13 and Ψ_k, the two-component spinor associated to the populations of the g and e states, is initialized as $\Psi_k(t=0) = (1,0)$, a condition that corresponds to the whole population in the g state. The ramp parameters are chosen so that the ramp duration does not exceed the coherence time of the laser (we set typical values of the order of $T = 15$ ms) and in such a way that the residual time-dependent oscillation of the g and e populations at the end of the sweep are of the order of few percent independently respect to the quasimomentum k. For $\Omega \simeq 2\pi \times 600$ Hz, for example, we found as optimal ramp parameters $\delta_0 = 2\pi \times 8$ kHz, $T = 15$ ms and $\tau = 4.5$ ms. The experimental verification of the adiabaticity of the dressed state loading procedure is performed by executing a frequency-reversed-sweep ramp after the first detuning ramp and checking that, at the end of the unloading process, the atomic population is transferred again in the g state.

After loading the ground state of the ladder Hamiltonian the 578 nm coupling light is suddenly turned off and the momentum distribution relative to the g state is measured with the band mapping technique described in section 1.3.2. In order to increase the SNR, each momentum distribution is the result of the average of at least 20 images acquired in the same experimental conditions. To this averaged momentum distribution we subtract an averaged image of the background that helps to remove residual gradients or fringes due to imperfections of the imaging setup. At the time when these measurements were performed an imaging system for the e state was not available and consequently only the momentum distribution of the g leg of the ladder was observable. An example of normalized momentum distribution relative to the g state measured after the dressed-state loading procedure ($\Omega = 2\pi \times 590$ Hz, $\phi = 0.58\pi$, $t = 2\pi \times 138$ Hz) is shown in figure 4.7. While along the $\hat{e}_y$ direction we observe an uniform square distribution due to the presence of the strong confinement lattices along the directions orthogonal to the tubes, the distribution $n_g(k)$ along $\hat{e}_x$ features an evident asymmetry with respect to the center of the Brillouin zone, that we characterize with the quantity J_g

$$J_g = \int_0^{\pi} n_g(k) - n_g(-k)\,\mathrm{d}k \tag{4.15}$$

that we associate to the strength of the chiral current. In the figure the distribution is compared with the case in which no clock laser coupling, and so no asymmetry, is present. The value of J_g relative to the example shown in the figure is $J_g = +0.080 \pm 0.015$ which is in agreement with the theoretical prediction, if we assume a temperature of the Fermi gas $T = 0.6\,t$, as explained in detail in the following section.

A further validation of our experimental method is provided by an additional experiment in which we loaded the higher dressed state of the ladder Hamiltonian 4.11. This can be done by performing a reversed loading frequency sweep that starts blue-detuned with respect to the resonance. The experimental result of this procedure if shown in figure 4.8 where the g momentum distribution measured at the end of this

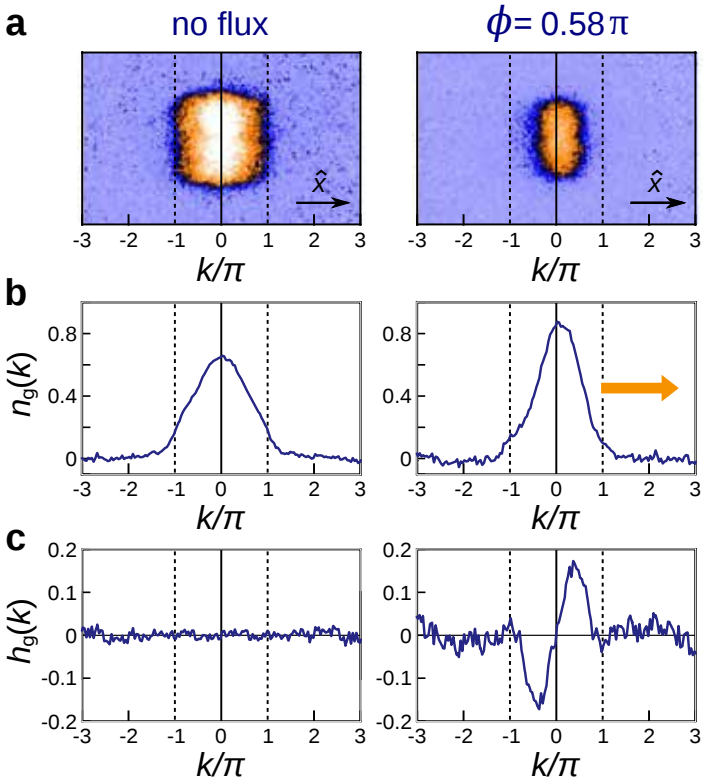

Figure 4.7: **a:** Time-of-flight images of the g atoms for decoupled legs ($\Omega = 0$, left) and for coupled legs after adiabatic loading ($\Omega = 2\pi \times 590$ Hz, $\Phi = 0.58\pi$, $t = 2\pi \times 138$ Hz). **b:** Integrated lattice momentum distribution $n_g(k)$ along the ladder direction for the data reported in panel a. **c:** Asymmetry function $h_g(k) = n_g(k) - n_g(-k)$, evidencing the chiral current in the presence of the flux.

reversed detuning ramp is reported for the Hamiltonian parameters $\Omega = 2\pi \times 590$ Hz, $\phi = 1.31\pi$ and $t = 2\pi \times 138$ Hz. We observe a distribution that features a "hole" for momenta near the center of the Brillouin zone that is complementary to the one relative to the lower dressed state of the Hamiltonian, in which, on the contrary, no population is observed for high momenta. As it can be evinced from the band dispersion reported in the figure, this distribution is in qualitatively good agreement with the one expected for the higher dressed state of the Hamiltonian, and consequently its observation can be assumed as a validation of our experimental procedures. As a final note, it should be observed that the loading of the higher dressed state is complicated by the presence of the lattice blue sideband, that for our experimental conditions ($s = 6$) becomes resonant with the frequency sweep as the detuning is varied from 8 kHz to 0. The excitation of the sideband is avoided preparing the system at a higher lattice depth ($s = 20$) and then decreasing the depth from $s = 20$ to $s = 6$ with an adiabatic ramp simultaneous to the frequency sweep.

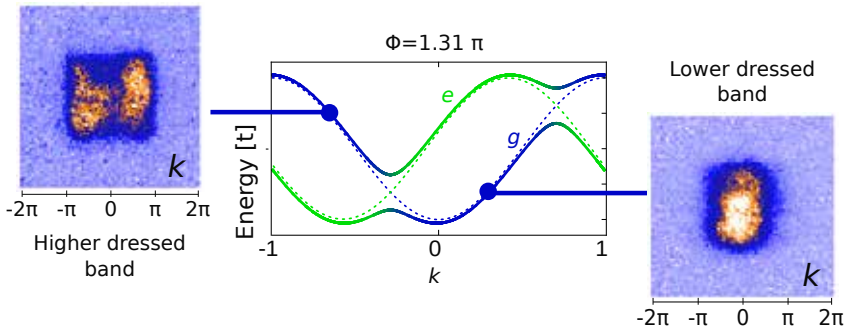

Figure 4.8: Sketch of the ladder Hamiltonian dispersion bands for $\Phi = 1.31\pi$. The colors reflect the composition of the dressed state (blue = g, green = e). On the sides of the dispersion spectrum the time-of-flight images of the g atoms momentum distribution relative to the lower and higher dressed state of the Hamiltonian are reported (experimental conditions: $\Omega = 2\pi \times 590$ Hz, $\Phi = 1.31\pi$, $t = 2\pi \times 138$ Hz).

4.2.3 Tuning the synthetic flux

The rather simple approach discussed so far for the implementation of a quantum simulator of the Hamiltonian 4.2 makes it particularly easy to tune the flux piercing the ladder by just changing the angle at which the clock laser beam intersects the fermionic wires. In particular, indicating the intersection angle with θ, we have for the synthetic flux

$$\Phi(\theta) = \pi \frac{k_C}{k_L} \cos(\theta) \tag{4.16}$$

where k_C and κ_L are, respectively, the clock laser and lattice wavenumbers. This relation implies that in our system the flux can be continuously tuned from $\Phi = 0$ to $\Phi = 1.31\pi$. In figure 4.9-a several experimental values of the chiral current strength J are reported as a function of the synthetic flux Φ. All the measurements have been acquired with the experimental parameters $\Omega = 2\pi \times 590$ Hz and $t = 2\pi \times 138$ Hz, and the flux Φ has been tuned changing the direction of the clock beam relative to the fermionic wires (see figure 4.9-b,c). The data clearly show an inversion of the sign of the chiral current for $\Phi > \pi$, a behaviour that, at a qualitative level, can be explained on the basis of the symmetries of the system, since the flux per plaquette is defined modulo 2π ($J(\Phi) = J(\Phi + 2\pi)$) and the current changes sign when the flux is inverted ($J(\Phi) = -J(-\Phi)$) because of its chiral nature. The experimental points are compared with the result of a single-particle calculation based on the exact diagonalization of a system of fermions in the two-leg ladder, showing a very good agreement.

The theoretical model that we elaborated in order to estimate the value of J as a function of the flux Φ is based on the assumption, verified numerically (see appendix A), that, at fixed maximum number of particles N_{max} per fermionic wire, the number of wires containing $N \leq N_{max}$ particles is constant. The wires containing the maximum number of particles are located in the central region of the lattice, where the confining harmonic potential induced by the lattice intensity profile is stronger. Taking into account our lattice geometry and considering that the number of atoms loaded

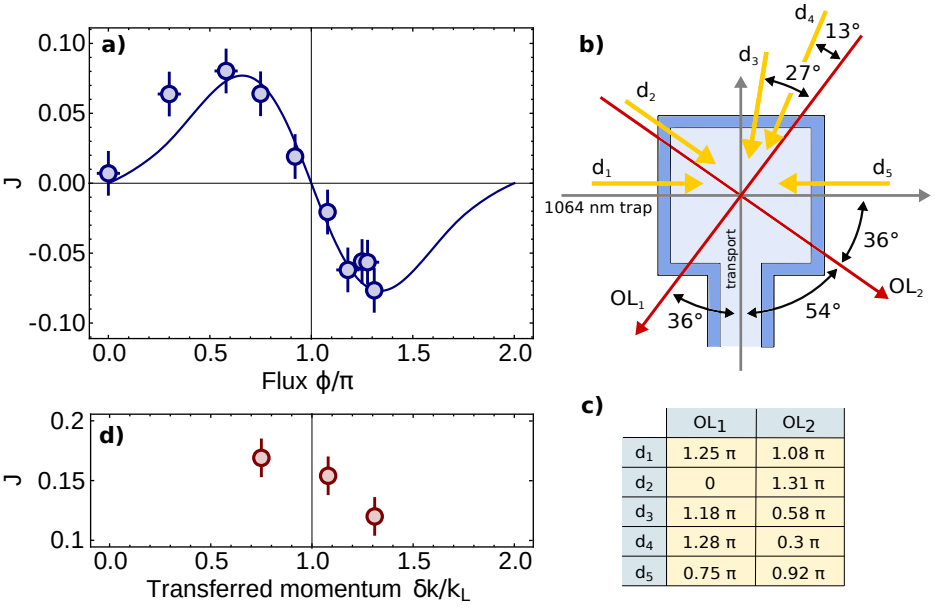

c)

	OL_1	OL_2
d_1	1.25 π	1.08 π
d_2	0	1.31 π
d_3	1.18 π	0.58 π
d_4	1.28 π	0.3 π
d_5	0.75 π	0.92 π

Figure 4.9: **a:** Dependence of the chiral currents J on the flux Φ. Vertical error bars are the standard deviation of a representative set of measurements, while horizontal error bars arise from the uncertainty on the angle θ. The solid curve is the expectation of a theoretical single-particle model (see main text). Experimental parameters: $\Omega = 2\pi \times 590$ Hz and $t = 2\pi \times 138$ Hz. **b:** Sketch of all the directions of the clock laser beam ($d_{1...5}$) relative to the optical lattices OL_1 and OL_2 (red lines) employed for the measurements reported in (a). **c:** Table of the synthetic fluxes realized for the directions $d_{1...5}$ reported in (b) for fermionic wires realized along OL_1 - OL_2. **d:** Chiral currents in the absence of the lattice along the direction of the ladders. In this "continuum" configuration, where a 2D unit cell is not defined, no inversion of J is observed at large SOC momentum transfer δk. We note that the horizontal scales of the two plots coincide as $\Phi/\pi = \delta k/k_L$.

in the lattice before the loading of the dressed state is $N_{atoms} \simeq 10^4$, we estimate $N_{max} = 28$, which means that we expect N_w wires with 28 particles, N_w wires with 27 particles and so on down to N_w wires with 1 particle. This means that, if we indicate with $n_N(k)$ the normalized momentum distribution associated to a wire with N particles, then the overall momentum distribution will be given by

$$n(k) = \sum_{N=1}^{N_{max}} N\, n_N(k) \tag{4.17}$$

where the multiplication factor N takes into account that wires with more particles contribute more to the signal. The distribution $n(k)$ is the sum of the momentum distributions associated to the two legs of the ladder, $n_g(k)$ and $n_e(k)$, which have opposite asymmetry with respect to the center of the Brillouin zone as a consequence of the effect of the SOC interaction. Here we are interested only in the determination of $n_g(k)$,

that is our observable, for which a relation similar to the 4.17 must hold

$$n_g(k) = \sum_{N=1}^{N_{max}} N\, n_{N,g}(k) \tag{4.18}$$

where $n_{N,g}(k)$ is the N-particles g-leg momentum distribution. To estimate $n_{N,g}(k)$ we perform an exact diagonalization of the Hamiltonian 4.11 including also the harmonic potential that is present along the wires as a consequence of the confinement along the orthogonal directions. This potential can be easily included in the tight-binding Hamiltonian simply by adding a $\hbar\, f_x\, (j - L/2)^2\, \hat{a}_j^\dagger \hat{a}_j$ term on the diagonal elements, where L is the number of lattice sites chosen for the calculation. The constant f_x is related to the strength of the harmonic confinement by the relation

$$\frac{1}{2} m\, \omega_x^2 a^2\, j^2 = \hbar\, f_x\, j^2 \tag{4.19}$$

where m is the atomic mass, j is an integer associated to the site position in the lattice, a is the lattice spacing and $\omega_x/(2\pi)$ is the harmonic oscillator frequency. We experimentally determined $\omega_x = 2\pi \times 44$ Hz by inducing and detecting dipole oscillations in the experimental conditions $s_x = 6$ and $s_y = s_z = 20$. The presence of the harmonic potential breaks the translational invariance of the lattice and, consequently, a diagonalization in momentum space is no longer possible. We have thus solved the problem in real space considering a ladder with 100 sites along the real dimension, a number high enough to have vanishing wavefunctions on the lattice edges thanks to the harmonic confinement. The diagonalization of the Hamiltonian provides the set of real-space wavefunctions ψ_ℓ allowed for each wire and the set of the corresponding eigenenergies $E(\ell)$, that we assume to be ordered for increasing energy ($E(1) < E(2) < ...$). From the ladder eigenstates we then extract the wavefunctions component relative to the two legs that we indicate with $\psi_{\ell,\alpha}$ with $\alpha = g, e$. A subsequent discrete Fourier transform of the $\psi_{\ell,\alpha}$ provides the set of normalized momentum-space leg-dependent wavefunction components $\psi^k_{\ell,\alpha}$.

Since we are dealing with fermionic particles, as a consequence of the Fermi-Dirac statistics, every allowed eigenstate can be occupied by no more than two atoms with different pseudospin. Taking into account the statistics, if we focus the attention on the g leg and fix the temperature T of the system and the number of particles N, the leg momentum distribution will be given by

$$n_{g,N}(k) = \frac{1}{N} \sum_\ell A\, \frac{1}{e^{(E(\ell) - E_F(N))/(k_B\, T)} + 1} \psi^k_{\ell,g}(k) \tag{4.20}$$

where A is the normalization constant $A = (\sum_\ell e^{(E(\ell) - E_F(N))/(k_B\, T)} + 1)^{-1}$ and $E_F(N)$, the Fermi energy, is defined as $E_F(N) = (E(N+1) + E(N))/2$. Once the $n_{g,N}$ are determined the global momentum distribution is simply given by the summation 4.18.

The role played by the trap frequency and the temperature in the definition of the asymmetry of the momentum distribution is shown in figure 4.10, where we report the chirality estimated for fermionic wires with different particle number as a function of the trap frequency (panel (a)) with the temperature fixed or as a function of the temperature (panel (b)) with the trap frequency fixed. In both cases we fixed the other relevant

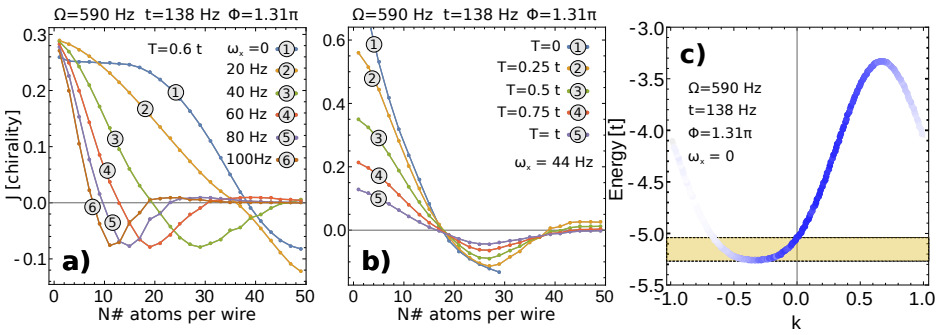

Figure 4.10: Theoretical evaluation of **a:** the chirality relative to the normalized momentum distribution of a single fermionic wire as a function of the atom number and of the trap frequency for $T = 0.6t$, **b:** the chirality relative to the normalized momentum distribution of a single fermionic wire as a function of the atom number and of the temperature for $\omega_x = 2\pi \times 44$ Hz. The values of t, Ω and ω_x reported in the figures are in units of 2π. **c:** Band dispersion relative to the lower band of the ladder Hamiltonian for $\Omega = 2\pi \times 590$ Hz, $t = 2\pi \times 138$ Hz, $\Phi = 1.31\pi$ and $\omega_x = 0$. The color intensity reflects the probability to find a particle in the lower dressed band of the Hamiltonian. The yellow zone denotes the states that contribute with negative chirality to the signal.

parameters of the Hamiltonian to the values adopted in the experiment: $\Omega = 2\pi \times 590$ Hz, $t = 2\pi \times 138$ Hz and $\Phi = 1.31\pi$. As a general rule, we can say that, fixed the number of particles in the wire, the chirality decreases monotonically as the temperature or the trap frequency are increased. The explanation of this behaviour is rather simple: the higher is the temperature, the higher is the probability to occupy wires with many particles. Wires with many particles are characterized by a momentum distribution that completely fills the Brillouin zone and, consequently, can not display chiral behaviour. On the other hand, if the trap frequency is increased, particles will localize at the center of the tube and their eigenstate will spread in momentum space, suppressing the chirality. A less intuitive explanation is needed to understand why the chirality changes sign as the particle number is increased, as it is clearly evident in figures 4.10-a,b. This behaviour is a consequence of the energy dispersion relative to the fundamental band of the ladder Hamiltonian, that for the experimental parameters considered here, displays a net asymmetry with respect to the center of the Brillouin zone, as it is shown in figure 4.10-c. Referring to the figure, fermionic particles will initially occupy the states at lower energy, that are characterized by negative momenta. Only when the states comprised in the yellow band are completely populated, particles will start to occupy states with opposite chirality, reversing the asymmetry of the momentum distribution. As the particle number is further increased the band starts to be completely full and the chirality vanishes again.

In our analysis we evaluated the g leg momentum distribution as a function of the flux for several values of the temperature T and the resulting curves have been compared with the experimental data. We found the best agreement for $T = \hbar 0.6\, t/k_B$ where $t = 2\pi \times 138$ Hz is the tunnelling energy. We note however, that the shape of the curve is robust against the fine tuning of the parameters, as it is fundamentally implied

by the symmetries of the problem. In particular, the inversion of the sign of J above π flux is a direct consequence of the discreteness of the Harper-Hofstadter Hamiltonian.

By removing the optical lattice along $\hat{e}_x$ we can synthesize a two-leg ladder in the continuum, where a unit cell is no longer defined and the symmetries arising from the discreteness of the system no longer hold. The measured values of J for this configuration are reported in 4.9-d as a function of the transferred SOC momentum δk. In this case we do not observe any inversion of J when δk exceeds k_L (corresponding to the π flux condition in figure 4.9-a).

4.3 Tuning the interactions in a $^1S_0 - {}^3P_0$ mixture

The interpretation of the experimental results reported in the previous section relies on single-particle models in which the interparticle interactions have not been taken into account. The interplay between magnetism and interactions is however responsible for many intriguing phenomena, the fractional quantum Hall effect (QHE) being only the most known example. The possibility to tune the interatomic interactions represents consequently a great opportunity to simulate, in the ultracold atoms context, this class of phenomena for which a solid-state implementation is not easily accessible.

In cold-atom physics, magnetic Feshbach resonances (MFR) can be regarded as the fundamental tool that allows the control of the collisional properties of a degenerate gas of atoms making it possible to tune the interactions and to access strongly interacting regimes (Chin et al., 2010). In alkali atoms the MFR mechanism is enabled by the presence of a $J = 1/2$ electronic spin which gives rise to a triplet and a singlet collisional channels in the fundamental atomic state, that are in general coupled by the hyperfine interaction. The Zeeman sensitivity of the energy levels associated to the two channels is in general different and, consequently, a magnetic field can be employed to tune their relative energy, eventually leading to a resonant scattering resonance. The presence of a fully occupied electronic shell prevents this mechanism to work in alkaline-earth and alkaline-earth-like atoms. Interactions can still be tuned exploiting optical Feshbach resonances, but such a scheme suffers from strong atomic loss and heating (Ciurylo et al., 2005; Enomoto et al., 2008; Blatt et al., 2011). In these classes of atoms however, the presence of a long-lived excited electronic state makes it possible to control the atomic collisional properties taking advantage of a recently proposed scheme (Zhang et al., 2015) that predicts the existence of a new class of Feshbach resonances in which the orbital degree of freedom plays the role of the electronic spin in the MFR of alkali atoms. In this section we discuss the experiment which led to the first observation (Pagano et al., 2015) of this new kind of Feshbach resonance, which we will refer to as *orbital Feshbach resonance* (OrbFR). The first part of the section is dedicated to a brief description of the OrbFR mechanism. After this theoretical introduction we will discuss the experimental realization of a strongly interacting gas of ^{173}Yb in which we demonstrated the existence of the predicted OrbFR investigating the hydrodinamic anisotropic expansion of the gas. OrbFR with ^{173}Yb atoms have been investigated also at MPQ in Munich in a closely related work (Höfer et al., 2015) where resonance properties have been characterized using cross-thermalization techniques.

4.3.1 Orbital Feshbach resonance mechanism

In order to understand how the OrbFR arises in alkaline-eart-like atoms we consider two fermionic atoms characterized by different spin ($\uparrow$ and $\downarrow$) and different electronic state ($|^1S_0\rangle = g$ and $|^3P_0\rangle = e$). At large interatomic separation the two atoms do not interact and the eigenstates of the two-particles system are given by

$$|o\rangle = |g\uparrow; e\downarrow\rangle \qquad\qquad |c\rangle = |e\uparrow; g\downarrow\rangle \tag{4.21}$$

which we name *open* and *closed* collisional channel, respectively. This nomenclature, as in a standard MFR, is associated to the asymptotic energy E_c and E_o of the two channels, being always $E_c > E_o$ with $E_c - E_o = \delta_m(B) = |h\,\delta_g \Delta m\, B|$, where Δm is the difference in the nuclear spin projection of the two states, $\delta_g = 113$ Hz/G for ^{173}Yb is the differential Landé factor for the states g and e and B is the external applied magnetic field. As the interparticle distance is reduced, the interaction energy increases and the scattering properties of the two-particles system depends on whether the two atoms interact in a spin triplet or singlet state. In this case, as a consequence of the antisymmetrization requirements of the two-particles fermionic wavefunction, we have that the appropriate basis to describe the scattering between the two particles is given by the states $|eg^{\pm}\rangle = \frac{1}{2}(|eg\rangle \pm |ge\rangle) \otimes (|\uparrow\downarrow\rangle \mp |\downarrow\uparrow\rangle)$ that we have already introduced in section 3.3 and that can be expressed in terms of $|c\rangle$ and $|o\rangle$ as

$$|eg^+\rangle = \frac{1}{\sqrt{2}}(|c\rangle - |o\rangle) \qquad\qquad |eg^-\rangle = \frac{1}{\sqrt{2}}(|c\rangle + |o\rangle). \tag{4.22}$$

The states $|eg^{\pm}\rangle$ define two different molecular potentials to which, in ^{173}Yb, the s-wave scattering lengths $a_{eg^-} = 219.5\,a_0$ (Scazza et al., 2014) and a_{eg^+} (the most recent estimated value of which is $a_{eg^+} = 1878\,a_0$ (Höfer et al., 2015)), are associated. In this basis interactions are well defined by the diagonal operator $V_{int} = \sum_{\alpha=eg^{\pm}} |\alpha\rangle\langle\alpha| V_{HY}(a_\alpha)$, where $V(a_\alpha)$ is the Huang-Yang pseudopotential (Huang and Yang, 1957; Huang, 1967) associated to the scattering length a_α

$$V_{HY}(a_\alpha) = \left(\frac{4\pi\hbar^2}{2\mu} a_\alpha\right) \delta(\mathbf{r}) \frac{\partial}{\partial r}(r\cdot). \tag{4.23}$$

Taking into account the expressions 4.22 and 4.23, and considering the Zeeman shift of the $|c\rangle$ state with respect to $|o\rangle$, the Hamiltonian that describes the two interacting particles in the $\{|c\rangle, |o\rangle\}$ basis reads

$$H = \underbrace{\begin{pmatrix} -\frac{\hbar^2}{2\mu}\nabla^2 + \delta_m(B) & 0 \\ 0 & -\frac{\hbar^2}{2\mu}\nabla^2 \end{pmatrix}}_{\text{free particles Hamiltonian}} + \underbrace{\begin{pmatrix} V_{HY}(a_d) & V_{HY}(a_{ex}) \\ V_{HY}(a_{ex}) & V_{HY}(a_d) \end{pmatrix}}_{\text{interaction Hamiltonian}} \tag{4.24}$$

where $V_{HY}(a_d)$ and $V_{HY}(a_{ex})$ are Huang-Yang potentials associated respectively to the direct scattering length

$$a_d = \frac{a_{eg^+} + a_{eg^-}}{2} \tag{4.25}$$

and to the exchange scattering length

$$a_{ex} = \frac{a_{eg^+} - a_{eg^-}}{2}. \tag{4.26}$$

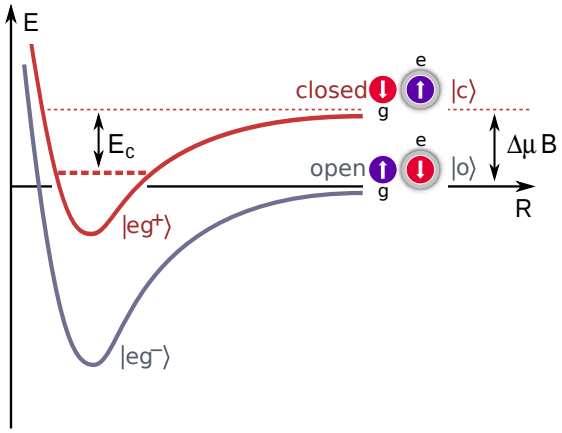

Figure 4.11: Schematic representation of the orbital Feshbach resonance mechanism in ^{173}Yb. See the main text for details.

With the Hamiltonian 4.24 our scattering problem is formally equivalent to the description of a standard two-channel MFR in alkali atoms, as it is pictorially shown in image 4.11: we have two channels whose energy separation can be tuned with an external magnetic field and that are coupled together by an interaction potential that in our case is represented by the *spin-exchange interaction* $|g\uparrow; e\downarrow\rangle \to |g\downarrow; e\uparrow\rangle$. The problem can be solved in the low-energy limit (Cheng et al., 2016) assuming that the scattering energy is much smaller than the interaction energy. In this limit, adopting standard results of the two particles scattering theory (Cohen-Tannoudji and Guéry-Odelin, 2011), and assuming that the open channel is coupled to a bound state in the closed channel, we can write the expression of the wavefunction of the open and closed channels respectively as

$$\psi_o(r) = \frac{(a_o - r)}{r} \qquad \psi_c(r) = C\frac{e^{-\sqrt{m\,\delta_m(B)/\hbar^2}r}}{r} \tag{4.27}$$

where a_o is the scattering length associated to the two-particles interaction. To determine a_o one has to solve the Schroedinger equation in the low-energy limit: $H|\Psi\rangle = 0$ where Ψ is the vector $|\Psi\rangle = \{\psi_c, \psi_o\}$. The equation can be easily solved for the radial part of the two wavefunctions 4.27: $|\Psi_r\rangle = |r\,\Psi\rangle = \{\exp\left(-\sqrt{m\,\delta_m(B)/\hbar^2}r\right),\ a_o - r\}$ as it is shown in appendix B. From the resolution of the Schroedinger equation in radial coordinates we obtain the scattering length

$$a_o = \frac{-a_d + \sqrt{m\,\delta_m(B)/\hbar^2}(a_d^2 - a_{ex}^2)}{a_d\sqrt{m\,\delta_m(B)/\hbar^2} - 1} \tag{4.28}$$

which clearly shows a magnetic-field dependence. The tunability of a_o with the magnetic field is possible only thanks to the spin-exchange interaction which mixes the open and closed channel. In absence of spin exchange $a_{ex} = 0$ and the value of a_o reduces to the constant value $a_o = a_d$. In particular, the scattering length 4.28 shows

a resonant behaviour for the magnetic field value

$$B = \frac{\hbar}{2\pi\, m\, \delta_g\, \Delta m\, a_d^2}. \tag{4.29}$$

Finite-range corrections of the potential can be taken into account by making the substitution $a_d \to (a_d - r_0)$ (Zhang et al., 2015), where $r_0 \simeq 84.8\, a_0$ is the van der Waals length (Zhang et al., 2015).

^{173}Yb is a privileged isotope for the observation of OrbFR since the large value of a_d set the value of the resonance in the range of tens to few hundreds of Gauss, depending on the difference of the spin projections Δm. This behaviour is completely different in other alkaline-earth elements: in ^{87}Sr, for example, the value of a_d is $\sim 100\, a_0$ (Zhang et al., 2014) and magnetic fields of the order of several thousands of Gauss are required to observe the resonance. Another interesting point is the scaling of the resonance position with Δm^{-1}, which is a direct consequence of the SU(N)-invariant behaviour of the interactions in Ytterbium, as we have seen in section 1.1.1.

4.3.2 Experimental realization of a strongly interacting ^{173}Yb gas

In order to realize a strongly interacting gas of ^{173}Yb atoms exploiting the OrbFR phenomenon, we start preparing a spin-balanced SU(2) degenerate mixture by evaporative cooling in the 1064 nm crossed optical dipole trap. We indicate the two nuclear spin projections of the particles in the degenerate gas as $m_\uparrow$ and $m_\downarrow$ with $m_\uparrow > m_\downarrow$. At the end of the evaporation the gas is loaded in a second crossed dipole trap operated at the magic wavelength $\lambda_L = 2\pi/k_L = 759$ nm for which the light shifts of the g and e electronic states are identical. The trap is realized exploiting two orthogonal laser beams, one of which is tightly focused on the atomic sample with a 30 μm waist, resulting in a cigar-shaped trap with frequencies $\{\omega_x, \omega_y, \omega_z\} = 2\pi \times \{13, 188, 138\}$ Hz. About 30×10^4 atoms per spin component with a temperature $T = 0.15\, T_F$ (where T_F is the Fermi temperature) are loaded in the "magic" trap, with a peak density of 2.3×10^{13} cm^{-3} at the center of the trap. The loading of the atoms in the magic trap is followed by an adiabatic turning off of the 1064 nm ODT in such a way that the magic trap remains the only confining potential. At this point, in order to prepare the system in the open channel of the OrbFR, atoms in the $m_\downarrow$ spin state are excited to the e state with a resonant spin-selective 578 nm clock laser pulse. The excitation is performed applying a magnetic field in the range 70 - 150 G in order to separate the two nuclear spin components. Additionally, a deep one-dimensional optical lattice ($s = 30\, E_r$ where $E_r = \hbar^2 k_L^2/2m$) is superimposed to the dipole trap and co-aligned with the clock beam, in order to exploit the Lamb-Dicke regime to transfer the population in the e state without imparting kinetic energy to the atoms. A 0.4 ms clock pulse duration allows us to transfer more than 80% of the atoms in the metastable state $|g\downarrow, e\uparrow\rangle$. Once the system has been initialized in the open channel of the resonance, the 1D optical lattice is turned off with a 100-ms-long adiabatic exponential ramp and the strongly interacting regime is accessed performing a fast 2-ms sweep of the magnetic field from the clock excitation value to the value B_f close to the magnetic field at which the resonance is expected.

At this point, in order to prove the onset of the strongly interacting regime, we suddenly switch off the trap and let the gas expand. The magnetic field is kept on at

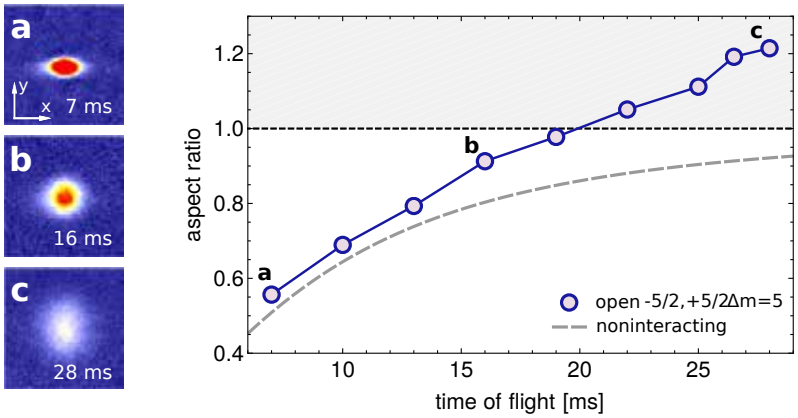

Figure 4.12: Anisotropic expansion of an interacting gas of ^{173}Yb near an orbital Feshbach resonance. The gas is initially prepared in the open channel of a spin mixture with $\Delta m = 5$ at a magnetic field $B_i \simeq 110$ G. The interacting regime is achieved lowering the magnetic field from B_i to $B_f \simeq 41$ G with a 2 ms ramp. The circles show the aspect ratio of the expanded g atomic cloud as a function of the time of flight. The long-dashed grey line shows the behaviour expected for an ideal Fermi gas. The short-dashed black line indicates the unit limit above which the experimental aspect ratio gets inverted because of hydrodynamic expansion. The three images in the insets *a, b, c* show the g cloud after an expansion time of 7, 16 and 28 ms.

the value B_f for the first 5 ms of the expansion, in such a way to let the atoms release their interaction energy into kinetic energy. The whole experimental sequence is summarized in image 4.13-b. We characterize the effect of the interactions by evaluating the aspect ratio of the atomic cloud $A_R = R_y/R_x$, where R_x and R_y are the atomic cloud dimensions obtained as result of a Gaussian fit as a function of the expansion time. Figure 4.12 (circles) reports the evolution of the aspect ratio of a $\Delta_m = 5$ spin mixture at a magnetic field $B_f = 41$ G for expansion times ranging from 6 to 28 ms. For expansion times greater than 18 ms we observe an inversion of A_R with the atomic cloud changing its shape from prolate to oblate. This behaviour clearly deviates from the one expected for a non-interacting gas (grey dashed line in figure 4.12), for which the aspect ratio is expected to approach one for increasing expansion times (Menotti et al., 2002). We interpret this inversion of the aspect ratio as the result of the gas entering in a *hydrodynamic regime* in which the collisional rate γ is larger than the geometric trapping frequency $\bar{\omega} = (\omega_x\,\omega_y\,\omega_z)^{1/3}$, causing a faster expansion along the tightly confined axis of the harmonic trap because of the larger density gradient. The observation of the aspect-ratio inversion is a hallmark of hydrodynamic expansion of the Fermi gas, which occurs in the regime of strong interactions, as observed for alkali fermionic gases close to MFR (O'Hara et al., 2002). We have thus adopted the inversion of the aspect ratio as an indicator of the strength of the interaction in the Fermi gas and used it to characterize the OrbFR. In figure 4.13-a the aspect ratio of a spin mixture with $\Delta_m = 5$ is reported as a function of the final magnetic field value for an expansion time of 28 ms (circles). The experimental data show a clear resonant

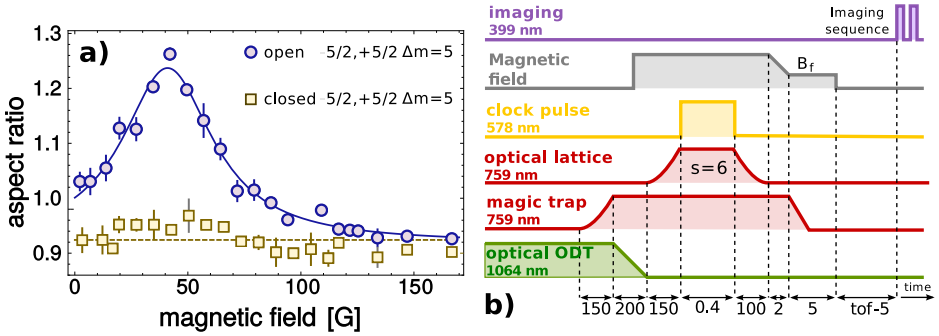

Figure 4.13: **a:** Aspect ratio of the atomic g cloud of a $e-g$ spin mixture with $\Delta m = 5$ after an expansion time of 28 ms as a function of the final value of the magnetic field ramp. The expansion of a gas initially prepared in the open channel of the resonance (circles) is compared with the expansion of a gas initially prepared in the closed channel (squares) for which no resonant behaviour is observed. The solid line is a lorentzian fit of the experimental data. **b:** Experimental sequence employed to realize a strongly interacting gas exploiting an orbital Feshbach resonance and to detect the onset of the strongly interacting regime. The times reported on the horizontal axis are expressed in ms.

behaviour that is a signal of enhancement of the elastic collisional rate at the orbital Feshbach resonance. By performing a Lorentzian fit (solid line in figure 4.13-a) we estimate the maximum to be located at $B = 41 \pm 1$ G. On the contrary, if the same experiment is performed preparing the system in the closed channel, no resonant feature is observable and the aspect ratio always remains slightly less than one for all the experimental accessible value of the magnetic field (yellow squares in figure 4.13-a).

A further validation of our interpretation of the experimental results is provided by another experiment in which we have verified the correct scaling of the resonance position as Δm^{-1}. The data relative to mixtures with $\Delta m = \{2, 3, 4, 5\}$ are reported in figure 4.14-a. Figure 4.14-b reports the same data, where for each mixture the magnetic field has been rescaled by a factor $\Delta m/5$. All the experimental data perfectly collapse on the $\Delta m = 5$ curve, verifying the OrbFR scaling law and evidencing SU(N) symmetry in the interactions of two-electron atoms.

4.4 Conclusions and Outlooks

In this chapter we described the experiments in which, by exploiting the orbital degree of freedom of ^{173}Yb, we have been able to synthesize the emergence of Spin-Orbit Interactions using the $^1S_0$ and $^3P_0$ levels as pseudospin states (Livi et al., 2016), engineer synthetic fermionic two-leg ladders with tunable magnetic fluxes (Livi et al., 2016) and realize a strongly interacting regime in a $^1S_0 - {}^3P_0$ spin-mixture (Pagano et al., 2015). As proposed in (Wall et al., 2016), we have detected the spin-orbit coupling as a broadening in the clock transition spectrum with fiber-link-enhanced clock spectroscopy, exploiting the possibility offered by our narrow clock laser to excite the

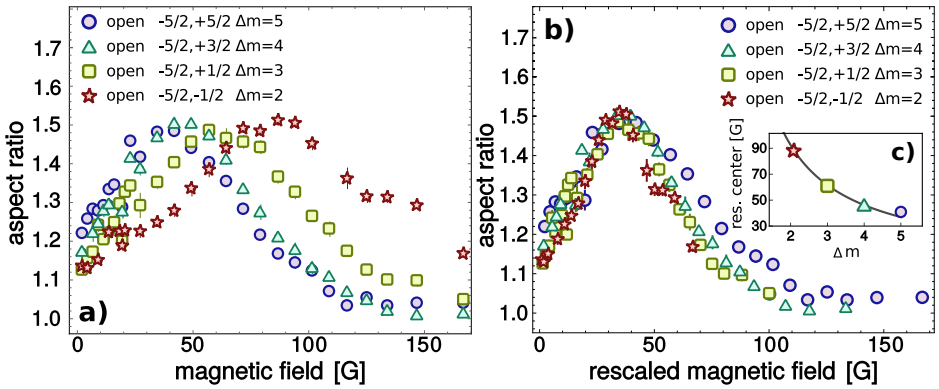

Figure 4.14: Comparison between open-channel mixtures with different Δm, plotted as a function of the real magnetic field (textbf(a) and of a rescaled magnetic field $\bar{B} = B\Delta m/5$ **(b)**. Different colors refer to different spin states, as explained in the legend. The collapse of the four curves onto a single one is a verification of orbital Feshbach resonance scaling low. The inset **(c)** reports the centers of the four resonances as a function of the Δm.

lattice band in an energy-selective way. Following the scheme proposed in reference (Celi et al., 2014), we also mapped the ${}^1S_0$ and ${}^3P_0$ states on an extra dimension and directly measured the emergence of chiral edge currents in an hybrid two-leg ladder, probing them as a function of the artificial magnetic field flux Φ per hybrid plaquette, for fluxes varying in the range $0 \leq \Phi \leq 1.31\pi$. On the other hand, the strongly interacting regime has been achieved exploiting the recently proposed orbital Feshbach resonance scheme and probed observing the hydrodynamic expansion of the gas (Zhang et al., 2015).

The results presented in this chapter pave the way to the realization of many experimental schemes that exploit the metastable $|{}^3P_0\rangle$ state of two-electron atoms. In this prospect ^{173}Yb represents an ideal candidate because, contrary to other commonly used alkaline-earth fermionic atoms (such as ^{87}Sr), this isotope features a remarkably high exchange interaction energy that constitutes a key ingredient for the investigation of many models of quantum magnetism, such as the Kondo lattice model (Gorshkov et al., 2009; Zhang et al., 2016). Exchange interactions, as we have discussed in the previous section, are also at the origin of the orbital Feshbach resonance (OrbFR) phenomenon that we have experimentally characterized. The observation of the OrbFR has triggered many theoretical proposals aimed at the investigation of strongly interacting regimes with two-electron atoms. Among the opportunities offered by this new kind of Feshbach resonance there is the possibility to investigate strongly interacting Fermi superfluids with two-electron atoms (Xu et al., 2016; He et al., 2016) or the two-order BEC-BCS crossover (Zhang et al., 2015). As a matter of fact, a complete experimental investigation of some basic properties of the OrbFR (such as the effective range or and binding energy of two-body bound state), is still lacking, but theoretical schemes to determine these parameters have been proposed (Cheng et al., 2017).

Orbital Feshbach resonances can also be employed in combination with SOC, for

example coupling different electronic and nuclear states with circularly polarized light. This would enable us to control the interactions between the two internal states allowing the investigation of synthetic flux ladders with tunable interleg interactions.

Finally, it is worth to mention a recent theoretical proposal (Iemini et al., 2017) in which SOC is exploited in conjunction with the spin-exchange interaction to realize Majorana quasiparticles as edge modes in one-dimensional cold atom gas.

Chapter 5
Synthetic dimensions with Raman

In chapter 4 we discussed how interpreting the two long lived electronic states of ^{173}Yb as a two-sites synthetic dimension it is possible to realize a hybrid two-leg ladder in which the clock laser coupling between the two atomic levels mimics the tunnelling in a real lattice and imprints on the atoms a phase shift that can be associated to an artificial magnetic flux piercing the ladder. In the present chapter we discuss an alternative approach in which the synthetic dimension is realized exploiting the nuclear spin states of the ground level of ^{173}Yb and the coupling between the synthetic sites is realixed by means of Raman transitions (Mancini et al., 2015). The first section of the chapter is devoted to a theoretical description of this method and, in particular, to the strategy adopted to realize a ladder with a tunable number of legs. Sections 5.2 and 5.3 are instead devoted to the experimental realization of ladders with two and three synthetic sites, respectively. For both the configurations we discuss the onset of chiral currents circulating on the edges of the system as a result of the presence of the Raman-induced artificial gauge field. Some preliminary results regarding the interplay between atom-atom interactions and chiral currents in the two-leg case are presented in section 5.2.2. For the three-leg configuration we also performed experiments aimed at the investigation of the dynamics of the chiral transport along the edges, that we report in section 5.3.2.

The following sections are mainly focused on the experimental results that we obtained in the framework of the synthetic dimension scheme. For an extensive characterization of the Raman setup the reader is referred to the PhD thesis of my former colleague Marco Mancini (Mancini, 2016).

5.1 Nuclear spin states as synthetic dimension of a Hall ribbon

The six nuclear spin states of the fundamental level $|^1S_0\rangle = g$ of ^{173}Yb are an ideal candidate to realize a synthetic dimension within our system, since they are stable states protected by SU(N) symmetry and this implies that spin-changing collisions are forbidden. As we have already discussed in section 2.3.2, the key ingredient that makes it possible to consider this internal state as an extra dimension, is a coherent synthetic coupling that connects the spins, mimicking the effect of the tunnelling in a real lattice. In order to realize this coupling, we exploit a series of two-photons Raman transitions connecting pairs of spin states and exploiting the $|^3P_1\rangle$ manifold as virtual level, as it

Lorenzo Francesco Livi, *New quantum simulations with ultracold Ytterbium gases*, © 2020 Author(s), content CC BY 4.0 International, metadata CC0 1.0 Universal, published by Firenze University Press (www.fupress.com), ISSN 2612-8020 (online), ISBN 978-88-6453-989-8 (online PDF)

is pictorially shown in figure 5.1-a. While the mapping of the synthetic dimension on the two long-lived electronic states of ^{173}Yb allowed only the realization of two-leg ladders (see section 4.2), with the nuclear spin approach we can extend the number of sites up to six, realizing geometries more similar to a real two-dimensional lattice. This extended ladder, which we refer to also as *Hall ribbon*, is naturally pierced by an artificial magnetic field that, as in the case of the clock-laser-induced gauge field, is related to the phase acquired by an atom that moves along the synthetic dimension exchanging photons with the Raman field. Following exactly the same argumentation discussed in sections 2.3.2 and 4.2.1, we can associate this artificial gauge field to a magnetic flux piercing the plaquettes of the hybrid ladder uniformly. In particular, in the present case, the magnetic flux per plaquette is

$$\Phi = 2\pi \times \frac{q_x^R}{2k_L} \tag{5.1}$$

where k_L is the real optical lattice wavevector and q_x^R is the projection of the Raman wavevector on the lattice, that we assume to be oriented along the $\hat{e}_x$ direction. To determine q_x^R we have to consider the geometry of the Raman beams and their orientation with respect to the optical lattice. In our setup, Raman transition are induced exploiting two Raman beams with frequencies ω and $\omega + \delta\omega$ quasiresonant with the $|^3P_1\rangle$ level. The two beams propagate on the same plane as the horizontal lattices and intersect one the other with an angle $\theta = 19°$, as it is shown in figure 5.1-b (see also figure 1.5 for more details). The resulting Raman wavevector is aligned perpendicular to the bisector of the two beams and its value is $q^R = 2k_R \sin(\theta/2)$ where $k_R = 2\pi/\lambda_R$ with $\lambda_R = 556$ nm. As in the experiment discussed in section 4.2, we realize the real dimension of the hybrid ladder confining the atoms in one-dimensional tubes oriented along the direction $\hat{e}_x$. The strong confinement on the directions orthogonal to the tubes is provided by two deep $s = 30$ optical lattices oriented along $\hat{e}_y$ (OL_1 in figure) and $\hat{e}_z$, while along the tubes direction a shallow lattice is present (OL_2 in figure). Considering the angle $\phi = 35°$ between the Raman wavevector and the shallow lattice, we have for the synthetic flux the value

$$\Phi = 2\pi \times \frac{k_R}{k_L} \sin\left(\frac{\theta}{2}\right) \cos(\phi) = 0.37\pi. \tag{5.2}$$

Obviously, it is possible to realize the tubes also along the direction of the lattice OL_1, using the lattice OL_2 to provide the strong confinement along the direction orthogonal to the tubes. This configuration, which results in a flux $\Phi = 0.26\pi$, has not been used in the experiment described in this chapter.

5.1.1 Raman couplings in the fundamental level of ^{173}Yb

Let's now summarize some theoretical fundamental results concerning the Raman couplings of the ground-state nuclear sublevels in ^{173}Yb. In particular, we are interested in the determination of the strengths of these couplings, that are given by the Rabi frequencies $\Omega^R_{m_{g1},m_{g2}}$ relative to the Raman processes connecting the nuclear sublevels m_{g1} and m_{g2}, and on the spin dependent-light shifts V_{m_g} induced by the Raman light. The knowledge of these quantities is fundamental in the prospect to consider the six

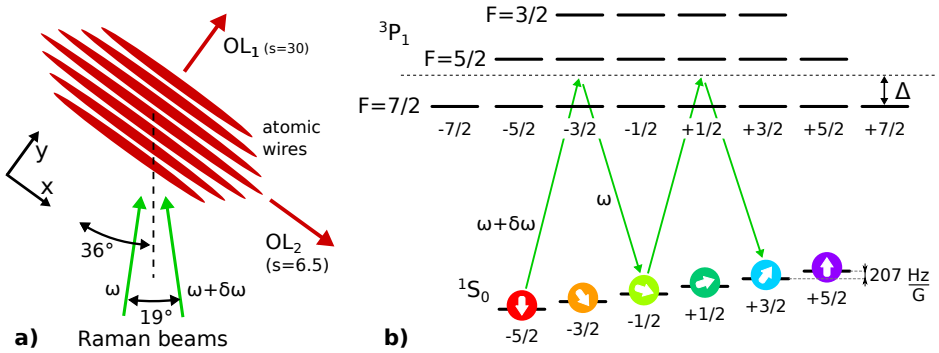

Figure 5.1: **a:** Scheme of the Yb levels involved in the Raman transitions. The value of the Raman detuning is $\Delta = 1.876$ GHz. **b:** Sketch of the experimental setup showing the relative position of the Raman beams with respect to the optical lattices and the one dimensional fermionic tubes.

nuclear sublevels as the lattice sites of an extra dimension, since in this picture the Rabi frequencies describe the strength of the coupling between neighbouring sites, while the light shifts act as an offset of the site energy.

In the following discussion we will consider two Raman beams with frequencies ω and $\omega + \delta\omega$ coupling the nuclear spins m_{g1} and $m_{g2} > m_{g1}$ of the g fundamental manifold of ^{173}Yb. At the first order (excluding the light shifts), the frequency difference $\delta\omega$ is given by the energy splitting between the two spin states. This splitting is provided by the Zeeman shift determined by an external magnetic field B, and for two nuclear spin states of the fundamental level is given by $\delta\omega \simeq 207 \Delta m\, B$ Hz/G where $\Delta m = m_{g2} - m_{g1}$. How large this magnetic field should be will be discussed later.

The Raman transitions exploit a Λ scheme in which the virtual levels belong to the $^3P_1$ fine structure multiplet. The two Raman frequencies are blue-detuned by $\Delta = 1.876$ GHz with respect to the $|^1S_0, F = \frac{5}{2}\rangle \rightarrow |^3P_1, F = \frac{7}{2}\rangle$ transition also used for the MOT. This detuning can be assumed to be the same for both the beams since the difference between the two frequencies $\delta\omega$ is always $\delta\omega \ll \omega, \Delta$. The value of Δ has been chosen in order to maximize the ratio between the Raman coupling and the inelastic scattering rate Γ_{sc} (Mancini, 2016).

Raman couplings strength

In the calculation of the Rabi couplings one has to take into account that the virtual excited state of the Raman transition is composed by the three levels of the $^3P_1$ multiplet characterized by $F_e = \{\frac{3}{2}, \frac{5}{2}, \frac{7}{2}\}$. The Raman process can be divided into two virtual single-photon transitions, one at frequency $\omega + \delta\omega$ connecting the m_{g1} spin state with the $|F_e, m_e\rangle$ state and the other at frequency ω connecting $|F_e, m_e\rangle$ with the m_{g2} nuclear spin of the fundamental level. Using standard results of the Raman theory (Steck,

2007), the overall Rabi frequency associated to the resulting Λ process is given by

$$\Omega^R_{m_{g1},m_{g2}} = \sum_{F_e=\left\{\frac{3}{2},\frac{5}{2},\frac{7}{2}\right\}} \sum_{m_e} \frac{\Omega_1\left(m_{\mathrm{g1}} \to F_e, m_e\right)\Omega_2\left(F_e, m_e \to m_{\mathrm{g2}}\right)}{2\left(\Delta - \delta_{F_e,m_e}(B)\right)} \tag{5.3}$$

where $\delta_{F_e,m_e}(B)$ is the magnetic-field-dependent detuning of the level $|F_e, m_e\rangle$ with respect to the magnetic-unperturbed $F = 7/2$ nuclear manifold and $\Omega_{1,2}$ are the Rabi frequencies associated to the single-photon transitions described above, that we suppose to be driven, respectively, by the higher- and lower-frequency beams. The detuning $\delta_{F_e,m_e}(B)$ depends on the external magnetic field B applied to resolve the nuclear structure of the fundamental state. While for the magnetic field values accessible in the experiment ($B < 200$ G) the Zeeman shift of the nuclear states of the fundamental level manifold is at most of the order of tens of kHz, the magnetic nature of the $|^3P_1\rangle$ state determines shifts up to tens of MHz of the nuclear levels of the $|^3P_1\rangle$ manifold. These shifts are a non-negligible fraction of the Raman detuning Δ and, consequently, have to be taken into account in the determination of the strength of the couplings. If now we suppose that the intensities of the two beams are I_1 and I_2, and assume their polarizations to be, respectively, q_1 and q_2, (where $q_\alpha = 0$ for fully π-polarized light and $q_\alpha = +1/-1$ for fully σ^+/σ^--polarized light), then it is possible to demonstrate that expression 5.3 becomes

$$\Omega^R_{m_{g1},m_{g2}} = \frac{2\sqrt{I_1 I_2}}{\epsilon_0\, c\, \hbar^2}|\langle J_e||d||J_g\rangle|^2 \sum_{F_e=\left\{\frac{3}{2},\frac{5}{2},\frac{7}{2}\right\}} \sum_{m_e} \frac{\mathcal{S}\left(q_1, m_{\mathrm{g1}}, F_e, m_e\right)\mathcal{S}\left(q_2, m_{\mathrm{g2}}, F_e, m_e\right)}{2\left(\Delta - \delta_{F_e,m_e}\right)} \tag{5.4}$$

where $|\langle J_e||d||J_g\rangle|$ is the reduced matrix element of the dipole operator and

$$\mathcal{S}\left(q, m_g, F_e, m_e\right) = (-1)^{F_e+J_g+I}\sqrt{\left(2F_e+1\right)\left(2J_g+1\right)}\underbrace{\begin{Bmatrix} J_g & J_e & 1 \\ F_e & F_g & I \end{Bmatrix}}_{\text{6j symbol}}\underbrace{\langle F_g m_g|F_e m_e; 1q\rangle}_{\text{Clebsh-Gordan}} \tag{5.5}$$

defines the strength of the single-photon transitions, with $F_g = \frac{5}{2}$, $J_g = 0$, $J_e = 1$. A further simplification can be done expressing the reduced matrix element of the dipole operator as a function of the linewidth $\Gamma = 2\pi \times 182$ kHz of the transition (Steck, 2007)

$$\Gamma = \frac{\omega_0^3}{(3\pi c^3 \epsilon_0 \hbar)}\frac{2J_g+1}{2J_e+1}|\langle J_e||d||J_g\rangle|^2, \tag{5.6}$$

where $\omega_0/(2\pi)$ is the $g \to e$ transition frequency. The relation above, inserted in the expression 5.4, gives for the Rabi frequency

$$\Omega^R_{m_{g1},m_{g2}} = \frac{2J_e+1}{2J_g+1}\frac{3\pi c^2\Gamma}{2h\omega_0^3}\sqrt{I_1 I_2} \sum_{F_e=\left\{\frac{3}{2},\frac{5}{2},\frac{7}{2}\right\}} \sum_{m_e} \frac{\mathcal{S}\left(q_1, m_{\mathrm{g1}}, F_e, m_e\right)\mathcal{S}\left(q_2, m_{\mathrm{g2}}, F_e, m_e\right)}{\Delta - \delta_{F_e,m_e}} \tag{5.7}$$

The formula for the Rabi couplings derived above can be simplified if we take into account that, due to the angular momentum conservation rules, a two-photon Raman transition can connect only nuclear spins with $\Delta m = 1$ or $\Delta m = 2$, respectively if a $\sigma - \pi$ or a $\sigma^+ - \sigma^-$ transition is considered.

If we are interested only in the $\sigma^+ - \sigma^-$ case (as in the experiments described in this chapter), in order to prevent spurious $\sigma - \pi$ processes to be resonant as a consequence of an the power broadening of the transition, we apply a strong magnetic field $B \simeq 150$ G that removes the degeneracy among the six spin states of the g manifold, causing a splitting between neighbouring spins $\Delta E_z \simeq 31$ kHz. This splitting is also fundamental to ensure the directionality of the Raman momentum transfer, that is linked to which of the two Raman photons is absorbed or emitted. The fulfillment of this request is necessary in the synthetic dimension picture, since the direction in which momentum is transferred determines the phase associated to the synthetic gauge field induced by the Raman light. As an example, if the two spins connected by the Raman transition are degenerate and the process is driven with two fully σ^+ and σ^- polarized beams, atoms can absorb a photon from the σ^+ beam and re-emit it in the σ^-, gaining momentum in one direction, but can also do the opposite process acquiring in this way momentum in the opposite direction. A magnetic field puts one of the two processes $2\Delta E_z$ out of resonance, making it possible to transfer momentum always in the same direction. The drawback of the application of a magnetic field is that the Clebsh-Gordan-induced asymmetries in the strength of the couplings (apparent already in equation 5.5 and further discussed below) are further enhanced, making it very difficult to connect all the six spins with similar couplings.

Raman-induced light shifts

Also for the determination of the Raman induced light shifts, we have to take into account that the virtual level of the transition is composed by the three levels of the $^3P_1$ multiplet characterized by $F_e = \{\frac{3}{2}, \frac{5}{2}, \frac{7}{2}\}$. In this case the expression of the light shift of the nuclear level m_g of the fundamental state reduces to

$$V_{m_g} = \sum_q \frac{\hbar \Omega_q^2}{4} \left(\sum_{F_e = \left\{\frac{3}{2}, \frac{5}{2}, \frac{7}{2}\right\}} \sum_{m_e} \frac{\left| \mathcal{S}\left(q, m_\mathrm{g}, F_e, m_e\right) \right|^2}{\Delta - \delta_{F_e, m_e}} \right) \tag{5.8}$$

where Ω_q is the Rabi frequency associated to light with polarization q. It is possible again to express the Rabi frequency as a function of the light intensity and of the transition linewidth. With these substitutions the light shift becomes

$$V_{m_g} = \frac{2J_e + 1}{2J_g + 1} \frac{3\pi c^2 \Gamma}{2h\omega_0^3} \sum_q I_q \left(\sum_{F_e = \left\{\frac{3}{2}, \frac{5}{2}, \frac{7}{2}\right\}} \sum_{m_e} \frac{\left| \mathcal{S}\left(q, m_\mathrm{g}, F_e, m_e\right) \right|^2}{\Delta - \delta_{F_e, m_e}} \right) \tag{5.9}$$

where I_q is the total light intensity (considering both the Raman beams) with polarization q.

5.1.2 Two- and three-leg ladders

In the ideal case one expects to have six identical couplings for all the possible $m_g \rightarrow m_{g+1}$ Raman transitions and identical light shifts for all the six spins states, in such a way to perfectly mimic the physics of a real lattice. As we have seen in the previous

section, this is actually a tricky request that is impossible to fulfil (at least with only two Raman beams) because of the spin-dependent Clebsh-Gordan relations that enter the definition of the couplings and of the light shifts. However, these asymmetries can be exploited to couple only a defined subset of the six spins, reducing in this way the number of sites along the synthetic dimension and realizing ladders with a tunable number of legs. Taking advantage of this feature, we have engineered ladders with two and three synthetic sites. The extension of this approach to more than three sites is obviously possible, but experimentally more difficult to implement. Probably the best strategy to couple more than three spins is to use Raman beams with additional frequency sidebands and/or to employ additional detuned beams to tune the light shifts independently from the Raman couplings.

Three-leg ladders

In order to realize a *three-leg ladder* coupling together only three out of the six spin states, we exploit $\sigma^+ - \sigma^-$ transitions that naturally exclude three spins out of the Raman dynamics. This means that, starting from a spin-polarized sample, only the spins belonging to the triplet $\tau_1 = \{-\frac{5}{2}, -\frac{1}{2}, +\frac{3}{2}\}$ or the triplet $\tau_2 = \{-\frac{3}{2}, +\frac{1}{2}, +\frac{5}{2}\}$ will be involved in the Raman dynamics. The experiments described in this chapter always start from a $m_g = -\frac{5}{2}$ spin-polarized gas and, consequently, we can limit our discussion to the states of the triplet τ_1. Considering the basis $\{|-\frac{5}{2}\rangle, |-\frac{1}{2}\rangle, |+\frac{3}{2}\rangle\}$, after adiabatic elimination of the excited states and rotating wave approximations, the Raman dynamics is captured by the Hamiltonian[1]

$$H_R = \hbar \begin{pmatrix} V_1 & \Omega_1^R/2 & 0 \\ \Omega_1^R/2 & V_2 - \delta_R & \Omega_2^R/2 \\ 0 & \Omega_2^R/2 & V_3 - 2\delta_R \end{pmatrix} \tag{5.10}$$

where δ_R is the detuning with respect to the Raman transitions considering only the Zeeman shift and neglecting the light shifts, V_1, V_2 and V_3 are, respectively, the Raman-induced light shifts of the states $m_g = -5/2$, $m_g = -1/2$ and $m_g = +3/2$ while Ω_1^R and Ω_2^R are, respectively, the Rabi frequencies $\Omega^R_{-5/2,-1/2}$ and $\Omega^R_{-1/2,+3/2}$ introduced before.

The three spins considered can be coupled resonantly by taking advantage of the polarization dependence of the Raman-induced light shifts. In particular, if we set a "uniform" linear polarization

$$\hat{\epsilon}_{3L} = \frac{1}{\sqrt{3}}(\hat{\epsilon}_+ + \hat{\epsilon}_- + \hat{\epsilon}_\pi) \tag{5.11}$$

for both beams and choose a detuning $\delta_R = V_2 - V_1$ such that the Raman light is perfectly resonant with the transition $m_{-5/2} \rightarrow m_{-1/2}$, we have that the Hamiltonian 5.10 reduces to

$$H_R = \frac{\hbar\,\Omega_1^R}{2} \begin{pmatrix} 0 & 1 & 0 \\ 1 & 0 & \alpha \\ 0 & \alpha & 2\beta \end{pmatrix} \tag{5.12}$$

[1]Here we are interested in the Raman dynamics and consider only the real part of the Rabi frequencies.

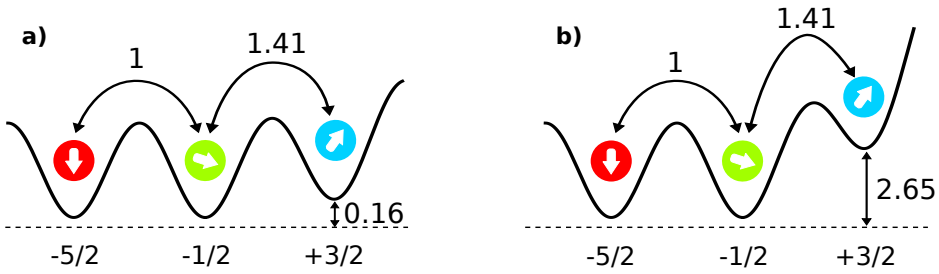

Figure 5.2: Nuclear spin states as lattice sites along a synthetic dimension. Raman coupling strengths (Rabi frequencies) and light shifts for the three spins $m_g = \{-\frac{5}{2}, -\frac{1}{2}, +\frac{3}{2}\}$ involved in the Raman process for **(a)** the three-leg configuration and **(b)** the two-leg configuration. The transition $m_{-5/2} \rightarrow m_{-1/2}$ is supposed to be perfectly resonant with the Raman light. The Rabi frequencies and light shifts are reported in units of $\Omega^R_{-5/2,-1/2}$.

where $\alpha = 1.41$ and $\beta = 0.16$. The low value of β makes reasonably equally coupled all the three spins, since the light shifts are approximately the same for all the states. The drawback of this method is that only 1/3 of the light intensity of each beam is effectively used to couple the spins while the remnant part only induces light shifts. A sketch of the three-leg couplings and light shifts is reported in figure 5.2-a.

Two-leg ladders

To further reduce the dynamics only to two spins, we can again exploit the polarization-dependent light shifts in order to offset the $m = +3/2$ spin state, isolating it from the dynamics. This can be done setting for both the beams the polarization vector

$$\hat{\epsilon}_{2L} = \frac{1}{\sqrt{2}}(\hat{\epsilon}_+ + \hat{\epsilon}_-) \tag{5.13}$$

that is equivalent to have horizontal polarization with respect to the vertical quantization axis defined by the magnetic field. Again, in the condition in which the Raman detuning makes the transition $m_{-5/2} \rightarrow m_{-1/2}$ perfectly resonant, the Hamiltonian 5.10 reduces to the matrix 5.12 with $\alpha = 1.41$ and $\beta = 2.65$, as it is shown in figure 5.2-b. In this case the high value of β causes the spin $m = +\frac{3}{2}$ to be only weakly coupled to the other two spins and, as a matter of fact, this limits the Raman dynamics to the spins $m = -\frac{5}{2}$ and $m = -\frac{1}{2}$.

We have also tried to add a non resonant 1 MHz detuned sideband on one of the two Raman beams, offsetting in this way the third spin by $7\Omega^R_1$. This anyway did not result in a significant change in the Raman dynamics.

Ladder Hamiltonian

After the previous discussion on the Raman couplings Ω^R_α and on the light shifts V_α that govern the dynamics in the synthetic dimension, we can write the overall ladder

Hamiltonian as

$$H_L = \hbar \left(\sum_{j=1}^{N} \sum_{\alpha=1}^{3} \left[-t(\hat{a}^{\dagger}_{j+1,\alpha} \hat{a}_{j,\alpha} + \text{H.c.}) \right] - \sum_{j=1}^{N} \sum_{\alpha=1}^{2} \left[-\frac{\Omega^R_\alpha}{2} e^{i\Phi j} (\hat{a}^{\dagger}_{j,\alpha+1} \hat{a}_{j,\alpha} + \text{H.c.}) \right] + \right.$$
$$\left. + \sum_{j=1}^{N} \sum_{\alpha=1}^{3} \left[V_\alpha + f_x \left(j - \frac{N+1}{2} \right)^2 \right] n_{j,\alpha} \right) \tag{5.14}$$

where N is the number of sites along the real lattice, α and j are integer indexes that identify a position respectively along the synthetic and the real dimensions, t is the optical lattice tunnelling energy, $\hat{a}^{\dagger}_{j,\alpha}$ is the creation operator for a fermion at position $\{j, \alpha\}$ in the hybrid lattice. In the Hamiltonian above we also take into account the effect of the harmonic confinement induced by the transverse lattices with the quadratic term proportional to f_x, which is defined as in equation 4.19.

5.2 Two-leg ladders

5.2.1 Chiral currents

Similarly to the experiment described in section 4.2, also in this case, at equilibrium, despite the presence of only two sites along the synthetic dimension, the two-leg ladder configuration is supposed to support chiral currents that circulate in opposite directions along the edges of the hybrid lattice, as investigated also in bosonic systems (Atala et al., 2014). In order to induce and detect these currents we follow exactly the same procedure described in section 4.2. Since the two experiments are similar the procedure adopted in the present case will be only summarized and the attention will be focused on the differences between the two experimental sequences. The starting point for our experiment is a ^{173}Yb ground-state spin-polarized degenerate Fermi gas in the nuclear-spin level $m_g = -\frac{5}{2}$ characterized by $N_{at} = 1.6 \times 10^4$ atoms at a temperature $T = 0.2\, T_F$ (where T_F is the Fermi temperature). Quantum degeneracy is achieved by forced evaporation in the crossed optical dipole trap at 1064 nm. The atoms are then confined in a three-dimensional cubic optical lattice operated at the wavelength $\lambda_L =$ 759 nm. The lattices are turned on with a 150 ms adiabatic exponential intensity ramp, after which the 1064 nm dipole trap is turned off. The three lattice depths are set to $s_x =$ 6.5 and $s_y = s_z = 30$ (where $E_r = h^2/(2m\lambda_L^2)$ where m is the atomic mass). Along $\hat{e}_y$ and $\hat{e}_z$ the tunneling rates ($t_{y,z}/(2\pi) \simeq 1$ Hz) are negligible on the timescale of the experiment, leading to the realization of an array of ≈ 1000 independent 1D fermionic wires characterized by a longitudinal harmonic confinement with frequency $\omega \simeq 2\pi \times$ 55 Hz. The dynamics is allowed only in the shallow lattice along direction $\hat{e}_x$ where $t/(2\pi) \simeq 90$ Hz. At this point, in order to load the fundamental dressed state of the ladder Hamiltonian 5.14, the magnetic field is set to 152 G and the Raman coupling is turned on with an initial detuning $\delta_{in} \simeq 25\, \Omega_1^R$. The detuning is subsequently reduced performing a frequency sweep characterized by the analytical form 4.13. The detuning at the end of the sweep is set to be $\delta_f = V_2 - V_1$ in such a way to be in resonance with the Raman process connecting the spins $m_g = -\frac{5}{2}$ and $m_g = -\frac{1}{2}$. The duration of the sweep is tuned between 20 and 80 ms accordingly to the Rabi frequency Ω_1^R.

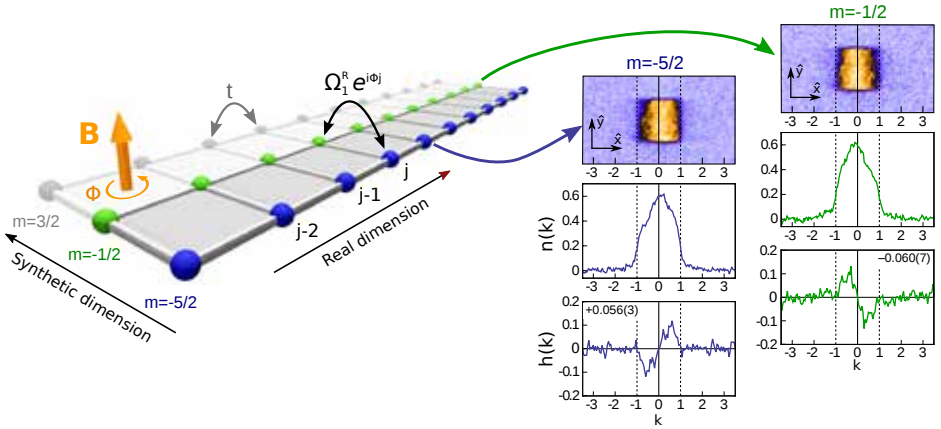

Figure 5.3: Chiral dynamics on a two-leg ladder. On the left we report a pictorial representation of the hybrid ladder in which the third spin ($m_g = +\frac{3}{2}$) is put out of resonance exploiting the polarization dependence of the light shifts, excluding it from the dynamics (see the main text for details). The panels on the right show on the top the time-of-flight images (averaged over ~ 30 realizations) of the momentum distributions relative to the legs $m_g = -\frac{1}{2}$ and $m_g = -\frac{5}{2}$. From the time-of-flight images we extract the integrated momentum distribution $n(k)$ along $\hat{e}_x$ (middle) from which we evaluate the asymmetry function $h(k) = n(k) - n(-k)$ (bottom). The experimental parameters are $\Omega_1^R = 2\pi \times 489$ Hz, $t = 2\pi \times 134$ Hz and $\Phi = 0.37\pi$.

Once the dresses state is loaded, the coupling along the synthetic dimension is suddenly switched off and the momentum distribution of the atoms is detected exploiting the band mapping technique described in section 1.3. Differently from to the analogous experiment performed exploiting the ${}^1S_0 - {}^3P_0$ electronic states as synthetic dimension, in this case the standard ${}^1S_0$ imaging procedure cannot be directly exploited to resolve the single legs of the ladder, due to the excessive linewidth of the transition $|{}^1S_0\rangle \rightarrow |{}^1P_1\rangle$, which is not spin-selective, at least at the magnetic fields accessible in the laboratory. In order to perform a single-site imaging along the synthetic dimension, we use a sequence of spin-selective laser pulses ("blast" pulses), in resonance with different components of the narrow intercombination transition $|{}^1S_0\rangle \rightarrow |{}^3P_1, F = 7/2\rangle$, to remove atoms in all the spin states but one. The sequence is carried out during the first 2.5 ms of ballistic expansion, after the band mapping. At this time the (real) magnetic field is $B_{blast} = 15$ G, leading to a Zeeman shift $\Delta E_z \simeq 50\Gamma/(2\pi)$ between adjacent spin components in the ${}^3P_1$ manifold (where $\Gamma = 2\pi \times 182$ kHz is the natural linewidth of the transition). This separation allows us to use two opportunely detuned σ^+/σ^- beams to remove the unwanted spin population, without causing any heating to the selected spin state left in the expanding cloud (see (Mancini, 2016) fore more details). After ballistic expansion, absorption imaging is performed on the dipole-allowed $|{}^1S_0\rangle \rightarrow |{}^1P_1\rangle$ transition. The asymmetries associated to the momentum distributions are then evaluated with the expression 4.15 obtaining the value J_α that characterizes the strength of the current carried by the leg α. Figure 5.3 reports an example of this kind of measurements for the experimental values $\Omega_1^R = 2\pi \times 489$

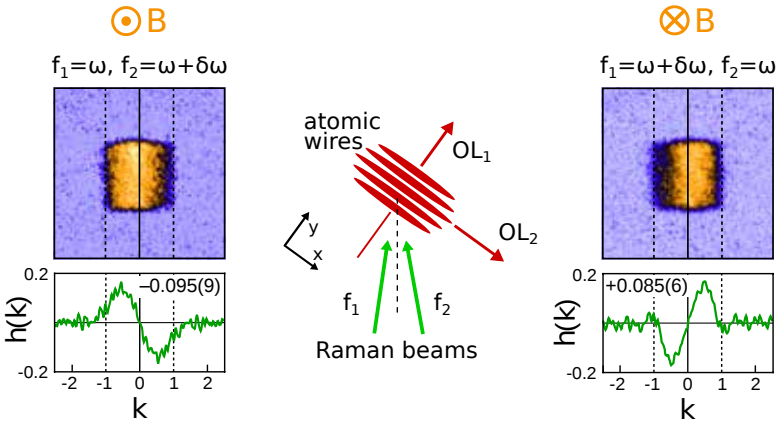

Figure 5.4: Time-of-flight images of the momentum distribution $n(k)$ and asymmetry function $h(k) = n(k) - n(-k)$ of the $-\frac{1}{2}$ spin state in the two-leg ladder configuration for opposite values of the effective magnetic field. The sign of the magnetic field is changed swapping the frequency of the two Raman beams. Experimental parameters adopted in the experiment: $\Omega_1^R = 2\pi \times 394$ Hz, $t = 2\pi \times 87$ Hz and $\Phi = \pm 0.37\pi$.

Hz, $t = 2\pi \times 134$ Hz and $\Phi = 0.37\pi$. The values of J calculated for the two legs are in this case $J_{-5/2} = +0.056(3)$ and $J_{-1/2} = -0.060(7)$. These values are approximately equal in intensity and opposite in sign, providing direct evidence for presence of chirality in the system.

The Raman approach to the realization of an artificial gauge field allows us to easily change the sign of the flux by simply swapping the frequencies of the two beams. In figure 5.4 we report the momentum distribution relative to the spin leg $m_g = -\frac{1}{2}$ for the two values of the synthetic flux $\Phi = \pm 0.37\pi$ and experimental parameters $\Omega_1^R = 2\pi \times 394$ Hz and $t = 2\pi \times 87$ Hz. The sign of the current inverts accordingly to the inversion of the flux, providing a further validation of the interpretation of our experimental data.

5.2.2 Interactions-induced effects on the chiral currents

Here we present some preliminary result related to the experimental investigation of how the chiral currents described in the previous section are affected by repulsive atom-atom interactions. These experiments are aimed at providing a groundwork for the simulation of phenomena in which the effects induced by magnetic fields and interactions on a fermionic gas are strongly intertwined, as it happens in the Fractional Quantum Hall Effect (Barbarino et al., 2015). In this prospect the role of interactions is also debated for the realization of robust quantum information protocols (Nayak et al., 2008) and for its implication in the definition of topological states of matter. For instance, in the presence of SOC, interactions are expected to give rise to fractional quantum spin Hall states in which the edge currents are spin-polarized (Galitski and Spielman, 2013). Alkaline-earth and alkaline-earth-like elements are particularly promising candidates for this kind of experiments as they offer the possibility to en-

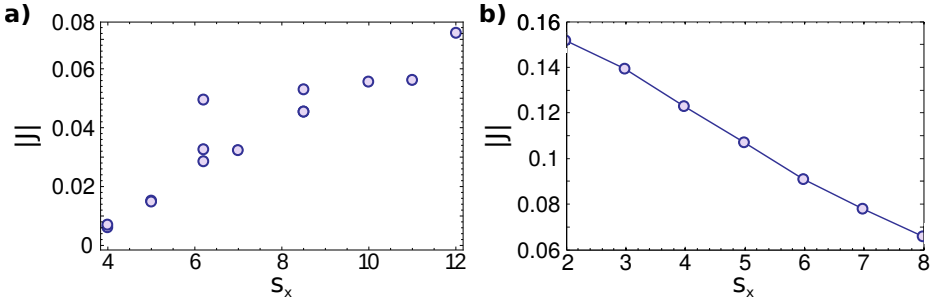

Figure 5.5: Chiral currents dependence on the lattice depth s_x for the experimental parameters $\Omega_1^R/t = 3.7$, $f_x = 2\pi \times 55$ Hz. The theoretical prediction based on DMRG simulation performed by the group of R. Fazio in Pisa (**b**) is compared with the experimental data (**a**).

hance the spectrum of accessible phenomena exploiting their SU(N) symmetry, in a configuration that is not accessible in solid-state systems. For instance, in the synthetic dimension picture, atom-atom interactions will exhibit an effective long-range character along the synthetic dimension, with atoms interacting with the same strength independently from the "distance" between their spin states. Interaction effects in our particular ladder system have been extensively studied, and theoretical schemes aimed at the investigation of the formation of helical liquids (Barbarino et al., 2015), fractional charge-pumping (Taddia et al., 2017) and Laughlin-like states in bosonic and fermionic ladders (Calvanese Strinati et al., 2017) have been proposed.

Our experiment is based on the scheme proposed in reference (Barbarino et al., 2016) by the group of R. Fazio at Scuola Normale Superiore in Pisa, in which the authors analyze, by means of DMRG simulations, the effect played by repulsive interactions on the onset of chiral currents in a hybrid two- and three-leg Hall ribbon, akin to the one described in this chapter. The general result showed in the reference is that repulsive interactions are expected to significantly enhance the chiral currents for the filling factors considered in our experiments (i.e. less than one atom per lattice site and negligible population in the higher dressed band). Note, however, that in the reference introduced above the influence of a harmonic trapping confinement and finite-temperature effects are not taken into account.

Since the fundamental level of ^{173}Yb is a non-magnetic state ($J = 0$), we cannot take advantage of a Feshbach resonance to tune the interactions. As a matter of fact, the only method we can adopt to change the lattice on-site interaction energy U_{int}, is to tune the 3D lattice depth s_α (with $\alpha = \{x, y, z\}$), which in the tight-binding regime is related to U_{int} by the relation

$$U_{int}(s_x, s_y, s_z) = \left[U_{int}(s_x)\, U_{int}(s_y)\, U_{int}(s_z)\right]^{1/3} \tag{5.15}$$

where

$$U_{int}(s_\alpha) = \frac{4\pi a_s\, \hbar^2}{m} \int w(\mathbf{r}, s_\alpha)^4\, \mathrm{d}^3\mathbf{r} \tag{5.16}$$

in which $a_s = 200\, a_0$ (Kitagawa et al., 2008) is the scattering length associated to scattering processes in the fundamental state of ^{173}Yb and $w(\mathbf{r}, s_\alpha)$ are the three-

dimensional lattice Wannier functions. Changing U_{int} by changing the lattice depth, however, inevitably affects other parameters of the ladder Hamiltonian. In particular, if the lattice depth s_x along the direction of the tubes is changed, also the tunnelling parameter t changes, while if we modify the transverse lattice depths s_y and s_z, this affects the harmonic trap frequency f_x. This issue can be overcome by taking into account that, neglecting the interactions, the physics described by the Hamiltonian 5.14 (and in particular the strength of the chiral currents) is invariant as long as the ratios Ω_1^R/t and f_x/t are kept constant. Similarly, we expect that the effect of interactions should depend on the parameter U_{int}/t. Keeping in mind these constraints, there are two strategies that can be followed in order to change only the parameter U_{int}/t and, thus, to observe a pure interactions-induced effect in our system: the first is to modify the transverse confinements s_y and s_z compensating the resulting alteration in f_x by changing t and Ω_1^R, the other is to modify s_x compensating the alteration in t by changing the Rabi couplings and the harmonic frequency. We decided to adopt the second strategy for two reasons: the first is that we cannot reduce the transverse depths $s_{y,z}$ too much and still remain in the regime for which we can consider the atoms confined in one-dimensional wires. The second reason is that, for the experimentally accessible values of $s_{y,z}$ for which we are in the atomic wires regime (we consider $20 < s_{y,z} < 30$), for a reasonable tunnelling strength along $\hat{e}_x$ (let's say $s_x = 5 \rightarrow t = 2\pi \times 131$ Hz) the values of U_{int}/t that we can explore are limited to $10.9 < U_{int}/t < 13.7$ only. On the other hand, keeping $s_y = s_z = 30$ constant, and changing t and Ω_1^R, we can tune s_x in the range $3 < s_x < 12$ exploring values of U_{int}/t that cover over an order of magnitude. A similar strategy was employed in the first experiments investigating the superfluid to Mott-insulator transition in ultracold lattice bosons (Greiner et al., 2002), where the different interactions regimes were studied by changing the optical lattice depth.

We have thus decided to tune the effective atom-atom interactions changing s_x. As we have discussed above, this implies that also Ω_1^R has to be modified in order to keep constant Ω_1^R/t. Keeping a constant value also for f_x/t is however more difficult. For example, if s_x is lowered in order to decrease U_{int}, t increases. In order not to affect the ratio f_x/t, f_x has consequently to be increased, but the only way to do this is by increasing the transverse confinement $s_{y,z}$, that in turn results in an increasing of U_{int}, vanishing in this way the original purpose. For this reason we kept constant only Ω_1^R/t, maintaining the same trap frequency for all the explored values of t.

Figure 5.5-a reports the strength of the chiral current J measured on the $m_g = -\frac{1}{2}$ leg of a two-leg ladder for s_x spanning from 4 to 12 (which means 24 Hz $< t/(2\pi) <$ 170 Hz) and $s_y = s_z = 30$ (which imply $6.8 < U_{int}/t < 98$ and $f_x = 2\pi \times 55$ Hz). Keeping constant $\Omega_1^R/t \simeq 4$ we observe a clear enhancement of the chiral currents for increasing values of s. This behaviour is opposite to the one predicted by our colleagues in Pisa, which, by means of DMRG simulations in the same experimental conditions, observe a suppression of the currents for increasing s, as it is shown in figure 5.5-b. It should be observed that the suppression of the current predicted by the DMRG model is an effect induced by the constant trap frequency (f_x/t increases for increasing s_x and, as we have seen in section 4.2.1, this determines a reduction of the chirality) while in absence of the trap the interactions are supposed to enhance the currents (Barbarino et al., 2016).

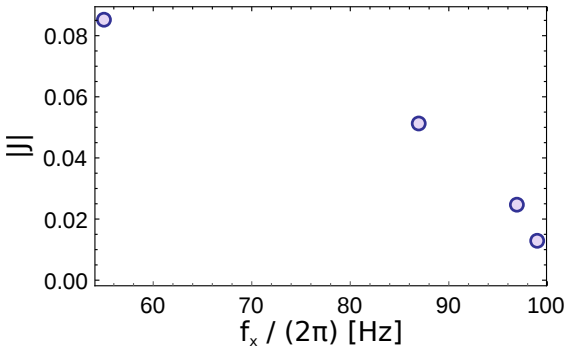

Figure 5.6: Chiral currents dependence on the trap frequency f_x for the experimental parameters $t = 2\pi \times 30$ Hz and $\Omega_1^R/t = 3.7$.

However, we exclude that the monotonically increasing behaviour of the current experimentally observed is determined by an effect induced purely by the trap. This affirmation is motivated by a second experiment in which we change only the ratio f_x/t, leaving the other parameters of the Hamiltonian (t, Ω_1^R and U_{int}) constant. To do this, we do not completely turn off the 1064 nm optical dipole trap at the end of the evaporative cooling, summing in this way its harmonic contribution to the one of the confinement lattices. The results of this measurement are reported in figure 5.6 for the experimental values $t = 2\pi \times 30$ Hz and $\Omega_1^R/t = 3.7$, and explore the range $1.93 < f_x/t < 2.42$. As expected, we observe a clear suppression of the chirality for increasing f_x/t, which induces us to suppose that the effect observed in figure 5.5-a is due to interactions or, at least, due to a combination of interactions and confinement. To shed light on these ambiguities we also measured the lifetime of the chiral currents in the two tunnelling configurations $t_1 = 2\pi \times 101$ Hz and $t_2 = 2\pi \times 30$ Hz keeping in both cases $\Omega_1^R/t = 3.7$ and $f_x = 2\pi \times 55$ Hz. We observe for the first case a lifetime $\tau_1 = (17 \pm 6)$ ms while for the other case we measure $\tau_2 = (65 \pm 8)$ ms. This seems to suggest that also the lifetime is related to the tunnelling strength or to the Rabi frequency. As the lifetime gets comparable with the time needed to prepare the initial state, we could attribute the small value of the currents at low s_x to a decay that starts already during the dressed-state preparation. Further experimental work has to be carried out in order to understand what is the limiting factor to the current lifetime (we exclude heating by the Raman beams, as the calculated single-photon scattering rate is significantly smaller than the inverse of the experimental timescale (Mancini, 2016)). Another possibility to explain the discrepancy observed between theory and experimental data, is that the temperature of the system T could depend on t and that in particular T could be higher for shallower lattice. Simulations that take in account also the temperature of the system are however needed to confirm this hypothesis.

The measurements presented in this section are very preliminary and further experimental and theoretical investigations are necessary to determine if the unexpected behaviour that we observe is due to technical issues or to some underlying physics that we are not considering. The limitations of this scheme, in which we can not tune the interactions strength directly without affecting other parameters of the Hamiltonian, are

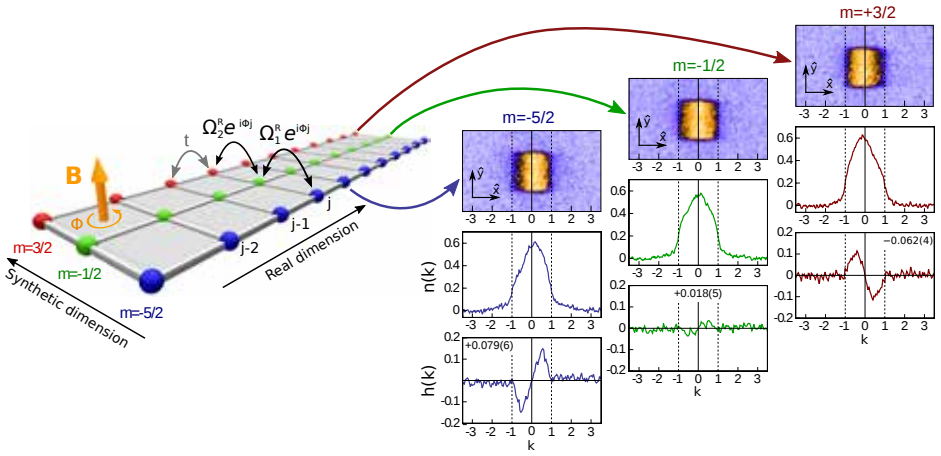

Figure 5.7: Chiral dynamics on a three-leg ladder. On the left we report a pictorial representation of the hybrid ladder. The panels on the right show on the top the time-of-flight images (averaged over ~ 30 realizations) of the momentum distributions relative to the legs $m_g = -\frac{5}{2}$, $m_g = -\frac{1}{2}$ and $m_g = +\frac{3}{2}$. From the time of flight images we extract the integrated momentum distribution $n(k)$ along $\hat{e}_x$ (middle) from which we evaluate the asymmetry function $h(k) = n(k) - n(-k)$ (bottom). The experimental parameters are $\Omega_1^R = 2\pi \times 620$ Hz, $t = 2\pi \times 94$ Hz and $\Phi = 0.37\pi$.

however evident and suggest to take in account other schemes, based, for example, on a pure tuning of the interactions exploiting the orbital Feshbach resonance introduced in section 4.3.

5.3 Three-leg ladders

5.3.1 Chiral currents

We performed also in the three-leg ladder configuration the experiment described in section 5.2.1, again detecting the chiral currents propagating on the edges of our hybrid lattice. A three-leg ladder represents the minimal configuration in which it is possible to investigate both the behaviour of the edges and of the "bulk" of the system, despite the latter being composed only by one site along the synthetic dimension. The experimental sequence adopted for this experiment is the same employed in the two-leg case. Figure 5.7 reports the momentum distributions of the three spin states involved in the dynamics after the loading of the lower dressed band of the Hamiltonian for the experimental parameters $\Omega_1^R = 2\pi \times 620$ Hz, $t = 2\pi \times 94$ Hz and $\Phi = 0.37\pi$. As expected for a larger 2D lattice in the Hall regime, we observe two non-zero chiral currents propagating along the two edges of our ribbon ($J_{-5/2} = +0.079(6)$ and $J_{+3/2} = -0.062(4)$) while the current carried by the central leg is roughly vanishing ($J_{-1/2} = +0.018(5)$). This behavior is akin to what is expected for a fermionic system described by the Harper-Hofstadter Hamiltonian. Bulk states exhibit only local circulations of current, which average to zero when all the different states enclosed by

the Fermi surface are considered. Only the edges of the system experience a nonzero current, because there the chiral nature of the states prevents this effect from occurring.

5.3.2 Skipping orbits

The presence of a bulk has allowed the realization of a quench experiment in which we investigated the properties of chiral transport along the edges. We started again from a spin-polarized sample in the $m_g = -\frac{5}{2}$ spin state (that corresponds to one of the two edge legs of the hybrid lattice) trapped in one-dimensional wires. Differently from the previous experiments, where the system was prepared adiabatically with a slow ramp of the Raman parameters, here the Raman couplings were suddenly switched on resonance, activating the complex tunnelling along the synthetic dimension. At this point we performed two different measurements: in the first we measured by optical Stern Gerlach detection (see section 1.2.4) the time dependence of the average magnetization:

$$\langle m(\tau)\rangle = -\frac{5}{2}\mathcal{P}_{-5/2}(\tau) - \frac{1}{2}\mathcal{P}_{-1/2}(\tau) + \frac{3}{2}\mathcal{P}_{+3/2}(\tau) \tag{5.17}$$

where $\mathcal{P}_\alpha(\tau)$ is the population of the spin-state α after a time τ. Figure 5.8-a reports the result of this measurement for the experimental parameters $\Omega_1^R = 2\pi\times 490$ Hz, $t = 2\pi\times 94$ Hz and $\Phi = 0.37\pi$. In the second measurement, instead, we studied the evolution of the momentum distribution $n(k,\tau)$ along $\hat{e}_x$ as a function of time. The Raman couplings induce synthetic SOC, which in turn determines an oscillating evolution of the average center of the momentum distribution, as it is possible to observe in figure 5.8-b. These data can be used to determine the evolution of the mean position $\langle x(\tau)\rangle$ considering along $\hat{e}_x$ the band dispersion $\varepsilon(k) = 2t[1-\cos(kd)]$ where d is the lattice spacing. Assuming the validity of the semiclassical equation of motion (Ashcroft and Mermin, 1976), starting from the lattice band dispersion we can compute the average velocity of the whole atomic cloud

$$\langle v(\tau)\rangle = \frac{1}{\hbar}\int_{BZ} n(k,\tau)\left.\frac{\mathrm{d}\epsilon(k')}{\mathrm{d}k'}\right|_{k'=k}\mathrm{d}k = \frac{2td}{\hbar}\int_{BZ} n(k,\tau)\sin(kd)\,\mathrm{d}k \tag{5.18}$$

where the integral domain is the whole Brillouin zone. Once $\langle v(\tau)\rangle$ is known, the average position is obtained simply integrating the velocity

$$\langle x(\tau)\rangle = \int_0^\tau \langle v(\tau')\rangle\,\mathrm{d}\tau'. \tag{5.19}$$

We combined the experimental data relative to the average magnetization with the average position in the real lattice determined with the relations 5.18 and 5.19 starting from the measured momentum distributions $n(k,\tau)$. By combining the two datasets, we eliminate the time dependence and obtain the dynamics in the position-magnetization plane. The resulting curve, reported in figure 5.8-c, shows a clear chiral behaviour that is analogous to the skipping orbits truncated by the presence of the edges, executed by an electron gas subjected to a magnetic field in a Hall bar, that we have introduced in section 2.1. The experimental data are in good agreement with the theoretical prediction (solid curve in figure 5.8-c) calculated by our colleagues Marcello Dalmonte, Marie Rider and Peter Zoller at IQOQI in Innsbruck. In particular, the theoretical curve

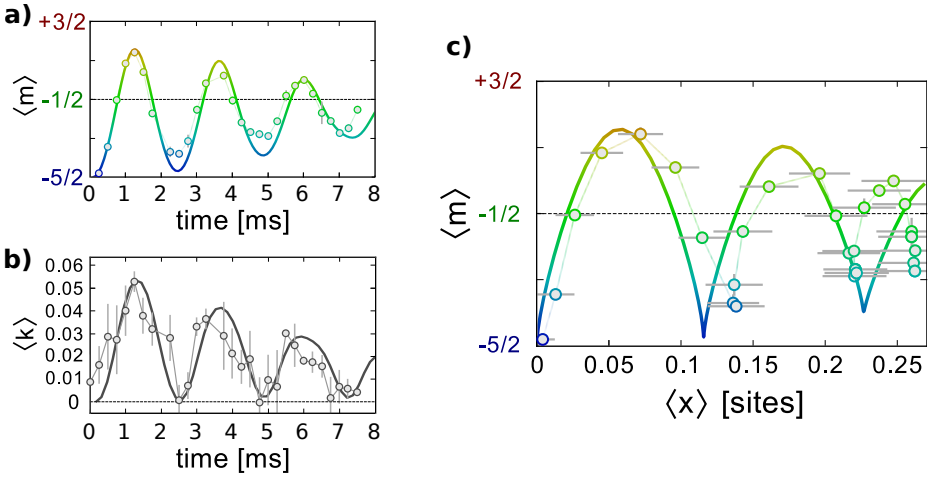

Figure 5.8: Edge cyclotron orbits. **a:** Time dependence of the average position $\langle m \rangle$ in the synthetic direction after a quench on the synthetic tunneling. **b:** time dependence of the average lattice momentum $\langle k \rangle$ along the $\hat{e}_x$ direction. **c:** Average position in $m - x$ space evidencing the skipping-obit-like dynamics. The experimental error increases monotonically with x as a consequence of the time integration 5.19. The solid curve is the theoretical prediction elaborated by our colleagues in Innsbruck. The mismatch between theory and experiment could possibly be ascribed to an accumulation of integration error in the data analysis, which amplifies the effects of the assumptions in the model (such as not accounting for interactions). The experimental parameters employed for this experiment are: $\Omega_1^R = 2\pi \times 490$ Hz, $t = 2\pi \times 94$ Hz and $\Phi = 0.37\pi$.

is able to capture the damping of the oscillation, that can be attributed to a dephasing effect induced by the fermionic nature of the gas and by the presence of wires with different densities inside the sample.

5.4 Conclusions and outlooks

In the present chapter we demonstrated how exploiting the synthetic-dimension scheme proposed in (Celi et al., 2014), we have been able to realize two- and three-leg hybrid ladders in which the nuclear spins of the fundamental level of ^{173}Yb play the role of an extra dimension (Mancini et al., 2015). An artificial magnetic field orthogonal to the ladder is naturally induced as a consequence of the Raman couplings connecting the spins, and realizes, in the present case, a magnetic flux $\Phi = 0.37\pi$ per hybrid plaquette. The chiral behaviour of the edge states have been investigated both observing edge currents and inducing a skipping-orbit-like dynamics in a quench experiment. Finally, following the theoretical predictions of reference (Barbarino et al., 2016), we also executed a series of groundwork measurements aimed at the investigation of the role played by interactions in the onset of chirality.

The Raman approach to the realization of hybrid lattices makes it possible to extend the synthetic dimension up to six sites when ^{173}Yb atoms are considered, thus

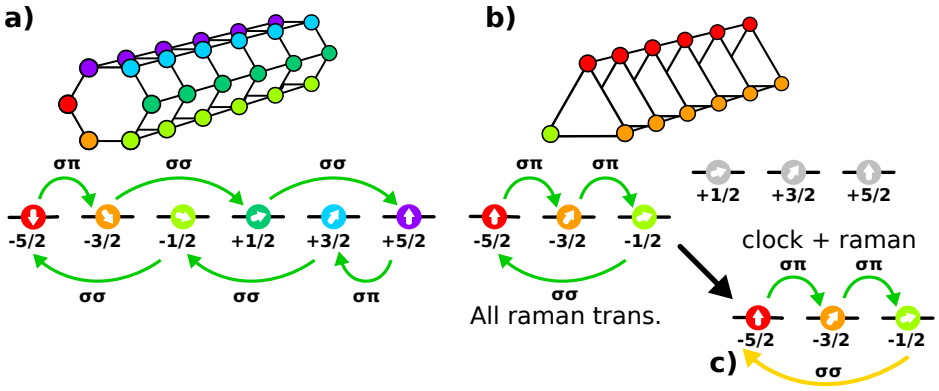

Figure 5.9: Periodic boundary conditions (PBC) in the synthetic dimension realized **(a)** coupling all the six spin states with Raman transitions or **(b-c)** coupling only three out of the six spin states while the others are put out of resonance. In **(c)** $\sigma\sigma$ clock laser coupling (yellow line) is used in combination with the conventional Raman $\sigma\pi$ couplings (solid lines) to realize PBC.

allowing the investigation of both edge and bulk topological matter. It would be interesting to exploit the flexibility offered by this scheme to engineer periodic boundary conditions (PBC) along the synthetic dimension, which would enable several interesting experiments starting from the observation of the bulk Hofstadter fractal spectrum. PBC can be engineered with several schemes, involving all or a reduced subset of the six spins, as respectively sketched in figure 5.9-a and 5.9-b. We can also imagine to realize PBC combining the Raman and the clock-transition scheme described in section 4.2.1, as it is shown in figure 5.9-c. PBC would enable to realize the Laughlin pump (Laughlin, 1981), to measure the quantization of the Hall conductivity and extract the corresponding Chern numbers. If combined with interactions, PBC would also enable the observation of exotic phases of matter (Barbarino et al., 2015).

Topological quantities can actually be derived also for reduced geometries, as proposed in reference (Mugel et al., 2017), where the Chern number of the fundamental and excited bands of a Hofstadter strip is derived inducing Bloch oscillations on the long dimension of a spin ladder.

With an appropriate engineering of the complex and real couplings, it would also be possible to realize exotic geometries (Suszalski and Zakrzewski, 2016), such as thoroidal systems or Moebius strips (Boada et al., 2015). Remarkably, if a spin-dependent real lattice is considered, in which different spins are trapped at different positions, also zig-zag geometries are possible (Anisimovas et al., 2016), in which the synthetic tunneling is accompained by a spatial displacement of the atoms.

Chapter 6
Clock transition spectroscopy on ^{174}Yb

In this chapter we report on some very recent results (Franchi et al., 2017) related to high-resolution clock spectroscopy of ^{174}Yb bosons trapped in the lowest band of a 3D optical lattice in a Mott insulator regime. In particular, we show that addressing the clock transition $|^1S_0\rangle = g \rightarrow |^3P_0\rangle = e$ we have been able to resolve the site occupancy of the insulator state. This approach to the investigation of the Mott insulator regime is similar to those reported in references (Campbell et al., 2006; Kato et al., 2016) where different radiofrequency or optical transitions are exploited. We use the spectroscopic information to determine scattering lengths and loss rate coefficients for collisions involving atoms in the e state, that were previously unknown, differently from fermionic case (Cappellini et al., 2014; Scazza et al., 2014; Ludlow et al., 2011). The knowledge of the scattering properties involving atoms in the e state is fundamental for all the applications relying on the manipulation of atoms in the metastable state that spans from quantum simulation (Gorshkov et al., 2009) to quantum information (Daley et al., 2008). A related series of measurements performed by Yb BEC group at LKB (Bouganne et al., 2017) validates our experimental results.

The chapter is organized as follows: after a first introductive section in which the physical mechanism that enables the excitation of the clock transition in ^{174}Yb is explained, in section 6.2 we discuss the strategy employed to perform high-resolution spectroscopy. Section 6.3 is instead devoted to a description of the measurements employed to determine the scattering lengths a_{ge} and a_{ee} which characterize the s-wave collisions, respectively, between one atom in the g and one atom in the e state or two atoms in the e state. Our spectroscopic investigation terminates with section 6.4, in which we present some preliminary results regarding the excitation of atoms in higher lattice bands. The possibility to coherently excite the clock transition, a fundamental requirement in many quantum simulation schemes, is instead discussed in section 6.5. Finally, in section 6.6 we present the measurement of the loss rate coefficients relative to the $e-g$ and $e-e$ interaction channels.

6.1 Magnetic-field-induced spectroscopy

Due to the absence of a nuclear spin, the excitation of the $|^1S_0\rangle \rightarrow |^3P_0\rangle$ clock transition through the hyperfine mixing mechanism described in section 3.1 is forbidden for the ytterbium bosonic isotopes. For these isotopes the direct excitation of the clock

Lorenzo Francesco Livi, *New quantum simulations with ultracold Ytterbium gases*, © 2020 Author(s), content CC BY 4.0 International, metadata CC0 1.0 Universal, published by Firenze University Press (www.fupress.com), ISSN 2612-8020 (online), ISBN 978-88-6453-989-8 (online PDF)

transition is enabled by a different mixing scheme which exploits the presence of a static external magnetic field to couple the $|^3P_0\rangle$ state with the $|^3P_1\rangle$ (Taichenachev and Yudin, 2006; Ovsyannikov and Chaplygin, 2001; Barber et al., 2006) [1]. As a result of this coupling, excitation of the atoms to the $|^3P_0\rangle$ state becomes possible thanks to the weak allowed intercombination transition $|^1S_0\rangle \rightarrow |^3P_1\rangle$. To understand how this magnetic-field-induced spectroscopy works, let's consider the Hamiltonian describing the interaction of a static magnetic field with one atom, which is given by

$$H_B = \boldsymbol{\mu} \cdot \mathbf{B} \tag{6.1}$$

where $\mathbf{B}$ is the magnetic field and $\boldsymbol{\mu}$ is the atomic magnetic dipole operator. For a magnetic field aligned with the z-axis ($\mathbf{B} = B\,\hat{e}_z$) the hamiltonian 6.1 can be expressed as

$$H_B = \mu_0\, B\, (L_z + 2S_z) \tag{6.2}$$

where L_z and S_z are, respectively, the projections of the total atomic angular momentum and spin operators along $\hat{e}_z$ and μ_0 is the Bohr magneton. As a consequence of the presence of an external magnetic field, in the perturbation theory framework, the state $|^3P_0\rangle$ is no longer a good eigenstate of the system and at the first perturbative order the new atomic eigenstate is expressed by (Taichenachev and Yudin, 2006)

$$|^3P_0'\rangle = |^3P_0\rangle + \frac{\langle ^3P_0|H_B|^3P_1\rangle}{\Delta}|^3P_1\rangle = |^3P_0\rangle + \frac{\Omega_B}{\Delta}|^3P_1\rangle \tag{6.3}$$

where $\Delta = E(^3P_0) - E(^3P_1)$ is the energy splitting between the $|^3P_0\rangle$ and the $|^3P_1\rangle$ states and $\Omega_B = \langle ^3P_0|H_B|^3P_1\rangle$ is the matrix element describing the magnetic coupling. To evaluate Ω_B it is useful to express the states $|^3P_0\rangle$ and $|^3P_1\rangle$ in the $|L, S, L_z, S_z\rangle$ basis. In this basis we have

$$|^3P_0\rangle = \frac{1}{\sqrt{3}}\left(|1,-1\rangle - |0,0\rangle + |-1,1\rangle\right) \tag{6.4}$$

and

$$|^3P_1\rangle(m_J = 0) = \frac{1}{\sqrt{2}}\left(|1,-1\rangle + |-1,1\rangle\right) \tag{6.5}$$

where in the kets only the $|L_z, S_z\rangle$ part is reported, being always $|L, S\rangle = |1, 1\rangle$. Given the expressions 6.4 and 6.5 we have

$$\Omega_B = \sqrt{\frac{2}{3}}\,\mu_0\, B. \tag{6.6}$$

The non-zero magnetic coupling 6.6 implies the possibility to address the $|^3P_0'\rangle$ state thanks to the mixing with the $|^3P_1\rangle$, which, in the presence of an electric field $\mathbf{E}$ resonant with the clock transition, is coupled to the ground state with a Rabi frequency given by

$$\Omega_L = \langle ^3P_1|\mathbf{d} \cdot \mathbf{E}|^1S_0\rangle \tag{6.7}$$

[1] The excitation of the clock transition in even isotopes of alkaline-earth and alkaline-earth-like elements is also possible exploiting multiphoton schemes (Santra et al., 2005; Hong et al., 2005) that, however, are difficult to realize requiring the use of multiple stabilized lasers, non-linear optics and good control over laser field intensities.

being **d** the electric dipole operator. Taking into account the expression which relates this Rabi frequency to the $|^3P_1\rangle$ decay rate $\Gamma = 2\pi \times 180$ kHz, it is possible to write the 6.7 as (Steck, 2007)

$$\Omega_L = \sqrt{\frac{3\lambda^3\Gamma}{4\pi^2\hbar c}}\sqrt{I} \tag{6.8}$$

where $\lambda = 556$ nm and I is the intensity of the clock laser. This last expression, combined with the 6.3, allows us to express the effective Rabi frequency for the excitation of the clock transition as

$$\Omega = \frac{\Omega_L\,\Omega_B}{\Delta} = \alpha\, B[\mathrm{G}]\sqrt{I\left[\frac{\mathrm{mW}}{\mathrm{mm}^2}\right]} \tag{6.9}$$

with $\alpha = 2\pi \times 0.19$. Typical experimental accessible parameters, such as I =10 mW mm^{-2} and $B = 100$ G, result in a Rabi frequency of the order of $2\pi \times 60$ Hz. This last expression clearly evidences how for this "unconventional" transition we have two tools at our disposal to tune the Rabi frequency and the linewidth of the transition, one consisting in the intensity of the external magnetic field, and the other in the intensity of the clock laser light.

Differently from the fermionic case, the Yb bosonic isotopes show only a quadratic dependence of the clock transition frequency as a function of the applied magnetic field. Being the ground state $|^3P_0\rangle$ completely amagnetic, this quadratic Zeeman shift arises from the corrections to the unperturbed $|^3P_0\rangle$ state energy given by the Hamiltonian 6.2. Being zero the first-order correction $\Delta E_1 = \langle {}^3P_0|H_B|{}^3P_0\rangle = 0$, the leading correction to the level energy is the second order

$$\Delta E_2 = \frac{|\langle {}^3P_1|H_B|{}^3P_0\rangle|^2}{\Delta} = \frac{1}{4\pi^2}\frac{\Omega_B^2}{\Delta} \tag{6.10}$$

which is of the order of $\Delta E_2 \approx -10^{-2}$ [Hz G^{-2}].

6.2 Clock transition spectroscopy

To address the clock transition we start preparing a BEC in a crossed dipole trap with trapping frequencies $\omega_{x,y,z} = 2\pi \times \{92.8, 72.6, 86.3\}$ Hz via evaporative cooling. At the end of the evaporation stage the degenerate gas, which consists of about 2×10^5 atoms, is loaded inside a 3D cubic optical lattice with depth that can be tuned up to 40 E_r, being E_r the lattice recoil energy. The lattice is operated at the magic wavelength of 759.4 nm (Barber et al., 2008) in order to minimize the position dependent differential light shift between the ground and the clock states. Once the lattice is loaded, the crossed optical trap is adiabatically turned off and the atoms remain trapped only by the lattice beams. Roughly half of the bosons are lost during this process and we end up with a sample consisting of about 1.2×10^5 atoms, a number that can be easily lowered changing the waiting time in the lattice after the optical trap has been turned off. A waiting time of 3 s, for example, is required to remain with a sample containing 5×10^4 atoms.

Clock spectroscopy is then performed shining a long 578 nm light pulse on the sample, that results in the excitation of part of the population from the $|^1S_0\rangle = g$ state

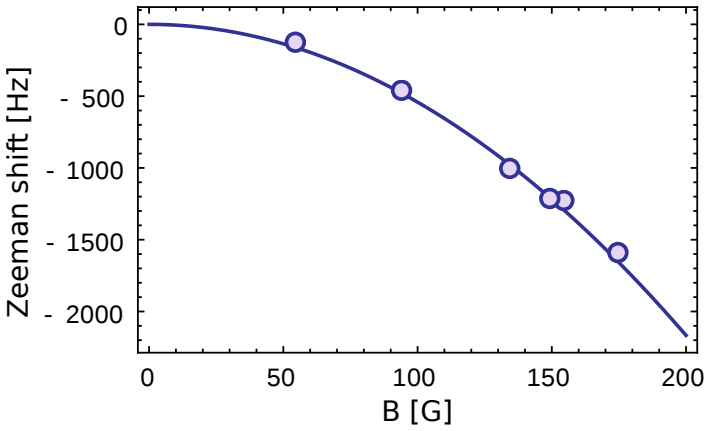

Figure 6.1: Second order Zeeman shift of the clock transition in ^{174}Yb. The solid line is a fit of the experimental data with a parabolic function.

to the metastable $|^3P_0\rangle = e$. The clock beam is π-polarized and intensities up to $\sim$100 mW/mm^2 can be reached depending on which specific beam path (each with a different beam waist) is chosen.

To compensate for the isotopic clock shift between ^{173}Yb and ^{174}Yb, $\delta\nu = \nu_{173} - \nu_{174} = 551.54$ MHz (Clivati et al., 2016), the AOM on the ULE branch of the clock laser setup (see figure 1.3) had to be replaced. Being the isotopic shift smaller than the ULE mode spacing, the lock is performed on the same ULE mode for both the isotopes. No other "hardware" operations are necessary to switch between bosonic and fermionic clock spectroscopy. All the measurements presented in this chapter are performed with the laser drift compensated in its linear part only, without taking advantage of the optical-link reference provided by INRiM. This means that transitions can be probed for relatively short times that depend on the linewidth of the transition itself. For large power-broadened linewidths (let's say about 1 kHz) the resonance can be continuously addressed for up to one hour. On the other side, for linewidths comparable with the laser width (<50 Hz), 15 min could be enough to put the laser completely out of resonance.

In order to acquire the resonance spectra, atoms have been probed with 500 ms to 1 s long interrogation pulses. Atoms remaining in the ground state are then recorded as a function of the laser frequency, meaning that the spectroscopic signature is a dip in the atom number. The clock excitation is always performed in the Lamb-Dicke regime, with isotropic lattice depths spanning from $s = 15$ to $s = 40$. Since the clock beam path is overlapped with one of the lattice beams, to fulfil the Lamb-Dicke condition it is enough that the lattice co-propagating with the clock beam is sufficiently deep. No constraints on the depth are required for the other lattices.

In a first experiment, we investigated the dependence of the clock transition frequency on the external applied magnetic field. We excited the transition with a 500 ms long pulse characterized by an intensity of 10 mW mm^{-2} in correspondence of the atomic sample. We acquired several resonances for values of the applied magnetic field ranging from 50 to 175 G. The centres of the resonances, reported as a function

of the magnetic field in figure 6.1, have then been fitted with a pure parabolic function. From the fit we obtain the quadratic Zeeman shift value δz=(-0.054 $\pm$ 0.002) Hz/G^2. This value is in good agreement with the one found by in reference (Poli et al., 2008) that is $\delta z = -0.062(10)$ Hz/G^2.

All of the resonances of figure 6.1 are characterized by a width of the order of 500 Hz regardless of the different values of applied magnetic field, a feature not in agreement with the linear scaling between the Rabi frequency and the magnetic field of equation 6.9. This suggests the existence of a substructure hidden by the power broadening. The investigation of this substructure is the core of the following sections.

6.3 Interaction-peaks resolved spectroscopy

Reducing the coupling to the e state by lowering the intensity of the clock laser and the external magnetic field applied, we observe the appearance of a series of peaks that in the previous measurements were hidden because of the excessive power broadening. We ascribe these peaks to processes in which a single atom in a n-particles-occupied lattice site is excited to the clock state e, a process that we represent with the $|(n)g\rangle \rightarrow |(n-1)g\,e\rangle$ notation.

Figure 6.2-a reports a typical spectrum acquired starting from a sample containing about 5×10^4 atoms trapped in a $s = 30$ isotropic three-dimensional lattice. A 55 G magnetic field and a clock laser intensity of 1 mW mm^{-2} have been used for the measurement. We identify the highest energy peak with the $|g\rangle \rightarrow |e\rangle$ process. This attribution is justified by two different experiments in which the transition is probed changing, respectively, the number of atoms in the sample and the number of multi-particle-occupied sites in the lattice. In the first experiment (figure 6.2-c) we performed spectroscopy starting from samples containing a different atom number. The progressive reduction of the lower-energy peaks area as the atom number is lowered (and so the mean number of particles in each lattice site is reduced), suggests that these peaks can be ascribed to $|(n)g\rangle \rightarrow |(n-1)g\,e\rangle$ processes with $n > 1$. On the other hand, the area of the highest energy peak increases as the atom number is reduced, confirming our hypothesis.

In the second experiment we shine a photoassociation (PA) pulse on the sample before performing clock spectroscopy. PA is performed using a 5-ms-long pulse having a frequency red-detuned by 20 MHz with respect to the to the $^1S_0 \rightarrow {}^3P_1$ intercombination resonant frequency and an intensity of 3×10^{-3} W mm^{-2}. This frequency corresponds to the third red-detuned PA resonance starting from the single-atom resonant frequency, as it is reported in reference (Kim et al., 2016) and experimentally verified in the spectrum reported in figure 6.3-a. PA associates atoms in molecules and removes particles in multi-occupied lattice sites from the system, leaving a sample containing roughly only singly-occupied sites. Starting from more than 1×10^5 atoms, PA leaves in the lattice about 3×10^4 atoms, as it can be observed in figure 6.3-b. With this PA light intensity, the final atom number remains constant for pulses longer than 2 ms, suggesting that we effectively obtain a sample containing only atoms in singly-occupied sites. In the clock spectrum after PA, which is reported in figure 6.2-b, no other peaks with the exception of the highest-energy one are present, a strong proof of the validity of our hypothesis about the identification of the resonances observed.

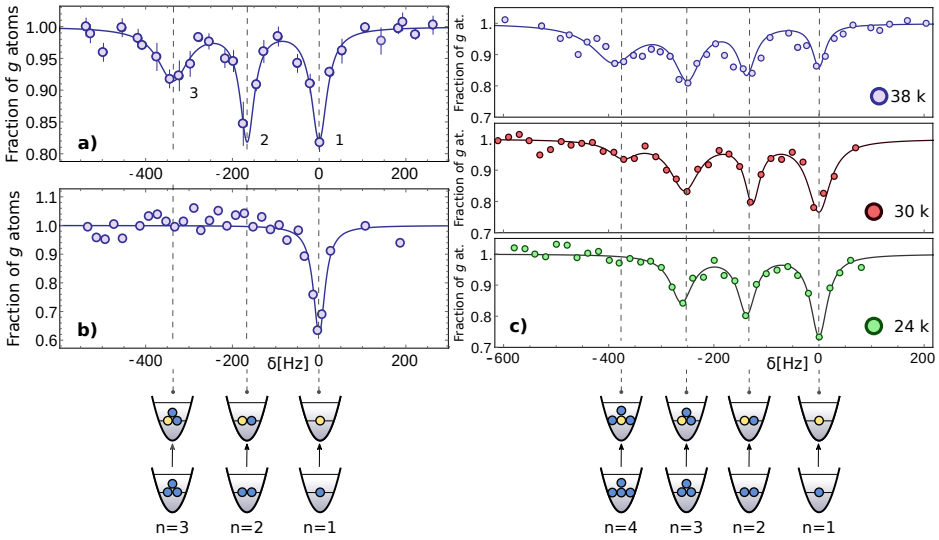

Figure 6.2: Clock spectroscopy of a ^{174}Yb atomic sample in a 3D optical lattice. All the images report the fraction of ground state atoms remaining after the clock excitation pulse. **a:** Several equally-spaced absorption peaks are observed in a typical spectrum. We ascribe these features to interaction energy shifts that depend on the number of particles contained in each lattice site. **b:** Clock spectroscopy performed after the application of a photoassociation pulse. PA removes atoms in multi-particle occupied lattice sites allowing the unambiguous identification of the single particle transition peak. **c)**: Clock spectroscopy performed for several values of the number of atoms contained in the sample. As the atom number is decreased, the area of the higher energy peaks increases, a feature in agreement with the identification of the highest energy peak with the transition in which atoms in single-particle-occupied lattice sites are probed.

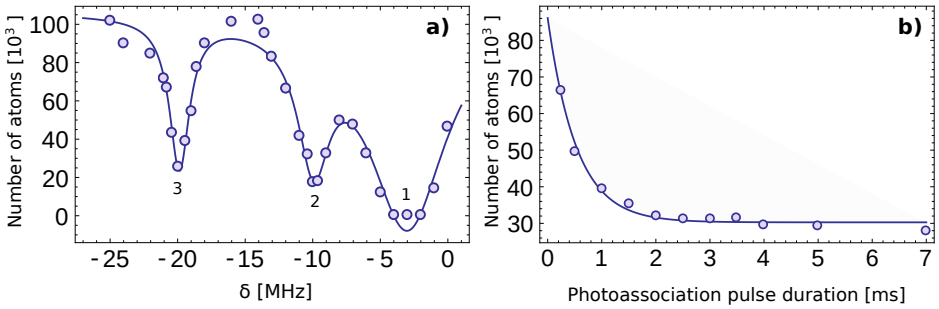

Figure 6.3: **a:** Photoassociation (PA) resonances spectrum as a function of the detuning with respect to the $^1S_0 \rightarrow {}^3P_1$ intercombination resonant frequency. The PA frequency adopted in this work is correspondent to the peak labelled as (3) in the spectrum. **b:** Number of atoms remaining in the sample as a function of the PA pulse duration. For pulses longer than 2 ms the number of remaining atoms approaches a constant non-zero value, suggesting that no multi-particles occupied lattice sites are left.

6.3.1 Measurement of the e-g scattering length

The identification of the various peaks observed in figure 6.2-a represents the starting point for the determination of the scattering length a_{eg}, whose value, at our knowledge, was not reported in literature before.

Assuming the validity of the relation 1.23 which defines the two-particle interaction energy in the fundamental band of a 3D tight-binding lattice, the quantity $\delta a = a_{eg} - a_{gg}$ can be directly evaluated starting from the energy separation ΔU_{eg} between the peak associated to the $|g\rangle \to |e\rangle$ process with respect to the one associated with the $|gg\rangle \to |ge\rangle$, whose value is given by

$$\Delta U_{eg} = \frac{4\pi\hbar^2(a_{eg} - a_{gg})}{m} \int w^4(\mathbf{r})\, d\mathbf{r}. \tag{6.11}$$

Since the value of a_{gg} is known to be equal to $104.9(1.5)\, a_0$ (Kitagawa et al., 2008), being a_0 the Bohr radius, once ΔU_{eg} is measured, a_{eg} can be easily determined. The values of ΔU_{eg} measured for several depths of the lattice and obtained as the result of a Lorentzian fit of the resonances in the spectra, are reported in figure 6.4 (circular points). The experimental points have been fitted with the function 6.11, leaving the differential scattering length δa as the only free parameter. The result of the fit (solid line) corresponds to a best-fitting value

$$a_{eg} - a_{gg} = -10.19\,(0.13)\, a_0\,. \tag{6.12}$$

Combining this determination with the known value of a_{gg} results in a value for the $g - e$ scattering length

$$a_{eg} = +94.7\,(1.6)\, a_0\,. \tag{6.13}$$

In figure 6.4 we also plot the interaction shift ΔU_{gge} of the $n = 3$ resonance (labeled as (3) in figure 6.2-a) relative to the $n = 1$ resonance (square points). If only two-body interactions are taken into account, the total interaction energy of three interacting bosons should be $3U_{gg}$ if the particles are all in the g state and $U_{gg} + 2U_{eg}$ if one atom is excited to the e state. This means that we expect the interaction energy shift to be $\Delta U_{gge} = 2(U_{eg} - U_{gg}) = 2\Delta U_{eg}$, i.e. twice that measured for the $n = 2$ case. However, the expected shift (solid line in figure 6.4), evaluated on the basis of the previous determination of a_{eg}, clearly deviates from the experimental points. We ascribe this deviation to an additional energy correction arising from elastic three-body effective interactions. This correction was introduced in reference (Johnson et al., 2009) for the case of n indistinguishable interacting bosons in the lowest vibrational state of a 3D optical lattice, and was observed experimentally in references (Johnson et al., 2009; Will et al., 2010). Following the derivation of (Johnson et al., 2009), for three particles in the same quantum state, at the first perturbative order, this correction reads

$$\delta U_3(a, s) = \frac{\beta\, U_2(a, s)^2}{\hbar\,\omega(s)}, \tag{6.14}$$

where $U_2(a, s)$ is the two-particle interaction energy, which depends on the scattering length a and the lattice depth s, $\omega(s)/(2\pi)$ is the harmonic frequency characterizing the confinement within one lattice site and $\beta = -1.34$ is a constant. Intuitively, the

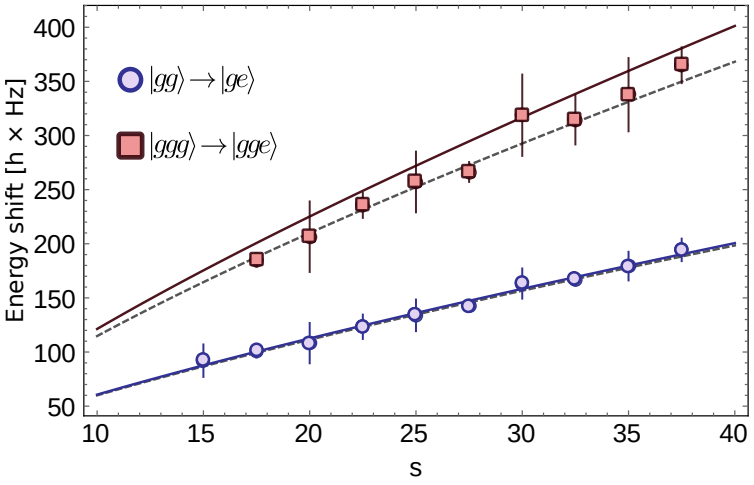

Figure 6.4: Interaction energy shift of the clock transition for two interacting ^{174}Yb bosons (circles) and for three interacting bosons (squares) as a function of the optical lattice depth. The lower solid curve is a fit of the experimental data with the function 6.11. The upper solid line, instead, is the energy shift expected for the three particle peak if only two-particle interactions are taken into account. The dashed curve is a simultaneous fit of the two experimental datasets that takes into account the three-body interaction energy correction reported in (Johnson et al., 2009).

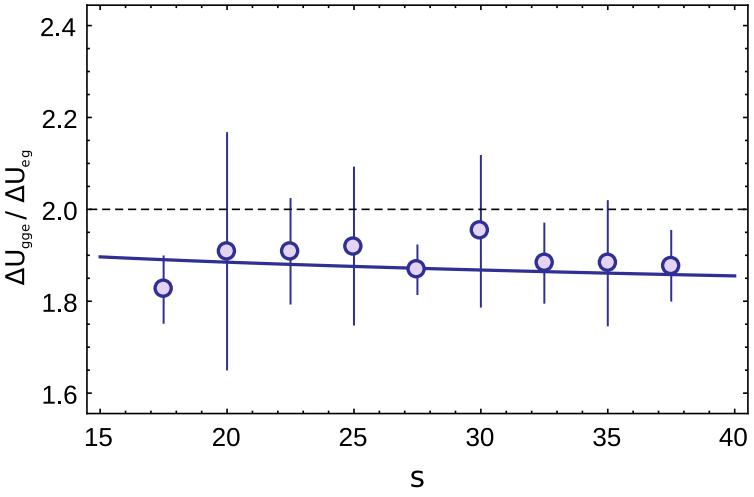

Figure 6.5: Ratio between the energy shift relative to the three-particles peak ($|ggg\rangle \rightarrow |gge\rangle$ transition) and the one relative to the two-particles peak ($|gg\rangle \rightarrow |ge\rangle$ transition). The line is the theoretical prediction evaluated using the equation 6.15.

physical origin of this energy shift can be ascribed to a broadening of the on-site wavefunction due to repulsive interactions, which reduces the effective interaction energy when more than two particles are confined in the same lattice site (Dutta et al., 2011; Daley and Simon, 2014). The expression 6.14 allows us to evaluate the second-order correction to the interaction energy for the $|ggg\rangle$ state. For the $|gge\rangle$ state, however, the three interacting particles are not identical, and the theoretical approach of reference (Johnson et al., 2009) could not be adequate. If we assume that the three-body elastic interaction in the $|gge\rangle$ state could still be described by equation 6.14, with an average scattering length given by the geometric mean $\bar{a}_{gge} = (a_{gg}a_{eg}a_{eg})^{1/3} \simeq 98\, a_0$, also the measured $|ggg\rangle \to |gge\rangle$ interactions shifts can be used to estimate a_{eg}. First of all, we verify the validity of this simplified model for the interaction energy of three bosons in different electronic states, calculating the ratio between the interaction shift relative to three and two particles. This ratio, taking into account the relation 6.14, is given by the expression

$$\frac{\Delta U_{gge}}{\Delta U_{eg}} = 2 + \frac{\delta U_3(a_{gg}, s) - \delta U_3(\bar{a}_{gge}, s)}{U_{gg}(s) - U_{ge}(s)}. \tag{6.15}$$

which, evaluated as a function of the lattice depth, shows a very good agreement with the experimental data, as it can be observed in figure 6.5.

The good agreement of our model with the measured interaction shifts allows us to perform a combined fit of the data relative to the two- and three-particles interaction shifts as a function of the lattice depths, leaving again the differential scattering length δa as the only free parameter. From the fit, which gives now a very good agreement with both datasets (dashed lines in figure 6.4), we extract the only fit parameter $\Delta a = -10.08\,(0.05)\, a_0$, which is consistent with the previous determination that does not rely on the knowledge of the elastic three-body contribution.

6.3.2 Measurement of the e-e scattering length

In our spectra, an increased coupling on the clock transition reveals the presence of an additional peak blue-shifted by $\Delta f_{ee} \simeq 160$ Hz (for $s \simeq 30$) with respect to the single-particle one, as shown in figure 6.6-a (circular points). We identify this resonance with the two-photon process $|gg\rangle \to |ee\rangle$, which transfers two particles trapped in the same lattice site from the $|gg\rangle$ to the $|ee\rangle$ state, via an intermediate $|ge\rangle$ state.

The two-photon nature of this excitation is validated by a "two-color" spectroscopy experiment in which the transition is excited by a clock laser with two frequency components $f_{+,-} = f \pm \delta f$ simultaneously probing the atomic sample. The result of this experiment, performed fixing $\delta f = 800$ Hz and scanning f, is reported in figure 6.6-a (square points). The broad excitation profiles at the edges of the spectrum can be identified with two replicas of the single-photon absorption spectra, frequency-shifted by $+\delta f$ and $-\delta f$ respectively, as expected for a single-photon excitation driven by each of the two frequency components (the interactions sidebands are unresolved in this spectrum because of a larger laser intensity resulting in an increased power broadening). In addition, we still observe a weaker resonance at the same detuning $\Delta f_{ee} \simeq 160$ Hz as in the single-color spectrum, which is a strong indication of its two-photon nature. The absence of frequency shift for this resonance can be explained if we assume that a pair of atoms in the same lattice site absorbs simultaneously two photons with frequencies

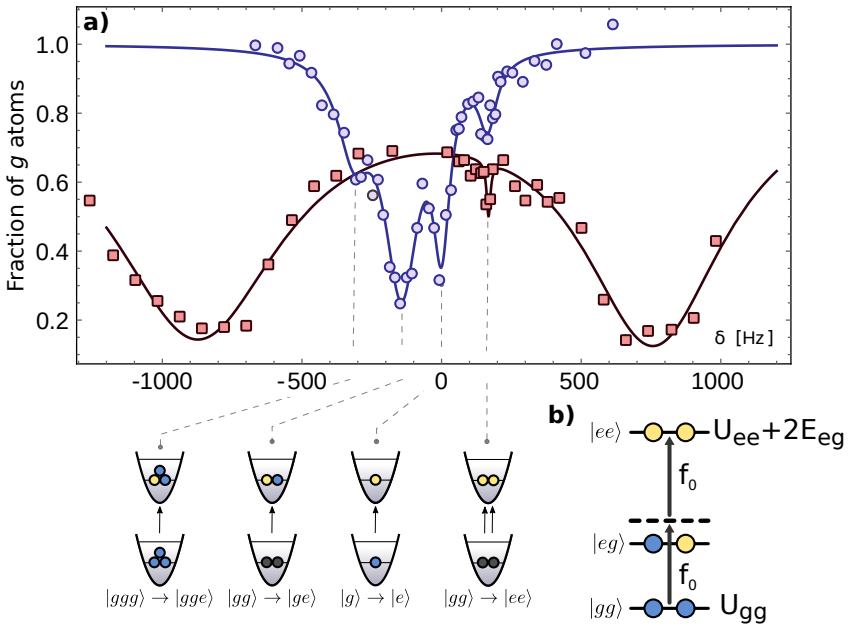

Figure 6.6: **a:** Single-frequency (circles) and two-frequency (squares) clock spectroscopy of an atomic ^{174}Yb sample trapped in a 3D optical lattice with $s = 30$. In the single-color spectrum, we identify the weak resonance at positive detuning as a signature of the two-particle/two-photon $|gg\rangle \rightarrow |ee\rangle$ process. This identification is confirmed by the presence of a resonance having the same frequency in the two-color spectrum taken at frequencies $f-\delta f$ and $f+\delta f$ (see text for more details). We note that the two-color spectrum has been recorded at a higher laser intensity in order to make the two-photon peak visible, causing the structure of the single-photon sidebands to be unresolved because of power broadening. **b:** Pictorial representation of the energy conservation relations involved in the $|gg\rangle \rightarrow |ee\rangle$ process which exploits the state $|eg\rangle$ as intermediate level. In the single-color spectroscopy, two photons of equal energy $h \times f_0 = E_{eg} + (U_{gg} - U_{ee})/2$ are necessary to excite the $|gg\rangle \rightarrow |ee\rangle$ transition, where E_{eg} is the energy required to promote one g atom in the e state. This implies that the measured shift of the $|ee\rangle$ peak with respect to the single-particle one is half of the interaction energy shift.

$f + \delta f$ and $f - \delta f$ each, in such a way that the total energy transferred to the system is $2h \times f$ (where h is the Planck constant), as in the case of a two-photon transition occurring for a single-color excitation.

The identification of the $|gg\rangle \rightarrow |ee\rangle$ resonance allows the experimental determination of the interaction energy shift $\Delta U_{ee} = U_{ee} - U_{gg}$. Since we are now dealing with a two-photon transition, the energy shift ΔU_{ee} is not equal to the shift of the $|ee\rangle$ peak with respect to the single-particle one, because in this case the energy conservation relation $U_{gg} + 2h\, f_0 = 2E_{eg} + U_{ee}$ (where E_{eg} is the energy required to excite a single atom to the e state) must be fulfilled. This implies that the shift that we experimentally measure is half of the interaction shift ΔU_{ee}, as it is pictorially reported in figure 6.6-b.

Adopting an argumentation similar to the one carried on in section 6.3.1, it is possible to link this interaction shift to the scattering length a_{ee} via the relation

$$\Delta U_{ee} = \frac{4\pi\hbar^2}{m}\left(a_{ee} - a_{gg}\right)\int w^4(\mathbf{r})\, d\mathbf{r}\,. \tag{6.16}$$

Using this equation and averaging over several spectra (both single-color and two-color) acquired at a mean lattice depth $s = 29.3(0.3)$, we determine the differential scattering length

$$a_{ee} - a_{gg} = +21.8\,(1.8)\,a_0\,. \tag{6.17}$$

Combining this measurement with the known value of $a_{gg} = +104.9\,(1.5)\,a_0$ reported in reference (Kitagawa et al., 2008) results in a value for the ee scattering length

$$a_{ee} = +126.7\,(2.3)\,a_0\,. \tag{6.18}$$

6.4 Spectroscopy of higher lattice bands

We extended our spectroscopic measurements with the characterization of the properties relative to the clock excitation of the atomic sample from the fundamental to higher lattice bands. In order to do this, the frequency ν of the photon must fulfill the energy conservation relation $h\nu = E_{g\to e} + W_n(s)$ where $E_{g\to e}$ is the energy required to excite one atom from the g to the e electronic state and $W_n(s)$ is the energy separation between the fundamental and the $n-$th excited lattice bands, that depends on the lattice depth s. Hereafter, we will identify particles in the $|g\rangle/|e\rangle$ electronic states belonging to the n-th lattice band using the $|g_n\rangle/|e_n\rangle$ notation.

Figure 6.7 (circular points) reports an example of spectrum in which the transition $|g_0\rangle \to |e_1\rangle$ is probed. The clock excitation is performed on a sample trapped in an anisotropic 3D lattice characterized by the depths $s_{x,y,z} = \{15, 30, 15\}$ with the clock beam aligned along the y direction, meaning that only the blue sideband relative to the lattice having depth s_y is revealed. We identify the blue sideband with the peak labeled as *2a* in figure 6.7-a, validating this identification taking into account that its shift with respect to peak *1* is 19.4 kHz, a value in reasonable agreement with the frequency separation between the fundamental and the first excited lattice bands at $s = 30$. An additional peak, labeled as *2b* and redshifted by $\sim$1.9 kHz with respect to the blue sideband, appears in the spectrum. We identify the resonance *2b* with the excitation of multiparticles-occupied lattice sites. This hypothesis is confirmed by a second experiment (square points in figure 6.7-a), in which a photoassociation pulse is shined on the sample before the clock spectroscopy pulse. The peak *2b* completely disappears in this second spectrum, suggesting that this feature is the result of the excitation of atoms in multiparticles occupied lattice sites. An additional series of measurements, in which the energy difference ΔE_{ab} of the peak $2b$ with respect to the blue sideband is recorded as a function of the transverse lattice depth ($s_{x,z}$) keeping $s_y = 30$, is shown in the inset 6.7-b. We observe a monotone increment of ΔE_{ab} as the transverse lattice depths are increased, suggesting that the resonance $2b$ is associated to an interaction peak. Yet, we have not been able to clearly identify the physical origin of this peak and reserve its characterization to future experiments.

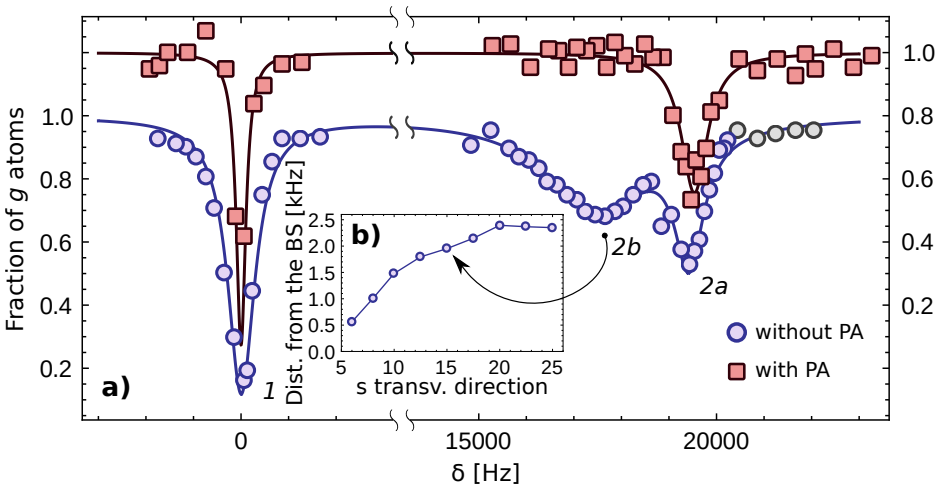

Figure 6.7: **a:** Clock spectroscopy of a ^{174}Yb atomic sample trapped in an anisotropic 3D lattice characterized by the depths $s_{x,y,z} = \{15, 30, 15\}$ with and without a previous photoassociation pulse (respectively, square and circular points). In the spectrum acquired without photoassociation the clock excitation, which is performed along the y direction, reveals the presence of three main peaks: one associated to the $|g_0\rangle \rightarrow |e_0\rangle$ transition, labeled as *(1)*, one relative to its blue sideband $|g_0\rangle \rightarrow |e_1\rangle$, labeled as *(2a)*, and a third peak, labeled as *(2b)*, that we ascribe to an interband clock transition involving lattice sites containing at least two particles. The multiparticle nature of the peak *(2b)* is confirmed by the spectrum after photoassociation (squares), in which this feature is not present. **b:** frequency shift of the peak *2b* with respect to the blueside-band as the depth of the transverse lattices $s_{x,z}$ is changed, keeping constant $s_y = 30$ and the atom number in the sample. Square points are offset upward for presentation purposes. Consider the vertical scale on the right for these points.

In a last set of experiments, reported in figure 6.8, we acquired several spectra near the lattice first blue sideband as a function of the number of atoms in the sample, keeping the lattice depths $s_{x,y,z} = \{15, 30, 15\}$ for all the measurements. As the number of atoms is reduced, a third peak, labelled as *2c* in the figure, appears between the interaction peak *2b* and the blue sideband *2a*. A mechanism capable to explain the presence of this third peak is the one discussed in reference (Anderlini et al., 2007), where the authors investigate how the exchange symmetry of the wavefunction of two identical bosons having a Hilbert space characterized by two possible spin and vibrational states leads to a spin-exchange dynamics. Adapting this work to our case, we have to consider that, starting from two ground-state particles in the same lattice site (a state that we can identify with $|g_0\, g_0\rangle$), the bosonic symmetrization rule makes it possible to populate two states with different exchange symmetry simply exciting one of the two atoms to the electronic e clock state. Actually, if the clock excitation transfers one of the two atoms in the first excited lattice band, the symmetrization of the wavefunction predicts the existence of two states, one having the vibrational and orbital parts both symmetric and the other both antisymmetric for particles exchange. We can express

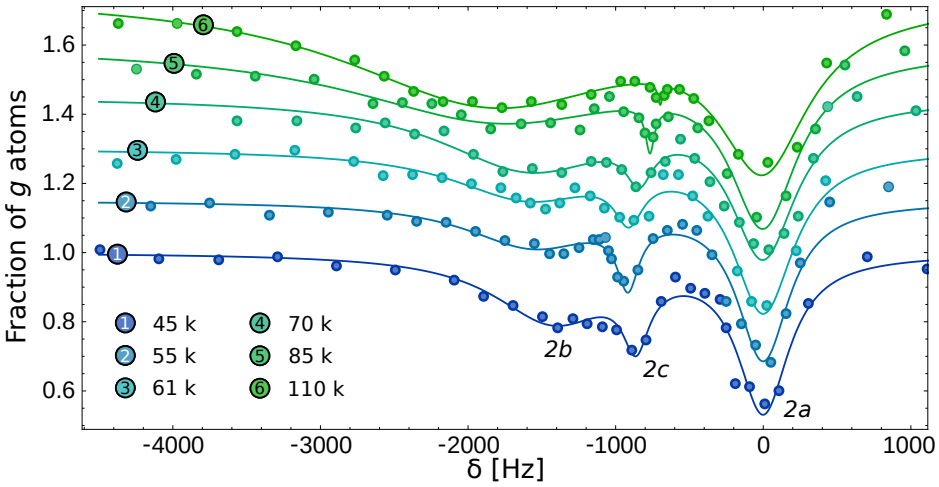

Figure 6.8: Clock spectroscopy as a function of the atom number performed in an anisotropic 3D lattice characterized by the depths $s_{x,y,z} = \{15, 30, 15\}$. An additional peak (labelled as *2c*) is revealed between the peaks *2b* and the blue sideband (*2a*) as the atom number is reduced (see the main text for details). Frequency offsets are given with respect to the peak *2a*.

these states as

$$|eg_{\pm}\rangle = \frac{1}{2}\left(|g_0(x_1)e_1(x_2)\rangle \pm |g_1(x_1)e_0(x_2)\rangle \pm |e_0(x_1)g_1(x_2)\rangle + |e_1(x_1)g_0(x_2)\rangle\right) \tag{6.19}$$

where $x_{1,2}$ are the position of the two atoms. These two states are formally identical to the ones derived in section 1.1.2 for the fermionic isotope ^{173}Yb where the role played by the nuclear spin is now assumed by the lattice band index. It should be observed that, while the wavefunction of the $|eg_+\rangle$ is not vanishing for $x_1 = x_2$, the one relative to the $|eg_-\rangle$ state vanishes as the two particles overlap. This means that the two atoms cannot interact in the $|eg_-\rangle$ state and so an energy redshift equal to U_{gg} with respect to the blue sideband is expected for this state. In the experimental condition of the spectra of figure 6.8 we have $U_{gg} \sim h \times 1.1$ kHz, meaning that it is possible to identify the peak $2c$, whose distance with respect to the blue sideband is approximately 1 kHz, with the resonance relative to the $|eg_-\rangle$ state. On the other hand, we expect for the $|eg_+\rangle$ state an interaction shift given by

$$\delta U_{eg_+} = \frac{4\pi\hbar^2}{2m}\int \left(a_{ge} w_0^2(\mathbf{r}) w_1^2(\mathbf{r}) - a_{gg} w_0^4(\mathbf{r})\right) d\mathbf{r}. \tag{6.20}$$

where $w_{0,1}(\mathbf{r})$ are respectively the Wannier functions relative to the fundamental and first excited lattice bands. A resonance characterized by this shift, that in our experimental conditions is equal to few tens of Hz, can not be observed in the spectra reported in figure 6.8 because of the excessive power broadening. As a final point, it should be observed that the area relative to the peak $2c$ increases as the atom number is reduced, while the area relative to the peak $2b$ decreases. This confirms the identification of the

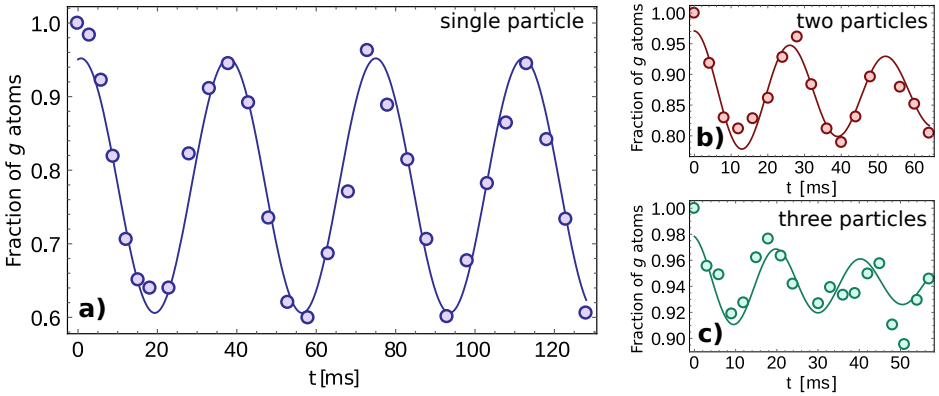

Figure 6.9: Rabi oscillation relative to the selective excitation of **(a)** the single-particle peak, **(b)** the two-particles peak and **(c)** the three-particles peak in an atomic ^{174}Yb sample in a 3D optical lattice. In the pictures the fraction of ground-state atoms remaining after the clock excitation pulse is reported.

peak $2c$ with a two-particles resonance and suggests that the peak $2b$ is related with the excitation of states with more than two particles. A deeper investigation of the nature of this peak is left for future works.

6.5 Coherent addressing of the transition

The possibility to resolve lattice sites containing a different number of particles gives us the opportunity to induce Rabi oscillations separately for all the processes $|(n)g\rangle \rightarrow |(n-1)g\,e\rangle$ described in the previous sections.

An example of Rabi oscillations relative to the process in which only single occupied lattice sites are probed is reported in figure 6.9-a. The magnetic field and the clock laser intensity adopted for the measurement are respectively 55 G and 1 mW mm^{-2}, while the lattice depth is set to $s = 30$ in all directions, meaning that we have an energy splitting between different interaction peaks of the order of $h\times$200 Hz. The resulting oscillation, which is characterized by a frequency of 26.9 Hz, displays a very long coherence time being still undamped for excitation times greater than 100 ms.

Note that at the π-pulse only a fraction of the population is transferred in the clock state despite the excitation being resonant. This is because we are addressing only the singly-occupied lattice sites and particles in sites with an occupation number greater than one do not participate to the dynamics.

We also tried to selectively induce Rabi oscillations in two- and three- particles-occupied lattice sites, that we report, respectively, in figures 6.9-b and 6.9-c. For these processes, in the same experimental conditions, we expect to observe a Rabi frequency greater than the one measured in the single-particle case. The reason of this behaviour is a direct consequence of the bosonic wavefunction symmetrization. In particular, if we consider the two-particles case, the ground state $|gg\rangle$ is coupled by the laser light to the state $(|ge\rangle + |eg\rangle)/\sqrt{2}$, meaning that the Rabi frequency associated to the process

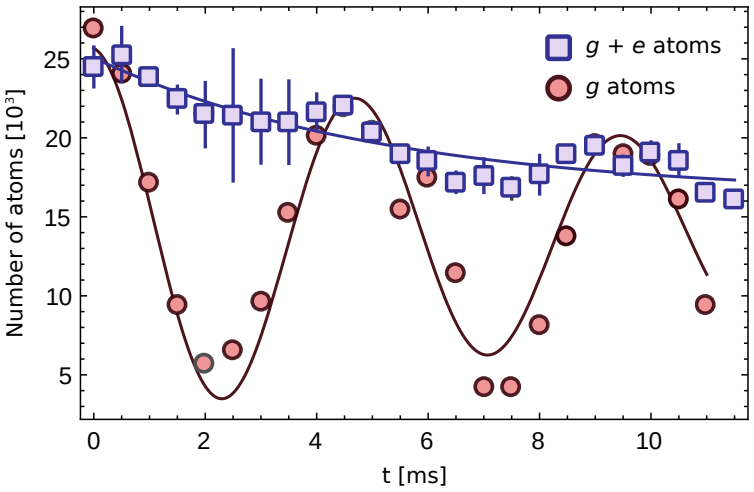

Figure 6.10: Rabi oscillation relative to a photoassociated sample in which roughly only single particle occupied lattice sites are present. The population remaining in the in the g state after the coherent clock excitation is reported as a function of time (circular points). The simultaneous imaging of atoms in the g and e states (square points) reveals a decay in the total population of the sample which can be ascribed to inelastic collisions between atoms in doubly occupied lattice sites not removed by the photoassociation.

(limited to its electric-field-dependent part Ω_L, see equation 6.9) will be

$$\Omega_{L,2} = \frac{1}{\hbar}\frac{\langle gg|\mathbf{d}\cdot\mathbf{E}|ge\rangle + \langle gg|\mathbf{d}\cdot\mathbf{E}|eg\rangle}{\sqrt{2}} = \sqrt{2}\,\Omega_{L,1} \tag{6.21}$$

where $\Omega_{L,1}$ is the single-particle Rabi frequency. With a similar argumentation, a Rabi frequency $\Omega_{L,3} = \sqrt{3}\,\Omega_{L,1}$ is expected for the three-particles case. The measured value of the Rabi frequency for the two- and three-particles processes confirms the theoretical prediction $\Omega_n = \sqrt{n}\,\Omega_1$, being respectively $\Omega_2 = 2\pi\times 36.8$ Hz $= 0.97\sqrt{2}\,\Omega_1$ and $\Omega_3 = 2\pi \times 45.5$ Hz $= 0.98\sqrt{3}\,\Omega_1$. The correct experimental scaling of the Rabi frequency with the particle number validates our interpretation of the interaction peaks nature.

In a second experiment we have studied the Rabi dynamics relative to a photoassociated sample. Since in this case only atoms in singly-occupied lattice sites are expected to be present, no other process with the exception of the single-particle one is probed, even if the power broadening of the transition exceeds the interaction energy shifts. In this way we can induce fast Rabi dynamics avoiding the loss of coherence that would results from the simultaneous excitation of sites with a different number of particles, that, as we discussed before, are characterized by a different Rabi frequency.

A magnetic field of 175 G and an intensity of the clock laser of 50 mW/mm^{-2} allow us to induce a Rabi oscillation which is characterized by a frequency of 208(4) Hz, as it can be observed in figure 6.10 (circular points). At the first π pulse ($\sim$ 2 ms) we observe now a larger transfer of the population to the *e* state, as it is expected for a sam-

ple containing roughly only single-particle-occupied lattice sites. At longer times the oscillation displays an unusual behaviour characterized by an almost complete depletion of the g population at the second π pulse ($\sim$ 7 ms) accompanied by a simultaneous reduction of the oscillation amplitude. This behaviour can not be explained with a loss of coherence in the dynamics, since in that case we would expect to observe a smaller depletion at the second π pulse, but, instead, it is in agreement with a reduction of the number of atoms contained in the sample. This hypothesis is confirmed by a second experiment (square points in figure 6.10) in which, for each time sampled in the oscillation, we simultaneously measure the number of atoms in the g and the e state (more details on the repump scheme and the imaging of atoms in the metastable clock state will be given in the following section). The decay observed in the total population (g + e atoms) can be ascribed to inelastic collisions occurring between atoms in a small fraction of doubly-occupied lattice sites not removed by the photoassociation and represents a hint of a fast loss rate associated to $g-e$ or $e-e$ collisions. Note that the number of repumped atoms stabilizes for longer pulses, even in the incoherent regime, validating our hypotesis. The characterization of these collisions is the core of the following section.

6.6 Detection of state-dependent inelastic collisions

In a last set of experiments we determined the loss rate coefficients relative to the inelastic collisions occurring in the $e-g$ and $e-e$ interaction channels. These experiments require a measurement of the number of g and e atoms as a function of the holding time in the optical trap after the interaction channels have been opened. While the detection of the population in the g state is trivial, to measure the number of atoms remaining in the e state we adopt the repumping scheme based on a 1388.8 nm laser described in section 1.2.5. Using $\sim$10 mW of repumping light focused on a waist of 150 μm we are able to achieve a power-broadened linewidth of the $|^3P_0\rangle \rightarrow |^3D_1\rangle$ repump transition of the order of 2 GHz, as it is shown in figure 6.11-a. This value is $\sim 10^4$ times greater than the natural linewidth of the transition, which is of the order of 300 kHz, meaning that the intensity of the repumping light is $\sim 10^8$ times greater than the saturation intensity of the transition. Moreover, this power-broadened linewidth experimentally exceeds the daily frequency drift of the 1388.8 nm laser (which is in free running) and, as a consequence of this, the frequency of the repumping light does not need to be readjusted for several days. The detection of the e atoms is performed following the procedure reported in figure 6.11-b. After turning off of optical trap, we firstly remove the atoms in the g state using a 100 μs long pulse resonant with the $|^1S_0\rangle \rightarrow |^1P_1\rangle$ transition. The repump light is then turned on for the whole duration of the time of flight (TOF), which lasts for 10 ms. At the end of the TOF the fraction of e atoms decayed in the g state thanks to the repumping procedure is recorded using the usual g-imaging scheme. The repumping efficiency, evaluated exciting the whole population of an atomic sample consisting only of single-particle-occupied lattice sites to the e state with a fast (< 3 ms) π-pulse and then performing the e-imaging procedure described above, results to be higher than 90%.

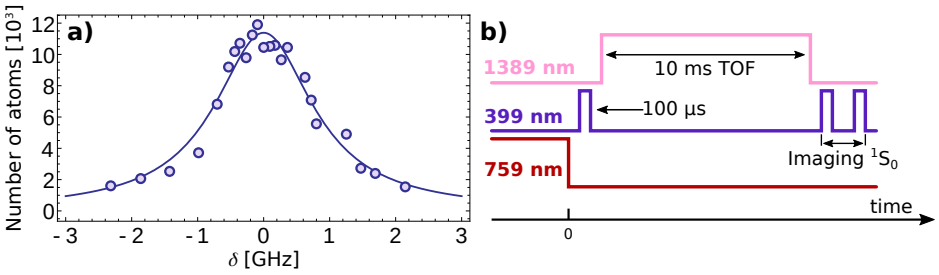

Figure 6.11: **a:** Number of repumped atoms as a function of the 1388.8 nm repumping laser detuning. From a lorentzian fit of the experimental data (solid line) we estimate a width of the repumping transition of the order of 1.8 GHz. **b:** Experimental sequence employed for the detection of the atoms in the e state. After the release of the lattice (759 nm line) a 100 μs pulse resonant with the ${}^1S_0 \rightarrow {}^1P_1$ imaging transition (399 nm line) is used to remove atoms in the g state. The repump light is then turned on for all the TOF time (1389 nm line). At the end of this sequence the usual imaging procedure for atoms in the g state is performed.

6.6.1 Inelastic $e - g$ collisions

In a first experiment, we investigate the $e - g$ losses by loading the atomic sample in a 3D optical lattice with an average depth $s \simeq 29.7$. The waiting times in the trap (before the lattice loading) and in the lattice are adjusted in order to maximize the number of doubly-occupied sites and, at the same time, minimizing the number of sites with more than two atoms. The atoms in the $|gg\rangle$ state are then excited to the $|eg\rangle$ state by means of a 10-ms-long π-pulse of the clock laser selectively resonant with the $|gg\rangle \rightarrow |eg\rangle$ transition, and after a variable holding time in the lattice the number of atoms in the e and in the g states is measured. The collected data are reported in figure 6.12 where the circular and square points of panel 6.12a display, respectively, the number of atoms in the g state with and without performing the excitation pulse to the e state, while the circular points of panel 6.12b display the number of e atoms after the excitation pulse. In both panels, the solid lines are exponential fits to the data as guides to the eye.

The data clearly show that atoms in the e state decay on a timescale of the order of the second. To better understand this behavior, in figure 6.12-b we compare the number of atoms in the e state (circles) to the difference between the number of atoms in the g state without and with the clock laser pulse (squares). At short times, this difference is equal to the number of atoms in the e state, as can be reasonably expected. On longer timescales of the order of 1 s, instead, while the atoms in the e state are lost, the difference between the g atoms without and with the excitation is approximately constant, implying that the losses in the e state are not caused by inelastic collisions with g atoms, otherwise this difference should have increased (the slow decrease of the number of g atoms could be attributed to the finite single-particle lifetime of the atoms in the lattice). The decay rate $\gamma = 1/\tau$ of the atoms in the e state can be estimated with an exponential fit to the data, obtaining $0.66(0.06)$ s^{-1}. This timescale is comparable with the tunneling rate ~ 1 Hz at the lattice depth of the experiment, suggesting that the e atoms, initially in lattice sites with g atoms, could be lost after tunnelling to

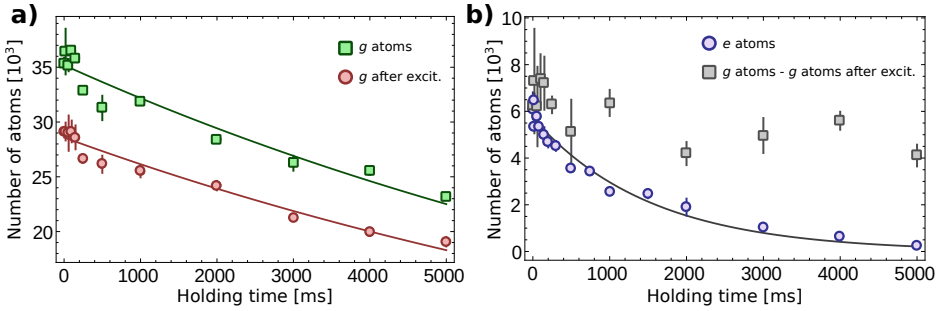

Figure 6.12: Experimental characterization of the loss rates associated to inelastic $e-g$ collisions. Inelastic $e-g$ collisions have been investigated by exciting atoms from the $|gg\rangle$ state to the $|eg\rangle$ state by selectively addressing the $|gg\rangle \rightarrow |eg\rangle$ transition in a 3D optical lattice ($s = 27.5$). **a:** The number of atoms remaining in g after the clock pulse (circles) is compared with the number of atoms in the absence of clock excitation (squares) as a function of the holding time in the lattice (the slow decay of both datasets shows the finite single-particle lifetime in the lattice). Lines are exponential fits of the experimental data that must be intended as guides to the eye. **b:** The number of atoms detected in the e state (circles) is shown as a function of the holding time in the lattice after the excitation of the transition. This number is compared with the difference between the number of g atoms without and with the clock excitation (squares), which displays an approximately time-independent behavior. The solid line is an exponential fit of the experimental data.

neighboring sites via $e-e$ inelastic collisions. Since the timescale of the observed losses is determined by the tunnelling time before the actual interaction events, it is difficult to extract a reliable $e-e$ loss rate coefficient from those data.

Nevertheless, the observed dynamics allows us to give an upper bound to the $e-g$ inelastic loss rate coefficient. Two-body $e-g$ losses would be described by the rate equation $\dot{n}_g = -\beta_{eg} n_e n_g = -\gamma_{eg} n_g$, where β_{eg} is the density-dependent loss rate coefficient. Requesting $\gamma_{eg} = \beta_{eg} n_e \ll \gamma$ and determining the in-site density n_e from the calculated Wannier functions in the 3D lattice, we obtain

$$\beta_{eg} \ll 10^{-14} \text{ cm}^3/\text{s} \, . \tag{6.22}$$

6.6.2 Inelastic $e-e$ collisions

A different strategy had to be implemented for the determination of the $e-e$ losses. As a matter of fact, we could not coherently excite a detectable number of atoms in the $|ee\rangle$ state by means of π-pulses on the $|gg\rangle \rightarrow |ee\rangle$ transition, possibly due to an insufficient broadening of the two-photon transition. We then switched to a different geometry and loaded the atoms in a 1D vertical optical lattice at a depth $s = 27.5$, obtaining an array of 2D pancakes with a radial trapping frequency $\omega_r = 2\pi \times 34.5$ Hz. A fraction of g atoms is excited to the e state with a 10-ms-long pulse of clock laser light directed along the pancakes plane, followed by a variable hold time in the lattice. Finally, the number of atoms in the e and g states is measured. As shown

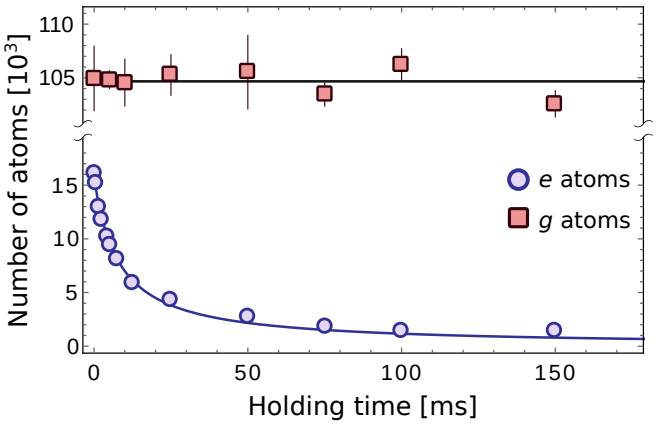

Figure 6.13: Experimental characterization of the loss rates associated to inelastic $e-e$ collisions Number of e atoms (circles) and g atoms (squares) as a function of the holding time in the lattice after a clock excitation pulse in an 1D lattice. The upper line represents the mean value of g atoms, while the lower line is the result of a fit to the e data with the model in equation (6.23), assuming the scaling in equation (6.30).

in figure 6.13, the data exhibit fast losses in the e state (circular points) on the ms timescale, while the g population (square points) is constant (the upper solid line in figure represents the mean of the experimental data). On this timescale, as seen in the previous experiment, other loss channels are negligible, so, assuming only $e-e$ two-body inelastic scattering (that is the dominant loss mechanism observed with different Yb and Sr isotopes, see e.g. references (Traverso et al., 2009; Scazza et al., 2014), and attributed to principal-number-changing collisions), the losses can be modeled with the rate equation $\dot{n}_e = -\beta_{ee} n_e^2$, where n_e is the density of e atoms and whose solution is given by

$$n_e(t) = \left(\frac{1}{n_{e0}} - \beta_{ee} t \right)^{-1} , \tag{6.23}$$

where n_{e0} is the initial e atom density and β_{ee} is the two-body loss rate coefficient. In order to extract a value for β_{ee} from our data, we developed a simplified theoretical model to determine the density in the pancakes from the measured atom number.

The starting point of our model is a calculation of the atomic density in the crossed optical dipole trap at the end of the evaporative cooling, before the loading of the 1D optical lattice. From a bimodal fit of the time-of-flight images of the atomic cloud at the end of evaporation, we determine the condensed fraction of the sample to be $f_{C_{3D}} \simeq 65\%$ of the total atom number, while the remaining thermal fraction results to be characterized by a temperature $T_{3D} = 60$ nK. This means that we can model the density inside the trap with the sum of a Thomas-Fermi distribution and a thermal distribution characterized by a temperature T_{3D}, each weighted for the corresponding

population fraction. The resulting density in the trap thus will be

$$n_{3D} = \frac{f_{C_{3D}}}{g}\left(\mu_{3D} - \frac{1}{2}m(\omega_x^2\,x^2 + \omega_y^2\,y^2 + \omega_z^2\,z^2)\right) + \frac{(1-f_{C_{3D}})\,N_{at}}{\pi^{3/2}\,r_x\,r_y\,r_z}\,e^{-\left(\frac{x^2}{r_x^2}+\frac{y^2}{r_y^2}+\frac{z^2}{r_z^2}\right)} \tag{6.24}$$

where $\{\omega_x, \omega_y, \omega_z\} = 2\pi\,\{92.8, 72.6, 86.3\}$ Hz are the trap frequencies, $g = 4\pi\hbar^2 a_{gg}/m$ is the interaction parameter, $N_{at} \simeq 180 \times 10^3$ is the atom number, $r_i = \sqrt{2\,k_B\,T_{3D}/(m\,\omega_i)}$ are the thermal distribution radii and μ_{3D}, the chemical potential, is given by (Petrov, 2003; Dalfovo et al., 1999)

$$\mu_{3D} = \left(\frac{15\,g\,N_{at}\,m^{3/2}\,\omega_x\,\omega_y\,\omega_z}{\pi\,2^{9/2}}\right)^{2/5}. \tag{6.25}$$

Starting from the density distribution in the 3D trap we then evaluate the atom number in each pancake assuming no population redistribution during the loading of the lattice. In order to do this, the 3D distribution is cut along the z direction in slices having a thickness equal to the lattice periodicity ($\lambda_L/2 = 379.5$ nm). As for the 3D distribution, perform a bimodal fit of the experimental data to estimate the condensed fraction in the pancakes to be $f_{C_{1D}} \simeq 20\%$, while the temperature of the thermal part results to be $T_{1D} \simeq 45$ nK. These values are used to compute the radial density in each pancake, that again we model as the sum of a 2D Thomas-Fermi and a 2D thermal distributions

$$n_{rad}(x,y,i) = \frac{f_{C_{1D}}}{g_{2D}}\left(\mu_{2D} - \frac{1}{2}m\,\omega_r^2(x^2+y^2)\right) + \frac{(1-f_{C_{3D}})\,N_i}{\pi\,r_{2D}^2}\,e^{-\left(\frac{x^2+y^2}{r_{2D}^2}\right)} \tag{6.26}$$

where $\omega_r = 2\pi \times 34.5$ Hz is the radial frequency in the pancake, $r_{2D} = \sqrt{2\,k_B\,T_{1D}/(m\,\omega_{2D})}$ is the thermal distribution radius, N_i is the atom number in the i-th pancake and $g_{2D} = g/(\sqrt{2\pi}\,a_{ho}^z)$ is the interaction parameter in 2D, being a_{ho}^z the harmonic oscillator length along the strongly confined $\hat{e}_z$ direction. It should be observed that the expression used for g_{2D} is valid only in the limit $a_{gg} \ll a_{ho}^z$ (Petrov, 2003), a condition fulfilled with our experimental parameters being $a_{ho}^z \simeq 998\,a_0$ at $s = 27.5$, the lattice depth at which the experiment is performed. Lastly, the 2D chemical potential μ_{2D}, can be evaluated for each pancake starting from the 2D Thomas-fermi radius

$$r_{TF} = \left(\frac{4\,g_{2D}\,N_i}{\pi\,m\,\omega_r}\right)^{1/4} \tag{6.27}$$

being $\mu_{2D} = 1/2\,m\,\omega_r^2\,r_{TF}^2$. The 3D density function in each pancake, $n_{2D}(x,y,z,i)$, is evaluated multiplying the in-plane 2D density by the square of the fundamental state eigenfunction of a 1D harmonic oscillator aligned along the $\hat{e}_z$ direction and characterized by the harmonic oscillator length a_{ho}^z. So, finally, we have

$$n_{2D}(x,y,z,i) = n_{rad}(x,y,i)\,\frac{1}{\sqrt{\pi}a_{ho}^z}\,e^{-\frac{z^2}{(a_{ho}^z)^2}}. \tag{6.28}$$

For each pancake the mean density is then evaluated

$$\bar{n}_{2D}(i) = \frac{\int n_{2D}^2(x,y,z,i)\,d^3r}{\int n_{2D}(x,y,z,i)\,d^3r} \tag{6.29}$$

and from the average of the various $\bar{n}_{2D}(i)$ a mean density n_{g0} of the sample is obtained.

We then assume a linear relation between the atom number and the density (justified by the short timescale of the excitation with respect to the trap periods $\sim \omega_i^{-1}$), so that the e-state density $n_e(t)$ after the clock laser excitation can be determined as

$$n_e(t) = \frac{n_{g0}}{N_{g0}} N_e(t), \tag{6.30}$$

where $N_e(t)$ is the measured number of atoms in the e state. Using this relation, we convert $N_e(t)$ into a density $n_e(t)$ and fit it with equation (6.23), from which the parameter β_{ee} can be determined from the measured atom number $N_e(t)$ as

$$\beta_{ee} = 1.3(0.7) \times 10^{-11}\ \mathrm{cm}^3\,\mathrm{s}^{-1}, \tag{6.31}$$

to which we attribute a conservative error due to the several assumptions in our theoretical model. The lower solid line in figure 6.13 is the result of the fit, converted back to atom number following the scaling of equation 6.30.

6.7 Conclusions

In conclusion, we have performed high-resolution spectroscopy of a Mott insulator of ultracold ^{174}Yb bosons in a 3D optical lattice by exciting them on the ultranarrow $^1\mathrm{S}_0 \rightarrow {}^3\mathrm{P}_0$ clock transition. The metrological character of the transition and the narrow spectroscopic signals that we have demonstrated allow for the characterization of the Mott insulator state and for the determination of the lattice sites occupancies.

Our spectroscopic resolution allowed us to precisely determine the scattering lengths for $e-g$ and $e-e$ collisions in ultracold ^{174}Yb atoms, that were previously unknown. These results are important in quantum information and quantum simulation applications, as well as for the development of optical lattice clocks based on bosonic isotopes of two-electron atoms, where the simpler internal structure (due to the absence of a nuclear spin) could provide advantages over the more commonly used fermionic isotopes.

We have also detected the effect of inelastic collisions involving the atoms in the e state. While the observed lifetimes appear to be severely limited by inelastic $e-e$ losses, no inelastic collisions in the $e-g$ channel could be observed on the timescale and with the sensitivity of our experiment. This system offers rich possibilities for quantum simulation, for instance for the investigation of two-component Bose-Hubbard models with different mobility of the species, e.g. for the study of impurity physics (a state-dependent lattice can be used to freeze the motion of the e atoms in such a way to inhibit inelastic losses), or for the realization of dissipative lattice models when $e-e$ losses are taken into account.

On a more general perspective, the spectroscopic approach that we have employed could be extended in future works to the use of the same ultranarrow clock transition to probe excitation spectra of more complex quantum many-body states of either bosonic or fermionic atoms with metrological accuracy.

Appendix A
Number of atoms in fermionic wires

The determination of the atom-number distribution in one-dimensional fermionic wires realized by means of the intersection of two deep orthogonal optical lattices is a problem that often emerges during this thesis. When two orthogonal optical lattices intersect, several wires are formed (see figure A.1-a), the number of which depends, in first approximation, on the waist of the lattices. The number of atoms contained in each wire is not uniform but, instead, depends on the potential offset of the considered wire calculated with respect to the central tube, as it is shown in figure A.1-b. This offset arises as a consequence of the finite waist size of the two lattices forming the wires which determines a spatial dependence of the induced dipole potential. The larger is the value of this offset, the less is the number of particles required to fill the tube up to the Fermi energy, which is fixed for the whole system and depends on the geometry and the total number of particles.

Near the center of the lattice we can approximate the offset potential as a 3D harmonic well. We want now to demonstrate that, with this assumption, the number of tubes containing the same number of particles is uniform up to the highest number of particles, which is reached in the central tube. To prove this we fix N_0 the number of particles in the central tube and assume the existence of a range of offset potentials $0 < V < \Delta V$ for which tubes characterized by offsets in this range also contain N_0 particles. Tubes with offsets slightly higher than ΔV reach the Fermi energy with a particle less and consequently contain $N_0 - 1$ atoms. Since the offset potential monotonically increases with the distance from the center, all tubes with offsets in the range $\Delta V < V < 2\Delta V$ contain $N_0 - 1$ particles. In the same way tubes with offsets in the range $2\Delta V < V < 3\Delta V$ contain $N_0 - 2$ particles and so on. As shown in figure A.1-c, this argumentation defines a central circular region (labelled as Z_1 in the figure) with radius r_1 in the plane orthogonal to the tubes containing only tubes with N_0 particles. The area Z_1 is enclosed in an annular region (labelled as Z_2) with radius r_2, containing only tubes with $N_0 - 1$ atoms. In the same way another annular region Z_3, with radius r_3, and characterized by tubes with $N_0 - 2$ particles, encloses Z_2. Due to the harmonic assumption for the potential shape, the radii of neighbouring regions fulfil the relation

$$\frac{1}{2}m\omega^2(r_n^2 - r_{n-1}^2) = \Delta V = \text{const.} \tag{A.1}$$

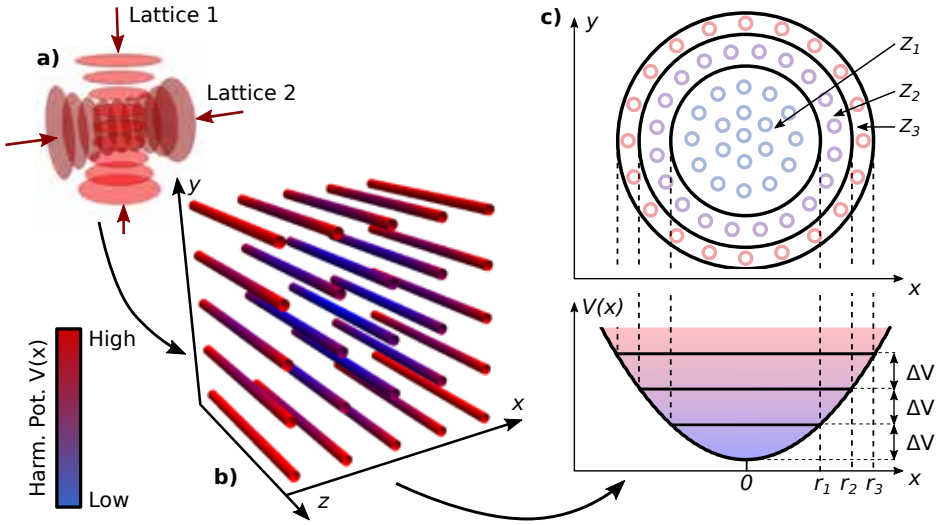

Figure A.1: **a:** fermionic wires are realized by means of two deep optical lattices propagating along orthogonal directions. **b:** the harmonic confinement induced by the confining lattices offsets the energy of the tubes. The color of the tubes reflect the spatial dependence of the harmonic potential strength from low (white) to high (dark). **c:** in case of pure harmonic confining potential zone with the same potential difference ΔV defines annular regions (Z_1, Z_2, Z_3) in the plane orthogonal to the tubes containing the same number of tubes. See the text fore more details.

from which we have that the area enclosed in each region

$$\pi(r_n^2 - r_{n-1}^2) = \frac{2\pi\Delta V}{m\omega^2} = \text{const.} \tag{A.2}$$

has a constant value. Since the area occupied by each tube depends only on the lattice spacing and not on the position of the tube within the lattice, we have that each region Z_n, consisting of tubes with $N_0 - n$ atoms, contains the same number of tubes.

In order to determine N_0 we use a numerical zero-temperature simulation in which we model the lattice confining potential as the sum of three harmonic potentials with frequencies determined by relation 1.17. Since during the lattice loading also the 1064 nm crossed trap in which the final evaporation is performed is present, also the harmonic contribution of this trap is taken into account. The space comprised within the lattice is then subdivided in cubic regions with dimensions $d \times d \times d$, where d is the lattice spacing, and the potential energy at the center of each cubic region is then evaluated.

In order to take into account the Fermi statistic, regions are then filled with at most one atom starting from the one with the lowest potential energy. Regions with increasing energy are then filled up to the total number of particles N_{at} that we determine through time-of-flight images. The result of the simulation easily allows to determine the number of atoms in the central tube N_0.

Appendix B
Scattering length in the open channel of an orbital Feshbach resonance

In order to determine the scattering length associated to the open channel of an orbital Feshbach resonance, we start from the Hamiltonian 4.24 which describes the coupling between closed and open channels, to which we refer, respectively, with the quantum states $|c\rangle, |o\rangle$. In the $\{|c\rangle, |o\rangle\}$ base the stationary Schroedinger equation associated to the Hamiltonian is

$$\begin{pmatrix} -\frac{\hbar^2}{2\mu}\nabla^2 + \Delta_B + V(a_d) & V(a_{ex}) \\ V(a_{ex}) & -\frac{\hbar^2}{2\mu}\nabla^2 + V(a_d) \end{pmatrix} \Psi = E\,\Psi \tag{B.1}$$

where μ is the reduced mass (in our case, for identical atoms, $\mu = m/2$ with m the atomic mass), $\delta_m(B)$ is the magnetic energy $\delta_m(B) = |h\,\delta_g\,\Delta m\,B|$ with δ_g the differential Landé factor, Δm the particles spin difference and B the magnetic field and $V(a)$ is the Huang-Yang pseudopotential

$$V(a) = \left(\frac{4\pi\hbar^2}{\mu}a\right)\delta(\mathbf{r})\frac{\partial}{\partial r}(r\cdot). \tag{B.2}$$

calculated for the s-wave scattering length a. The *direct* and *exchange* scattering lengths a_d and a_{ex} are respectively defined by expressions 4.25 and 4.26.

We assume the wavefunction to be given by the expressions 4.27, which is characterized by the radial part

$$\Psi_r(r) = \frac{\Psi(r)}{r} = \begin{pmatrix} u_o(r) \\ u_c(r) \end{pmatrix} = \begin{pmatrix} r - a_o \\ C\,e^{-\eta\,r} \end{pmatrix} \tag{B.3}$$

where $\eta = \sqrt{\mu\,\delta_m(B)/\hbar^2}$ and C is a normalization constant. In order to solve the problem, we have to take into account that in presence of a δ potential the radial Schroedinger equation (RSE) is modified by the presence of an extra $\delta(\mathbf{r})$ term appearing in the definition of the Laplacian operator (Khelashvili and Nadareishvili, 2015). In particular, in this case, the RSE reads

$$\frac{1}{r}\left[\frac{\partial^2 u(r)}{\partial r^2} - \frac{\ell(\ell+1)}{r^2}u(r)\right] - \frac{\delta(r)}{r^2}u(r) + \frac{2\mu}{\hbar^2}\left[E - U(r)\right]\frac{u(r)}{r} = 0 \tag{B.4}$$

where $U(\cdot)$ is the external potential and $u(\cdot)$ the radial wavefunction.

In our case, solving the problem in the low-energy limit ($E = 0$) for s waves ($\ell = 0$) and taking into account that in spherical coordinates $\delta(\mathbf{r}) = \delta(r)/(4\pi\, r^2)$, we have that the RSE reduces to the two coupled equations

$$\begin{cases} \frac{1}{r}\frac{\partial^2 u_o(r)}{\partial r^2} - \frac{\delta(r)}{r^2}u_o(r) - a_d\frac{\delta(r)}{r^2}\frac{\partial u_o(r)}{\partial r} - a_{ex}\frac{\delta(r)}{r^2}\frac{\partial u_c(r)}{\partial r} = 0 \\ \frac{1}{r}\frac{\partial^2 u_c(r)}{\partial r^2} - \frac{2\mu}{\hbar^2}\delta_m(B)u_c(r) - \frac{\delta(r)}{r^2}u_c(r) - a_d\frac{\delta(r)}{r^2}\frac{\partial u_c(r)}{\partial r} - a_{ex}\frac{\delta(r)}{r^2}\frac{\partial u_o(r)}{\partial r} = 0 \end{cases} . \tag{B.5}$$

We now multiply both equations by r^2 and integrate in dr from 0 to $\epsilon \to 0$. All the terms not containing $\delta(r)$ vanish and we end up with the system

$$\begin{cases} u_o(0) + a_d\, u_o'(0) + a_{ex}\, u_c'(0) = 0 \\ u_c(0) + a_d\, u_c'(0) + a_{ex}\, u_o'(0) = 0 \end{cases} \tag{B.6}$$

in which we replace u_o and u_c with the expressions B.3. The value a_o of the open channel scattering length (see expression 4.28) easily follows from this substitution.

Considerazioni conclusive

Fra gli innumerevoli versi spesi nel corso dei secoli per dipingere il cammino dell'uomo verso la conoscenza, fra i più significativi sono sicuramente quelli che Lucrezio dedica al filosofo greco Epicuro[1] , che il poeta descrive come il primo uomo che ribellandosi alla miseria della condizione umana, riesce a spingersi dove nessuno prima aveva mai osato, infrangendo *le porte sbarrate dell'Universo* e rivelando all'umanità le leggi che governano la Natura, ossia *ciò che può e non può essere e la ragione di ogni cosa*. Solo attraverso la conoscenza l'uomo riesce a sconfiggere la superstizione, una vittoria che lo rende *uguale al cielo*. Mi piace pernsare che ancora oggi, per quanto l'idea di *fisica* sia radicalmente mutata da quella di Lucrezio, l'ambizione ultima di chiunque si occupi di scienza sia contribuire almeno di un infinitesimo al cammino iniziato da Epicuro, spingendo l'orizzonte sempre un po' più oltre a quelle *mura fiammeggianti del mondo* che tanto intimorivano gli antichi. Non siamo fortunatamente soli come il filosofo greco in questa impresa e per quanto riguarda me, gli esperimenti che ho presentato nel corso di queste pagine non sarebbero mai stati possibili se non come frutto della collaborazione di tutti coloro che durante il mio dottorato hanno partecipato all'attività di ricerca del laboratorio 69 del dipartimento di Fisica dell'Università di Firenze. Leonardo Fallani innanzitutto, supervisore di questa tesi e di cui ormai da qualche anno apprezzo le straordinarie capacità, prima come insegnante e poi come fisico. Devo soprattutto a lui il progresso della mia carriera scientifica, da studente a (quasi) ricercatore. Jacopo Catani, anima pratica di questo gruppo di ricerca, senza le cui conoscenze nei più disparati ambiti della tecnica poco funzionerebbe in laboratorio. I dottorandi e poi postdoc Guido Pagano, Marco Mancini e Giacomo Cappellini, che mi hanno insegnato come si vive in un laboratorio di fisica atomica e i cui insegnamenti io ho contraccambiato con qualche esotica funzione di Mathematica. Lorenzo Franchi e Daniele Tusi, ultimi dottorandi ad essere arrivati qua, e con i quali è stato un piacere condividere le giornate di gioie e dolori della vita di laboratorio. Un ringraziamento infine a Fabrice Gerbier dell'LKB di Parigi e Leticia Tarruell dell'ICFO di Barcellona per l'attento lavoro di revisione di questa tesi.

[1] Tito Lucrezio Caro, *De rerum natura*, Libro I vv. 62-79

Bibliography

Ablowitz, M. J. and Fokas, A. S. (2003). *Complex variables: introduction and applications*. Cambridge University Press.

Aharonov, Y. and Bohm, D. (1959). Significance of electromagnetic potentials in the quantum theory. *Phys. Rev.*, **115**:3.

Aidelsburger, M., Atala, M., Lohse, M., Barreiro, J. T., Paredes, B., and Bloch, I. (2013). Realization of the Hofstadter Hamiltonian with Ultracold Atoms in Optical Lattices. *Phys. Rev. Lett.*, **111**:185301.

Aidelsburger, M., Atala, M., Nascimbène, S., Trotzky, S., Chen, Y.-A., and Bloch, I. (2011). Experimental realization of strong effective magnetic fields in an optical lattice. *Phys. Rev. Lett.*, **107**:255301.

Aidelsburger, M., Lohse, M., Schweizera, C., Atala, M., Barreiro, J. T., Nascimbène, S., Cooper, N. R., Bloch, I., and Goldman, N. (2015). Measuring the Chern number of Hofstadter bands with ultracold bosonic atoms. *Nat. Physics*, **11**:162.

An, F. A., Meier, E. J., and Gadway, B. (2017). Direct observation of chiral currents and magnetic reflection in atomic flux lattice. *Science Advances*, **3**:4.

Anderlini, M., Lee, P. J., Brown, B. L., Sebby-Strabley, J., Phillips, W. D., and Porto, J. V. (2007). Controlled exchange interaction between pairs of neutral atoms in an optical lattice. *Nature*, **448**:452.

Anderson, M. H., Ensher, J. R., Matthews, M. R., Wieman, C. E., and Cornell, E. A. (1995). Observation of Bose-Einstein condensation in a dilute atomic vapor. *Science*, **26**9:198.

Anisimovas, E., Raciunas, M., Sträter, C., Eckardt, A., Spielman, I. B., and Juzeliunas, G. (2016). Semisynthetic zigzag optical lattice for ultracold bosons. *Phys. Rev. A*, **94**:063632.

Ashcroft, N. W. and Mermin, N. D. (1976). *Solid state physics*. Harcourt College Publishers.

Atala, M., Aidelsburger, M., Lohse, M., Barreiro, J. T., Paredes, B., and Bloch, I. (2014). Observation of chiral currents with ultracoldatoms in bosonic ladders. *Nat. Phys.*, **10**:588.

Lorenzo Francesco Livi, *New quantum simulations with ultracold Ytterbium gases*, © 2020 Author(s), content CC BY 4.0 International, metadata CC0 1.0 Universal, published by Firenze University Press (www.fupress.com), ISSN 2612-8020 (online), ISBN 978-88-6453-989-8 (online PDF)

Avron, J. E., Osadchy, D., and Seiler, R. (2003). A topological look at the quantum Hall effect. *Physics Today*, **56**:38.

Barbarino, S., Taddia, L., Rossini, D., Fazio, R., and Mazza, L. (2015). Magnetic crystals and helical liquids in alkaline-earth fermionic gases. *Nat. Comm.*, **6**:8134.

Barbarino, S., Taddia, L., Rossini, D., Mazza, L., and Fazio, R. (2016). Synthetic gauge fields in synthetic dimensions: interactions and chiral edge modes. *New Jour. Phys.*, **18**:035010.

Barber, Z. W., Hoyt, C. W., Oates, C. W., Hollberg, L., Taichenachev, A. V., and Yudin, V. I. (2006). Direct excitation of the forbidden clock transition in neutral ^{174}Yb atoms confined to an optical lattice. *Phys. Rev. Lett.*, **96**:083002.

Barber, Z. W., Stalnaker, J. E., Lemke, N. D., Poli, N., Oates, C. W., Fortier, T. M., Diddams, S. A., Hollberg, L., Hoyt, C. W., Taichenachev, A. V., and Yudin, V. I. (2008). Optical lattice induced light shifts in an Yb atomic clock. *Phys. Rev. Lett.*, **100**:103002.

Bernevig, B. A. (2013). *Topological insulators and topological superconductors*. Princeton University Press.

Black, E. D. (2001). An introduction to Pound–Drever–Hall laser frequency stabilization. *American Journal of Physics*, **69**:79.

Blagoev, K. B. and Komarovskii, V. A. (1994). Lifetimes of levels of neutral and singly ionized lanthanides atoms. *Atomic Data and Nuclear Data Tables*, **56**:No. 1, Table XXV.

Blatt, S., Nicholson, T. L., Bloom, B. J., Williams, J. R., Thomsen, J. W., Julienne, P. S., and Ye, J. (2011). Measurement of optical Feshbach resonances in an ideal gas. *Phys. Rev. Lett.*, **107**:073202.

Bloch, I. (2005). Ultracold quantum gases in optical lattices. *Nat. Phys.*, **1**:23.

Bloch, I., Dalibard, J., and Nascimbène, S. (2012). Quantum simulations with ultracold quantum gases. *Nat Phys.*, **8**:267–376.

Bloch, I., Dalibard, J., and Zwerger, W. (2008). Many-body physics with ultracold gases. *Rev. Mod. Phys.*, **80**:885.

Bloom, B. J., Nicholson, T. L., Williams, J. R., Campbell, S. L., Bishof, M., Zhang, X., Zhang, W., Bromley, S. L., and Ye, J. (2014). An optical lattice clock with accuracy and stability at the 10^{-18} level. *Nature*, **506**:71.

Boada, O., Celi, A., Latorre, J. I., and Lewenstein, M. (2012). Quantum simulation of an extra dimension. *Phys. Rev. Lett.*, **108**:133001.

Boada, O., Celi, A., Rodríguez-Laguna, J., Latorre, J. I., and Lewenstein, M. (2015). Quantum simulation of non-trivial topology. *New J. Phys.*, **17**:045007.

Bouganne, R., Aguilera, M. B., Dareau, A., Soave, E., Beugnon, J., and Gerbier, F. (2017). Clock spectroscopy of interacting bosons in deep optical lattices. *New J. of Phys.*, **19**:113006.

Boyd, M. M., Zelevinsky, T., Ludlow, A. D., Blatt, S., Zanon-Willette, T., Foreman, S. M., and Ye, J. (2007). Nuclear spin effects in optical lattice clocks. *Phys. Rev. A*, **76**:022510.

Bransden, B. and Joachain, C. (2003). *Physics of atoms and molecules*. Addison-Wesley.

Buluta, I. and Nori, F. (2009). Quantum simulators. *Science*, **326**:108.

Busch, T., Englert, B., Rzazewski, K., and Wilkens, M. (1998). Two cold atoms in a harmonic trap. *Found. Phys.*, **28**:549.

Calonico, D., Bertacco, E. K., Calosso, C. E., Clivati, C., Costanzo, G. A., Frittelli, M., Godone, A., Mura, A.and Poli, N., Sutyrin, D. V., Tino, G., Zucco, M. E., and Levi, F. (2014). High-accuracy coherent optical frequency transfer over adoubled 642-km fiber link. *Appl. Phys. B*, **117**:979.

Calvanese Strinati, M., Cornfeld, E., Rossini, D., Barbarino, S., Dalmonte, M., Fazio, R., Sela, E., and Mazza, L. (2017). Laughlin-like states in bosonic and fermionic atomic synthetic ladders. *Phys. Rev. X*, **7**:021033.

Campbell, G. K., Mun, J., Boyd, M., Medley, P., Leanhardt, A. E., M., L. G., Pritchard, D. E., and Ketterle, W. (2006). Imaging the Mott insulator shells by using atomic clock shifts. *Science*, **313**:649.

Cappellini, G. (2012). *Development of a laser system for the encoding of qubits on degenerate Ytterbium atoms*. University of Florence.

Cappellini, G. (2016). *Two-orbital quantum physics in Yb Fermi gas esexploiting the* $^1S_0 \rightarrow {}^3P_0$ *clock transition*. Università degli studi di Firenze.

Cappellini, G., Lombardi, P., Mancini, M., Pagano, G., Pizzocaro, M., Fallani, L., and Catani, J. (2015). A compact ultranarrow high-power laser system for experiments with 578 nm Ytterbium clock transition. *Review of Scientific Instruments*, **86**:073111.

Cappellini, G., Mancini, M., Pagano, G., Lombardi, P., Livi, L., Siciliani de Cumis, M., Cancio, P., Pizzocaro, M., Calonico, D., Levi, F., Sias, C., Catani, J., Inguscio, M., and Fallani, L. (2014). Direct observation of coherent inter-orbital spin-exchange dynamics. *Phys. Rev. Lett.*, **113**:120402.

Cazailla, M. A. and Rey, A. M. (2014). Ultracold Fermi gases with emergent SU(N) symmetry. *Rep. on Prog. in Phys.*, **77**:124401.

Celi, A., Massignan, P., Ruseckas, J., Goldman, N., Spielman, I. B., Juzeliunas, G., and Lewenstein, M. (2014). Synthetic gauge fields in synthetic dimensions. *Phys. Rev. Lett.*, **112**:043001.

Cheng, Y., Zhang, R., and Zhang, P. (2016). Orbital Feshbach resonances with a small energy gap between open and closed channels. *Phys. Rev. A*, **93**:042708.

Cheng, Y., Zhang, R., and Zhang, P. (2017). Quantum defect theory for the orbital Feshbach resonance. *Phys. Rev. A*, **95**:013624.

Cheuk, L. W., Sommer, A. T., Hadzibabic, Z., Yefsah, T., Bakr, W. S., and Zwierlein, M. W. (2012). Spin-injection spectroscopy of a spin-orbit coupled Fermi gas. *Phys. Rev. Lett.*, **109**:095302.

Chin, C., Grimm, R., Julienne, P., and Tiesinga, E. (2010). Feshbach resonances in ultracold gases. *Rev. Mod. Phys.*, **82**:1225.

Ciurylo, R., Tiesinga, E., and Julienne, P. S. (2005). Optical tuning of the scattering length of cold alkaline-earth-metal atoms. *Phys. Rev. A*, **71**:030701.

Clark, D. L., Cage, M. E., Lewis, D. A., and Greenlees, G. W. (1979). Optical isotopic shifts and hyperfine splittings for Yb. *Phys. Rev. A*, **20**:239.

Clivati, C., Cappellini, G., Livi, L. F., Poggiali, F., de Cumis, M. S., Mancini, M., Pagano, G., Frittelli, M., Mura, A., Costanzo, G. A., Levi, F., Calonico, D., Fallani, L., Catani, J., and Inguscio, M. (2016). Measuring absolute frequencies beyond the GPS limit via long-haul optical frequency dissemination. *Opt. Express*, **24**:11865.

Clivati, C., Mura, A., Calonico, D., Levi, F., Costanzo, G. A., Calosso, C. E., and Godone, A. (2011). A planar-waveguide external cavity laser stabilization for an optical link with 10^{-19} frequency stability. *IEEE Trans. Ultrason. Ferroelectr.Freq. Control*, **58**:2582.

Cohen-Tannoudji, C. and Guéry-Odelin, D. (2011). *Advances in atomic physics*. World Scientific.

Cooper, N. (2008). Rapidly rotating atomic gases. *Advances in Physics*, **57**:539.

Daley, A. J., Boyd, M. M., Ye, J., and Zoller, P. (2008). Quantum computing with alkaline-earth-metal atoms. *Phys. Rev. Lett.*, **101**:170504.

Daley, A. J. and Simon, J. (2014). Effective three-body interactions via photon-assisted tunneling in an optical lattice. *Phys. Rev. A*, **89**:053619.

Dalfovo, F., Giorgini, S., Pitaevskii, L., and Stringari, S. (1999). Theory of Bose-Einstein condensation in trapped gases. *Rev. Mod. Phys*, **71**:463.

Dalibard, J. (2015). *Introduction to the physics of artificial gauge fields*. Proceedings of the International School of Physics "Enrico Fermi" of July 2014, "Quantum matter at ultralow temperatures".

Dalibard, J., Gerbier, F., Juzeliunas, G., and Öhberg, P. (2011). Artificial gauge potentials for neutral atoms. *Rev. Mod. Phys.*, **83**:146802.

Das, D., Barthwal, S., Banerjee, A., and Natarajan, V. (2005). Absolute frequency measurements in Yb with 0.08 ppb uncertainty: Isotope shifts and hyperfine structure in the 399 nm ${}^1S_0 \rightarrow {}^1P_1$ line. *Phys. Rev. A*, **72**:032506.

Davis, K. B., Mewes, M. O., Andrews, M. R., van Druten, N. J., Durfee, D. S., Kurn, D. M., and Ketterle, W. (1995). Bose-Einstein condensation in a gas of Sodium atoms. *Phys. Rev. Lett.*, **75**:3969.

DeMarco, B. and Jin, D. S. (1999). Onset of Fermi degeneracy in a trapped atomic gas. *Science*, **285**:1703.

Derevianko, A. and Katori, H. (2011). Colloquium: Physics of optical lattice clocks. *Rev. Mod. Phys.*, **83**:331.

Dicke, R. H. (1953). The effect of collisions upon the Doppler width of spectral lines. *Phys. Rev.*, **89**:472.

Dutta, O., Eckardt, A., Hauke, P., Malomed, B., and Lewenstein, M. (2011). Bose–Hubbard model with occupation-dependent parameters. *New J. of Phys.*, **13**:023019.

Dzuba, V. A. and Derevianko, A. (2010). Dynamic polarizabilities and related properties of clock states of the Ytterbium atom. *Journal of Physics B*, **43**:074011.

Enomoto, K., Kasa, K., Kitagawa, M., and Takahashi, Y. (2008). Optical Feshbach Resonance Using the Intercombination Transition. *Phys. Rev. Lett.*, **101**:203201.

Feynman, R. P. (1982). Simulating physics with computers. *International Journal of Theoretical Physics*, **21**:467.

Fläschner, N., Rem, B. S., Tarnowski, M., Vogel, D., Lühmann, D.-S., Sengstock, K., and Weitenberg, C. (2016). Experimental reconstruction of the Berry curvature in a Floquet Bloch band. *Science*, **352**:1091.

Foot, C. J. (2012). *Atomic physics*. Oxford University Press.

Franchi, L. (2016). *Controllo di fermioni ultrafreddi con una transizione ottica di orologio: accoppiamento spin-orbita e dimensioni sintetiche*. Università degli studi di Firenze.

Franchi, L., Livi, L. F., Cappellini, G., Binella, G., Inguscio, M., Catani, J., and Fallani, L. (2017). State-dependent interactions in ultracold ^{174}Yb probed by optical clock spectroscopy. *New Journal of Physics*, **19**:103037.

Frohlich, B., Lahaye, T., Kaltenhäuser, B., Kübler, H., Müller, S., Koch, T., Fattori, M., and Pfau, T. (2007). Two-frequency acousto-optic modulator driver to improve the beam pointing stability during intensity ramps. *Review of Scientific Instruments*, **78**:043101.

Galitski, V. and Spielman, I. B. (2013). Spin–orbit coupling in quantum gases. *Nature*, **494**:49.

Georgescu, I. M., Ashhab, S., and Nori, F. (2014). Quantum simulation. *Rev. Mod. Phys.*, **86**:153.

Gerbier, F. and Dalibard, J. (2010). Gauge fields for ultracold atoms in optical superlattices. *New J. Phys.*, **12**:033007.

Girvin, S. M. (1999). *The quantum Hall effect: Novel excitation and broken symmetries*. Springer (Part of the book "Topological aspects of low dimensional systems").

Giuliani, G. and Vignale, G. (2005). *Quantum theory of the electron liquid*. Cambridge University Press.

Goldman, N., , Juzeliunas, G., Öhberg, P., and Spielman, I. (2014). Light-induced gauge fields for ultracold atoms. *Rep. Prog. Phys.*, **77**:126401.

Goldman, N., Budich, J. C., and Zoller, P. (2016). Topological quantum matter with ultracold gases in optical lattices. *Nat. Phys.*, **12**:639.

Gorshkov, A. V., Hermele, M., Gurarie, V., Xu, C., Julienne, P. S., Ye, J., Zoller, P., Demler, E., Lukin, M. D., and Rey, A. M. (2009). Two-orbital SU(N) magnetism with ultracold alkaline-earth atoms. *Nature Physics*, **6**:289.

Greiner, M., Bloch, I., Mandel, O., Hänsch, T. W., and Esslinger, T. (2001). Exploring Phase Coherence in a 2D Lattice of Bose-Einstein Condensates. *Phys. Rev. Lett.*, **87**:160405.

Greiner, M., Mandel, O., Esslinger, T., Hansch, T. W., and Bloch, I. (2002). Quantum phase transition from a superfluid to a Mott insulator in a gas of ultracold atoms. *Nature*, **415**:39.

Grimm, R., Weidemüller, M., and Ovchinnikov, Y. B. (2000). Optical dipole traps for neutral atoms. *Advances In Atomic, Molecular, and Optical Physics*, **42**:95.

Gross, C. and Bloch, I. (2017). Quantum simulations with ultracold atoms in optical lattices. *Science*, **357**:995.

Halperin, B. I. (1982). Quantized Hall conductance, current-carrying edge states, and the existence of extended states in a two-dimensional disordered potential. *Phys. Rev. B*, **25**:2185.

Hansch, T. and Couillaud, B. (1980). Laser frequency stabilization by polarization spectroscopy of a reflecting reference cavity. *Optics Communications*, **35**:441.

Harper, P. G. (1955). Single Band Motion of Conduction Electrons in a Uniform Magnetic Field. *Proc. of the Physical Society A*, **68**:874.

Hasan, M. Z. and Kane, C. L. (2010). Topological insulators. *Rev. Mod. Phys.*, **82**:3045.

Hatsugai, Y. (1993). Chern number and edge states in the integer quantum Hall effect. *Phys. Rev. Lett.*, **71**:3697.

Hatsugai, Y. (1997). Topological aspects of the quantum Hall effect. *Journal of Physics*, **9**:2507.

He, L., Wang, J., Peng, S., Liu, X., and Hu, H. (2016). Strongly correlated Fermi superfluid near an orbital Feshbach resonance: Stability, equation of state, and Leggett mode. *Phys. Rev. A*, **94**:043624.

Hinkley, N., Sherman, J. A., Phillips, N. B., Schioppo, M., Lemke, N. D., Beloy, K., Pizzocaro, M., Oates, C. W., and Ludlow, A. D. (2013). An Atomic Clock with 10^{-18} Instability. *Science*, **341**:6151.

Ho, T.-L. (1998). Spinor Bose condensates in optical traps. *Phys. Rev. Lett.*, **81**:742.

Höfer, M., Riegger, L., Scazza, F., Hofrichter, C., Fernandes, D. R., Parish, M. M., Levinsen, J., Bloch, I., and Fölling, S. (2015). Observation of an orbital interaction-induced Feshbach resonance in ^{173}Yb. *Phys. Rev. Lett.*, **115**:265302.

Hofstadter, D. R. (1976). Energy levels and wave functions of bloch electrons in rational and irrational magnetic fields. *Phys. Rev. B*, **14**:2239.

Hong, T., Cramer, C., Nagourney, W., and Fortson, E. N. (2005). Optical clocks based on ultranarrow three-photon resonances in alkaline earth atoms. *Phys. Rev. Lett.*, **94**:050801.

Hoyt, C. W., Barber, Z. W., Oates, C. W., Fortier, T. M., Diddams, S. A., and Hollberg, L. (2005). Observation and absolute frequency measurements of the $^1S_0$-$^3P_0$ optical clock transition in neutral Ytterbium. *Phys. Rev. Lett.*, **95**:083003.

Huang, K. (1967). *Statistical Mechanics*. Wiley.

Huang, K. and Yang, C. (1957). Quantum mechanical many-body problem with hard-sphere interaction. *Phys. Review*, **105**:767.

Hügel, D. and Paredes, B. (2014). Chiral ladders and the edges of quantum Hall insulators. *Phys. Rev. A*, **89**:023619.

Hundt, B. (2011). *Momentum-Resolved Optical Lattice Modulation Spectroscopy on Bose-Fermi Mixtures*. Universität Hamburg.

Iemini, F., Mazza, L., Fallani, L., Zoller, P., Fazio, R., and Dalmonte, M. (2017). Majorana quasiparticles protected by $\mathbb{Z}_2$ angular momentum conservation. *Phys. Rev. Lett.*, **118**:200404.

Inguscio, M. and Fallani, L. (2013). *Atomic physics: precise measurements & ultracold matter*. Oxford University Press.

Jaksch, D. and Zoller, P. (2003). Creation of effective magnetic fields in optical lattices: the Hofstadter butterfly for cold neutral atoms. *New J. Phys.*, **5**:56.

Jaksch, D. and Zoller, P. (2005). The cold atom Hubbard toolbox. *Annals of Physics*, **315**:52.

Jiménez-García, K., LeBlanc, L. J., Williams, R. A., Beeler, M. C., Perry, A. R., and Spielman, I. B. (2012). Peierls substitution in an engineered lattice potential. *Phys. Rev. Lett.*, **108**:225303.

Johnson, P. R., Tiesinga, E., Porto, J. V., and Williams, C. J. (2009). Effective three-body interactions of neutral bosons in optical lattices. *New J. Phys.*, **11**:093022.

Kane, C. and Moore, J. (2011). Topological insulators. *Physics World*, **24**:32.

Kane, C. L. and Mele, E. J. (2005). Z2 topological order and the quantum spin Hall effect. *Phys. Rev. Lett.*, **95**:146802.

Kato, S., Inaba, K., Sugawa, S., Shibata, K., Yamamoto, R., Yamashita, M., and Takahashi, Y. (2016). Laser spectroscopic probing of coexisting superfluid and insulating states of an atomic Bose–Hubbard system. *Nat. Comm.*, **7**:11341.

Kennedy, C. J., Siviloglou, G. A., Miyake, H., Burton, W. C., and Ketterle, W. (2013). Spin-orbit coupling and quantum spin Hall effect for neutral atoms without spin llips. *Phys. Rev. Lett.*, **111**:225301.

Khelashvili, A. A. and Nadareishvili, T. P. (2015). Singular behavior of the Laplace operator in polar spherical coordinates and some of its consequences for the radial wave function at the origin of coordinates. *Physics of Particles and Nuclei Letters*, **12**:11.

Kim, M., Lee, J., Shin, Y., and Mun, J. (2016). Measurements of optical Feshbach resonances of ^{174}Yb atoms. *Phys. Rev. A*, **94**:042703.

Kitagawa, M., Enomoto, K., Kasa, K., Takahashi, Y., Ciury□o, R., Naidon, P., and Julienne, P. S. (2008). Two-color photoassociation spectroscopy of Ytterbium atoms and the precise determinations of s-wave scattering lengths. *Phys. Rev. A*, **77**:012719.

Klitzing, K. v., Dorda, G., and Pepper, M. (1980). New method for high-accuracy determination of the fine-structure constant based on quantized Hall resistance. *Phys. Rev. Lett.*, **45**:494.

Köhl, M., Moritz, H., Stöferle, T., Günter, K., and Esslinger, T. (2005). Fermionic atoms in a three dimensional optical lattice: observing Fermi surfaces, dynamics, and interactions. *Phys. Rev. Lett.*, **94**:080403.

Kohmoto, M. (1985). Topological invariant and the quantization of the Hall conductance. *Annals of Physics*, **160**:343.

Kolkowitz, S., Bromley, S. L., Bothwell, T., Wall, M. L., Marti, G. E., Koller, A. P., Zhang, X., Rey, A. M., and Ye, J. (2017). Spin–orbit-coupled fermions in an optical lattice clock. *Nature*, **542**:66.

Laughlin, R. B. (1981). Quantized Hall conductivity in two dimensions. *Phys. Rev. B*, **23**:5632.

Levi, F., Calonico, D., Calosso, C. E., Godone, A., Micalizio, S., and Costanzo, G. A. (2014). Accuracy evaluation of ITCsF2: a nitrogen cooled caesium fountain. *Metrologia*, **51**:270.

Levi, F., Calonico, D., Mura, A., Frittelli, M., Calosso, C. E., Zucco, M., Clivati, C., Costanzo, G. A., Ambrosini, R., Galzerano, G., De Natale, P., Mazzotti, D., Sutyrin, N. P. D. V., and Tino, G. M. (2013). *LIFT-the Italian link for time and frequency*. In

European Frequency and Time Forum International Frequency Control Symposium (EFTF/IFC), Joint, pages 477–480.

Lewenstein, M., Sanpera, A., and Ahufinger, V. (2012). *Ultracold Atoms in Optical Lattices: Simulating quantum many-body systems*. Oxford University Press.

Lewenstein, M., Sanpera, A., Ahufinger, V., Damski, B., Sen(De), A., and Sen, U. (2007). Ultracold atomic gases in optical lattices: mimicking condensed matter physics and beyond. *Advances in Physics*, **56**:243.

Lide, D. R. (2004). *Handbook of chemistry and physics*. CRC Press.

Lin, Y. J., Compton, R. L., Jimenex-Garcia, K., Porto, J. V., and Spielman, I. B. (2009a). Synthetic magnetic fields for ultracold neutral atoms. *Nature*, **462**:7273.

Lin, Y.-J., Compton, R. L., Perry, A. R., Phillips, W. D., Porto, J. V., and Spielman, I. B. (2009b). Bose-Einstein condensate in a uniform light-induced vector potential. *Phys. Rev. Lett.*, **102**:130401.

Lin, Y. J., Jimenez-Garcia, K., and Spielman, I. B. (2011). Spin-orbit-coupled Bose-Einstein condensates. *Nature*, **471**:83.

Livi, L. F. (2012). *Trasporto ottico di atomi ultrafreddi a lunga distanza*. Università degli studi di Firenze.

Livi, L. F. (2014). *Creazione di stati atomici coerenti tramite transizioni proibite in gas di fermioni ultrafreddi*. Università degli studi di Firenze.

Livi, L. F., Cappellini, G., Diem, M., Franchi, L., Clivati, C., Frittelli, M., Levi, F., Calonico, D., Catani, J., Inguscio, M., and Fallani, L. (2016). Synthetic dimensions and spin-orbit coupling with an optical clock transition. *Phys. Rev. Lett.*, **117**:220401.

Lombardi, M. (2008). The use of GPS disciplined oscillators as primary frequency standards for calibration and metrology laboratories. *NCSLI Measure: J. Meas. Sci.*, **3**:56.

Ludlow, A. D., Boyd, M. M., Ye, J., Peik, E., and Schmidt, P. O. (2015). Optical atomic clocks. *Rev. Mod. Phys.*, **87**:637.

Ludlow, A. D., Lemke, N. D., Sherman, J. A., Oates, C. W., Quéméner, G., von Stecher, J., and Rey, A. M. (2011). Cold-collision-shift cancellation and inelastic scattering in a Yb optical lattice clock. *Phys. Rev. A*, **84**:052724.

Mancini, M. (2016). *Quantum simulation with Ytterbium atoms in synthetic dimensions*. Università degli studi di Firenze.

Mancini, M., Pagano, G., Cappellini, G., Livi, L. F., Rider, M., Catani, J., Sias, C., Zoller, P., Inguscio, M., Dalmonte, M., and Fallani, L. (2015). Observation of chiral edge states with neutral fermions in synthetic Hall ribbons. *Science*, **349**:6255.

Manoharan, H. C. (2010). Topological insulators: A romance with many dimensions. *Nature Nanotechnology*, **5**:477–479.

Marzari, N., Mostofi, A. A., Yates, J. R., Souza, I., and Vanderbilt, D. (2012). Maximally localized Wannier functions: Theory and applications. *Rev. Mod. Phys.*, **84**:1419.

Meggers, W. F. and Tech, J. L. (1978). The first spectrum of ytterbium (yb i). *Journal of Research of the National Bureau of Standards*, **83**:No. 1.

Menotti, C., Pedri, P., and Stringari, S. (2002). Expansion of an interacting Fermi gas. *Phys. Rev. Lett.*, **89**:250402.

Moore, J. E. (2010). The birth of topological insulators. *Nature*, **464**:194.

Mugel, S., Dauphin, A., Massignan, P., Tarruell, L., Lewenstein, M., Lobo, C., and Celi, A. (2017). Measuring Chern numbers in Hofstadter strips. *SciPost Phys.*, **3**:12.

Nagourney, W. (2010). *Quantum electronics for atomic physics*. Oxford University Press.

Nayak, C., Simon, S. H., Stern, A., Freedman, M., and Das Sarma, S. (2008). Non-Abelian anyons and topological quantum computation. *Rev. Mod. Phys.*, **80**:1083.

Nenciu, G. (1991). Dynamics of band electrons in electric and magnetic fields: rigorous justification of the effective Hamiltonians. *Rev. Mod. Phys.*, **63**:91.

O'Hara, K. M., Hemmer, S. L., Gehm, M. E., Granade, S. R., and Thomas, J. E. (2002). Observation of a strongly interacting degenerate Fermi gas of atoms. *Science*, **298**:2179.

Ovsyannikov, V. D. and Chaplygin, E. V. (2001). Radiative properties of Zeeman components of atomic multiplets: Magnetically induced decay of metastable $^3P_2$ and $^3P_0$ states of inert gases. *Optics and Spectroscopy*, **90**:149.

Ozawa, T., Price, H. M., Goldman, N., Zilberberg, O., and Carusotto, I. (2016). Synthetic dimensions in integrated photonics: From optical isolation to four-dimensional quantum Hall physics. *Phys. Rev. A*, **93**:043827.

Pagano, G. (2011). *Raffreddamento e intrappolamento di atomi di Itterbio*. University of Roma "La Sapienza".

Pagano, G. (2015). *Many-body physics with Ytterbium Fermi gases in optical lattices: from one-dimensional systems to orbital magnetism*. Scuola Normale Superiore, Pisa.

Pagano, G., Mancini, M., Cappellini, G., Livi, L., Sias, C., Catani, J., Inguscio, M., and Fallani, L. (2015). Strongly interacting gas of two-electron fermions at an orbital Feshbach resonance. *Phys. Rev. Lett.*, **115**:265301.

Paredes, B., Zoller, P., and Cirac, J. I. (2003). Fractional quantum Hall regime of a gas of ultracold atoms. *Solid State Communications*, **127**:155.

Peierls, R. (1933). Zur Theorie des Diamagnetismus von Leitungselektronen. *Z. Physik*, **80**:763.

Petrov, D. S. (2003). *Bose-Einstein condensation in low-dimensional trapped gases*. University of Amsterdam.

Pini, M. (2014). *Atomi ultrafreddi in reticoli ottici: soluzioni numeriche e applicazioni in computazione quantistica*. Università di Firenze.

Poli, N., Barber, Z. W., Lemke, N. D., Oates, C. W., Ma, L. S., Stalnaker, J. E., Fortier, T. M., Diddams, S. A., Hollberg, L., Bergquist, J. C., Brusch, A., Jefferts, S., Heavner, T., and Parker, T. (2008). Frequency evaluation of the doubly forbidden $^1S_0 \rightarrow ^3P_0$ transition in bosonic ^{174}Yb. *Phys. Rev. A*, **77**:050501.

Poli, N., Oates, C. W., Gill, P., and Tino, G. M. (2013). Optical atomic clocks. *La Rivista del Nuovo Cimento*, **36**:12.

Porsev, S. G. and Derevianko, A. (2003). Hyperfine quenching of the metastable $^3P_{0,2}$ states in divalent atoms. *Phys. Rev. A*, **69**:042506.

Porsev, S. G., Derevianko, A., and Fortson, E. N. (2004). Possibility of an optical clock using the ^{3}P$_0$ transition in Yb atoms held in an optical lattice. *Phys. Rev. A*, **69**:021403.

Porsev, S. G., Rakhlina, Y. G., and Kozlov, M. G. (1999). Electric-dipole amplitudes, lifetimes, and polarizabilities of the low-lying levels of atomic Ytterbium. *Phys. Rev. A*, **60**:2781.

Price, H. M., Ozawa, T., and Goldman, N. (2017). Synthetic dimensions for cold atoms from shaking a harmonic trap. *Phys. Rev. A.*, **95**:023607.

Price, H. M., Zilberberg, O., Ozawa, T., Carusotto, I., and Goldman, N. (2015). Four-dimensional quantum Hall effect with ultracold atoms. *Phys. Rev. Lett.*, **115**:195303.

Qi, X. and s. Zhang (2010). The quantum spin Hall effect and topological insulators. *Physics Today*, **63**:33.

Santra, R., Arimondo, E., Ido, T., Greene, C. H., and Ye, J. (2005). High-accuracy optical clock via three-level coherence in neutral bosonic ^{88}Sr. *Phys. Rev. Lett.*, **94**:173002.

Scazza, F., Hofrichter, C., Höfer, M., Groot, P. C. D., Bloch, I., and Fölling, S. (2014). Observation of two-orbital spin-exchange interactions with ultracold SU(N)-symmetric fermions. *Nature Physics*, **10**:779.

Steck, D. A. (2007). *Quantum and Atom Optics*. Oregon Center for Optics and Department of Physics, University of Oregon.

Steck, D. A. (2015). Rubidium 87 D Line Data.

Stellmer, S., Grimm, R., and Schreck, F. (2011). Detection and manipulation of nuclear spin states in fermionic strontium. *Phys. Rev. A*, **84**:043611.

Struck, J., Ölschläger, C., Weinberg, M., Hauke, P., Simonet, J., Eckardt, A., Lewenstein, M., Sengstock, K., and Windpassinger, P. (2012). Tunable gauge potential for neutral and spinless particles in driven optical lattices. *Phys. Rev. Lett.*, **108**:225304.

Stuhl, B. K., Lu, H.-I., Aycock, L. M., Genkina, D., and Spielman, I. B. (2015). Visualizing edge states with an atomic Bose gas in the quantum Hall regime. *Science*, **349**:6255.

Sugawa, S., Takasu, Y., Enomoto, K., and Takahashi, Y. (2013). *Ultracold Ytterbium: Generation, many-body physics and molecules (part of the book "Annual review of cold atoms and molecules", volume 1*.

Suszalski, D. and Zakrzewski, J. (2016). Different lattice geometries with a synthetic dimension. *Phys. Rev. A*, **94**:033602.

Taddia, L., Cornfeld, E., Rossini, D., Mazza, L., Sela, E., and Fazio, R. (2017). Topological fractional pumping with alkaline-earth-like atoms in synthetic lattices. *Phys. Rev. Lett.*, **118**:230402.

Taichenachev, A. V. and Yudin, V. I. (2006). Magnetic field-induced spectroscopy of forbidden optical transitions with application to lattice-based optical atomic clocks. *Phys. Rev. Lett*, **96**:083001.

Taie, S., Takasu, Y., Sugawa, S., Yamazaki, R., Tsujimoto, T., Murakami, R., and Takahashi, Y. (2010). Realization of a $SU(2) \times SU(6)$ system of fermions in a cold atomic gas. *Phys. Rev. Lett.*, **105**:190401.

Thouless, D. J., Kohmoto, M., Nightingale, M. P., and den Nijs, M. (1982). Quantized Hall conductance in a two-dimensional periodic potential. *Phys. Rev. Lett.*, **49**:6.

Tong, D. (2016). *Lectures on the quantum Hall effect*.

Traverso, A., Chakraborty, R., Martinez de Escobar, Y. N., Mickelson, P. G., Nagel, S. B., Yan, M., and Killian, T. C. (2009). Inelastic and elastic collision rates for triplet states of ultracold strontium. *Phys. Rev. A*, **79**:060702.

Trotzky, S., Chen, Y., Flesch, A., McCulloch, I. P., Schollwöck, U., Eisert, J., and Bloch, I. (2012). Probing the relaxation towards equilibrium in an isolated strongly correlated one-dimensional Bose gas. **8**:325.

Van Hove, L. (1953). The occurrence of singularities in the elastic frequency distribution of a crystal. *Phys. Rev.*, **89**:1189.

Wall, M. L., Koller, A. P., Li, S., Zhang, X., Cooper, N. R., Ye, J., and Rey, A. M. (2016). Synthetic apin-orbit coupling in an optical lattice clock. *Phys. Rev. Lett.*, **116**:035301.

Wang, P., Yu, Z., Fu, Z., Miao, J., Huang, L., Chai, S., Zhai, H., and Zhang, J. (2012). Spin-orbit coupled degenerate Fermi gases. *Phys. Rev. Lett.*, **109**:095301.

Widera, A., Gerbier, F., Fölling, S., Gericke, T., Mandel, O., and Bloch, I. (2006). Precision measurement of spin-dependent interaction strengths for spin-1 and spin-2 87 Rb atoms. *New J. Phys.*, **8**:152.

Will, S., Best, T., Schneider, U., Hackermüller, L., Lühmann, D., and Bloch, I. (2010). Time-resolved observation of coherent multi-body interactions in quantum phase revivals. *Nature*, **465**:197.

Xu, J., Zhang, R., Cheng, Y., Zhang, P., Qi, R., and Zhai, H. (2016). Reaching a Fermi-superfluid state near an orbital Feshbach resonance. *Phys. Rev. A*, **94**:033609.

Yamaguchi, A. (2008). *Metastable state of ultracold and quantum degenerate Ytterbium atoms*. Kyoto University.

Yoshioka, D. (2002). *The quantum Hall effect*. Springer.

Zhai, H. (2012). Spin–orbit coupled quantum gases. *Int. Journal of Modern Phys. B*, **26**:1230001.

Zhai, H. (2015). Degenerate quantum gases with spin–orbit coupling: a review. *Rep. on Prog. in Phys.*, **78**:026001.

Zhang, R., Cheng, Y., Zhai, H., and Zhang, P. (2015). Orbital Feshbach resonance in alkali-earth atoms. *Phys. Rev. Lett.*, **115**:135301.

Zhang, R., Zhang, D., Cheng, Y., Chen, W., Zhang, P., and Zhai, H. (2016). Kondo effect in alkaline-earth-metal atomic gases with confinement-induced resonances. *Phys. Rev. A*, **93**:043601.

Zhang, X., Bishof, M., Bromley, S. L., Kraus, C. V., Safronova, M. S., Zoller, P., Rey, A. M., and Ye, J. (2014). Spectroscopic observation of SU(N)-symmetric interactions in Sr orbital magnetism. *Science*, **345**:1467.

ANNO 2007

Bracardi M., *La Materia e lo Spirito. Mario Ridolfi nel paesaggio umbro*

Coppi E., *Purines as Transmitter Molecules. Electrophysiological Studies on Purinergic Signalling in Different Cell Systems*

Mannini M., *Molecular Magnetic Materials on Solid Surfaces*

Natali I., *The Ur-Portrait.* Stephen Hero *ed il processo di creazione artistica in* A Portrait of the Artist as a Young Man

Petretto L., *Imprenditore ed Università nello start-up di impresa. Ruoli e relazioni critiche*

ANNO 2008

Bemporad F., *Folding and Aggregation Studies in the Acylphosphatase-Like Family*

Buono A., *Esercito, istituzioni, territorio. Alloggiamenti militari e «case Herme» nello Stato di Milano (secoli XVI e XVII)*

Castenasi S., *La finanza di progetto tra interesse pubblico e interessi privati*

Colica G., *Use of Microorganisms in the Removal of Pollutants from the Wastewater*

Gabbiani C., *Proteins as Possible Targets for Antitumor Metal Complexes: Biophysical Studies of their Interactions*

ANNO 2009

Decorosi F., *Studio di ceppi batterici per il biorisanamento di suoli contaminati da Cr(VI)*

Di Carlo P., *I Kalasha del Hindu Kush: ricerche linguistiche e antropologiche*

Di Patti F., *Finite-Size Effects in Stochastic Models of Population Dynamics: Applications to Biomedicine and Biology*

Inzitari M., *Determinants of Mobility Disability in Older Adults: Evidence from Population-Based Epidemiologic Studies*

Macrì F., *Verso un nuovo diritto penale sessuale. Diritto vivente, diritto comparato e prospettive di riforma della disciplina dei reati sessuali in Italia*

Pace R., *Identità e diritti delle donne. Per una cittadinanza di genere nella formazione*

Vignolini S., *Sub-Wavelength Probing and Modification of Complex Photonic Structures*

ANNO 2010

Fedi M., *«Tuo lumine». L'accademia dei Risvegliati e lo spettacolo a Pistoia tra Sei e Settecento*

Fondi M., *Bioinformatics of genome evolution: from ancestral to modern metabolism. Phylogenomics and comparative genomics to understand microbial evolution*

Marino E., *An Integrated Nonlinear Wind-Waves Model for Offshore Wind Turbines*

Orsi V., *Crisi e Rigenerazione nella valle dell'Alto Khabur (Siria). La produzione ceramica nel passaggio dal Bronzo Antico al Bronzo Medio*

Polito C., *Molecular imaging in Parkinson's disease*

Romano R., *Smart Skin Envelope. Integrazione architettonica di tecnologie dinamiche e innovative per il risparmio energetico*

ANNO 2011

Acciaioli S., *Il* trompe-l'*œil letterario, ovvero il sorriso ironico nell'opera di Wilhelm Hauff*

Bernacchioni C., *Sfingolipidi bioattivi e loro ruolo nell'azione biologica di fattori di crescita e citochine*

Fabbri N., *Bragg spectroscopy of quantum gases: Exploring physics in one dimension*

Gordillo Hervás R., *La construcción religiosa de la Hélade imperial: El Panhelenion*

Mugelli C., *Indipendenza e professionalità del giudice in Cina*

Pollastri S., *Il ruolo di TAF12B e UVR3 nel ciclo circadiano dei vegetali*

Salizzoni E., *Paesaggi Protetti. Laboratori di sperimentazione per il paesaggio costiero euro-mediterraneo*

ANNO 2012

Evangelisti E., *Structural and functional aspects of membranes: the involvement of lipid rafts in Alzheimer's disease pathogenesis. The interplay between protein oligomers and plasma membrane physicochemical features in determining cytotoxicity*

Bondì D., *Filosofia e storiografia nel dibattito anglo-americano sulla svolta linguistica*

Petrucci F., *Petri Candidi Decembrii Epistolarum iuvenilium libri octo. A cura di Federico Petrucci*

Alberti M., *La 'scoperta' dei disoccupati. Alle origini dell'indagine statistica sulla disoccupazione nell'Italia liberale (1893-1915)*

Gualdani R., *Using the Patch-Clamp technique to shed light on ion channels structure, function and pharmacology*

Adessi A., *Hydrogen production using Purple Non-Sulfur Bacteria (PNSB) cultivated under natural or artificial light conditions with synthetic or fermentation derived substrates*

Ramalli A., *Development of novel ultrasound techniques for imaging and elastography. From simulation to real-time implementation*

ANNO 2013

Lunghi C., *Early cross-modal interactions and adult human visual cortical plasticity revealed by binocular rivalry*

Brancasi I., *Architettura e illuminismo: filosofia e progetti di città nel tardo Settecento francese*

Cucinotta E., *Produzione poetica e storia nella prassi e nella teoria greca di età classica*

Pellegrini L., *Circostanze del reato: trasformazioni in atto e prospettive di riforma*

Locatelli M., *Mid infrared digital holography and terahertz imaging*

Muniz Miranda F., *Modelling of spectroscipic and structural properties using molecular dynamics*

Bacci M., *Dinamica molecolare e modelli al continuo per il trasporto di molecole proteiche - Coarse-grained molecular dynamics and continuum models for the transport of protein molecole*

Martelli R., *Characteristics of raw and cooked fillets in species of actual and potential interest for italian aquaculture: rainbow trout (oncorhynchus mykiss) and meagre (argyrosomus regius)*

ANNO 2014

Lana D., *A study on cholinergic signal transduction pathways involved in short term and long term memory formation in the rat hippocampus. Molecular and cellular alterations underlying memory impairments in animal models of neurodegeneration*

Lopez Garcia A., *Los* Auditoria *de Roma y el* Athenaeum *de Adriano*

Pastorelli G., *L'immagine del cane in Franz Kafka*

Bussoletti A., *L'età berlusconiana. Il centro-destra dai poli alla Casa della Libertà 1994-2001*

Malavolti L., *Single molecule magnets sublimated on conducting and magnetic substrates*

Belingardi C., *Comunanze urbane. Autogestione e cura dei luoghi*

Guzzo E., *Il tempio nel tempio. Il tombeau di Rousseau al Panthéon di Parigi*

ANNO 2015

Lombardi N*., MEREAFaPS: uno Studio di Farmacovigilanza Attiva e Farmacoepidemiologia in Pronto Soccorso*

Baratta L*., «A Marvellous and Strange Event». Racconti di nascite mostruose nell'Inghilterra della prima età moderna*

Richichi I.A*., La teocrazia: crisi e trasformazione di un modello politico nell'Europa del XVIII secolo*

Palandri L*., I giudici e l'arte. Stati Uniti ed Europa a confronto*

Caselli N*., Imaging and engineering optical localized modes at the nano scale*

Calabrese G*., Study and design of topologies and components for high power density dc-dc converters*

Porzilli S*., Rilevare l'architettura in legno. Protocolli metodologici per la documentazione delle architetture tradizionali lignee: i casi studio dei villaggi careliani in Russia*

ANNO 2016

Martinelli S.*, Study of intracellular signaling pathways in Chronic Myeloproliferative Neoplasms*

Abbado E.,*"La celeste guida". L'oratorio musicale a Firenze: 1632-1799*

Focarile P., *I Mannelli di Firenze. Storia mecenatismo e identità di una famiglia fra cultura mercantile e cultura cortigiana*

Nucciotti A., *La dimensione normativa dell'imprenditorialità accademica. Tre casi di studio sugli investigatori principali, i loro gruppi di ricerca e i fattori di innesco dell'imprenditorialità accademica*

Peruzzi P., *La inutilizzabilità della prestazione*

Lottini E., *Magnetic Nanostructures: a promising approach towards RE-free permanent magnets*

Uricchio T., *Image Understanding by Socializing the Semantic Gap*

ANNO 2017

Valenti R., *Cerebral Small Vessel Disease and Cerebral Amyloid Angiopathy: neuroimaging markers, cognitive features and rehabilitative issues*

Starnini M., L'uomo tutto intero*. Biografia di Carlo Livi, psichiatra dell'Ottocento*

Verardi D., *La scienza e i segreti della natura a Napoli nel Rinascimento: la magia naturale di Giovan Battista Della Porta*

Minicucci G., *Il dolo nella bancarotta. Alla ricerca della tipicità soggettiva della fattispecie patrimoniale*

Pattelli L., *Imaging light transport at the femtosecond scale: a walk on the wild side of diffusion*

Egea Molines M.T., *Etnobotánica en el Alto Valle del Reno (Toscana y Emilia-Romaña, Italia). Etnobotanica nell'Alta Valle del Reno (Toscana ed Emilia-Romagna, Italia)*

Romano I.M., *Pressione turistica sul Centro Storico di Firenze - sito UNESCO. Un modello per la valutazione dell'impatto percettivo*

ANNO 2018

Costa A., *Histaminergic neurotransmission as a gateway for the effects of the fat sensing molecule Oleoylethanolamide. Focus on cognition and stress-reactivity*

Solera D., *«Sotto l'ombra della patente del Santo Officio». I* familiares *dell'Inquisizione romana tra XVI e XVII secolo*

Landi G., *Secession and Referendum. A new Dimension of International Law on Territorial Changes?*

Sacchetti A., *La costituente libertaria di Camillo Berneri. Un disegno politico tra federalismo e anarchismo*

Livi L.F., *New quantum simulations with ultracold Ytterbium gases*

Bellini E., *Ambienti sensoriali "terapeutici" che rendano Abili. Un progetto integrato di vita per persone con Disturbi dello Spettro Autistico*

Piscitelli L.R., *Serviceability and post-failure behaviour of laminated glass structural elements*